UNIVERSIDAD NACIONAL AUTÓNOMA DE MÉXICO
PROGRAMA DE POSGRADO EN CIENCIAS DE LA TIERRA, INSTITUTO DE GEOLOGÍA, ERNO

Petrología y geocronología del Complejo Metamórfico Sonobari y su implicación para la evolución tectónica del noroeste de México

T E S I S
QUE PARA OPTAR POR EL GRADO DE
DOCTOR EN CIENCIAS DE LA TIERRA

P R E S E N T A
ALICIA SARMIENTO VILLAGRANA

TUTOR
Dr. Ricardo Vega Granillo, UNISON

COMITÉ TUTOR
Dr. Martín Valencia Moreno, ERNO, UNAM
Dr. Thierry Calmus, ERNO, UNAM
Dr. Oscar Talavera Mendoza, UAGRO

Hermosillo, Sonora, marzo, 2018

Dedicada especialmente a las personas que

mueven mi mundo

Mi esposo

Juan René

y

Mis hijos

Isaac Neri y Diego René

Agradecimientos

Un agradecimiento especial al Consejo Nacional de Ciencia y Tecnología (CONACYT) por haberme otorgado la beca para el doctorado durante el periodo 2013-2017.

Un agradecimiento muy especial al Dr. Ricardo Vega por invitarme a participar en su proyecto CONACYT **"Petrología, deformación, termobarometría, geoquímica y geocronología de las rocas metamórficas del norte de Sinaloa y sur de Sonora"** con número: 177668, del cual fue financiada esta tesis doctoral. Gracias maestro por su tiempo dedicado para guiarme hacia la conclusión de este proyecto, por todos los gratos momentos de discusiones, por sus comentarios y revisiones de esta tesis, por su confianza y amistad.

Un agradecimiento al Dr. Joaquín Ruiz de la Universidad de Arizona por aceptar ser mi cotutor durante mi estancia en esa universidad y por las facilidades prestadas en los laboratorios de la misma universidad.

También quiero agradecer a mi comité tutor: Dr. Martín Valencia, Dr. Oscar Talavera y Dr. Thierry Calmus por formar parte de este proyecto, ustedes fueron parte fundamental durante todo el proceso y conclusión de esta tesis doctoral. Gracias por sus comentarios y revisiones para mejor esta tesis.

Sin duda un agradecimiento muy especial al Dr. Sergio Salgado por su apoyo incondicional y asesoramiento durante mi estancia en la Universidad de Arizona. Un agradecimiento muy especial Juan René Gómez por su apoyo incondicional durante todo el doctorado. A mis hijos Isaac y Diego por todo su apoyo y cariño siempre.

Muchas gracias a mi comité de grado el Dr. Fernando Ortega, Dr. Martín Valencia, Dr. Luis Delgado, Dr. Francisco Paz y Dr. Ricardo Vega por sus valiosos comentarios para mejorar esta tesis doctoral.

A la Geól. Aimée Orci técnico del Laboratorio de Laminación del Instituto de Geología, Estación Regional del Noroeste, por el apoyo con la elaboración de láminas delgadas de la tesis doctoral.

A los estudiantes de la UNISON Javier García Huerta, Angélica Bourjac y Víctor Hugo Vázquez quienes me acompañaron en algunas salidas a campo, ¡Gracias por su compañerismo!. A los estudiantes de maestría de la UAGro, Fredy y Ana quienes colaboraron durante la etapa de cromatografía y análisis de los isótopos de Pb y Sr. ¡Gracias amigos por hacer de las estancias en Arizona algo inolvidable!. A mis compañeros de la ERNO Alejandra, Arturo, David y Yesi por su amistad y momentos inolvidables.

A la universidad Autónoma de Guerrero, Escuela Regional de Ciencias de la Tierra quien colaboró con la separación de zircones de muchas muestras y quienes realizaron la catodoluminiscencia de alta resolución en los zircones.

Al departamento de Geología de la Universidad de Sonora por su colaboración con la elaboración de láminas delgadas.

Índice general

Resumen

El Complejo Sonobari (CS) del noroeste de México está compuesto por rocas metamórficas derivadas de protolitos sedimentarios e ígneos con edades que van del Paleozoico al Mesozoico. Estas rocas presentan migmatización, foliación penetrativa y plegamiento. Las litologías previas están intrusionadas por plutones y diques sin metamorfismo. Este complejo ha sido interpretado como un orógeno paleozoico o como la extensión del basamento proterozoico del norte de Sonora. En algunos trabajos se ha propuesto como basamento del terreno Guerrero. En el presente estudio se propone un modelo distinto para el origen del complejo con base en geocronología U-Pb, geoquímica, isótopos y geotermobarometría. Los resultados obtenidos indican que el magmatismo en el CS inició durante el Triásico Temprano, posterior a la colisión de Gondwana-Laurencia y continuó hasta el Campaniano. Posteriormente, se emplazaron plutones durante el Paleoceno y Eoceno. El magmatismo posterior a la colisión descarta claramente la correlación con basamentos precámbricos del norte de Sonora. Las firmas geoquímicas e isotópicas sugieren que las rocas del CS se generaron y evolucionaron en un ambiente de arco continental, donde ocurrieron procesos de subducción, extensión y contaminación cortical por un basamento heterogéneo que pudo quedar como remanente de Pangea. El ambiente de arco continental del CS difiere del contexto de arco oceánico del superterreno Guerrero-Alisitos, indicando que no hay una correlación entre estos bloques como se ha propuesto. En este trabajo se propone una correlación entre el Batolito Peninsular oriental de Baja California caracterizado por plutones emplazados en rocas paleozoicas continentales. A principios del Cretácico Tardío el complejo registró un evento compresional con dirección de acortamiento NNW-SSE que causó el empuje, engrosamiento de la corteza y hundimiento de las unidades litológicas causando metamorfismo de alto grado en facies de anfibolita de las rocas occidentales, el cual fue fechado en ~91 Ma. El evento de engrosamiento que causó el metamorfismo pudo ser causado por la colisión del arco Alisitos contra el margen continental occidental mexicano.

Abstract

The Sonobari Complex (SC) in northwestern Mexico is composed by metamorphic rocks derived from sedimentary and igneous protoliths from Paleozoic to Mesozoic ages. These rocks show migmatitic structures, pervasive foliation, and some folding phases. Previous rocks are cut by abundant post-tectonic unmetamorphosed dikes and plutons. This complex was previously interpreted as a Paleozoic orogenic belt or as the southern extension of the Proterozoic basement of northern Sonora. Also, some authors have considered the Sonobari Complex as part of the basement of the composite Guerrero terrane. A new model for the origin of the Sonobari Complex is proposed in this thesis, which is supported by U-Pb geochronology, geochemical, isotopic, and geothermobarometric data. The results of this work indicate that magmatism in the SC began at least from the Early Triassic, after the Gondwana-Laurentia collision and carried on until Campanian time. Afterwards, Paleocene and Eocene plutons were emplaced. The former statements clearly dismiss the correlation with the Precambrian basements of northern Sonora. Geochemical and isotopic signatures suggest that rocks from the SC were originated and evolved in a continental arc setting involving subduction and extensional processes, as well as crustal contamination of a heterogeneous basement that could remain after the Pangea break-up. The continental arc setting of the SC differs from the oceanic arc context of the Guerrero-Alisitos superterrane, indicating that there is no genetic relation between these blocks as previously proposed. A relationship with the eastern Peninsular Ranges Batholith of Baja California is proposed in this work, which is characterized by hosted plutons in paleozoic continental rocks. During the earliest Late Cretaceous, the complex recorded a contractional tectonic event with NNW-SSE shortening direction, which caused thrusting, thickening of the crust, and sinking of the lithological units. This event caused high metamorphism of amphibolite facies conditions in rocks of the western complex. The thermal peak that yielded this metamorphic event occurred around 91 Ma. On the basis of its age and contractional character, the thickening event originating the metamorphism may be related with the collision of the Alisitos island arc against cortical blocks of Mexico.

1

GENERALIDADES

I. Introducción

El Complejo Sonobari definido por de Cserna y Kent, 1961, está ubicado en el noroeste de México, es un bloque constituido por un conjunto de rocas metamórficas de distinta naturaleza y edad. El estudio de este complejo es clave para descifrar la evolución geológica después de la amalgamación de Gondwana contra Laurencia, el cual finalizó en la consolidación del supercontinente Pangea. Este complejo ha sido estudiado durante las últimas décadas por diversos autores (Mullan et al., 1978; Anderson y Schmidt, 1983; Poole et al., 2005, Keppie et al., 2006, Vega-Granillo et al., 2008, 2011, 2012, 2013), quienes han interpretado que representa: 1) la extensión del basamento proterozoico del norte de Sonora (Mullan et al., 1978; Valencia-Moreno et al., 2001); 2) las zonas internas de un orógeno paleozoico relacionado a la colisión de Gondwana y Laurencia durante el ensamble de Pangea (Peiffer-Rangin, 1979; Poole et al., 2005); y, 3) parte del basamento del terreno Guerrero (Campa y Coney, 1983; Centeno-García et al., 2008), o bien como un terreno distinto denominado terreno Tahue (Sedlock et al., 1993). Considerando la controversia sobre su origen y posición, se hizo un estudio detallado de geocronología U-Pb, geoquímica, isótopos (Nd, Sr y Pb) y geotermobarometría en las rocas metamórficas e ígneas intrusivas con la finalidad de constreñir las edades de la actividad magmátic y del metamorfismo, así como de la petrogénesis de ambos tipos de roca con lo que se propone un modelo de evolución tectónica para el suroeste de Norteamérica.

Esta tesis consta de tres capítulos integrados por tres artículos: 1) el primero incluye un estudio detallado de geocronología U-Pb, para determinar las edades magmáticas y del metamorfismo, considerando que existe gran diversidad litológica en los protolitos de las rocas metamórficas y en los cuerpos intrusivos postectónicos; 2) un estudio geoquímico e isotópico de los diferentes eventos magmáticos para determinar la petrogénesis y el ambiente tectónico de las rocas ígneas y protolitos, y 3) un estudio petrográfico, termobarométrico y geocronológico del oeste del complejo para determinar las condiciones de presión-temperatura y edad del metamorfismo.

II. Marco geológico

El Complejo Sonobari aflora en el noroeste de México. Está limitado al norte por rocas sedimentarias paleozoicas de cuenca; hacia el este, por el magmatismo terciario de la Sierra Madre Occidental; hacia el sur, por rocas que han sido asignadas al terreno Guerrero; y al occidente, limita con las llanuras costeras del Golfo de California. Las características de los límites del Complejo Sonobari con los terrenos aledaños no se conocen, debido a que éstos están obliterados por procesos tectónicos terciarios relacionados a la apertura del Golfo de California y por sedimentos recientes que cubren dichos límites. Uno de los primeros antecedentes geológicos conocidos sobre la geología del Complejo Sonobari, es el mapa geológico elaborado por de Cserna y Kent (1961). Posteriormente, Mullan (1978) hizo un trabajo geológico donde presenta una descripción detallada de las unidades geológicas del área de El Fuerte y de las sierras San Francisco y Sonobari. En trabajos más recientes, el CS fue dividido en dos áreas geológicamente distintas:

1) El área Este (El Fuerte), integrada en su mayoría por rocas metasedimentarias polideformadas que constituyen la Formación Río Fuerte, la cual contiene conodontos del

Ordovícico Medio-Tardío (Mullan, 1978; Poole et al., 2005; 2010; Vega-Granillo et al., 2008). Esta formación está cortada por cuerpos intrusivos deformados del Jurásico Tardío (Vega-Granillo et al., 2008) e intrusivos del terciario sin deformación (Damon et al., 1983). Los metasedimentos de la Formación Río Fuerte están cabalgando a rocas volcano-sedimentarias foliadas del Jurásico Tardío que integran la Formación Topaco (Vega-Granillo et al., 2008).

2) El área Oeste, está constituida por el Gneis Francisco (Mullan, 1978) que consiste en rocas metasedimentarias paleozoicas (?), cuya procedencia sugerida por estudios de geocronología U-Pb en circones detríticos es Laurenciana (Vega-Granillo et al., 2013), ortogneises del Triásico (Anderson y Schmidt, 1983; Keppie et al., 2006; Vega-Granillo et al., 2013) y anfibolitas de edad desconocida. Vega-Granillo et al. (2013) determinó una edad ^{40}Ar-^{39}Ar de 67 Ma para estas rocas, la cual es interpretada como una edad de enfriamiento. Todas las unidades están cortadas por una gran cantidad de diques pegmatíticos y plutones no metamorfizados. Se encuentran expuestas en la sierra Sonobari y sierra San Francisco, las cuales se alargan en dirección N-S y se extienden entre los estados de Sonora y Sinaloa. La complejidad tectónica del complejo se debe a que ésta es una zona de traslapo donde han ocurrido una gran cantidad de procesos tectónicos que comenzaron durante el Paleozoico con la amalgamación de Gondwana y Laurencia, posteriormente durante el Mesozoico ocurrió intenso magmatismo, acreción de terrenos sospechosos (Campa y Coney, 1983), y finalmente un proceso de extensión que finalizó con la apertura del Golfo de California.

Figura 1. Localización del área de estudio en un mapa de terrenos tectonoestratigráficos del noroeste de México (Mapa modificado de Campa y Coney, 1983; y Poole et al.,2005; en Vega-Granillo et al., 2008).

III. Objetivos

Objetivo general

El objetivo general de este trabajo, es el estudio de las rocas metamórficas del Complejo Sonobari a través del uso de geocronología U-Pb, geoquímica e isotopía radiogénica de roca total y geotermobarometría, lo que nos permitirá determinar su edad, origen, presión-temperatura (P-T) y proponer un modelo de evolución tectonometamórfica.

Objetivos particulares

- Realizar un estudio detallado de petrografía y geocronología U-Pb en el área Oeste del complejo para definir las distintas unidades metamórficas e ígneas, lo que nos permitirá establecer la litoestratigrafía.

- Realizar un estudio geoquímico e isotópico (Nd, Sr y Pb) de los distintos eventos magmáticos para determinar la petrogénesis y el ambiente tectónico de la parte Este y Oeste del complejo y así determinar si existe una relación genética con el terreno Guerrero.
- Llevar acabo un estudio de geotermobarometría en las rocas metamórficas para determinar las condiciones de presión y temperatura (P-T) en que ocurrió el metamorfismo. Realizar pseudosecciones a partir de la composición química de anfibolitas, ortogneises y paragneises con el programa PERPLEX para determinar las fases presentes y evaluar la consistencia con los datos obtenidos a partir de la termobarometría. Así como, determinar la edad del metamorfismo con el método U-Pb en los sobrecrecimientos de zircones.
- Con los datos obtenidos se desarrollará un modelo tectónico de evolución para el suroeste de Norteamérica.

IV. Metodología

Para entender el origen y evolución del Complejo Sonobari se aplicaron distintas técnicas analíticas. Para resolver los objetivos planteados en este trabajo de investigación se procedió en primera instancia a realizar salidas de campo que consistieron en el reconocimiento, descripción y muestreo de las unidades geológicas. Debido a la variabilidad litológica, se llevó a cabo un muestreo detallado de las distintas unidades litológicas, tomando como criterio la composición mineralógica, la intensidad de la deformación, considerando que la mayoría de las rocas son ortogneises graníticos que muestran características texturales y mineralógicas similares. A todas

las muestras colectadas se les hizo petrografía y se seleccionaron muestras representativas para geocronología, geoquímica, isótopos de Nd, Sr, Pb y geotermobarometría.

Metodología U-Pb

Para los estudios geocronológicos se seleccionaron las muestras considerando su diferencia en composición mineralógica, la intensidad de deformación, sus relaciones geológicas con otras rocas y las evidencia de metamorfismo. Un total de veintiún muestras fueron fechadas por el método U-Pb en zircones. Los análisis se presentan en el Anexo 1, 2 y 3. Se fecharon diecisiete muestras para determinar la edad de los protolitos de las rocas metamórficas y algunos intrusivos ígneos y también se fecharon cuatro muestras de leucosoma para determinar la edad del metamorfismo y migmatización. Se colectaron alrededor de 5 o 6 kg de esquirlas limpias por cada muestra, cuidando que la roca estuviera fresca. Previamente a la trituración, las muestras fueron lavadas y secadas perfectamente para eliminar posibles contaminantes de suelos. La separación de zircones de la mitad de las muestras se llevó a cabo en la Universidad Autónoma de Guerrero y la otra mitad fueron procesadas en los laboratorios de Geociencias de la Universidad de Arizona, de la forma siguiente: 1) las muestras fueron trituradas con una quebradora de quijada hasta reducir la muestra al tamaño de las gravas; 2) se molieron en una pulverizadora de rodillos hasta reducirla al tamaño de las arenas (~0.063 – 2 mm); 3) se pasaron por una mesa Wilfley para separar las fracciones livianas de las densas, concentrando en la fracción densa los zircones; 4) la fracción densa se pasó por un separador magnético Frantz y en la fracción no magnética se recuperaron los zircones; 5) esta fracción no magnética se separó de nuevo ahora con líquidos pesados utilizando Methyl Iodine para obtener la fracción con zircones; 6) los zircones recuperados fueron montados en resina epóxica junto con sus respectivos estándares y fueron ligeramente pulidos para su análisis.

Previo a los fechamientos, se tomaron imágenes de catodoluminiscencia en alta resolución con la finalidad de ver la estructura interna de los zircones y, en su caso, de los sobrecrecimientos metamórficos. Las imágenes de alta resolución fueron obtenidas con un JEOL IT300 SEM en el Laboratorio de Microscopía Electrónica de Barrido de la Unidad Académica de Ciencias de la Tierra, Universidad Autónoma de Guerrero. Las imágenes de baja resolución se tomaron en un Hitachi 3400N SEM en el Laboratorio de LaserChron SEM de la Universidad de Arizona. La geocronología U-Pb en zircones se determinó utilizando un Photon Machine Analyte-G2 excimer laser ablation system, acoplado a un Nu Plasma HR multi-collector MC-ICP-MS en el laboratorio del Departamento de Geociencias de la Universidad de Arizona. Los datos geocronológicos fueron obtenidos durante varias sesiones entre los años 2013 y 2015. Los fechamientos se realizaron con un spot de 35 μm en los zircones de mayor tamaño, en los zircones de menor tamaño y en los sobrecrecimientos se hizo detalle utilizando un spot de 15 μm. Entre 40 y 80 granos fueron analizados por cada muestra, se analizaron centros y bordes. El fraccionamiento isotópico fue monitoreado mediante el análisis de los estándares SL y R33. Estos estándares fueron analizados una vez por cada tres análisis desconocidos. La edad fue calculada usando $^{206}Pb/^{238}U$ para zircones menores a 1.0 Ga y la edad $^{207}Pb/^{235}U$ para circones más antiguos. El procesamiento de datos se hizo mediante el software Isoplot de Ludwig (2003). Para mayores detalles sobre los procedimientos de separación y analíticos U-Pb revisar Gehrels et al. (2006, 2008, 2009).

Geoquímica e isótopos de Nd, Sr y Pb

Se analizaron un total de 44 muestras por roca total para determinar la concentración de elementos mayores y traza (los análisis se muestran en el Anexo 2). La preparación de las pulpas se realizó en un molino de ágata en los laboratorios de la Universidad de Arizona. Los análisis

geoquímicos de roca total se realizaron en el Laboratorio de ALS-Chemex en Vancouver, Canadá. Los elementos mayores se analizaron en un ICP-AES, los elementos traza y REE en un ICP-MS. Se analizaron 42 muestras de roca total por isótopos de Pb, 21 por isótopos de Sr y 16 por isótopos de Nd. La preparación de las muestras consistió en una trituracion de las muestras al tamaño arena y posteriormente fueron pulverizadas en un molino de ágata al tamaño arcilla (<0.002 mm). La digestión, cromatografía y análisis de los isótopos de Pb, Sr y Nd se realizaron en el laboratorio de Geociencias de la Universidad de Arizona. Se realizó digestión total de la muestra utilizando los estándares de calidad y protocolos de preparación utilizados del mismo laboratorio. Para todo el proceso de digestión, cromatografía y análisis se utilizaron ácidos 2X y agua Milli-Q (Millipore, 18.2 MΩ). Para los isótopos de Pb y Sr se pesaron entre 100 - 200 mg de cada muestra en parr bombs. Las muestras se digirieron con HF 29N y HNO_3 16N en un horno a 150 °C durante una semana. Una vez digerida la muestra, se le agregó $HCLO_4$ para eliminar la materia orgánica y se evaporó a 200°C. La separación del Pb y Sr consistió en los siguientes pasos: 1) Se acondicionaron las columnas y se agregó Sr-Spect TM hasta el cuello de la columna; 2) Se limpió la Sr-Spect TM agregando dos veces los siguientes reactivos: 0.5 ml HCL 2X 8M, 1ml de HNO_3 2X 0.1M, 2 ml de HNO_3 2X 8M; 3) Se centrifugó la muestra y se colocó en la columna; 4) Se lavó la muestra con los siguientes reactivos dos veces: 1ml de HNO_3 2X 8M, 1ml de HNO_3 2X 3M, 1ml de HNO_3 2X 8M y 1ml de HNO_3 2X 3M una vez; 5) Se lixivió el Rb de las muestras agregando una vez 200 µL de HNO_3 2X 0.1M. El Sr se recolectó agregando dos veces 1 ml de HNO_3 2X 0.1M, 2 ml de HNO_3 2X 0.1M y 0.5 ml de HCl 2X 2N. El Pb se recolectó agregando 1 ml de HCl 2X 8N dos veces. Finalmente, se evaporó la muestra recolectada, se agregó 1 ml de HNO_3 2X al 2% a cada muestra y se calentó en una plancha a 60 °C por un día. Los análisis de los isótopos de Pb fueron llevados a cabo de acuerdo al procedimiento descrito por Thibodeau et al. (2013). Los análisis de isótopos de Sr fueron

analizados siguiendo los protocolos descritos por Thibodeau et al. (2015). La cromatografía y análisis de Nd fueron realizados y analizados siguiendo la metodología descrita por Ducea et al. (2002). Para más detalles de la metodología de isótopos vea Sarmiento-Villagrana et al. (2017).

Geotermobarometría

Se seleccionaron muestras de unidades metamórficas e ígneas que incluyen anfibolitas, ortogneises, hornblenditas, gabros y granodioritas con mineralogía clave para determinar los análisis y cálculos geotermobarométricos. La preparación consistió en hacer primero una sección delgada y posteriormente se pulió al alto brillo. Las secciones delegadas y al alto brillo se elaboraron en el Departamento de Geología de la Universidad de Sonora y en el Instituto de Geología, Estación Regional del Noroeste, UNAM. La química mineral fue realizada en una Microsonda Electrónica CAMECA SX-100 del Laboratorio Lunar y Planetario del Departamento de Ciencias Planetarias de la Universidad de Arizona. Para más detalles sobre la metodología consulte Vega-Granillo et al. (2017). Los análisis se presentan en el Anexo 3.

2

Nuevas restricciones de edad para el magmatismo y metamorfismo del Complejo Sonobari Occidental y sus implicaciones para una orogenia del Cretácico Tardío más temprano en el noroeste de México

Artículo:

Sarmiento-Villagrana, A., Vega-Granillo, R., Talavera-Mendoza, O., and Vidal-Solano, J. R., 2016, New age constraints on magmatism and metamorphism of the Western Sonobari Complex and their implications for an earliest Late Cretaceous orogeny on northwestern Mexico: Revista Mexicana de Ciencias Geológicas, v. 33, no. 2, p. 170-182.

Contribuciones individuales de los autores:

Alicia Sarmiento Villagrana. Realización del trabajo de campo y muestreo, separación de zircones en el Franz, obtención de los fechamientos U-Pb. Elaboración y correcciones del manuscrito.

Ricardo Vega Granillo. Consecución del financiamiento. Trabajo de campo y muestreo. Obtención de fechamientos U-Pb y revisión del manuscrito para mejorar la versión final.

Oscar Talavera Mendoza. Participación en campo, separación de zircones, colaboración para la obtención de los fechamientos U-Pb. Realización de la catodoluminiscencia de alta resolución en los zircones. Revisión de la versión del manuscrito final.

Jesús Vidal Solano. Participación en campo y levantamiento de muestras. Revisión del manuscrito y aporte de ideas para mejor la versión final.

New age constraints on magmatism and metamorphism of the Western Sonobari Complex and their implications for an earliest Late Cretaceous orogeny on northwestern Mexico

Alicia Sarmiento-Villagrana[1], Ricardo Vega-Granillo[2,*], Oscar Talavera-Mendoza[3], and Jesús Roberto Vidal-Solano[2]

[1] *Instituto de Geología, Universidad Nacional Autónoma de México, Luis Donaldo Colosio esq. Madrid s/n, Hermosillo, Sonora, México, 83000.*
[2] *Departamento de Geología, Universidad de Sonora, Rosales y Encinas S/N, Hermosillo, Sonora, México, 83000.*
[3] *Unidad Académica de Ciencias de la Tierra, Universidad Autónoma de Guerrero, Taxco el Viejo, Guerrero, México, 40323.*
**rvega@ciencias.uson.mx*

ABSTRACT

The Western Sonobari Complex in northwestern Mexico is composed of orogenic metamorphic rocks intruded by a variety of unmetamorphosed plutons and dikes. Petrologic studies and U-Pb geochronology allow dividing the protolith of orthogneisses in the next groups: a) Lower Triassic granodiorite and quartz monzodiorite (249.6–241.3 Ma); b) Upper Triassic granodiorite (213.7–203.5 Ma); c) Upper Jurassic tonalite and granodiorite (162.9–159.1 Ma); and d) Lower Cretaceous diorite (99.9–98.8 Ma). Most of these rocks display amphibolite facies metamorphism, pervasive foliation and several stages of folding. Recrystallized zircon rims yield U-Pb ages of 92.3±4.1 and 90.1±1.3 Ma, which are interpreted to date the orogenic metamorphism. Metamorphic rocks are intruded by numerous post-orogenic granitic dikes dated at 83.9±0.5 to 80.6±1.7 Ma. Geochronology of igneous rocks indicates that the Cordilleran magmatic belts including Triassic and Jurassic plutons continue through northwestern-central Mexico apparently without displacement by the Mojave-Sonora megashear. Correlation based on the age, lithology of protoliths and metamorphic imprint suggests that the earliest Late Cretaceous orogen extends at least from southern California up to Nayarit in west-central Mexico. On the basis of its age and contractional character, the orogenic metamorphism event is related to the collision of the Alisitos arc against the western margin of Pangea but occurring inland the continent not at the contact between these blocks.

Key words: U-Pb geochronology; Mesozoic magmatism; orogenic metamorphism; Sonobari Complex; NW Mexico.

RESUMEN

El Complejo Sonobari Occidental en el noroeste de México está compuesto por rocas con metamorfismo orogénico con protolitos ígneos y sedimentarios, que son intrusionadas por diques y plutones no metamorfoseados. Estudios petrológicos y geocronología U-Pb permiten dividir el protolito de los ortogneises en los siguientes grupos: a) cuarzo monzodiorita y granodiorita del Triásico Inferior (249.6–241.3 Ma); b) granodiorita del Triásico Superior (213.7–203.5 Ma); c) granodiorita y tonalita del Jurásico Superior (162.9–159.1 Ma); y d) diorita del Cretácico Inferior (99.9–98.8 Ma). La mayoría de esas rocas muestran un metamorfismo de facies de anfibolita, foliación penetrativa y algunas etapas de plegamiento. Bordes de recristalización en zircón produjeron edades de 92.3±4.1 y 90.1±1.3 Ma, las cuales se interpreta que fechan el metamorfismo orogénico. Las rocas metamórficas son cortadas por numerosos diques graníticos post-orogénicos fechados entre 89.6±1.7 y 83.9±0.5 Ma. La geocronología de las rocas ígneas indica que los cinturones magmáticos cordilleranos incluidos los del Triásico y Jurásico continúan a través de la parte noroccidental-central de México aparentemente sin desplazamiento por la megacizalla Mojave-Sonora. Correlaciones basadas en la edad, litología de los protolitos y el carácter metamórfico, sugieren que el orógeno del Cretácico Tardío más temprano se extiende al menos desde el sur de California hasta Nayarit en México centro-oriental. Con base en su edad y su carácter compresivo, el evento de metamorfismo orogénico se atribuye a la colisión del arco Alisitos contra el margen occidental de Pangea, pero ocurriendo hacia el interior del continente, no en el contacto entre esos bloques.

Palabras clave: Geocronología U-Pb; magmatismo mesozoico; metamorfismo orogénico; Complejo Sonobari; NW de México.

INTRODUCTION

In spite of their complexity, orogenic metamorphic rocks play a crucial role on deciphering the tectonic evolution of mountain belts. The Sonobari Complex of northwestern Mexico is an assemblage of metamorphic rocks regarded either as an extension of the Paleoproterozoic basement of northern Sonora (Mullan, 1978) or as the internal zones of a Paleozoic orogen related to the collision of Gondwanaland against

Sarmiento-Villagrana A., Vega-Granillo, R., Talavera-Mendoza,O., Vidal-Solano, J.R., 2016, New age constraints on magmatism and metamorphism of the Western Sonobari Complex and their implications for an earliest Late Cretaceous orogeny on northwestern Mexico: Revista Mexicana de Ciencias Geológicas, v. 33, núm. 2, p. 170-182.

southern Laurentia during the Pangea assembly (Peiffer-Rangin, 1979; Poole *et al*., 2005). On the basis of provenance data, protolith ages, lithology, and metamorphic imprint, Vega-Granillo *et al*. (2013) divided the Sonobari Complex into the Eastern Sonobari Complex dominated by Middle-Upper Ordovician, low-grade metasedimentary sequences of Gondwanan provenance (Poole *et al*., 2005; Vega-Granillo, *et al*., 2008); and, the Western Sonobari Complex made of lower Mesozoic (248–206 Ma), medium-grade metaigneous rocks (Anderson and Schmidt, 1983; Keppie *et al*., 2006; Vega-Granillo *et al*., 2013), whose evolution seems rather be related to the geologic evolution of the Cordilleran chain. In this context, the Western Sonobari Complex seems to represent locally-exhumed Mesozoic igneous suites previously preserved in the mid-lower crust, which may be a link between the Baja California and Sonora batholiths to the north, and the Sinaloa and Nayarit batholiths to the south. Parts of these igneous belts remain buried under younger sequences, or they were fragmented during opening of the Gulf of California. Continuity of the Cordilleran igneous and metamorphic belts is important for the tectonic reconstruction of Mexico, whose assemblage was mostly completed during the Mesozoic (*e.g.* Dickinson and Lawton, 2001).

Our field studies indicate the Western Sonobari Complex is made of a variety of protoliths, which underwent orogenic metamorphism, and were subsequently intruded by diverse igneous rocks. Considering the lithological diversity, current geochronological data are insufficient, and for that reason a detailed geochronologic study was carried out in this work, in order to constrain the ages of metamorphism and magmatic events. The obtained data allowed us to refine the geological evolution of the Western Sonobari Complex, to establish lithostratigraphic and to gain a more precise understanding of its role in the construction of the southern Cordilleran orogenic belt.

GEOLOGICAL SETTING

The Sonobari Complex is a low- to medium-grade metamorphic assemblage outcropping in southern Sonora and northern Sinaloa, northwestern Mexico (Figure 1), which was preliminarily mapped by de Cserna and Kent (1961). Mullan (1978) enhanced the cartography separating the western Francisco Gneiss from the eastern Río Fuerte, Corral Falso, and Topaco formations. The Río Fuerte Formation is a thick siliciclastic sequence with very scarce calcareous layers containing Middle-Late Ordovician conodonts (Poole *et al*., 2005; Poole *et al*., 2010), which underwent low-P greenschist facies metamorphism (Vega-Granillo *et al*., 2011). U-Pb geochronology in quartzite indicates a Gondwanan provenance (Vega-Granillo *et al*., 2008). The Corral Falso Formation was described as a metasedimentary sequence very similar to the Río Fuerte Formation, but the original criteria for separating these formations are no longer sustained (Vega-Granillo *et al*., 2008). Metamorphic rocks are intruded by Upper Jurassic (~155–151 Ma) granite stock and sills, and covered in nonconformity by the Upper Jurassic volcanosedimentary Topaco Formation. All previous units are deformed and metamorphosed by a second event tentatively ascribed to the Late Jurassic (Mullan, 1978; Vega-Granillo *et al*., 2008; 2011), and grouped into the Eastern Sonobari Complex by Vega-Granillo *et al*. (2013).

The Western Sonobari Complex is mainly exposed in the Sonobari and San Francisco ranges (Figure 1), which are limited by ~N-S Oligocene-Miocene normal faults bordering wide alluvial valleys. The main unit of this complex is the Francisco Gneiss, which consists of orthogneisses (Figure 2a, 2d, 2e), minor tabular bodies of amphibolite (Figure 2b, 2c), scarce paragneisses and schists, which underwent amphibolite facies metamorphism (Mullan, 1978; Keppie *et al*., 2006; Vega-Granillo *et al*., 2013). Facies assigment was based on the presence of amphibolite (*sensu stricto*, according to definition in Fettes and Desmons, 2007) and the mineral assemblage in orthogneisses (Best, 2003), which consists of plagioclase (andesine-oligoclase) + K feldspar + quartz + biotite ± muscovite ± hornblende. Metamorphic rocks display widespread migmatization developing stromatic leucosome bands, net-like veinlets, and disperse patchs of leucosome (Figure 2a, 2c, 2d, 2e). Detrital zircon data in paragneisses suggest a Laurentian provenance (Vega-Granillo *et al*., 2013) contrasting with the Gondwanan provenance of the Eastern Sonobari Complex. Orthogneisses yielded U-Pb ages of ~220 Ma (Anderson and Schmidt, 1983), ~206 Ma (Keppie *et al*., 2006), and an upper intercept age of 248±28 interpreted as a crystallization age (Vega-Granillo *et al*., 2013). At least one ENE-WSW oriented pervasive foliation overprints the metamorphic rocks, although some metasediments display two foliations. Some phases of north-verging isoclinal to open folds bend the foliation causing fold superposition structures (Figure 2e). These rocks are intruded by unmetamorphosed coarse-grained diorite to gabbro bodies, which in turn are cut by ultramafic and dioritic dikes (Figure 2f). Numerous pegmatite to aplite dikes, intrude previous lithologies (Figure 2d). Metamorphic rocks are also intruded by the lowermost Paleocene Los Parajes Granodiorite (64 Ma; U-Pb zircon) and by the Eocene Macochin Gabbro (54 Ma, ^{40}Ar-^{39}Ar hornblende) (Vega-Granillo *et al*., 2013), both exposed in the southern Sonobari range.

METHODS

Rock modal classification was performed through detailed petrography of selected samples. Samples include a variety of orthogneisses, and different types of non-foliated felsic rocks, which intrude the tectonites. Details of the procedures for sampling and analyzing are described in the supplemental file S1. Low-resolution cathodoluminiscence images were obtained in the Arizona LaserChron Center, while high-resolution images were obtained in the Facultad de Ciencias de la Tierra de la Universidad Autónoma de Guerrero. The U-Pb analyses were performed by LA-ICPMS at the Arizona LaserChron Center (Tucson, Arizona). Data were collected during several analytical sessions from 2013 and 2015, utilizing a Nu Plasma ICPMS connected to a Photon Machines Analyte G2 excimer laser. A complete Excel dataset is included in the supplemental file S2.

RESULTS OF U-PB GEOCHRONOLOGY

Metamorphic rocks

The oldest orthogneisses in the area derive from medium-grained mesocratic granodiorite and quartz monzodiorite corresponding to the samples SFO-159 and SFO-56 (Figures 2a, 2b). Location and mineralogical composition of each sample are included in Table 1. These rocks yielded Early Triassic weighted average ages of 249.6±2.1 Ma and 241.3±2.4 Ma, respectively (Figure 3a, 3b). Scarce lower Paleozoic ages in the sample SFO-56 were obtained from inherited zircons, although most of the dated cores yielded similar or slightly older ages than the rims.

A second group of ages is given by five Upper Triassic rocks. Orthogneiss SFO-155 is a medium-grained leucocratic granodiorite that yielded a weighted mean age of 213.7±1.6 Ma (Figure 3c). Zircons in this sample do not display inherited cores but several have irregular recrystallized rims. The next three dated orthogneisses are medium-grained leucocratic granodiorites very similar in mineralogy

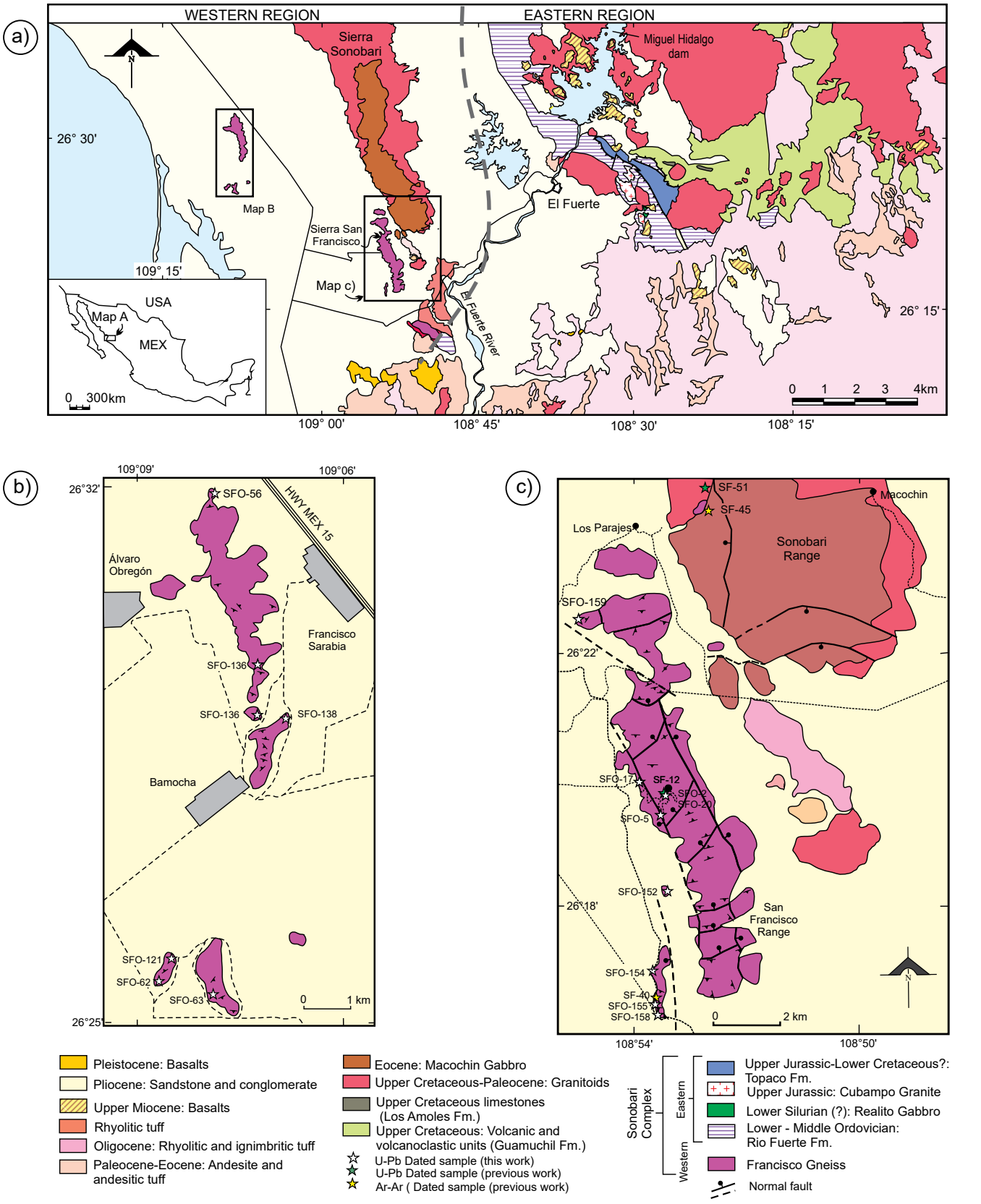

Figure 1. a) Geological map of the Sonobari Complex (modified from Escamilla-Torres *et al.*, 2000); b) Geological map of the western exposures; c) Geological map of the eastern exposures.

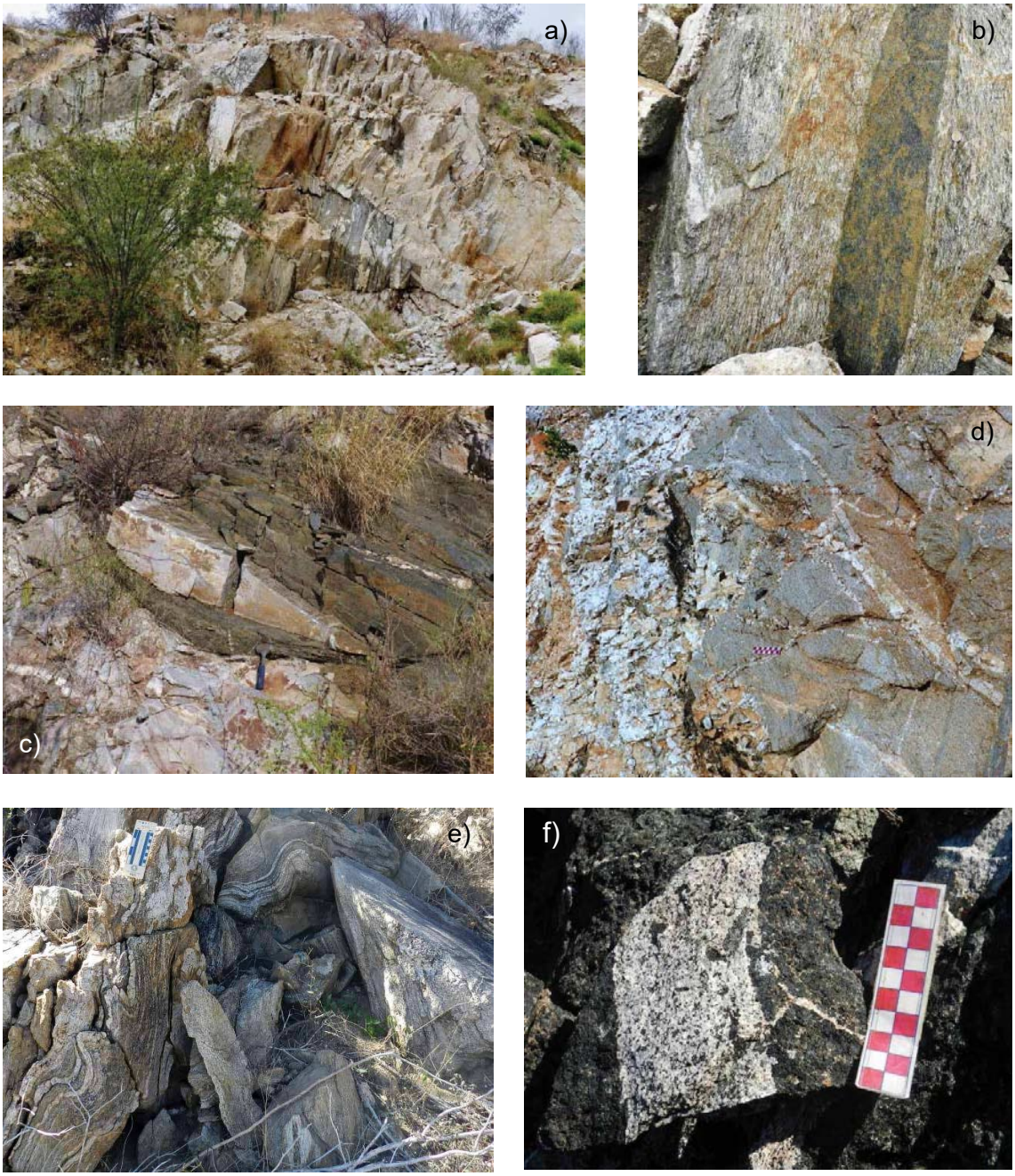

Figure 2. Outcrop images of the Western Sonobari Complex: a) Xenoliths of Lower Triassic quartz monzodiorite gneiss surrounded by Upper Cretaceous leucocratic aplite and pegmatite; b) Detail of the Lower Triassic quartz monzodiorite gneiss transected by amphibolite, foliation is parallel to the amphibolite-gneiss contact; c) Amphibolite dikes crosscutting Upper Triassic granodiorite gneiss, leucosome bands follow the foliation in both types of rocks, which is parallel to the amphibolite-gneiss contact; d) Upper Jurassic granodiorite gneiss transected by leucocratic pegmatite; e) Upper Jurassic tonalite gneiss with stromatic leucosome layers; f) Upper Cretaceous leucocratic diorite traversing melanocratic gabbro.

(Figure 2c, 2d; Table 1). Samples SFO-20, SFO-5, and SFO-158 yielded weighted mean ages of 207.4±1.7 Ma, 205.9±2.9 Ma, and 205.5±2.6 Ma, respectively (Figure 3d, 3e). Several zircons of the SFO-5 and SFO-20 samples indicate a trend to younger ages culminating at ~90 Ma. Sample SFO-154 is a granodioritic orthogneiss that yielded a weighted average age of 203.5±1.4 Ma (Figure 3f). Ten younger ages of this sample are considered to reflect Pb-loss caused by the metamorphic imprint and were not included in the age calculation. Zircons of the sample SFO-20 display recrystallized rims with irregular shape (Figure 4). Some of these rims were dated with a 15 μm diameter beam yielding an age of 92.3±4.1 Ma (Figure 5a).

The third group of ages comprises four Middle-Upper Jurassic rocks. Samples SFO-62 and SFO-121 are medium-grained leucocratic granodiorites that yielded weighted mean ages of 162.9±2.5 Ma and 159.1±1.1 Ma, respectively (Figure 3g, 3j). In both samples, some zircons yield dispersed Middle Ordovician to Middle Triassic ages derived of inherited zircons. The sample SFO-63 is a medium-grained melanocratic rock of tonalitic composition (Figure 2e) that yielded a mean

age of 161.0±1.5 Ma (Figure 3h). Although this sample has a similar age than the previous two samples, the rock is more mafic, schistose, commonly with stromatic leucosome bands. The sample SFO-152 is a medium-grained mesocratic rock of granodioritic composition that yielded a weighted mean age of 160.3±0.6 Ma (Figure 3i). The four oldest zircons yielded Middle Permian to Early Triassic ages. A trend to younger ages is found in all the samples of this group, probably indicating mixing between igneous zircon and recrystallized zircon rims. In sample SFO-152 the six younger data obtained from the rims yielded a weighted mean age of 90.1±1.3 Ma (Figure 5b).

A fourth group of orthogneisses is represented by one lowermost Upper Cretaceous rock, sample SFO-138, which is a foliated diorite yielding an average age of 98.8±1.3 Ma (Figure 3k). Foliation in this rock is subparallel to the overall tectonic foliation and is made by preferred orientation of amphibole, elongation of plagioclase, and minor grain boundary recrystallization. Deposition of minerals in low-strain sites perpendicular to the foliation low-strain sites also occurs.

Undeformed igneous rocks

In several places of the westernmost exposures, coarse-grained melanocratic plutons lacking pervasive foliation intrude the deformed metamorphic rocks. In turn, these rocks are intruded by coarse-grained holomelanocratic pyroxenite, and by irregular coarse-grained leucocratic diorite dikes consisting of plagioclase-hornblende-clinopyroxene-biotite (Figure 2f, Table 1). A melanocratic gabbro is made of amphibole with minor plagioclase-clinopyroxene-titanite-rutile, with epidote-zoisite partially replacing plagioclase. A leucocratic dioritic dike (sample SFO-136) that crosscut the gabbro, yielded a mean age of 99.9±1.1 Ma (Figure 3l).

Numerous leucocratic granite dikes with thickness varying from several meters to centimeters crosscut the foliation of the metamorphic rocks (Figure 2a, 2d). Sample SFO-142 is a pegmatite dike from the western exposures (Figure 1) that yielded a weighted mean age of 83.9±0.5 Ma (Figure 6a). Sample SFO-17 is a pegmatite dike crosscuting the paragneisses in the western foothills of the Francisco range, which yields a mean age of 82.9±1.0 Ma (Figure 6b). The sample SFO-02 obtained uphill in the same range (Figure 1) is a medium-grained rock that yielded a weighted mean age of 80.6±1.7 (Figure 6c) coincident with that obtained from the pegmatite dike.

DISCUSSION

Chronology of magmatic events

The oldest metasedimentary rocks in the Western Sonobari Complex are paragneisses and micaschists that crop out in the lower western hillside of the San Francisco Range (Vega-Granillo *et al.*, 2013). These rocks were intruded by several magmatic pulses dated in this work, most of them preceding an orogenic metamorphism event. The first magmatic pulse is indicated by Lower and Middle Triassic

Table 1. U-Pb geochronology of the Western Sonobari Complex.

Event	Sample	UTM Zone 12 R		Rock type	Petrography	Mineralogy	Age (Ma)
		E	N				
1st Pulse	SFO-159	707,809	2'918,858	Orthogneiss	Medium-grained mesocratic granodioritic rock	Pl + Qtz + Bt + Amp + Ep + Zr	249.6 ± 2.1
	SFO-56	686,235	2'935,748	Orthogneiss	Medium-grained mesocratic quartz monzodiorite, migmatized with stromatic bands	Pl + Qtz + Bt + Amp + Ep + Sph + Zr	241.3 ± 2.4
2nd Pulse	SFO-155	710,474	2'907,659	Orthogneiss	Medium-grained leucocratic granodiorite rock	Pl + Qtz + Bt + Ms + Zr	213.7 ± 1.6
	SFO-20	710,652	2'913,886	Orthogneiss	Medium-grained and foliated leucocratic granodiorite	Pl + Qtz + Bt + Kfs + Sph + Zr	207.4 ± 1.7
	SFO-5	710,515	2'913,490	Orthogneiss	Medium-grained leucocratic granodiorite with penetrative foliation	Pl + Qtz + Bt + Ep + Zr	205.9 ± 2.9
	SFO-158	710,536	2'907,194	Orthogneiss	Medium-grained leucocratic granodiorite	Pl + Qtz + Bt + Pl + Zr	205.5 ± 2.6
	SFO-154	710,382	2'908,478	Orthogneiss	Medium-grained leucocratic granite	Pl + B t+ Qtz + Ep + Zr	203.5 ± 1.4
3rd Pulse	SFO-62	685,013	2'923,976	Orthogneiss	Medium-grained leucocratic granodiorite with patch migmatites estructures	Qtz + Pl + Bt + Kfs + Sph + Zr	162.9 ± 2.5
	SFO-63	686,202	2'923,555	Orthogneiss	Medium-grained melanocratic rock of tonalitic composition, schistose, and migmatized, with common stromatic leucosome bands	Bt + Amp + Pl + Qtz + Ep + Zr	161.0 ± 1.5
	SFO-152	710,928	2'910,966	Orthogneiss	Medium-grained mesocratic granodiorite	Pl + Qtz + Bt + Ep + Zr	160.3 ± 0.62
	SFO-121	685,220	2'924,370	Orthogneiss	Medium-grained leucocratic granodiorite	Pl + Qtz + Bt + Ep + Zr	159.1 ± 1.1
4th Pulse	SFO-136	687,358	2'930,299	Diorite dike	Coarse-grained leucocratic and undeformed diorite	Pl + Amp + Qtz + Sph + Px + Z r + Rt	99.9 ± 1.1
	SFO-138	687,942	2'930,260	Diorite	Medium-grained diorite with penetrative foliation	Pl + Amp + Qtz + Kfs + Bi + Ep + Zr	98.8 ± 1.3
5th Pulse	SFO-142	687,267	2'931,609	Pegmatite dike	Coarse-grained muscovite pegmatite	Kfs + Qtz + Pl + Ms + Grt + Zr	83.9 ± 0.5
	SFO-17	709,909	2'913,987	Pegmatite dike	Coarse-grained muscovite pegmatite with dynamic recrystallization	Kfs + Qtz + Pl + Ms + Grt + Zr	82.9 ± 0.7
	SFO-02	710,652	2'913,886	Aplite dike	Medium grained granitic rock with magmatic foliation	Qtz + Pl + Bt + Grt+ Zr	80.6 ± 1.7

Note: Qtz=Quartz, Pl=Plagioclase, Bt-=Biotite, Ms=Muscovite, Amp=Amphibole, Grt=Garnet, Ep=Epidote, Kfs=K-feldspar, Sph=Sphene, Zr=Zircon.

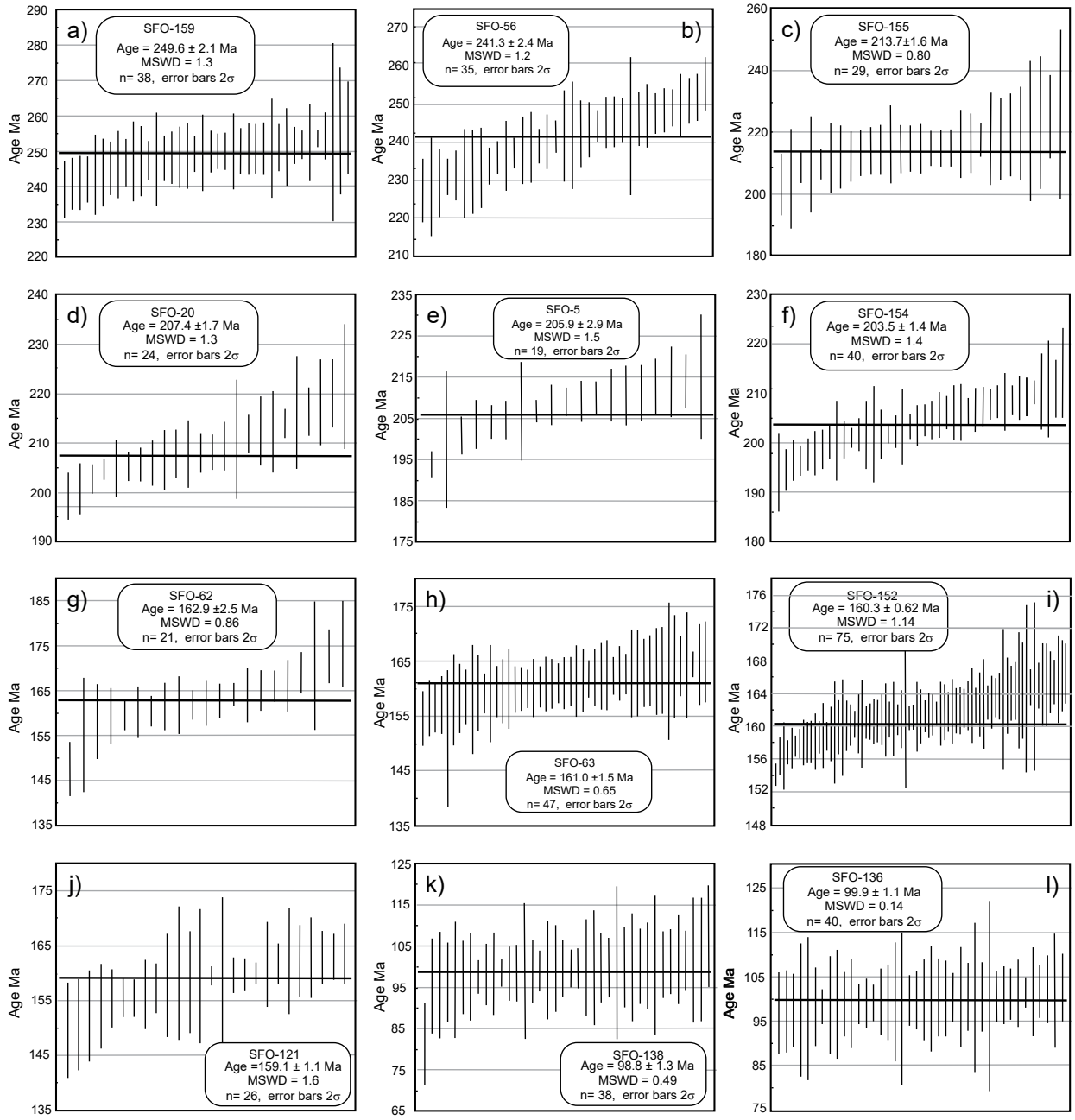

Figure 3. Weighted average ages of the Francisco Gneiss.

(249–241 Ma) granodiorite and quartz monzodiorite plutons. A second magmatic stage occurred in the Late Triassic (Norian-Rhaetian) with intrusion of two-mica granodiorite (213 Ma) followed by leucocratic biotite granodiorite (207–203 Ma). The latter rocks made the larger rock volume in the Francisco range although coeval rocks were not founded in the western exposures. The biotite granodiorite probably corresponds to the ~206 Ma age reported by Keppie *et al.* (2006) and the ~220 Ma age reported by Anderson and Schmidt (1983), considering the radiogenic Pb input of inherited zircons that cannot be avoided in the latter datation. The third magmatic pulse is made up of granodioritic plutons locally with garnet, and melanocratic tonalite, which yield Late Jurassic ages (Oxfordian, 163–159 Ma). All previous rocks are traversed by mafic tabular bodies, currently amphibolites, from which zircons cannot be extracted; therefore the age of their protolith remains unknown. Geochemistry and field relationships of the amphibolites suggest these rocks are tholeiitic basalts emplaced as dikes in a back-arc setting (Keppie *et al.*, 2006; Vega-Granillo *et al.*, 2013). The fourth group of orthogneisses is represented only for a tonalite dated at 98 Ma, which is coeval to the undeformed diorite dike dated at 99 Ma (Figure 2f). The undeformed diorite dike and its gabbro host are interpreted as segregations of a same parental magma based on mineralogy similarity and field relationships, and hence, they are considered nearly contemporaneous. The lacking of observable deformation of the gabbro and the crosscuting dike, while coeval dioritic rocks display well-developed foliations, can be ascribed to differences in competence caused by the coarser grain-size and predominant mafic mineralogy of the gabbro pluton. Alternatively, diorite foliation may be ascribed to magmatic or sub-magmatic flow caused by forced

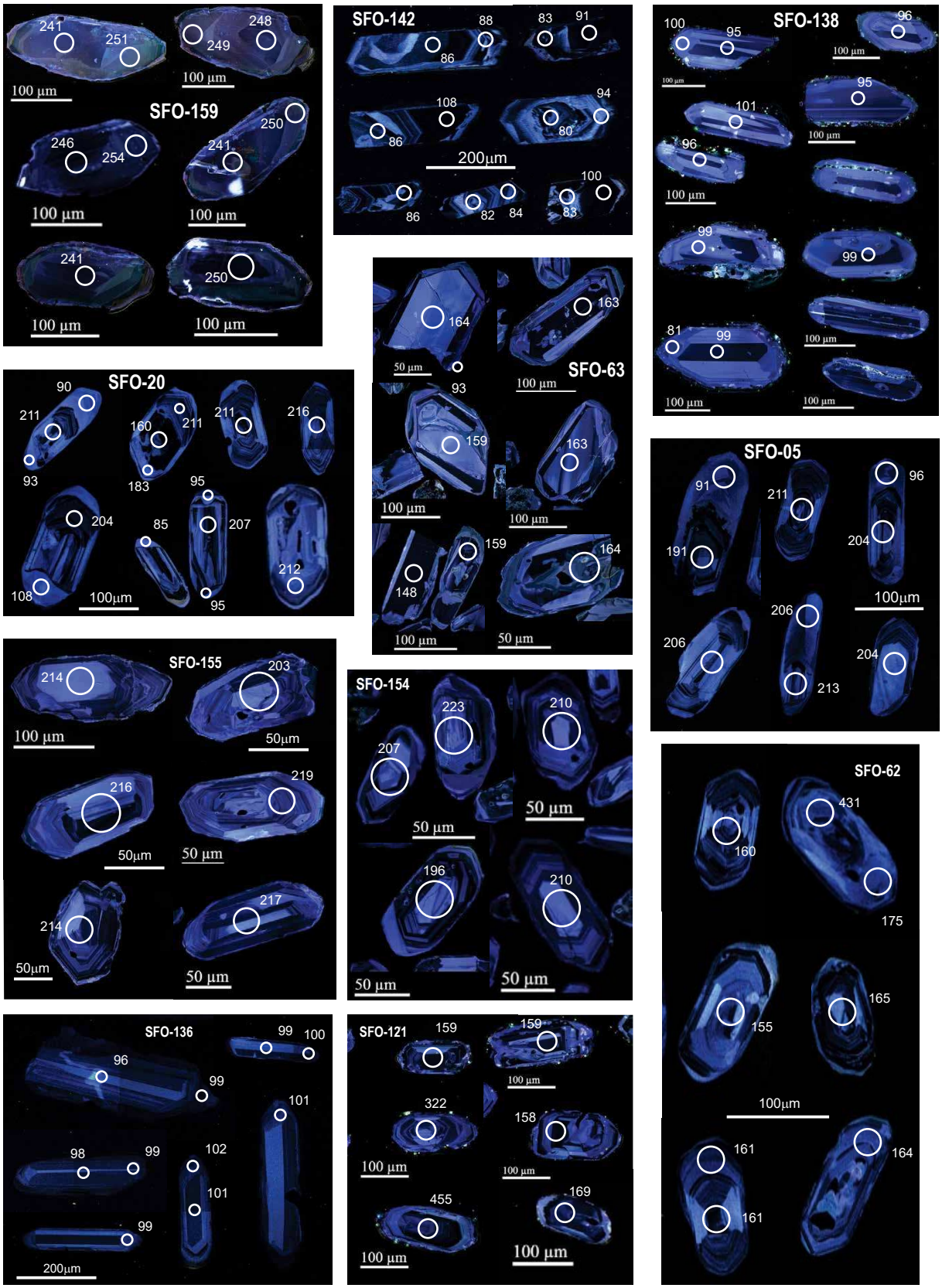

Figure 4. Cathodoluminscence images showing selected laser spots in zircons derived from metamorphosed and unmetamorphosed igneous rocks of the Western Sonobari Complex.

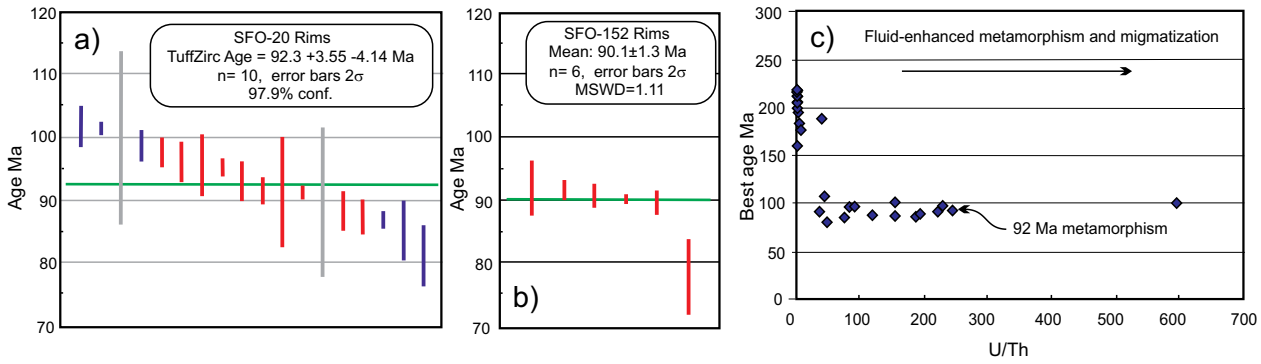

Figure 5. a) TuffZirc ages from recrystallized zircon rims of the Upper Triassic gneiss, sample SFO-20; b) Weighted average age of recrystallized zircon rims of the Upper Jurassic granodiorite gneiss sample SFO-152. c) Best ages versus U/Th content in the zircon Samples SFO-152 and SFO-20. Red bars were data used for age calculation.

emplacement. Anyway, parallelism of the diorite foliation to the overall orogenic foliation suggests that tectonic stresses were active during the diorite emplacement.

On the basis of the lithology and age similarities, the Lower to Upper Triassic magmatism in the Western Sonobari Complex may be related to the Permo-Triassic magmatism in the southwestern Cordillera (Figure 7), which has been classically ascribed to subduction of an oceanic plate under the North American plate (Burchfield and Davis, 1972; Kistler and Peterman, 1973; Dickinson, 1981). The magmatic arc dated from ~260 to 207 Ma in southwestern USA (Miller, 1978; Miller *et al*., 1995; Barth and Wooden, 2006; Anderson *et al*., 2010; Barth, 2010; Ehret *et al*., 2010; Barth *et al*., 2011; Riggs *et al*., 2012) was constructed over Proterozoic crust and its Paleozoic metasedimentary cover, and on accreted oceanic terranes or thinned continental crust to the north, and obliquely to the Paleozoic structural trends. Besides, a belt of Permo-Triassic granitoids (287–232 Ma) extends from Sonora along the entire length of Mexico (Figure 7), crossing various terrane boundaries (Damon *et al*., 1981; Yáñez *et al*., 1991; Torres *et al*., 1999; Schaaf *et al*., 2002; Weber *et al*., 2005; Arvizu *et al*., 2009). That belt continues in South America from Venezuela to Peru, yielding ages from 275 to 223 Ma (Cochrane *et al*., 2013 and references therein), although in this region it is interpreted as emplaced during continental rifting following the Pangea assembly.

Upper Jurassic granodiorite and tonalite intrusions dated in this study are partially coeval to a Lower to Upper Jurassic magmatic belt in the southwestern Cordillera (Figure 7), which includes plutons and a thick volcano-sedimentary sequence (Riggs *et al*., 1993; Anderson *et al*., 2005; Haxel *et al*., 2005). Coeval plutonic rocks occur in the Peninsular Ranges batholith of Baja California (Thompson and Girty, 1994; Schmidt and Paterson, 2002; Shaw *et al*., 2003; Valencia *et al*., 2006), the Eastern Sonobari Complex (Vega-Granillo *et al*., 2008), central Sinaloa (Cuéllar-Cárdenas *et al*., 2012), the Islas Marías offshore of the Nayarit coast (Pompa-Mera *et al*., 2013). Dickinson and Lawton (2001) proposed that the Jurassic arc in Mexico was east-facing and entirely exotic to North America prior to its collision in the Cretaceous. However, Schmidt *et al*. (2014) argue that these intrusions are intimately related with Triassic-Jurassic turbidite sequences of North American origin and thus, the Middle Jurassic arc must has formed *in situ* and was not exotic to North America. In eastern Mexico, the Middle-Late Jurassic Nazas Formation yielding ages from ~198 to 158 Ma (López-Infanzón, 1986; Bartolini and Spell, 1997; Barboza-Gudiño *et al*., 2004; 2008; Fastovsky *et al*., 2005; Zavala-Monsiváis *et al*., 2009; Barboza-Gudiño, 2012) has been also proposed as the extension of the northern Sonora Jurassic arc (Figure 7), but displaced by the left-lateral Mojave-Sonora megashear (Jones *et al*., 1995). That displacement has been challenged based on differences in the basements of each region (Molina-Garza and Iriondo, 2007), as well as on significant discrepancy in detrital zircon plots of sandstones intercalated within the volcanic sequences of each region (Lawton and Molina-Garza, 2014). If the Jurassic magmatism in our area and that of the Nazas arc were not displaced, then a wide magmatic arc must have occurred at that time, because more than 600 km separate both areas (Figure 7). An example of a wider than 600 km continental magmatic arc occurred in the Andean Cordillera from the Oligocene to Holocene times (*e.g.* Trumbull *et al*., 2006).

The earliest Late Cretaceous magmatic pulse dated in this study also occurred in the Sierra Nevada batholith (*e.g.* Sams and Saleeby, 1988; Saleeby *et al*., 2008); the Peninsular Ranges batholith (Schmidt and Paterson, 2002; Johnson *et al*., 2003; Wetmore *et al*., 2005; Peña-Alonso *et al*., 2012; Kimbrough *et al*., 2015), and central Sinaloa (Henry

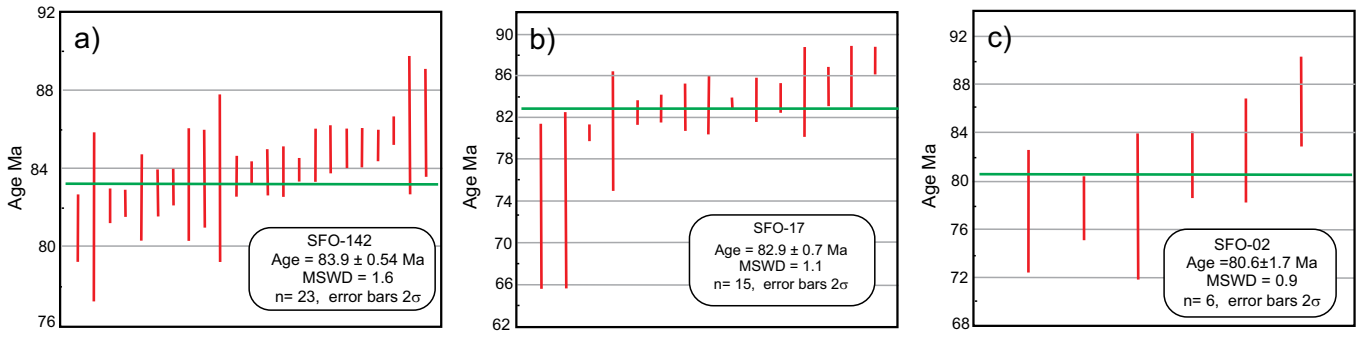

Figure 6. Weighted average ages of leucocratic pegmatite and aplite dikes that crosscut the metamorphosed rocks of the Francisco gneiss.

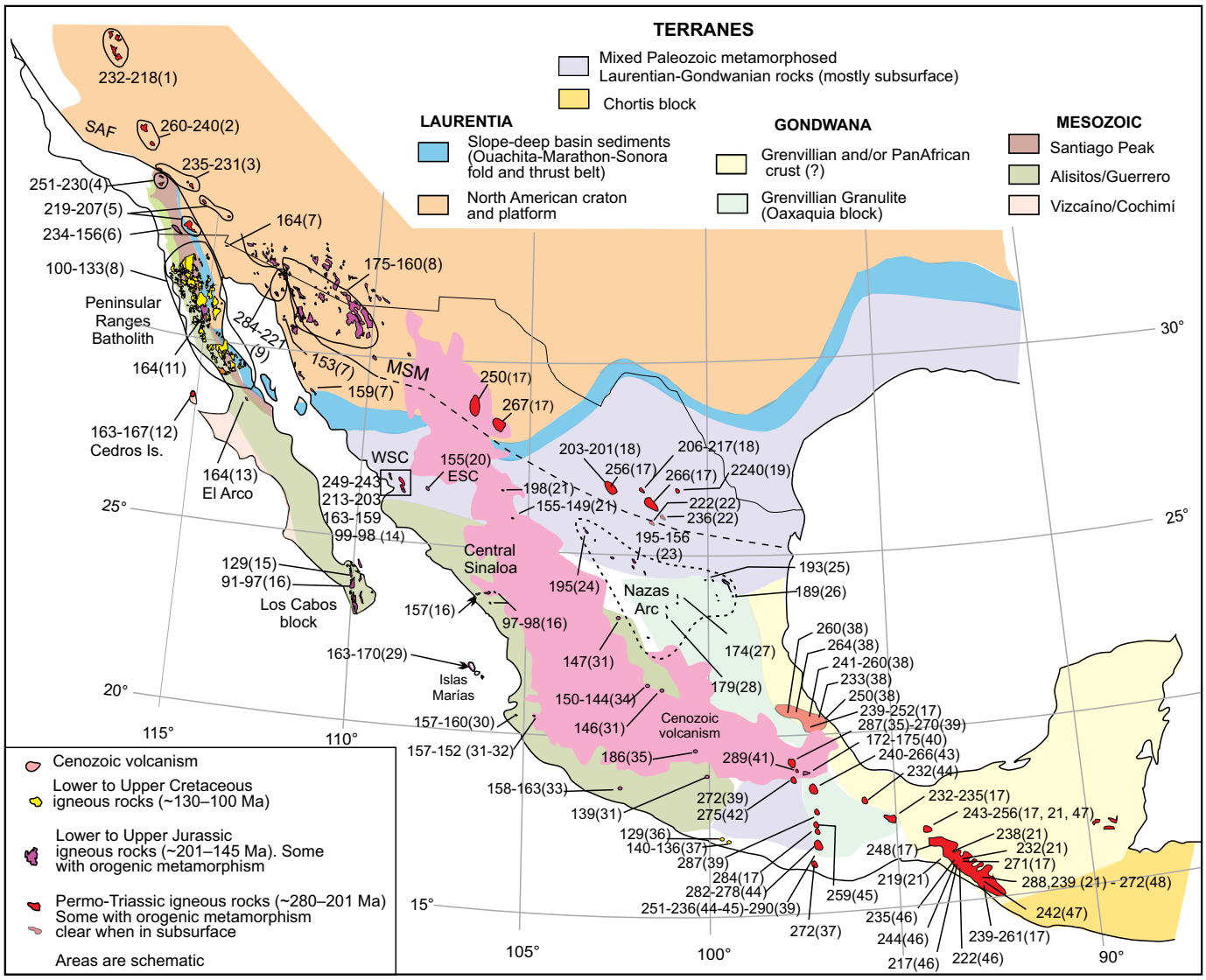

Figure 7. Map of terranes of Mexico and adjacent regions, mainly based on Poole *et al.* (2005); Campa and Coney (1983); Ortega-Gutiérrez *et al.* (1995); and Sedlock *et al.* (1993). Numbered references: 1: Anderson *et al.*, 2010; Ehret *et al.* (2010); Barth *et al.* (2010, 2011); 2: Miller *et al.* (1995); 3: Miller (1978); Barth and Wooden (2006); 4: Barth and Wooden (2006); 5: Barth *et al.* (1990); Barth and Wooden (2006); 6: Thompson and Girty (1994); 7: Anderson *et al.* (2005); 8: Anderson *et al.* (2005); Haxel *et al.* (2005); 9: Arvizu *et al.* (2009); Riggs *et al.* (2009; 2010); 10: Schmidt *et al.* (2014); 11: Schmidt and Paterson (2002); 12: Kimbrough and Moore (2003); 13: Valencia *et al.* (2006); 14: this work; 15: Schaaf *et al.* (2000); 16: Cuéllar-Cárdenas *et al.* (2012); 17: Murillo and Torres (1987, *in* Torres *et al.*, 1999); 18: Denison *et al.* (1969); Molina-Garza (2005); 19: McKee *et al.* (1990); 20: Vega-Granillo *et al.* (2008); 21: Damon *et al.* (1981); 22: Denison *et al.* (1975, *in* Grajales-Nishimura *et al.*, 1992); 23: Fries and Rincón-Orta (1965); López-Infanzón (1986); Jones *et al.* (1995); 24: Bartolini and Spell (1997); 25: Barboza-Gudiño *et al.* (2008); Zavala-Monsiváis *et al.* (2009); 26: Fastovsky *et al.* (2005); Zavala-Monsiváis *et al.* (2009); 27: Barboza-Gudiño *et al.* (2004); 28: Zavala-Monsiváis *et al.* (2012); 29: Pompa-Mera *et al.* (2013); 30: Schaaf *et al.* (2003); Valencia *et al.* (2013); 31: Mortensen *et al.* (2008); 32: Bissig *et al.* (2008); 33: López-Infanzón and Grajales-Nishimura (1984); Centeno-García *et al.* (2003); 34: Martini *et al.* (2011); 35: Elías-Herrera *et al.* (2000); 36: Solari *et al.* (2007); 37: Ducea *et al.* (2004); 38: Jacobo (1986); 39: Ortega-Obregón *et al.* (2013); 40: Yáñez *et al.* (1991); 41: Kirsch *et al.* (2012); 42: Solari *et al.* (2001); 43: Torres *et al.* (1986); 44: Grajales-Nishimura (1988); 45: Grajales-Nishimura *et al.* (1985, in Torres et al. 1999); 46: Schaaf *et al.* (2002); 47: Damon (1975); 48: Weber *et al.* (2007).

et al., 2003) (Figure 7). This magmatic belt can have resulted from the subduction resuming after collision of the Alisitos arc.

Chronology of the orogenic metamorphism

The recrystallized zircon rims of samples SFO-20 and SFO-152 render well defined ages of 92.3±4.1 Ma and 90.1±1.3 Ma, respectively (Figures 5a, b). Concordance and coincidence of ages from some zircon rims in these samples suggest that metamorphism caused either complete radiogenic Pb-loss in the recrystallized sectors of the original zircons or formed new zircon overgrowths. The U/Th ratios of the zircon rims in both samples are higher than 23.5 (Figure 5c). High U/Th values have been regarded as indicative of metamorphic imprint (Mezger and Krogstad, 1997; Rubatto 2002; Gehrels *et al.*, 2009). Also, several samples display a trend to younger ages culminating at ~90 Ma. The 92–90 Ma age of the metamorphic event is consistent with the 83 to 80 Ma ages of the leucocratic granitic dikes that clearly crosscut and postdate the orogenic foliation (Figures 6a - 6c). The ages of recrystallized zircon postdate concordant U-Pb titanite ages ranging from 112 to 98 Ma, and coincide with the oldest U-Pb xenotime ages varying from 91 to 51 Ma (Keppie *et al.*, 2006). A 67 ± 5 Ma $^{40}Ar/^{39}Ar$

hornblende age reported for the amphibolite of the Francisco range was interpreted as a cooling age after an orogenic event or after intrusion of the Los Parajes Granodiorite 64 Ma ago (Vega-Granillo *et al*., 2013), which could produce an overprinting contact metamorphism on the Francisco Gneiss.

On the basis of metamorphic facies, anatexis, folation development, and isoclinal folding, it is inferred that the orogenic metamorphism must require crustal shortening and thickening, and thus was originated in a contractional regime. Orogenic metamorphic rocks coeval to those in the study area have been reported from California to central Mexico. In the southernmost Sierra Nevada, Lower Cretaceous orthogneisses are intruded by lowermost Upper Cretaceous plutons (Sams and Saleeby, 1988), and ductile deformation is constrained to take place about 90 Ma (Saleeby *et al*., 2008). In the central zone of the southern Peninsular Ranges batholith, peak metamorphism reaching upper-amphibolite facies was achieved at ~100 Ma (Schmidt *et al*., 2014). The orogenic metamorphism and deformation in the Los Cabos block supposedly occured between 129 and 94 Ma (Pérez-Venzor, 2013). Two mylonitic gneisses of the same region yield $^{40}Ar/^{39}Ar$ ages of 91.5 and 97.1 Ma, obtained from biotite and muscovite respectively, which are considered as indicating the age of metamorphism (Cuéllar-Cárdenas *et al*., 2012). Deformed plutons in the Los Cabos block yield K-Ar ages older than 98 Ma, while post-tectonic intrusives yield K-Ar ages between 98 and 65 Ma (Aranda-Gómez and Pérez-Venzor, 1989). In central Sinaloa, syntectonic intrusions yield K-Ar hornblende ages ranging from 98 to 90 Ma; which are interpreted as cooling after regional metamorphism (Henry *et al*., 2003). In the same area, tonalites regarded as syntectonic were dated at 98.0 and 97.1 Ma (U-Pb zircon), while schist yielded a $^{40}Ar/^{39}Ar$ muscovite age of 94.47 Ma (Cuéllar-Cárdenas *et al*., 2012), while post-tectonic intrusions were emplaced nearly continuously between 90 and 45 Ma (Henry *et al*., 2003). In the Islas Marías, two dated rims from a latest Middle Jurassic orthogneiss yielded 87 and 83 Ma ages that are interpreted as indicating the metamorphic event (Pompa-Mera *et al*., 2013). Metamorphic rocks in these islands are intruded by 80.8-83.4 Ma (U-Pb, zircon) granites and overlain by Upper Cretaceous volcanic rocks dated at -80.6–71.6 Ma (Ar-Ar, sanidine; Pompa-Mera *et al*., 2013).

On the basis of its age and contractional character, the earliest Late Cretaceous orogenic event in the study area can be ascribed to the collision of the Late Jurassic-Early Cretaceous Alisitos arc against western North America. Most of the authors agree that the above mentioned arc was separated from the continent by a Cretaceous ocean basin of uncertain width (*e.g.*, Busby *et al*., 1998; Johnson *et al*., 1999; Wetmore *et al*., 2003). The closure of this ocean basin began between by ~115 and 110 Ma and was completed between 108 and 105 Ma (Wetmore *et al*., 2002; 2003; Alsleben *et al*., 2008; Peña-Alonso *et al*., 2015). The impingement of the Alisitos arc against the North American margin caused greenschist to lower-amphibolite facies metamorphism in the marginal rocks of both blocks (Wetmore *et al*., 2002; Schmidt *et al*., 2012). Such tectonic event could have spread inland the continent causing metamorphism and deformation in the study area several millions of years after collision.

Although Campa and Coney (1983) trace the limit of the Guerrero terrane through southern Sonora, in our view, irrefutable evidence of volcanic sequences similar to those of the Alisitos arc does not exist in the study area. Instead, the Triassic and Jurassic Cordilleran magmatic belts seem to extend from southern California until northern Sinaloa and possibly farther south. As a consequence of this continuity, the Mojave-Sonora Megashear may not cause the mentioned ~800 km of left-lateral displacement in Late Jurassic time as originally proposed (Campbell and Anderson, 2003; Anderson and Silver, 2005).

CONCLUSIONS

The Western Sonobari Complex is made of sedimentary rocks intruded by granitic plutons and dikes that underwent orogenic metamorphism. An extended history of magmatism is revealed by U-Pb geochronology, with five pulses encompassing from Early Triassic to Late Cretaceous, which continued until the Eocene according to previous works (Vega-Granillo *et al*., 2013). That plutonic suite indicates that Permo-Triassic to Late Cretaceous magmatic belts of the southwestern Cordillera extend along the Peninsular Ranges batholith and northwestern Sonora at least as far as the studied region and probably farther south, offshore of the Nayarit coast (*e.g.* Ortega-Gutiérrez *et al*., 2014. From California until Nayarit, the Permian to Lower Cretaceous plutons and their host rocks underwent a medium-grade orogenic metamorphism and deformation, which is well-constrained in the study area at ~92–90 Ma on the basis of U-Pb geochronology of zircon rims. Continued high-thermal gradients are indicated by the intrusion of numerous post-orogenic leucocratic pegmatite and aplite dikes between 83 and 80 Ma. The orogenic event occurred in a tectonic setting defined by collision-accretion of the Alisitos arc against the margin of the North America craton. In consequence, the Western Sonobari Complex is mostly related to the Mesozoic evolution of the North America Cordillera and evidence of the role of its oldest rocks in the Pangea assembly has not been found.

ACKNOWLEDGEMENTS

The research for this paper was financed by a CONACYT (177668) grant to Ricardo Vega-Granillo. Authors thank to Rafael Barboza Gudiño and Tomás A. Peña Alonso by their thorough and helpful reviews.

SUPPLEMENTARY MATERIAL

Supplemental files S1 "Methods" and S2 "U-Pb geochronological data" can be found at the journal web site <http: //rmcg. unarm. mx/>, in the table of contents of this issue.

REFERENCES

Alsleben, H., Wetmore, P.H., Schmidt, K.L., Paterson, S.R., Melis, E.A., 2008, Complex deformation during arc–continent collision: Quantifying finite strain in the accreted Alisitos arc, Peninsular Ranges batholith, Baja California: Journal of Structural Geology, 30(2), 220-236, DOI:10.1016/J.JSG.2007.11.001.

Anderson, J.L., Paterson, S., Memeti, V., Zhang, T., Economos, R., Barth, A.P., Pignotta, G., Mundil, R., Foley, B., Schmidt, K., 2010, Episodic downward crustal flow during Triassic to Cretaceous magma surges in the central Sierra arc: Geological Society of America Abstracts with Programs, 42(4), 51.

Anderson, T.H., Schmidt, V.A., 1983, A model of the evolution of Middle America and the Gulf of Mexico–Caribbean Sea region during Mesozoic time: Geological Society of America Bulletin, 94, 941–966.

Anderson, T.H., Silver, L.T., 2005, The Mojave-Sonora megashear-Field and analytical studies leading to the conception and evolution of the hypothesis: Geological Society of America Special Paper 393, 1-50, DOI.ORG/10.1130/0-8137-2393-0.1.

Anderson, T.H., Rodríguez-Castañeda, J.L., Silver, L.T., 2005, Jurassic rocks in Sonora, Mexico: Relations to the Mojave-Sonora megashear and its inferred northwestward extension. Geological Society of America Special Papers 393, 51-95.

Aranda-Gómez, J.J., Pérez-Venzor, J.A., 1989, Estratigrafía del complejo cristalino de la región de Todos Santos, Estado de Baja California Sur: Universidad Nacional Autónoma de México, Instituto de Geología, Revista, 8(2), 149-170.

Arvizu, H.E., Iriondo, A., Izaguirre, A., Chávez-Cabello, G., Kamenov, G.D., Solís-Pichardo, G., Foster, D.A., Lozano-Santa Cruz, R., 2009, Rocas graníticas pérmicas en la Sierra Pinta, NW de Sonora, México: Magmatismo de subducción asociado al inicio del margen continental activo del SW de Norteamérica: Revista Mexicana de Ciencias Geológicas, 6(3), 709-728.

Barboza-Gudiño, J.R., 2012, Sedimentary tectonics and stratigraphy: The early Mesozoic record in central to northeastern Mexico, *in* Elitok, Ö. (ed.), Stratigraphic Analysis of Layered Deposits: InTech, 255-277.

Barboza-Gudiño, J.R., Hoppe, M., Gómez-Anguiano, M., Martínez-Macías, P.R., 2004, Aportaciones para la interpretación estratigráfica y estructural de la porción noroccidental de la Sierra de Catorce, San Luis Potosí, México: Revista Mexicana de Ciencias Geológicas, 21(3), 299-319.

Barboza-Gudiño, J.R., Orozco-Esquivel, M.T., Gómez-Anguiano, M., Zavala-Monsiváis, A., 2008, The Early Mesozoic volcanic arc of western North America in northeastern Mexico: Journal of South American Earth Sciences, 25(1), 49-63, DOI:10.1016/J.JSAMES.2007.08.003.

Barth, A.P., 2010, Birth of the Sierra Nevada batholith: age and composition of the Scheelite Intrusive Suite and coeval volcanic rocks in the Saddlebag Lake Pendant, eastern California: Geological Society of America Abstracts with Programs, 42(5), 102.

Barth, A.P., Wooden, J.L., 2006, Timing of magmatism following initial convergence at a passive margin, southwestern US Cordillera, and ages of lower crustal magma sources: Journal of Geology, 114(2), 231-245, DOI:10.1086/499573.

Barth, A.P., Tosdal, R.M., Wooden, J.L., 1990, A petrologic comparison of Triassic plutonism in the San Gabriel and Mule Mountains, southern California: Journal of Geophysical Research, 95(B12), 20075-20096, DOI: 10.1029/JB095iB12p20075.

Barth, A.P., Riggs, N.R., Walker, J.D., Wooden, J.L., Schweickert, R.A., 2010, Birth of the Sierra Nevada Batholith: Age and composition of the Scheelite Intrusive Suite and coeval volcanic rocks in the Saddlebag Lake Pendant, eastern California: Geological Society of America Abstracts with Programs, 42(5), 102.

Barth, A.P., Walker, J.D., Wooden, J.L., Riggs, N.R., Schweickert, R.A., 2011, Birth of the Sierra Nevada magmatic arc: Early Mesozoic plutonism and volcanism in the east-central Sierra Nevada of California: Geosphere, 7(4), 877-897, DOI: 10.1130/GES00737.1.

Bartolini, C., Spell, T., 1997, An early Jurassic age ($^{40}Ar/^{39}Ar$) for the Nazas Formation at the Cañada Villa Juárez, notheastern Durango, México: Geological Society of America, Abstracts with Programs, 29(2), 3.

Best, M.G., 2003, Igneous and Metamorphic Petrology: Turin, Blackwell Publishing, 729 pp.

Bissig, T., Mortensen, J.K., Tosdal, R.M., Hall, B.V., 2008, The rhyolite-hosted volcanogenic massive sulfide District of Cuale, Guerrero terrane, West-Central Mexico: silver-rich, base metal mineralization emplaced in a shallow marine continental margin setting: Economic Geology, 103(1), 141-159.

Burchfiel, B., Davis, G.A., 1972, Structural framework and evolution of the southern part of the Cordilleran orogen, western United States: American Journal of Science, 27(2), 97-118, DOI: 10.2475/AJS.272.2.97.

Busby, C., Smith, D., Morris, W., Fackler-Adams, B., 1998, Evolutionary model for convergent margins facing large ocean basins: Mesozoic Baja California, Mexico: Geology, 26(3), 227-230, DOI: 10.1130/0091-7613.

Campa, U.M.F., Coney, P., 1983, Tectono-stratigraphic terranes and mineral resource distributions of Mexico: Canadian Journal of Earth Sciences, 20, 1040-1051.

Campbell, P.A., Anderson, T.H., 2003, Structure and kinematics along a segment of the Mojave-Sonora megashear: A strike-slip fault that truncates the Jurassic continental magmatic arc of southwestern North America: Tectonics, 22(6), DOI:10.1029/2002TC001367.

Centeno-García, E., Olvera-Carranza, K., Corona-Esquivel, R., Camprubí, A., Tritlla, J., Sanchez-Martinez, S., 2003, Depositional environment and paleogeographic distribution of the Jurassic-Cretaceous arc in the western and northern Guerrero terrane, Mexico: Geological Society of America Abstracts with Program, 35(4), 76.

Cochrane, R., Spikings,R., Gerdes, A., Ulianov, A., Mora, A., Villagómez, D., Putlitz, B., Chiaradia, M., 2013, Permo-Triassic anatexis, continental rifting and the disassembly of western Pangea: Lithos, 190-191, 383-402. DOI. ORG/10.1016/J.LITHOS.2013.12.020.

Cuéllar-Cárdenas, M.A., Nieto-Samaniego, Á.F., Levresse, G., Alaniz-Álvarez, S.A., Solari, L., Ortega-Obregón, C., López-Martínez, M., 2012, Límites temporales de la deformación por acortamiento Laramide en el centro de México: Revista Mexicana de Ciencias Geológicas, 29(1), 179-203.

Damon, P.E., 1975, Dating of Mesozoic-Cenozoic metallogenetic provinces within the Republic of Mexico (1965-1975), *in* Salas, G.P. (ed)., Carta y Provincias Metalogenéticas de la República Mexicana: Consejo de Recursos Minerales, 50-71.

Damon, P.E., Shafiqullah, M., Clark, K.F., 1981, Evolución de los arcos magmáticos en México y su relación con la metalogénesis: Revista Mexicana de Ciencias Geológicas, 5(2), 223-238.

De Cserna, Z., Kent, B.H., 1961, Mapa geológico de reconocimiento y secciones estructurales de la región de San Blas y El Fuerte, Estado de Sinaloa, escala 1:100,000: Cartas Geológicas y Mineras No. 4, Instituto de Geología, Universidad Nacional Autónoma de México.

Denison, R.E., Kenny, G.S., Burke, W.H., Hetherington, E.A., 1969, Isotopic ages of igneous and metamorphic boulders from the Haymond Formation (Pennsylvanian), Marathon Basin, Texas, and their significance: Geological Society of America Bulletin, 80(2), 245-256.

Dickinson, W.R., 1981, Plate tectonics and the continental margin of California, *in* Ernst, W.G.. (ed)., The geotectonic development of California (Rubey volume 1): Englewood Cliffs, N.J., Prentice-Hall, 1-28.

Dickinson, W.R., Lawton, T.F., 2001, Carboniferous to Cretaceous assembly and fragmentation of Mexico: Geological Society of America Bulletin, 113(9), 1142-1160.

Ducea, M.N., Gehrels, G.E., Shoemaker, S., Ruiz, J., Valencia, V.A., 2004, Geologic evolution of the Xolapa Complex, southern Mexico: Evidence from U-Pb zircon geochronology. Geological Society of America Bulletin, 116(7-8), 1016-1025.

Ehret, P., Culbert, K., Paterson, S., Cao, W., Memeti, V., Schmidt, K., 2010, Comparisons of detrital zircon ages and characteristics of metasedimentary packages in the Saddlebag Lake pendant, Sierra Nevada: implications for depositional environments and tectonic histories: Geological Society of America Abstracts with Programs, 42(4), 65 pp.

Elías-Herrera, M., Sánchez-Zavala, J.L., Macías-Romo, C., 2000, Geologic and geochronologic data from the Guerrero terrane in the Tejupilco area, southern Mexico: New constraints on its tectonic interpretation: Journal of South American Earth Sciences, 13(4-5), 355-376.

Escamilla-Torres, T., Saldaña-Saucedo, G., Polanco-Salas, A., Quevedo-León, A., and Moreno-López, M.H., 2000, Carta Geológica-Minera "Huatabampo G12-6" scale 1:250,000: Servicio Geológico Mexicano, 1 map.

Fastovsky, D.E., Hermes, O.D., Strater, N.H., Bowring, S.A., Clark, J.M., Montellano, M., Rene, H. R., 2005, Pre–Late Jurassic, fossil-bearing volcanic and sedimentary red beds of Huizachal Canyon, Tamaulipas, Mexico: Geological Society of America Special Paper 393, 401-426.

Fettes, D., Desmons, J., 2007, Metamorphic rocks, a classification and glossary of terms, Cambridge UK, Cambridge University Press, 244 pp.

Fries, C.Jr., Rincón-Orta, C., 1965, Nuevas aportaciones geocronológicas y técnicas empleadas en el Laboratorio de Geocronometría: Universidad Nacional Autónoma de México, Instituto de Geología, Boletín, 73, 57-133.

Gehrels, G., Rusmore, M., Woodsworth, G., Crawford, M., Andronicos, C., Hollister, L., Patchett, J., Ducea, M., Butler, R., Klepeis, K., Davidson, C., Friedman, R., Haggart, J., Mahoney, B., Crawford, W., Pearson, G., Girard, J., 2009, U-Th-Pb geochronology of the Coast Mountains batholith in north-coastal British Columbia: Constraints on age and tectonic evolution: Geological Society of America Bulletin, 121(9-10), 1341-1361; DOI:10.1130/B26404.1.

Grajales-Nishimura, J.M., 1988, Geology, geochronology, geochemistry and tectonic implications of the Juchatengo green rock sequence, State of Oaxaca, southern Mexico: Tucson, Arizona, University of Arizona, M.S. Thesis, 145 pp.

Grajales-Nishimura, J.M., Terrel, D.J., Damon, P.E., 1992, Evidencias de la prolongación del arco magmático cordillerano del Triásico Tardío-Jurásico en Chihuahua, Durango y Coahuila: Boletín Asociación Mexicana de

Geólogos Petroleros, 62(2), 1-18.

Haxel, G.B., Wright, J.E., Riggs, N.R., Tosdal, R.M., May, D.J., 2005, Middle Jurassic Topawa Group, Baboquivari Mountains, south-central Arizona: Volcanic and sedimentary record of deep basins within the Jurassic magmatic arc: Geological Society of America Special Paper 393, 329-357.

Henry, C.D., McDowell, F.W., Silver, L.T., 2003, Geology and geochronology of granitic batholitic complex, Sinaloa, México: implications for Cordilleran magmatism and tectonics: Geological Society of America Special Paper 374, 237-273.

Jacobo, A.J., 1986, El basamento del Distrito de Poza Rica y su implicación en la generación de hidrocarburos: Revista del Instituto Mexicano del Petróleo, 18, 5-24.

Johnson, S.E., Tate, M.C., Fanning, C.M., 1999, New geologic mapping and SHRIMP U-Pb zircon data in the Peninsular Ranges batholith, Baja California, Mexico: Evidence for a suture?: Geology, 27(8), 743-746, DOI:10.1130/0091-7613.

Johnson, S.E., Fletcher, J.M., Fanning, C.M., Paterson, S.R., Vernon, R.H., Tate, M.C., 2003, Structure and emplacement of the San Jose tonalite pluton, Peninsular Ranges batholith, Baja California, Mexico: Journal of Structural Geology, 25, 1933–1957, DOI:10.1016/S0191-8141(03)00015-4.

Jones, N.W., McKee, J.W., Anderson, T.H., Silver, L.T.,1995, Jurassic volcanic rocks in northeastern Mexico: A possible remnant of a Cordilleran magmatic arc: Geological Society of America Special Paper 301, 179-190, DOI:10.1130/0-8137-2301-9.179.

Keppie, D.J., Dostal, J., Miller, B.V., Ortega-Rivera, A., Roldán-Quintana, J., Lee, J.W.K., 2006, Geochronology and geochemistry of the Francisco Gneiss: Triassic continental rift tholeiites on the Mexican margin of Pangea metamorphosed and exhumed in a Tertiary core complex: International Geology Review, 48(1), 1-16, DO:10.2747/0020-6814.48.1.1.

Kimbrough, D.L., Moore, T.E., 2003, Ophiolite and volcanic arc assemblages on the Vizcaino Peninsula and Cedros Island, Baja California Sur, Mexico: Mesozoic forearc lithosphere of the Cordilleran magmatic arc: Geological Society of America Special Paper 374, 43-71, DOI:10.1130/0-8137-2374-4.43.

Kimbrough, D.L., Grove, M., Morton, D.M., 2015, Timing and significance of gabbro emplacement within two distinct plutonic domains of the Peninsular Ranges batholith, southern and Baja California: Geological Society of America Bulletin, 127(1-2), 19-37, DOI:10.1130/B30914.1.

Kirsch, M., Keppie, J.D., Murphy, J.B., Solari, L.A., 2012, Permian–Carboniferous arc magmatism and basin evolution along the western margin of Pangea: Geochemical and geochronological evidence from the eastern Acatlán Complex, southern Mexico: Geological Society of America Bulletin, 124(9-10), 1607-1628.

Kistler, R.W., Peterman, Z.E., 1973, Variations in Sr, Rb, K, Na, and initial Sr^{87}/Sr^{86} in Mesozoic granitic rocks and intruded wall rocks in central California: Geological Society of America Bulletin, 84(11), 3489-3512.

Lawton, T.F., Molina-Garza, R.S., 2014, U-Pb geochronology of the type Nazas Formation and superjacent strata, northeastern Durango, Mexico: Implications of a Jurassic age for continental-arc magmatism in north-central Mexico: Geological Society of America Bulletin, 126 (9-10), 1181-1199, DOI:10.1130/B30827.1

López-Infanzón, M., 1986, Estudio petrogenético de las rocas ígneas en las Formaciones Huizachal y Nazas: Boletín de la Sociedad Geológica Mexicana, 47(2), 1-37.

López-Infanzón, M., Grajales-Nishimura, J.M., 1984, Nuevos datos K-Ar y petrografía de las rocas ígneas y metamórficas de la región sudoccidental del Estado de Michoacán *in* VII Convención Geológica Nacional: México, D. F., Sociedad Geológica Mexicana, Resúmenes, p. 199.

Martini, M., Mori, L., Solari, L., Centeno-García, E., 2011, Sandstone provenance of the Arperos Basin (Sierra de Guanajuato, central Mexico): Late Jurassic–Early Cretaceous back-arc spreading as the foundation of the Guerrero terrane; The Journal of Geology, 119(6), 597-617.

McKee, J.W., Jones, N.W., Long, L.E., 1990, Stratigraphy and provenance of strata along the San Marcos fault, central Coahuila, Mexico: Geological Society of America Bulletin, 102(5), 593-614, DOI:10.1130/0016-7606.

Mezger, K., Krogstad, E.J., 1997, Interpretation of discordant U-Pb zircon ages: An evaluation: Journal of Metamorphic Geology, 15, 127-140.

Miller, C.F., 1978, Monzonitic plutons, California, and a model for generation of alkali-rich, near silica-saturated magmas: Contributions to Mineralogy and Petrology, 67(4), 349-355.

Miller, J.S., Glazner, A.F., Walker, J.D., Martin, M.W., 1995, Geochronologic and isotopic evidence for Triassic-Jurassic emplacement of the eugeoclinal allochthon in the Mojave Desert region, California: Geological Society of America Bulletin, 107(12), 1441-1457, DOI:10.1130/0016-7606.

Molina-Garza, R.S., 2005, Paleomagnetic reconstruction of Coahuila, Mexico: the Late Triassic Acatita intrusives: Geofísica Internacional, 44(2), 197-210.

Molina-Garza, R.S., Iriondo, A., 2007, The Mojave-Sonora megashear: The hypothesis, the controversy, and the current state of knowledge: Geological Society of America Special Paper, 422, 233-259, DOI:10.1130/2007.2422(07).

Mortensen, J.K., Hall, B.V., Bissig, T., Friedman, R.M., Danielson, T., Oliver, J., Rhys, D.A., Ross, K.V., Gabites, J.E., 2008, Age and paleotectonic setting of volcanogenic massive sulfide deposits in the Guerrero Terrane of central Mexico: Constraints from U-Pb age and Pb isotope studies: Economic Geology, 103(1), 117-140, DOI:0361-0128/08/3720/117-24.

Mullan, H.S., 1978, Evolution of part of the Nevadan orogen in northwestern Mexico: Geological Society of America Bulletin, 89(8), 1175-1188, DIO:10.1130/0016-7606.

Ortega-Obregón, C., Solari, L., Gómez-Tuena, A., Elías-Herrera, M., Ortega-Gutiérrez, F., and Macías-Romo, C., 2013, Permian–Carboniferous arc magmatism in southern Mexico: U–Pb dating, trace element and Hf isotopic evidence on zircons of earliest subduction beneath the western margin of Gondwana: International Journal of Earth Sciences, 103(5), 1287-1300.

Ortega-Gutiérrez, F., Ruiz, J., Centeno-García, E., 1995, Oaxaquia, a Proterozoic microcontinent accreted to North America during the late Paleozoic: Geology, 23(12), 1127-1130, DOI:10.1130/0091-7613.

Ortega-Gutiérrez, F., Elías-Herrera, M., Morán-Zenteno, D.J., Solari, L., Luna-González, L., Schaaf, P., 2014, A review of batholiths and other plutonic intrusions of Mexico: Gondwana Research, 26(3), 834-868.

Peiffer-Rangin, F., 1979, Les zones isopiques du Paléozoique inférieur du NW Mexicain. Temoins du relais entre les Appalaches et la cordillère ouest-américaine. Comptes Rendus Academie Sciences, Paris t 288, série D, 1517-1519.

Peña-Alonso, T.A., Delgado-Argote, L.A., Weber, B., Velasco-Tapia, F., Valencia, V., 2012, Geology and emplacement history of the Nuevo Rosarito plutonic suite in the southern Peninsular Ranges batholith, Baja California, México, Revista Mexicana de Ciencias Geológicas, 29(1), 1-23.

Peña-Alonso, T.A., Delgado-Argote, L.A., Molina-Garza, R.S., 2015, Early Cretaceous pre-batholith dextral-transpression in the central Baja California peninsula: the record of the La Unión complex, Baja California, Mexico, International Geology Review, 57(1), 28-54.

Pérez-Venzor, J.A., 2013, Estudio geológico-geoquímico del borde oriental del Bloque de los Cabos, Baja California Sur, México: México, D.F., Universidad Nacional Autónoma de México, Ph.D. thesis, 297 pp.

Pompa-Mera, V., Schaaf, P., Hernández-Treviño, T., Weber, B., Solís-Pichardo, G., Villanueva-Lascurain, D., Layer, P., 2013, Geology, geochronology, and geochemistry of Isla María Madre, Nayarit, Mexico: Revista Mexicana de Ciencias Geológicas, 30(1), 1-23.

Poole, F.G., Perry Jr., W.J., Madrid, R.J., Amaya-Martínez, R., 2005, Tectonic synthesis of the Ouachita–Marathon–Sonora orogenic margin of southern Laurentia: Stratigraphic and structural implications for timing of deformational events and plate-tectonic model: Geological Society of America Special Paper 393, 543–596, DOI:10.1130/0-8137-2393-0.543.

Poole, F.G., Amaya-Martínez, R., Premo, W.R., Berry, W.B.N., Sandberg, C.A., Roldán-Quintana, J., Herrera-Urbina, S., 2010, Age and depositional setting of deep-marine Ordovician Río Fuerte and San José de Gracia formations in northern Sinaloa, Mexico: remnants of the early Paleozoic Iapetus ocean, Geological Society of America Abstracts with Programs, 42(5), 268 pp.

Riggs, N.R., 2010, Use of zircon geochemistry to tie volcanic detritus to source plutonic rocks: An example from Permian northwestern Sonora, Mexico: Geological Society of America Abstracts with Programs, 42(5), 267 pp.

Riggs, N.R., Mattinson, J.M., Busby, C.J., 1993, Correlation of Jurassic eolian strata between the magmatic arc and the Colorado Plateau: New U-Pb geochronologic data from southern Arizona: Geological Society of America Bulletin, 105(9), 1231-1246.

Riggs, N., Barth, A.P., Walker, D., 2009, Geochemistry and alteration patterns

in the early Mesozoic Cordilleran arc and arc-related rocks: evidence for sources of detritus in continental successions: American Geophysical Union, Fall Meeting, Abstracts, 1, 1714 pp.

Riggs, N.R., Barth, A.P., González-León, C.M., Jacobson, C.E., Wooden, J.L., Howell, E.R., Walker, J.D., 2012, Provenance of Upper Triassic strata in southwestern North America as suggested by isotopic analysis and chemistry of zircon crystals: Geological Society of America Special Paper 487, 13-36, DIO:10.1130/2012.2487(02).

Rubatto, D., 2002, Zircon trace element geochemistry: partitioning with garnet and the link between U–Pb ages and metamorphism: Chemical Geology, 184(1), 123-138.

Saleeby, J.B., Ducea, M.N., Busby, C.J., Nadin, E.S., Wetmore, P.H., 2008, Chronology of pluton emplacement and regional deformation in the southern Sierra Nevada batholith, California, *in* Wright, J.E., and Shervais, J.W., eds., Ophiolites, Arcs, and Batholiths: A Tribute to Cliff Hopson: Geological Society of America Special Paper 438, 397-427.

Sams, D.B., Saaleby, J.B., 1988, Geology and petrotectonic significance of crystalline rocks of the southernmost Sierra Nevada, California, *in* Ernst, W.G. (ed.), Rubey Volume VII, Metamorphism and Crustal Evolution in the Western United States: Englewood Cliffs, New Jersey, Prentice-Hall, 866-893.

Schaaf, P., Böhnel, H., Pérez-Venzor, J.A., 2000, Pre-Miocene palaeogeography of the Los Cabos Block, Baja California Sur: geochronological and palaeomagnetic constraints: Tectonophysics, 318(1), 53-69.

Schaaf, P., Weber, B., Weis, P., Gross, A., Ortega-Gutiérrez, F., Kohler, H., 2002, The Chiapas Massif (Mexico) revised: New geologic and isotopic data and basement characteristics: Neues Jahrbuch fur Geologie und Palaontologie-Abhandlungen, 225(1), 1-23.

Schaaf, P., Hall, B.V., Bissig, T., 2003, The Puerto Vallarta Batholith and Cuale Mining District, Jalisco, Mexico—High diversity parenthood of continental arc magmas and Kuroko-type volcanogenic massive sulphide deposits: Guidebook for the field trips of the 99th Geological Society of America Cordilleran Section Annual Meeting, Puerto Vallarta, Jalisco, Mexico, 31, 183-199.

Schmidt, K.L., Paterson, S.R., 2002, A doubly vergent fan structure in the Peninsular Ranges batholith: Transpression or local complex flow around a continental margin buttress?: Tectonics, 2(5), 14-1, DOI :10.1029/2001TC001353.

Schmidt, K.L., Wetmore, P.H., Alsleben, H., Paterson, S.R., 2014, Mesozoic tectonic evolution of the southern Peninsular Ranges batholith, Baja California, Mexico: Long-lived history of a collisional segment in the Mesozoic Cordilleran arc: Geological Society of America Memoirs, 211, 645-668, DOI:10.1130/2014.1211(20).

Sedlock, R.L., Ortega-Gutiérrez, F., Speed, R.C., 1993, Tectonostratigraphic terranes and tectonic evolution of Mexico: Geological Society of America Special Paper 278, 1-153, DOI:10.1130/SPE278-p1.

Shaw, S.E., Todd, V.R., Grove, M., 2003, Jurassic peraluminous gneissic granites in the axial zone of the Peninsular Ranges, southern California: Geological Society of America Special Paper 374, 157-183, DOI:10.1130/0-8137-2374-4.157.

Solari, L.A., Dostal, J., Ortega-Gutiérrez, F., Keppie, J. D., 2001, The 275 Ma arc-related La Carbonera stock in the northern Oaxacan Complex of southern Mexico: U-Pb geochronology and geochemistry. Revista Mexicana de Ciencias Geológicas, 18(2), 149-161.

Solari, L.A., de León, R.T., Pineda, G.H., Solé, J., Solís-Pichardo, G., Hernández-Treviño, T., 2007, Tectonic significance of Cretaceous–Tertiary magmatic and structural evolution of the northern margin of the Xolapa Complex, Tierra Colorada area, southern Mexico: Geological Society of America Bulletin, 119(9-10), 1265-1279.

Thompson, C.N., Girty, G. H., 1994, Early Cretaceous intra-arc ductile strain in Triassic-Jurassic and Cretaceous continental margin arc rocks, Peninsular Ranges, California: Tectonics, 13(5), 1108-1119, DOI:10.1029/94TC01649.

Torres, R., Murillo, M.G., Grajales-Nishimura, J.M., 1986, Estudio petrográfico y radiométrico de la porción límite entre los complejos Acatlán y Oaxaqueño, *in* VII Convención Geológica Nacional: México D.F., Sociedad Geológica Mexicana, Resúmenes, 148-149.

Torres, R., Ruiz, J., Patchett, P.J., Grajales, J.M., 1999, A Permo-Triassic continental arc in eastern Mexico: Tectonic implications for reconstructions of southern North America: Geological Society of America Special Paper 340, 191-196, DOI:10.1130/0-8137-2340-X.191.

Trumbull, R.B., Riller, U., Oncken, O., Scheuber, E., Munier, K., Hongn, F., 2006, The time-space distribution of Cenozoic volcanism in the South-Central Andes: a new data compilation and some tectonic implications, *in* Oncken, O., Chong, G., Franz, G., Giese, P., Götze, H.J., Ramos, V.A., Strecker, M.R., Wigger, P.n(eds.), The Andes active subduction orogeny, Springer Berlin-Heidelberg, 29-43.

Valencia, V.A., Barra, F., Weber, B., Ruiz, J., Gehrels, G., Chesley, J., Lopez-Martinez, M., 2006, Re–Os and U–Pb geochronology of the El Arco porphyry copper deposit, Baja California Mexico: implications for the Jurassic tectonic setting: Journal of South American Earth Sciences, 22(1), 39-51, DOI:10.1016/j.jsames.2006.08.005.

Valencia, V.A., Righter, K., Rosas-Elguera, J., López-Martínez, M., Grove, M., 2013, The age and composition of the pre-Cenozoic basement of the Jalisco Block: implications for and relation to the Guerrero composite terrane: Contributions to Mineralogy and Petrology,166(3), 801-824, DOI:10.1007/s00410-013-0908-z.

Vega-Granillo, R., Salgado-Souto, S., Herrera-Urbina, S., Valencia-Gómez, V., Ruiz, J., Meza-Figueroa, D., Talavera-Mendoza, O., 2008, U-Pb detrital zircon data of the Rio Fuerte Formation (NW Mexico): its peri-Gondwanan provenance and exotic nature in relation to southwestern North America: Journal South American Earth Sciences, 26, 343-354, DOI:10.1016/j.jsames.2008.08.011.

Vega-Granillo R., Salgado-Souto S., Herrera-Urbina S., Valencia-Gómez, V., Vidal-Solano, J.R., 2011, Metamorphism and deformation in the El Fuerte region: their role in the tectonic evolution of NW Mexico: Revista Mexicana de Ciencias Geológicas, 28(1), 10-23.

Vega-Granillo, R., Vidal-Solano, J., Solari, L., López-Martínez, M., Gómez-Juárez, O.S. Herrera-Urbina, S., 2013, Geochemical and geochronological constraints on the geologic evolution of the western Sonobari Complex, northwestern Mexico: Geologica Acta, 11(4), 443-463 DOI:10.1344/105.000002059.

Weber, B., Cameron, K.L., Osorio, M., Schaaf, P., 2005, A Late Permian tectonothermal event in Grenville crust of the southern Maya terrane: U-Pb zircon ages from the Chiapas Massif, southeastern Mexico: International Geology Review, 47(5), 509-529, DOI:10.2747/0020-6814.47.5.509.

Weber, B., Iriondo, A., Premo, W.R., Hecht, L., Schaaf, P., 2007, New insights into the history and origin of the southern Maya block, SE México: U-Pb SHRIMP zircon geochronology from metamorphic rocks of the Chiapas massif: International Journal Earth Sciences (Geologische Rundschau), 96, 253-269.

Wetmore, P.H., Schmidt, K.L., Paterson, S.R., Herzig, C., 2002, Tectonic implications for the along-strike variation of the Peninsular Ranges batholith, southern and Baja California: Geology, 30(3), 247-250, DOI:10.1130/0091-7613.

Wetmore, P.H., Herzig, C., Alsleben, H., Sutherland, M., Schmidt, K.L., Schultz, P.W., Paterson, S.R., 2003, Mesozoic tectonic evolution of the Peninsular Ranges of southern and Baja California: Geological Society of America Special Paper 374, 93-116, DOI:10.1130/0-8137-2374-4.93.

Wetmore, P.H., Alsleben, H., Paterson, S.R., Ducea, M.N., Gehrels, G.E., Valencia, V.A., 2005, Field trip to the northern Alisitos arc segment: Ancestral Agua Blanca fault region: Field Trip Guide for the VII International Meeting of the Peninsular Geological Society, 40 pp.

Yáñez, P., Ruiz, J., Patchett, P.J., Ortega-Gutierrez, F., Gehrels, G.E., 1991, Isotopic studies of the Acatlan complex, southern Mexico: Implications for Paleozoic North American tectonics: Geological Society of America Bulletin,103(6), 817-828, DOI:10.1130/0016-7606.

Zavala-Monsiváis, A., Barboza-Gudiño, J.R., Valencia, V.A., Rodríguez-Hernández, S.E., García Arreola, M.E., 2009, Las sucesiones volcánicas pre-Cretácicas en el noreste de México: Unión Geofísica Mexicana, GEOS, abstracts, 29(1), 53 pp.

Zavala-Monsiváis, A., Barboza-Gudiño, J.R., Velasco-Tapia, F., García-Arreola, M.E., 2012, Sucesión volcánica Jurásica en el área de Charcas, San Luis Potosí: Contribución al entendimiento del Arco Nazas en el noreste de México: Boletín de la Sociedad Geológica Mexicana, 64(3), 277-293.

Manuscript received: August 23, 2015
Corrected manuscript received: November 23, 2015
Manuscript accepted: November 24, 2015

3

Estudio geoquímico e isotópico del magmatismo mesozoico en el Complejo Sonobari del Oeste, México: Implicaciones para la evolución tectónica del suroeste de Norteamérica.

Artículo

Sarmiento-Villagrana, A., Vega-Granillo, R., Talavera-Mendoza, O., Salgado-Souto, S., Gomez-Landa, J.R., 2017, Geochemical and isotopic study of Mesozoic magmatism in the Sonobari Complex, western Mexico: Implications for the tectonic evolution of southwestern North America

Contribuciones individuales de los autores:

Alicia Sarmiento Villagrana. Recolección de las muestras en campo y preparación de las pulpas para geoquímica de roca total e isotopía radiogénica. Cromatografía de los isótopos de Pb y Sr, análisis de los isótopos de Pb. Petrografía de las muestras. Elaboración de las gráficas de geoquímica e isótopos. Concepción de las ideas, interpretación de los datos y redacción del manuscrito.

Ricardo Vega Granillo. Consecución del financiamiento, trabajo de campo y muestreo, revisión y aporte a la versión final del manuscrito.

Oscar Talavera Mendoza. Asesoramiento con el procesamiento de datos de Pb y Sr. Aporte de ideas para mejorar la versión final del escrito.

Sergio Adrián Salgado Souto. Su participación fue parte fundamental en la coordinación y asesoramiento del trabajo de laboratorio, en el cual participó con el trabajo de cromatografía y análisis de los isotopos de Sr y Pb en la Universidad de Arizona.

Juan René Gómez Landa. Su contribución se centró en trabajo de campo, muestreo y trituración de las muestras para isótopos y geoquímica. Realizó los mapas en el programa ArcMap.

Research Paper

GEOSPHERE

GEOSPHERE; v. 14, no. 1

doi:10.1130/GES01540.1

10 figures; 1 table; 1 supplemental file

CORRESPONDENCE:
sarmiento_geo@hotmail.com

CITATION: Sarmiento-Villagrana, A., Vega-Granillo, R., Talavera-Mendoza, O., Salgado-Souto, S.A., and Gómez-Landa, J.R., 2017, Geochemical and isotopic study of Mesozoic magmatism in the Sonobari Complex, western Mexico: Implications for the tectonic evolution of southwestern North America: Geosphere, v. 14, no. 1, doi:10.1130/GES01540.1.

Science Editor: Shanaka de Silva
Associate Editor: Nancy Riggs

Received 3 April 2017
Revision received 28 September 2017
Accepted 20 November 2017

Geochemical and isotopic study of Mesozoic magmatism in the Sonobari Complex, western Mexico: Implications for the tectonic evolution of southwestern North America

Alicia Sarmiento-Villagrana[1], Ricardo Vega-Granillo[2], Oscar Talavera-Mendoza[3], Sergio Adrián Salgado-Souto[3], and Juan René Gómez-Landa[2]

[1]Instituto de Geología, Universidad Nacional Autónoma de México, L.D. Colosio y Madrid S/N, Hermosillo, Sonora, México 1039, 83000
[2]Departamento de Geología, Universidad de Sonora, Rosales y Encinas S/N, Hermosillo, Sonora, México 83000
[3]Unidad Académica de Ciencias de la Tierra, Universidad Autónoma de Guerrero, Taxco el Viejo, Guerrero, México C.P. 40323

ABSTRACT

The Sonobari Complex in northwestern Mexico preserves evidence of the consolidation of Pangaea and the Cordilleran orogenic cycle. Six Mesozoic magmatic pulses extending from the Early Triassic to the Paleocene are recognized in this complex. The volumetrically predominant rocks are calc-alkaline metaluminous and peraluminous granitoids. Mafic rocks are mainly tholeiitic gabbros. All studied rocks show high concentrations of large ion lithophile elements (LILE) and negative Nb, Ta, and Ti anomalies. Initial Nd and Sr isotopic ratios in granitoids ($\varepsilon Nd_{(i)}$ = –5.7 to –0.5; $^{87}Sr/^{86}Sr_{(i)}$ = 0.70630–0.71302) point to evolved continental sources, while radiogenic Pb isotopes ($^{206}Pb/^{204}Pb_{(i)}$ = 16.292–19.17; $^{207}Pb/^{204}Pb_{(i)}$ = 15.503–15.666; $^{208}Pb/^{204}Pb_{(i)}$ = 35.257–38.984) indicate a heterogeneous basement. Initial Nd and Sr isotope ratios in mafic rocks ($\varepsilon Nd_{(i)}$ = –1.9 to +5.0; $^{87}Sr/^{86}Sr_{(i)}$ = 0.70384–0.70626) point to mantle sources with crustal assimilation, which is also supported by the radiogenic Pb values ($^{206}Pb/^{204}Pb_{(i)}$ = 18.412–19.081; $^{207}Pb/^{204}Pb_{(i)}$ = 15.595–15.672; $^{208}Pb/^{204}Pb_{(i)}$ = 38.147–38.988). Geochemical and isotopic signatures suggest that magmatic rocks in the complex originated from fractional crystallization with assimilation of a heterogeneous basement isotopically similar to the Grenville orogen of Mexico. Whole-rock compositions are compatible with volcanic-arc followed by back-arc tectonic settings, where subduction and extensional processes occurred. Therefore, the main granitic pulses in the Sonobari Complex originated after the late Paleozoic Gondwana-Laurentia collision, by subduction of oceanic plates or microplates along the western border of Pangea. Also, two extension-related magmatic pulses occurred after the Late Jurassic and in the Cenomanian, separated by a collisional orogenic event that is recorded by regional metamorphism. The continental arc setting of the Sonobari Complex differs from the oceanic arc context of the Guerrero-Alisitos superterrane, indicating that there is no genetic relation between these blocks as previously proposed; rather, a relationship with the eastern Peninsular Ranges batholith is proposed.

INTRODUCTION

The Sonobari Complex of northwestern Mexico is an enigmatic igneous-metamorphic block consisting of Ordovician to Late Cretaceous rocks, and whose petrogenesis and magmatic history are poorly understood. This complex is composed of metasedimentary rocks with North American and South American provenance (Vega-Granillo et al., 2008, 2013), and therefore played a role in the interaction between Laurentia and Gondwana during Pangea consolidation. The complex includes magmatic pulses of 249–241 Ma (Early Triassic), 213–203 Ma (Late Triassic), 161–150 Ma (Late Jurassic), post-162 Ma–pre-99 Ma (latest Jurassic–Early Creteaceous), 99–97 Ma (Cenomanian), 83–80 Ma (Campanian), and 64 Ma (Paleocene) ages (Keppie et al., 2006; Vega-Granillo et al., 2012, 2013; Sarmiento-Villagrana et al., 2016), which have been described in the southern North American Cordillera, particularly in the Peninsular Ranges batholith of Baja California. Some authors have considered the Sonobari Complex as part of the basement of the composite Guerrero terrane of western Mexico (e.g., Campa and Coney, 1983; Centeno-García et al., 2008). Others, pointing to significant differences, have regarded it as a separate terrane in its own right (Tahue terrane; Sedlock et al., 1993). In order to define the petrogenesis and tectonostratigraphic setting of the complex, we performed an extensive geochemical and Nd, Sr, and Pb isotopic study of magmatic and metaigneous rocks. Our data, coupled with previously published geochemical data, provide a framework for a discussion of the magmatic and tectonic evolution of the complex, as well as the nature of its basement, in order to establish its link with the magmatic provinces of the southern Cordilleran orogenic belt.

GEOLOGICAL SETTING

The Sonobari Complex is a ~60-km-long and ~100-km-wide crustal block cropping out across the boundary between Sonora and Sinaloa states in northwestern Mexico (Fig. 1). Recent studies demonstrated that the complex is com-

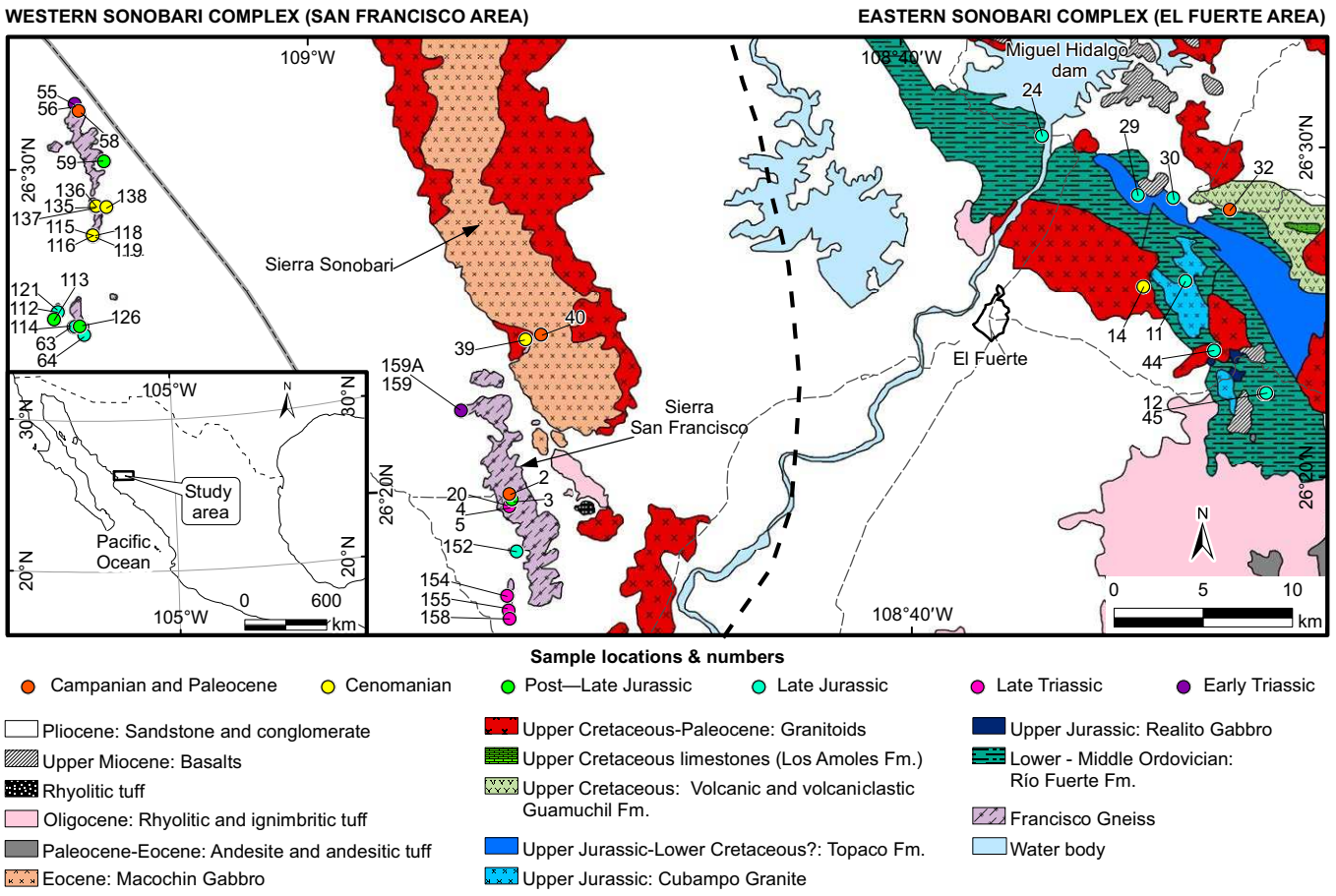

Figure 1. Geological map of the Sonobari Complex, northwestern Mexico (modified from Escamilla-Torres et al., 2000) showing location of analyzed samples (note: for clarity the prefix "SFO-" was removed from all sample names). Fm.—Formation. Gray-shaded dashed line—highway; thin dashed line—road; bold dashed line—proposed limit from the western and eastern Sonobari Complex. Sample SFO-167 is located outside of the geologic map.

posed of two distinctive assemblages: the Eastern Sonobari Complex of Gondwanan provenance and the Western Sonobari Complex of Laurentian affinity, which were juxtaposed in late Paleozoic time (Vega-Granillo et al., 2008, 2013).

Eastern Sonobari Complex

The Río Fuerte Formation is the oldest unit of the Eastern Sonobari Complex (ESC). This foliated metasedimentary unit contains Middle–Late Ordovician conodonts (Mullan, 1978; Poole et al., 2005, 2010). Neoproterozoic detrital zircon age groups in this formation point to a Gondwanan provenance (Vega-Granillo et al., 2008). The Río Fuerte is intruded by the Realito Gabbro, Cubampo Granite, and Capomos Granodiorite, and is thrust over the Topaco Formation. The Realito Gabbro includes a pluton of coarse-grained gabbro intruded by mafic dikes. The Cubampo Granite is composed by a larger body of two-mica granite and related sills and dikes, all characterized by large spheroidal quartz aggregates. These rocks yielded 155–151 Ma (Kimmeridgian) U-Pb zircon ages (Vega-Granillo et al., 2008). The Topaco Formation is a foliated volcano-sedimentary sequence made of metamorphosed epiclastic breccia intruded by mafic dikes, one of the later dated at 155 ± 3.5 Ma (U-Pb zircon; Vega-Granillo

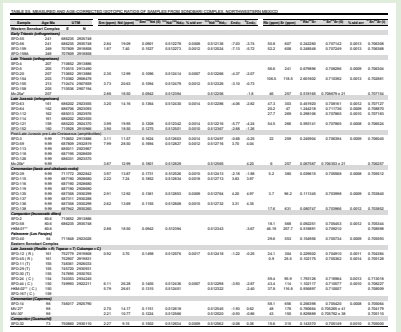

[1]Supplemental Data. Table S1: Geochronology; Table S2: Petrographic description; Tables S3 and S4: Geochemistry tables; and Table S5: Detailed isotopic analyses. Please visit http://doi.org/10.1130/GES01540.S1 or the full-text article on www.gsapubs.org to view the Supplemental Data.

et al., 2012). The breccia includes clasts of volcanic, metamorphic, and granitic rocks. One granitic clast was dated at 151 ± 1 Ma (U-Pb zircon; Vega-Granillo et al., 2011), indicating derivation from the Cubampo Granite previous to the tectonic juxtaposition of this unit against the Río Fuerte Formation. A heterogeneous mylonitic foliation and greenschist facies metamorphism overprint both the Topaco Formation and the Cubampo Granite. The Capomos pluton is a homogeneous coarse-grained hornblende biotite granodiorite (de Cserna et al., 1962). This rock was originally dated at 57.2 Ma (K-Ar; Damon et al., 1983), although a 97 Ma age is considered in this work based on U-Pb geochronology (sample SFO-14; Supplemental Data[1], Table S1). The Guamuchil Formation is a volcanic unit dated at 73 Ma (Campanian) by U-Pb in zircon (Vega-Granillo et al., 2012). This unit overlies the Topaco and Río Fuerte Formations in angular unconformity, and in turn, is overlain by Los Amoles Formation.

Western Sonobari Complex

The Western Sonobari Complex (WSC) is composed of metamorphic rocks, post-tectonic gabbro, and ultramafic dikes, all transected by aplitic-pegmatitic dikes. The complex geological relations prevent mapping of discrete units at the scale of Figure 1. The metamorphic rocks, known as the Francisco Gneiss (Mullan, 1978), consist of metasedimentary rocks, orthogneisses, and amphibolites. U-Pb detrital zircon ages in quartzite yield a maximum depositional age of 509 Ma, and main Paleo- and Mesoproterozoic age groups are interpreted as derived from Laurentian sources in northwestern Mexico and the southwestern USA (Vega-Granillo et al., 2013).

The oldest orthogneisses of the WSC yield U-Pb zircon ages of 249–241 Ma (Sarmiento-Villagrana et al., 2016). Younger biotite orthogneisses, originally dated at 220 Ma by U-Pb zircon (Anderson and Schmidt, 1983), yield younger U-Pb zircon ages ranging from 213 to 203 Ma (Keppie et al., 2006; Sarmiento-Villagrana et al., 2016). Two-mica quartz-feldspar orthogneisses yielded U-Pb zircon ages ranging from 163 to 159 Ma (Sarmiento-Villagrana et al., 2016). Orthogneisses and paragneisses are intercalated with tabular bodies of foliated amphibolite, interpreted as mafic dikes intruding the granitic and sedimentary protoliths. Crosscutting relations indicate that amphibolites postdate Late Jurassic orthogneiss and predate undeformed diorite dated at 100 Ma (Sarmiento-Villagrana et al., 2016). A regional metamorphism and related foliation overprint all units described above excluding the Cenomanian diorite. Thermobarometry yields average pressure (*P*) and temperature (*T*) of 8.0 ± 0.9 kb (kilobar) and 699 ± 42 °C, respectively, indicating a medium *P*/*T* amphibolite facies metamorphism (Vega-Granillo et al., 2017). Migmatization is common in orthogneisses and metasedimentary rocks mainly as stromatic bands, patches of leucosome, and veins, all indicating low melt volume. Metamorphism was dated at 91 Ma on recrystallized zircon rims (Sarmiento-Villagrana et al., 2016; Vega-Granillo et al., 2017).

Coarse-grained gabbro, diorite, hornblendite, and pyroxenite intrude the metamorphic rocks. A diorite dike transecting an undeformed gabbro yielded a 100 Ma zircon age (Sarmiento-Villagrana et al., 2016). This age is coeval with that obtained from a foliated diorite (99 Ma [Sarmiento-Villagrana et al., 2016]). Accordingly, the deformation event producing the main foliation in the area is regarded to have culminated 100 Ma. Otherwise, the undeformed Macochin Gabbro yielded a 54 Ma Ar-Ar age in hornblende (Vega-Granillo et al., 2013), which is considered as a cooling age; therefore, its crystallization age remains undefined. Non-foliated leucocratic aplitic and pegmatitic dikes transecting the tectonic foliation were dated at 82.0 to 80.6 Ma (U-Pb zircon; Sarmiento-Villagrana et al., 2016). Finally, the Los Parajes Granodiorite that intrudes the Sonobari Complex was dated at 64 Ma (U-Pb zircon; Vega-Granillo et al., 2013).

METHODOLOGY

Petrographic studies were performed on 130 rocks from the Sonobari Complex; locations and brief descriptions are given in the Supplemental Data (Table S2 [footnote 1]). From these, 44 samples were analyzed for major and trace element concentrations. Geochemical analyses were performed at the ALS Chemex laboratory in Vancouver, Canada. Major elements were analyzed by inductively coupled plasma–atomic emission spectroscopy (ICP-AES), while trace elements and rare earth elements (REEs) were analyzed with ICP–mass spectrometry (ICP-MS). Additionally, 42 samples were studied for lead isotopes, 21 for strontium isotopes, and 16 for neodymium isotopes (Table 1). Digestion, chromatography, and isotopic analyses were performed at the University of Arizona, Tucson, Arizona, USA. Between 100 and 200 mg of whole rock was digested for Pb and Sr isotopes, and between 43 and 55 mg for Nd, all from the same whole-rock aliquots. Digestion was done in Parr bombs with a mixture of ultrapure 29N HF and 16N HNO_3 and $HClO_4$ at 150 °C. Pb and Sr purification was done in columns with Sr-Spec resin (Eichrom Industries, Darien, Illinois, USA) using twice-distilled HCl and HNO_3 with different molarity. Lead isotope analyses were done according to procedures described by Thibodeau et al. (2013), on a GV Instruments multicollector–inductively coupled plasma–mass spectrometer (MC-ICP-MS). All samples were diluted below 50 ppb, and a Tl spike was added to each sample. For calculation of initial ratios, concentrations of U, Th, and Pb were obtained with ICP-MS in the Chemex laboratory. Then, $^{238}U/^{204}Pb$, $^{235}U/^{204}Pb$, and $^{232}Th/^{204}Pb$ were calculated using these concentrations and their respective atomic weights and isotopic abundances. Once these ratios were obtained, the initial Pb ratios were calculated using the age of the rock in the general formulae (Faure and Mensing, 2005). Isotopic fractionation of lead was monitored by analyzing the NBS-981 standard ($^{206}Pb/^{204}Pb$ = 16.9405, $^{207}Pb/^{204}Pb$ = 15.4963, and $^{208}Pb/^{204}Pb$ = 36.7219) reported by Galer and Abouchami (1998). Errors for Pb isotope ratios were calculated from the external reproducibility of the NBS-981 standard, and the external errors ranged between 0.0022% and 0.0081% for $^{206}Pb/^{204}Pb$, between 0.0029% and 0.0081% for $^{207}Pb/^{204}Pb$, and between 0.0077% and 0.020% for $^{208}Pb/^{204}Pb$ (2σ). Relative errors for the samples are between 0.011% and 0.052% (2σ). Strontium isotopes were measured at the University of Arizona using

TABLE 1. MEASURED AND AGE-CORRECTED ISOTOPIC RATIOS OF THE SONOBARI COMPLEX, NORTHWESTERN MEXICO

	Concentration (ppm)							Measured ratios							Initial ratios					
Sample (age)	Sm	Nd	Rb	Sr	Th	U	Pb	$^{147}Sm/^{144}Nd$	$^{143}Nd/^{144}Nd$	$^{87}Rb/^{86}Sr$	$^{87}Sr/^{86}Sr$	$^{206}Pb/^{204}Pb$	$^{207}Pb/^{204}Pb$	$^{208}Pb/^{204}Pb$	$^{143}Nd/^{144}Nd_{(i)}$	$\varepsilon Nd_{(i)}$	$^{87}Sr/^{86}Sr_{(i)}$	$^{206}Pb/^{204}Pb_{(i)}$	$^{207}Pb/^{204}Pb_{(i)}$	$^{208}Pb/^{204}Pb_{(i)}$
Western Sonobari Complex																				
Early Triassic																				
SFO-55 (241 Ma)	–	–	–	–	0.05	0.05	2	–	–	–	–	18.821	15.626	38.664	–	–	–	18.763	15.624	38.646
SFO-56 (241 Ma)	2.84	19.09	50.80	607	4.83	2.46	4	0.0901	0.512278	0.24228	0.707142	20.597	15.738	39.892	0.512136	–3.74	0.706308	19.175	15.666	38.984
SFO-159 (249 Ma)	1.87	7.40	52.2	608	1.79	0.65	10	0.1527	0.512273	0.24855	0.707249	18.663	15.607	38.498	0.512024	–5.72	0.706368	18.508	15.599	38.359
SFO-159A (249 Ma)	–	–	–	–	0.86	0.26	3	–	–	–	–	18.887	15.626	38.779	–	–	–	18.679	15.615	38.557
Late Triassic																				
SFO-4 (207 Ma)	–	–	–	–	6.97	1.46	6	–	–	–	–	19.035	15.635	39.088	–	–	–	18.553	15.610	38.338
SFO-5 (205 Ma)	–	–	56.60	241	12.25	2.98	3	–	–	0.67990	0.708286	19.482	15.656	39.659	–	–	0.706304	17.534	15.558	37.050
SFO-20 (207 Ma)	2.35	12.99	–	–	9.41	2.19	2	0.1096	0.512414	–	–	19.150	15.637	39.216	0.512266	–2.07	–	16.982	15.529	36.180
SFO-154 (203 Ma)	–	–	106.5	118.5	7.28	3.60	2	–	–	2.60180	0.710392	19.786	15.678	39.274	–	–	0.702881	16.292	15.503	36.971
SFO-155 (213 Ma)	3.73	20.63	–	–	12.10	1.60	2	0.1094	0.512479	–	–	19.190	15.637	39.275	0.512326	–0.73	–	17.560	15.555	35.257
SFO-158 (205 Ma)	–	–	–	–	8.22	1.78	2	–	–	–	–	19.362	15.651	39.465	–	–	–	17.617	15.563	36.839
Mv-25a* (207 Ma)	2.88	18.50	46	257	–	–	–	0.0942	0.512394	0.51816	0.708679	–	–	–	0.512256	–1.8	0.707154	–	–	–
Late Jurassic																				
SFO-63 (161 Ma)	3.20	14.16	47.30	303	3.32	0.76	2	0.1364	0.512430	0.45192	0.708161	18.738	15.616	38.869	0.512286	–2.82	0.707127	18.155	15.587	38.037
SFO-64 (162 Ma)	–	–	20.20	47	7.68	1.83	3	–	–	1.24422	0.711736	19.091	15.631	39.240	–	–	0.708870	18.149	15.584	37.948
SFO-112 (162 Ma)	–	–	27.70	269	13.50	2.64	3	–	–	0.29811	0.707865	19.848	15.675	40.418	–	–	0.707183	18.490	15.608	38.148
SFO-114 (161 Ma)	–	–	–	–	2.93	0.64	2	–	–	–	–	18.733	15.616	38.814	–	–	–	18.242	15.592	38.080
SFO-121 (159 Ma)	3.99	19.95	54.50	266	16.65	3.46	3	0.1208	0.512342	0.59314	0.707865	19.612	15.659	40.181	0.512216	–4.24	0.706524	17.865	15.573	37.433
SFO-152 (160 Ma)	3.90	18.50	–	–	5.92	2.08	2	0.1275	0.512501	–	–	19.276	15.645	39.067	0.512367	–1.26	–	17.690	15.567	37.592
Post–Late Jurassic, pre-Cenomanian																				
SFO-3 (99.9 Ma)	3.11	11.57	22	259	1.82	0.92	7	0.1624	0.512603	0.24590	0.706394	18.931	15.630	38.769	0.512497	–0.25	0.706045	18.806	15.624	38.689
SFO-59 (99.9 Ma)	7.99	28.50	–	–	0.86	0.33	8	0.1694	0.512827	–	–	18.457	15.601	38.427	0.512716	+4.04	–	18.418	15.599	38.394
SFO-113 (99.9 Ma)	–	–	–	–	6.24	2.82	2	–	–	–	–	20.417	15.703	39.957	–	–	–	19.081	15.639	38.988
SFO-118 (99.9 Ma)	–	–	–	–	0.35	0.13	2	–	–	–	–	18.736	15.611	38.540	–	–	–	18.675	15.608	38.486
SFO-126 (99.9 Ma)	–	–	–	–	0.08	0.13	2	–	–	–	–	18.911	15.627	38.750	–	–	–	18.849	15.624	38.737
Mv-25b* (99.9 Ma)	3.87	12.99	6	257	–	–	–	0.1801	0.512829	0.06759	0.706353	–	–	–	0.512565	+4.20	0.706257	–	–	–
Cenomanian																				
SFO-39 (99.9 Ma)	3.97	13.87	5.20	380	0.3	0.09	2	0.1731	0.512526	0.03962	0.705568	18.852	15.631	38.702	0.512413	–1.88	0.705512	18.809	15.629	38.655
SFO-115 (99.9 Ma)	2.22	7.24	–	–	0.09	0.08	2	0.1852	0.512834	–	–	18.782	15.617	38.592	0.512713	+3.97	–	18.744	15.615	38.578
SFO-116 (99.9 Ma)	–	–	–	–	0.18	2.09	2	–	–	–	–	19.460	15.651	38.592	–	–	–	18.470	15.604	38.564
SFO-119 (99.9 Ma)	–	–	–	–	0.63	0.28	2	–	–	–	–	19.169	15.646	38.980	–	–	–	19.036	15.640	38.882
SFO-135 (99.9 Ma)	2.91	12.92	3.70	96.2	0.24	0.45	2	0.1361	0.512853	0.11134	0.703998	18.939	15.620	38.623	0.512764	+4.97	0.703840	18.726	15.610	38.586
SFO-137 (99.9 Ma)	–	–	–	–	0.41	0.24	3	–	–	–	–	18.841	15.623	38.637	–	–	–	18.766	15.620	38.594
SFO-136 (99.9 Ma)	2.62	13.69	–	–	0.73	0.23	4	0.1155	0.512808	–	–	18.701	15.610	38.576	0.512732	4.35	–	18.646	15.608	38.519
SFO-138 (99.8 Ma)	–	–	17.6	631	0.9	0.62	2	–	–	0.08075	0.703966	18.763	15.609	38.535	–	–	0.703852	18.472	15.595	38.397
Campanian																				
SFO-2 (80.6 Ma)	–	–	–	–	1.27	1.71	16	–	–	–	–	18.949	15.634	38.666	–	–	–	18.868	15.630	38.646
SFO-58 (80.6 Ma)	–	–	18.1	568	2.60	0.59	11	–	–	0.09225	0.705453	18.747	15.617	38.569	–	–	0.705344	18.706	15.615	38.510
HKM01** (80.6 Ma)	2.88	18.50	46.19	257.7	–	–	–	0.0942	0.512394	0.51889	0.709210	–	–	–	0.512343	–3.67	0.708598	–	–	–
Paleocene																				
SFO-40 (64 Ma)	–	–	29.6	553	0.58	0.62	2	–	–	0.15496	0.705734	18.895	15.637	38.725	–	–	0.705593	18.707	15.629	38.667

(*continued*)

TABLE 1. MEASURED AND AGE-CORRECTED ISOTOPIC RATIOS OF THE SONOBARI COMPLEX, NORTHWESTERN MEXICO (*continued*)

	Concentration (ppm)							Measured ratios							Initial ratios					
Sample (age)	Sm	Nd	Rb	Sr	Th	U	Pb	$^{147}Sm/^{144}Nd$	$^{143}Nd/^{144}Nd$	$^{87}Rb/^{86}Sr$	$^{87}Sr/^{86}Sr$	$^{206}Pb/^{204}Pb$	$^{207}Pb/^{204}Pb$	$^{208}Pb/^{204}Pb$	$^{143}Nd/^{144}Nd_{(i)}$	$_{\varepsilon}Nd_{(i)}$	$^{87}Sr/^{86}Sr_{(i)}$	$^{206}Pb/^{204}Pb_{(i)}$	$^{207}Pb/^{204}Pb_{(i)}$	$^{208}Pb/^{204}Pb_{(i)}$
Eastern Sonobari Complex																				
Late Jurassic																				
SFO-12 (161 Ma)	0.92	3.70	24.1	304	0.85	0.28	2	0.1498	0.512576	0.22950	0.704910	18.804	15.637	38.714	0.512418	–0.25	0.704384	18.589	15.626	38.501
SFO-45 (161 Ma)	–	–	0.9	25.5	0.45	0.13	2	–	–	0.10218	0.705362	19.012	15.650	38.946	–	–	0.705128	18.912	15.645	38.833
SFO-11 (155 Ma)	–	–	–	–	1.49	0.58	3	–	–	–	–	19.007	15.686	39.111	–	–	–	18.721	15.672	38.871
SFO-29 (155 Ma)	–	–	–	–	1.61	0.42	2	–	–	–	–	18.722	15.615	38.535	–	–	–	18.412	15.599	38.147
SFO-30 (155 Ma)	–	–	–	–	2.03	0.66	9	–	–	–	–	18.755	15.645	38.700	–	–	–	18.646	15.639	38.591
SFO-24 (154 Ma)	–	–	59.4	95.9	6.33	1.62	3	–	–	1.79313	0.716964	19.357	15.687	39.397	–	–	0.713018	18.561	15.648	38.380
SFO-44 (150 Ma)	6.11	26.28	43.4	114	9.79	1.73	2	0.1405	0.512436	1.10212	0.710577	19.278	15.673	39.596	0.512298	–2.87	0.708227	18.036	15.612	37.298
HKM02** (150 Ma)	5.79	26.61	37.8	116.8	–	–	–	0.1315	0.512451	0.93690	0.710007	–	–	–	0.512322	–2.40	0.708009	–	–	–
SFO-167 (159 Ma)	–	–	–	–	11.95	2.27	25	–	–	–	–	18.825	15.647	38.813	–	–	–	18.688	15.641	38.577
Cenomanian																				
SFO-14 (98 Ma)	–	–	58.1	656	3.16	0.9	11	–	–	0.25640	0.705420	18.899	15.658	38.752	–	–	0.705064	18.823	15.655	38.665
MV-27* (98 Ma)	2.70	14.17	48	178	–	–	–	0.1151	0.512618	0.78066	0.705265	–	–	–	0.512545	+0.62	0.704179	–	–	–
MV-30* (98 Ma)	2.21	10.77	43	150	–	–	–	0.1224	0.512566	0.82989	0.705782	–	–	–	0.512488	–0.48	0.704638	–	–	–
Campanian																				
SFO-32 (73 Ma)	2.27	9.15	15.6	315	1.46	0.48	2	0.1502	0.512634	0.14337	0.705149	18.745	15.618	38.634	0.512562	+0.36	0.705000	18.579	15.610	38.469

Note: $_{\varepsilon}Nd$ was calculated by using present-day chondritic uniform reservoir (CHUR) values of $^{147}Nd/^{144}Nd = 0.1967$ and $^{143}Nd/^{144}Nd = 0.512638$. Sr isotopic ratios were normalized to $^{86}Sr/^{88}Sr = 0.1194$, whereas Nd ratios were normalized to $^{146}Nd/^{144}Nd = 0.7219$. Average of La Jolla standard $^{143}Nd/^{144}Nd = 0.511864 \pm 2$ ($n = 4$; 2σ). The NBS 987 standard $^{87}Sr/^{86}Sr = 0.7102594 \pm 0.0014$ ($n = 5$, 1σ). Estimated analytical ±2σ uncertainties for samples in this study are $^{143}Nd/^{144}Nd = 0.0007\%–0.0018\%$ and $^{87}Sr/^{86}Sr = 0.0008\%–0.0014\%$. External errors for NBS-981 standard $^{206}Pb/^{204}Pb$, $^{207}Pb/^{204}Pb$, and $^{208}Pb/^{204}Pb$ are between 0.0022% and 0.020% at ±2σ. Relative error samples are between 0.011% and 0.052% at ±2σ. En dash in cells indicates no data.

*Data recalculated from Valencia-Moreno et al. (2001).

**Data recalculated from Zurcher (2002).

a VG Sector 54 thermal ionization mass spectrometer (TIMS) following the protocol described by Thibodeau et al. (2015). The $^{87}Sr/^{86}Sr$ ratios were corrected for mass fractionation using $^{86}Sr/^{88}Sr = 0.1194$. The average value of the NBS-987 standard over all sample runs was 0.7102594 ± 0.0014 ($n = 5$, 1σ).

Whole-rock Nd isotopes were analyzed following procedures described by Ducea et al. (2002). Isotopic analyses were performed on a VG Sector 354 multicollector TIMS at the University of Arizona. Concentrations of Sm and Nd were determined by isotope dilution. The average $^{143}Nd/^{144}Nd$ of the La Jolla Nd standard measured during the analytical session was 0.511864 ± 2 ($n = 4$). Nd was normalized to $^{146}Nd/^{144}Nd = 0.7219$. The estimated analytical ±2σ uncertainties for samples in this study are $^{143}Nd/^{144}Nd = 0.0007\%–0.0018\%$.

RESULTS

Major and Trace Geochemistry

Petrographic descriptions are given in the Supplemental Data (Table S2 [footnote 1]). Major and trace elemental data are available for all samples in the Supplemental Data (Tables S3 and S4 [footnote 1]).

Triassic to Late Jurassic Orthogneisses and Granites (249–150 Ma)

Triassic to Late Jurassic orthogneisses and granites have SiO_2 content from 49.1 to 80.5 wt%, implying a compositional variation from gabbro to granite (Fig. 2A). Considering that classification with major elements could be altered by metamorphism, a classification diagram using immobile elements is included in Figure 2B. Magmatic differentiation is also indicated by the magnesium number (Mg#), which varies from 8.6 to 43. The TiO_2 contents in felsic rocks are mostly <1.0 wt%. An age-related compositional variation is not evident from either REE or multi-element diagrams. In general, primitive mantle–normalized multi-element diagrams display enrichment of large ion lithophile elements (LILE) with respect to the high field strength elements (HFSE), which is indicated by $(Rb/Yb)_N$ (N—normalized values) from 2.28 to 43.29. Patterns display negative anomalies in Nb, Ta, P, and Ti, and relative enrichment in K, Rb, Ba, and Th (Figs. 3A, 3C). In the REE diagrams (Figs. 3B, 3D), most samples are enriched in light REEs (LREEs) with respect to the heavy REEs (HREEs), except for one mafic sample, which displays a flatter pattern. This is evidenced by $(La/Yb)_N$ from 1.9 to 19.29. Many Late Jurassic samples display negative Eu anomalies. The Late Jurassic Cubampo granite has a peraluminous composition (Fig. 2C).

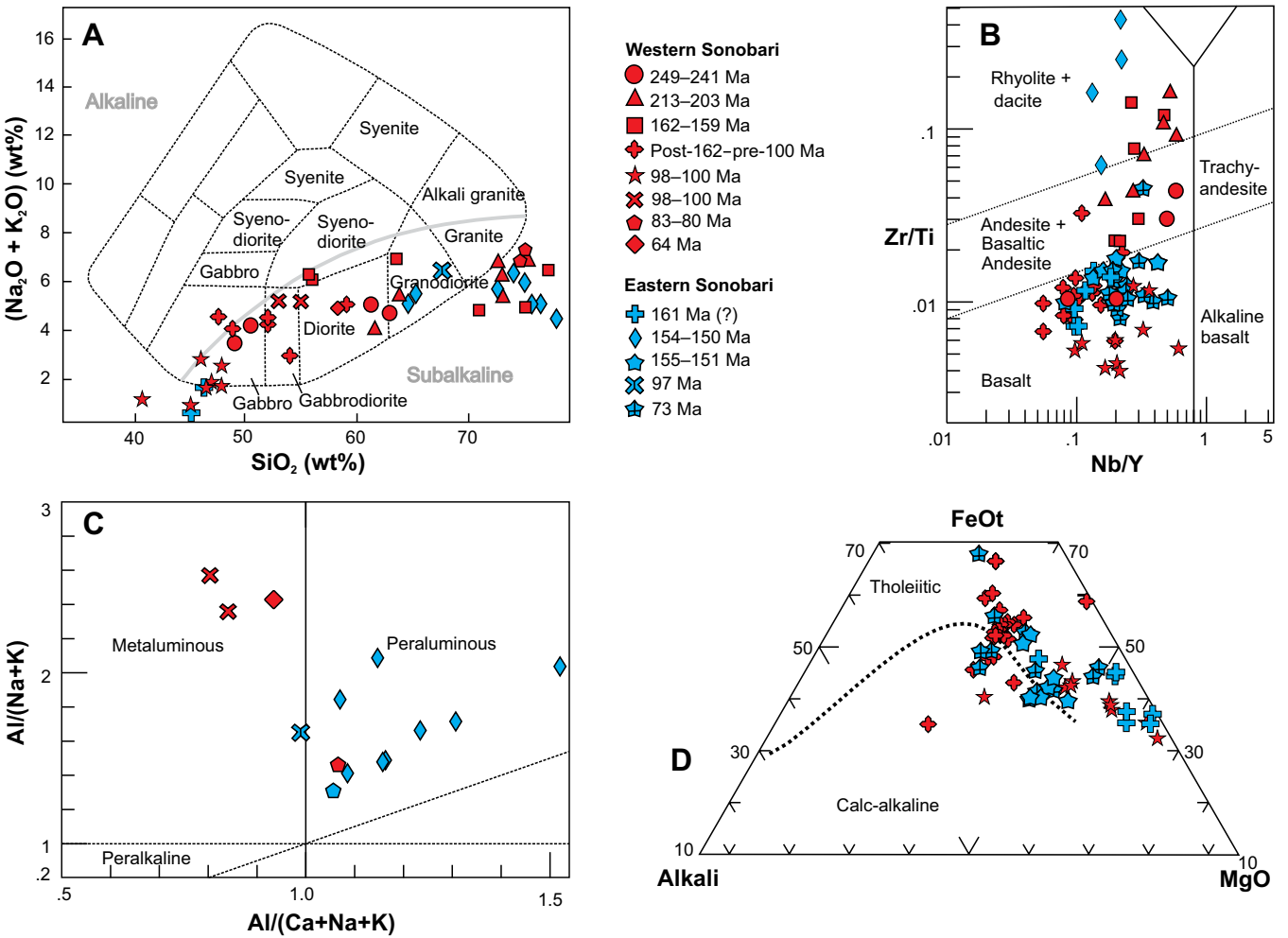

Figure 2. Classification diagrams of gneisses and magmatic rocks in the Sonobari Complex, northwestern Mexico. (A) Total alkali versus silica (TAS) classification diagram (adapted from Wilson, 2007). The curved gray line in the granite field separates the alkaline from subalkaline granite. (B) Nb/Y versus Zr/Ti diagram (Pearce, 1996; after Winchester and Floyd, 1977). (C) Shand's alumina saturation index (Maniar and Piccoli, 1989) for intermediate and felsic igneous rocks; metamorphic rocks were excluded from this diagram because major element contents in these rocks could have been mobilized. (D) Alkali-FeO total-MgO (AFM) diagram (Irvine and Baragar, 1971).

Late Jurassic Mafic Rocks (161–151 Ma)

The Late Jurassic Realito Gabbro and Topaco basic dikes have SiO_2 contents from 44 to 53 wt% (Fig. 2A) and Mg# from 65.6 to 37.3. In the Nb/Y versus Zr/Ti diagram, all samples have basic composition (Fig. 2B), and in the alkali-FeO_t(total)-MgO (AFM) diagram display tholeiitic affinity (Fig. 2D). The multi-element and the REE patterns of the Topaco dikes indicate that they are more enriched than the Realito Gabbro. Compared with Triassic–Jurassic felsic to intermediate rocks, the Nb-Ta anomaly in mafic rocks is less marked, the P and Ti negative anomalies are not present, and instead a positive anomaly in Sr is common (Fig. 3E). In the REE diagram, the Topaco and Realito rocks have a smooth slope with $(La/Yb)_N$ varying from 2.2 to 5.1, and two samples display positive Eu anomalies (Fig. 3F).

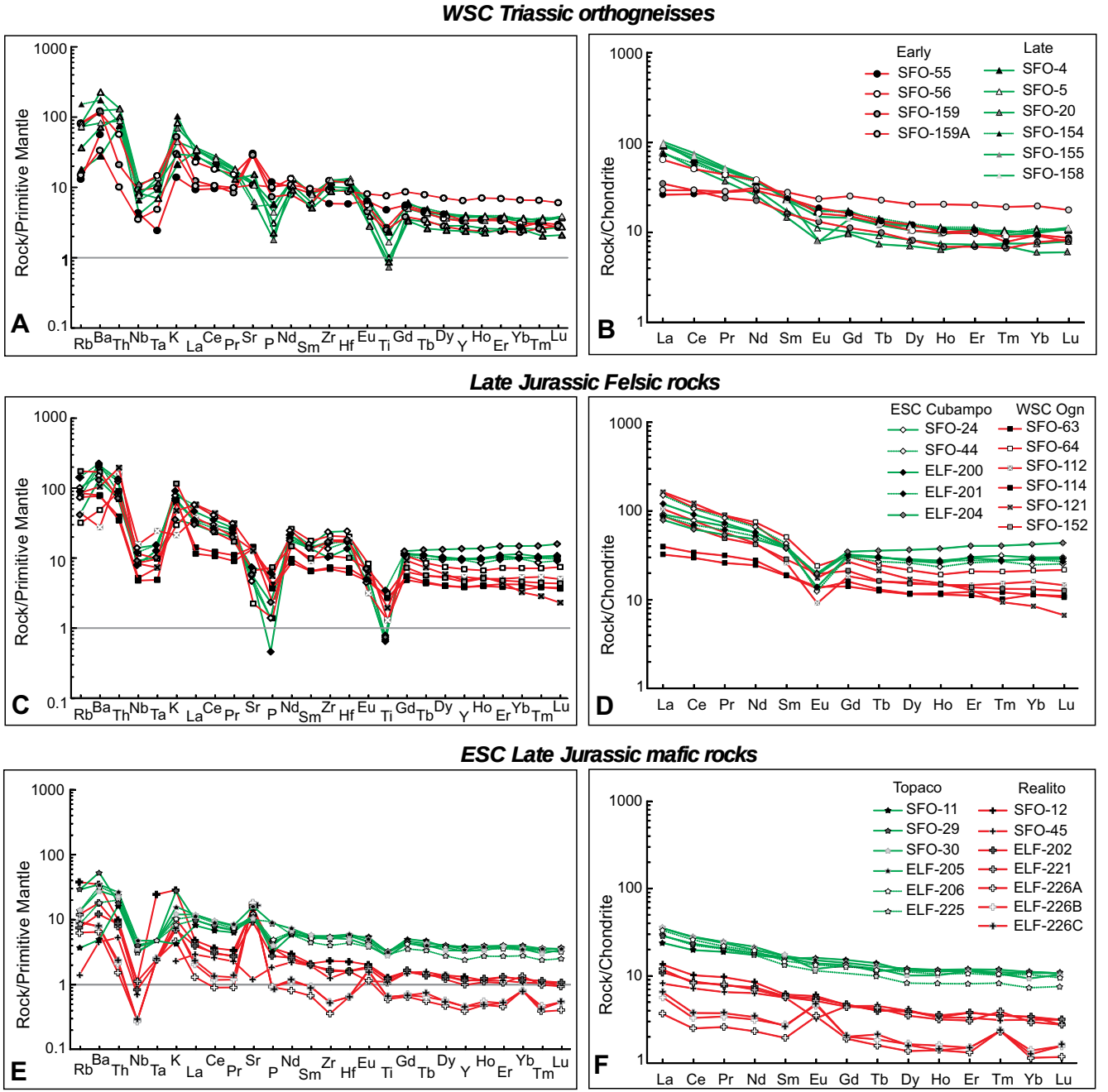

Figure 3 (*on this and following page*). Multi-element diagrams normalized to primitive mantle of Sun and McDonough (1989) (A, C, E, G, and I), and rare earth element patterns normalized to chondrite of Evensen et al. (1978) (B, D, F, H, and J). SFO samples from this work; ELF samples from Vega-Granillo et al. (2012). Clear green shaded area—mafic rocks from Vega-Granillo et al. (2013); clear pink shaded area—amphibolites from Keppie et al. (2006) and Vega-Granillo et al. (2013); clear orange shaded area—overlapping of green and pink zones; WSC—western Sonobari complex; ESC—Eastern Sonobari Complex; Ogn—orthogneiss; Grd—granodiorite.

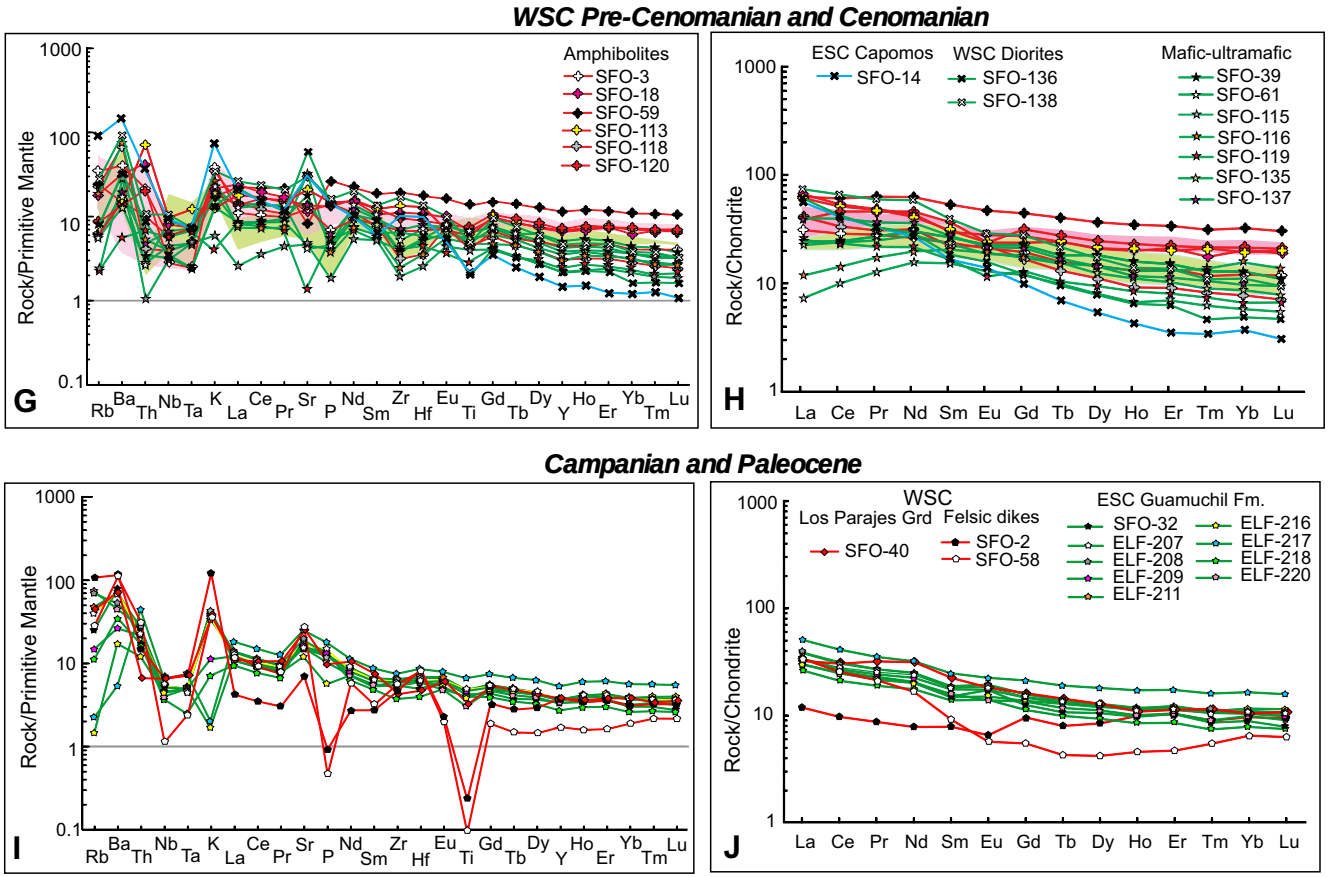

Figure 3 (*continued*).

Post–Late Jurassic Amphibolites and Cenomanian Intrusions (Post 162–98 Ma)

In the WSC, post–Late Jurassic amphibolites and Cenomanian intrusions have 40–58.6 wt% SiO_2 (Fig. 2A), with average of 49.75 wt% in amphibolites and 45.5 wt% in later rocks. These basic compositions are also evident in the Nb/Y versus Zr/Ti diagram (Fig. 2B), while in the AFM diagram a tholeiitic affinity is apparent (Fig. 2D). TiO_2 ranges from 0.9 to 2.9 wt%, with average of 1.6 wt% in amphibolites and 1.2 wt% in gabbros. In the multi-element diagram, these two units have similar normalized abundances, although amphibolites are slightly more enriched. The pattern has a mild slope with $(Rb/Yb)_N$ from 0.9 to 8.6. Most samples have negative anomalies in Nb and Ta. Amphibolites have positive anomalies in Th, while in the Cenomanian gabbro the anomaly is negative (Fig. 3G). Both pulses are enriched in REEs, although amphibolites have somewhat larger values and gabbros are slightly depleted in LREEs (Fig. 3H). The Capomos Granodiorite has 69.2 wt% SiO_2, and a moderately low Mg# of 33.6. The multi-element diagram for this rock displays enrichment in LILEs and HFSEs with $(Rb/Yb)_N$ of 71.60, negative anomalies in Nb, Ta, Sm, and Ti, and positive anomalies in K and Sr (Fig. 3G). The REE pattern displays high LREEs and HREEs with $(La/Yb)_N$ of 15.54 (Fig. 3H). The Shand index indicates that this rock is metaluminous (Fig. 2C).

Campanian Volcanic and Plutonic Rocks (80–73 Ma)

The Campanian Guamuchil Formation has 48.9–58.4 wt% SiO_2, but the rocks are mostly basic in composition, which is confirmed in the Nb/Y versus Zr/Ti diagram (Fig. 2B). In the AFM diagram, this unit shows a tholeiitic affinity (Fig. 2D). The TiO_2 average in these rocks is 0.96 wt%. The multi-element

patterns are very similar to those of the Cenomanian rocks, excepting the Th negative anomaly that is not present on this unit (Fig. 3I). The Campanian felsic leucogranites intruding the WSC display similar behavior to coeval mafic rocks, but with marked negative anomalies in Nb, Ta, P, and Ti, and positive anomalies in K and Sr (Fig. 3I). The Campanian rocks have a very similar REE pattern to the post–Late Jurassic to Cenomanian rocks (Fig. 3J). The leucogranites have peraluminous compositions (Fig. 2C).

Paleocene Los Parajes Granodiorite (64 Ma)

The Paleocene Los Parajes Granodiorite has 58 wt% SiO_2 (Fig. 2A), and a low Mg# of 31.6 indicating derivation from an evolved magma. The multi-element pattern indicates enrichment of LILEs with respect to HFSEs with $(Rb/Yb)_N$ of 13.52, displaying slight negative anomalies in Nb, Ta, and Ti, and positive anomalies in Kr and Sr (Fig. 3I). The REE patterns are enriched in LREEs with respect to HREEs with $(La/Yb)_N$ of 3.10 (Fig. 3J). In the Shand index diagram (Fig. 2C), this unit has a metaluminous character.

Nd, Sr, and Pb Isotopes

A summarized data set of isotopic values is included in Table 1 and a more detailed one in the Supplemental Data (Table S5 [footnote 1]). The Nd isotopic contents vary depending on the age and composition of the rocks. The Triassic and Jurassic intermediate and felsic orthogneisses and metagranites have $\varepsilon Nd_{(i)}$ values ranging from –5.7 to –0.73. Post–Late Jurassic amphibolites and Cenomanian gabbros have values from –1.9 to +4.97. The $\varepsilon Nd_{(i)}$ in the Late Jurassic Realito Gabbro is –0.25. In the Campanian Guamuchil Formation the $\varepsilon Nd_{(i)}$ is 0.36, while a negative value of –3.7 was reported from the Campanian leucogranites (Zurcher, 2002).

Three Triassic orthogneisses have initial Sr ratios ranging from 0.7063 to 0.7064, similar to the 0.7071 value obtained by Valencia-Moreno et al. (2001) in the same area. A low value of 0.7029 obtained in similar rocks can be ascribed to metamorphism as suggested by the low content in alkalis of that sample (SFO-154). The Late Jurassic Realito Gabbro has initial Sr ratios from 0.7044 to 0.7051, while coeval orthogneisses and the Cubampo Granite have ratios from 0.7065 to 0.7130. Post–Late Jurassic amphibolites have an initial Sr value of 0.7060 analogous to a previously obtained value of 0.7063 (Valencia-Moreno et al., 2001). Cenomanian gabbro, diorite, and granodiorite have initial Sr from 0.7038 to 0.7055. The Campanian Guamuchil Formation yields a value of 0.7050, while the Paleocene Los Parajes Granodiorite has initial Sr of 0.7056. In a $^{87}Sr/^{86}Sr_{(i)}$ versus $\varepsilon Nd_{(i)}$ correlation diagram (Fig. 4), the Triassic and Jurassic rocks and the Campanian leucogranites plot below the chondritic uniform reservoir (CHUR) in $\varepsilon Nd_{(i)}$ and toward higher $^{87}Sr/^{86}Sr_{(i)}$. Amphibolites and Cenomanian rocks have positive and negative values of $\varepsilon Nd_{(i)}$ following the mantle array evolution trend. The Realito, Capomos, and Guamuchil units have $\varepsilon Nd_{(i)}$ values near those of bulk Earth.

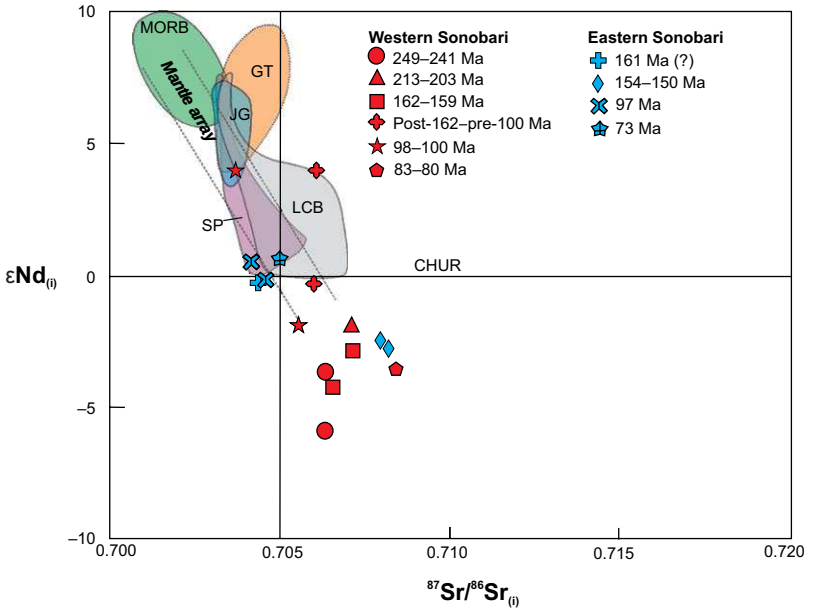

Figure 4. Initial εNd ($\varepsilon Nd_{(i)}$) versus $^{87}Sr/^{86}Sr_{(i)}$ of representative samples from the Sonobari Complex. The mantle array, displayed as dashed lines, is a linear correlation observed between Sr and Nd isotope ratios in oceanic rocks (DePaolo and Wasserburg, 1979). MORB—mid-ocean ridge basalt. Data fields for this diagram were obtained as follows: Guerrero terrane (GT)—Freydier et al. (2000), Centeno-García et al. (1993), Mendoza and Suastegui (2000); Jilotlan gabbros (JG)—Villanueva-Lascurain et al. (2016); Los Cabos block (LCB)—Schaaf et al. (2000); Santiago Peak (SP)—Herzig and Kimbrough (2014).

In the initial $^{207}Pb/^{204}Pb$ versus $^{206}Pb/^{204}Pb$ diagram (Fig. 5A), our values are arranged along the crustal evolution line of Stacey and Kramers (1975). The larger isotopic ratios are displayed by the Early Triassic, post-Late Jurassic, pre-Cenomanian, and Cenomanian rocks. The majority of the rocks in the ESC show higher values in $^{207}Pb/^{204}Pb$ than rocks of the WSC. Initial $^{208}Pb/^{204}Pb$ versus $^{206}Pb/^{204}Pb$ from all samples are placed in a narrow band with $^{208}Pb/^{204}Pb$ from 35 to 39 and $^{206}Pb/^{204}Pb$ from 16 to 19.5 (Fig. 5B).

DISCUSSION

Tectonic Setting

Diagrams by Pearce et al. (1984) and Whalen et al. (1987) were used to discriminate the tectonic setting of orthogneisses and igneous plutons. Most samples fall in the volcanic arc granite (VAG) field (Fig. 6A), excepting the Late Jurassic Cubampo Granite that crosses the boundary between VAG and within-plate granite (WPG). In the Zr versus Ga/Al diagram of Whalen et al. (1987), most granitoids are of I or S type (Fig. 6B), excepting the Late Triassic diorite, one Cubampo dike, and the Capomos Granodiorite, which fall in the field of anorogenic granitoids (A type).

Diagrams by Shervais (1982) and Cabanis and Thieblemont (1988) were used to distinguish the tectonic setting of volcanic and plutonic mafic rocks. In the Shervais (1982) diagram, samples of the Realito Gabbro fall in the low-Ti island arc tholeiite (IAT) field (Fig. 6C). Most of the Late Jurassic Topaco rocks plot in the IAT and MORB-BAB fields. Amphibolites and Cenomanian mafic rocks plot in mid-ocean ridge basalt—back-arc basin basalt (MORB-BAB) fields. In the diagram by Cabanis and Thieblemont (1988), the Realito, Topaco, and Guamuchil rocks mostly fall in the orogenic subdivision, with some Realito dikes lying in the continental basalt section. Amphibolites and Cenomanian gabbro and diorite are mostly located in or near the BAB field (Fig. 6D), with some samples plotting in the IAT and normal MORB (N-MORB) fields.

The Early Triassic to Late Jurassic orthogneisses and metagranites have TiO_2 contents mostly <1.0 wt%, similar to the average contents in modern island or continental arcs (Kovalenko et al., 2010). In contrast, amphibolites and Cenomanian mafic rocks have TiO_2 averaging 1.63 and 1.23 wt% respectively, the former value similar to the average 1.68 wt% of TiO_2 reported for MORB by Gale et al. (2013). TiO_2 as an immobile element suggests an arc setting for the Early Triassic to Late Jurassic magmatism, in spite of any metamorphic overprint, and a trend to MORB or BAB compositions for amphibolites and Cenomanian mafic rocks.

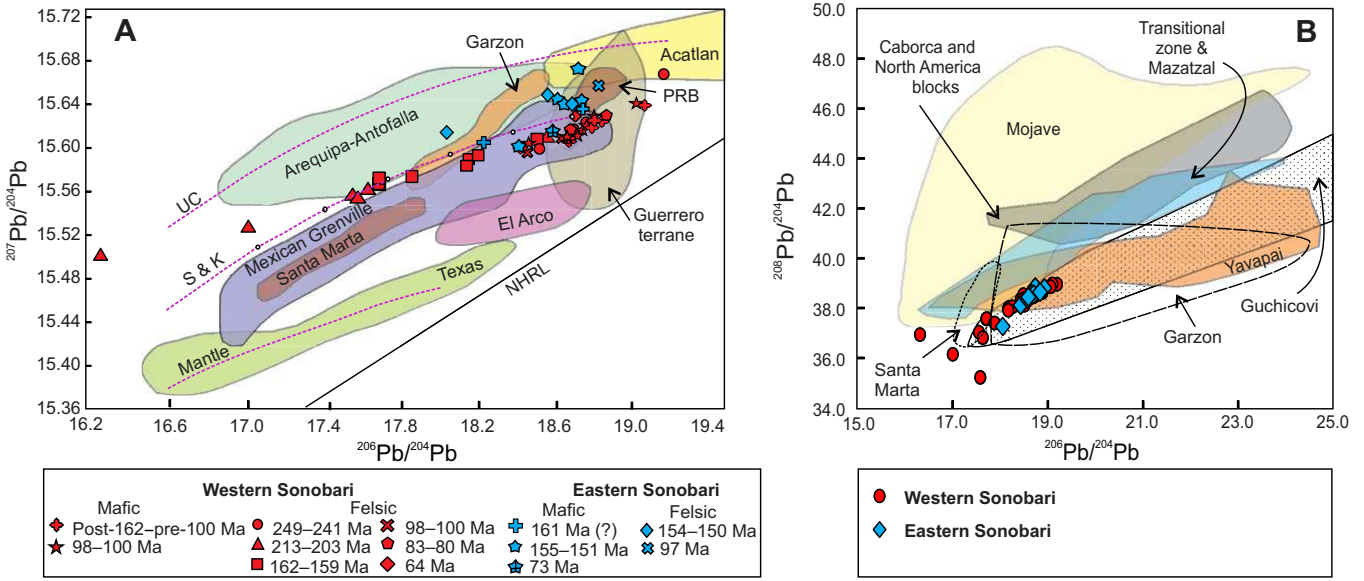

Figure 5. (A) Plot of initial $^{207}Pb/^{204}Pb$ versus $^{206}Pb/^{204}Pb$ for Sonobari Complex samples. Data sources are: Guerrero terrane—Potra et al. (2014); Acatlan Complex—Martiny et al. (1997); Mexican Grenville—Lopez et al. (2001); Texas—Cameron and Ward (1998), Smith et al. (1997); Santa Marta massif and Garzon—Ruiz et al. (1999); El Arco—Weber and López-Martínez (2006); Peninsular Ranges batholith (PRB)—Shaw et al. (2003); Arequipa-Antofalla (Tosdal, 1996). The Stacey and Kramers (1975) (S & K) line is the evolution curve for average crust. Growth curves for the upper crust (UC) and mantle (Doe and Zartman, 1979) are included for comparison. The northern hemisphere reference line (NHRL) is based on Hart (1984). (B) Plot of initial $^{208}Pb/^{204}Pb$ versus $^{206}Pb/^{204}Pb$. The Mojave, Mazatzal, Yavapai, and Caborca provinces are from Iriondo et al. (2004) and references therein; Garzon, Santa Marta, and Guchicovi areas from Ruiz et al. (1999).

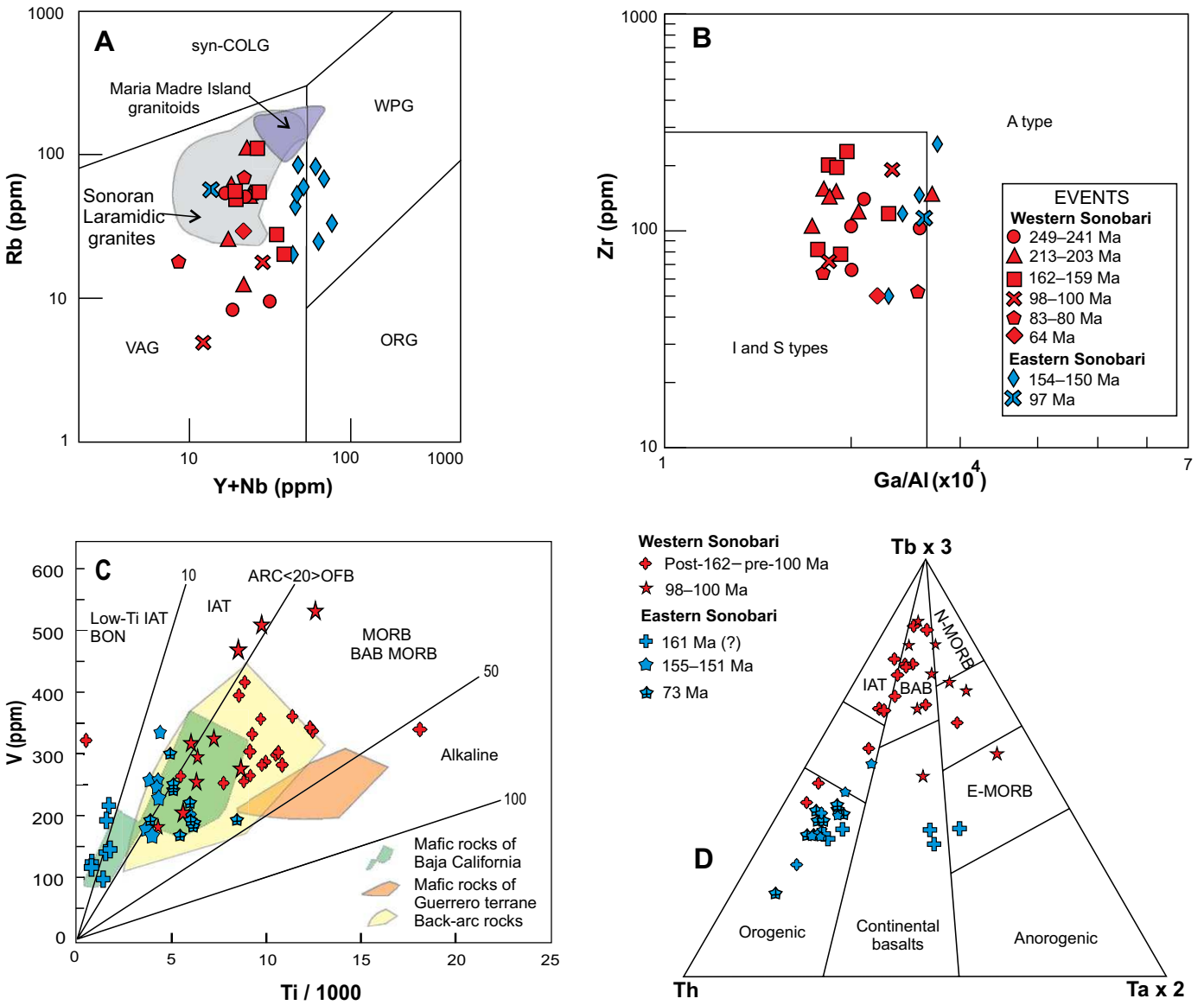

Figure 6. Tectonic discrimination diagrams for Sonobari Complex samples. (A) Rb versus Y + Nb diagram for granitic rocks (Pearce et al., 1984). Syn-COLG—syn-collisional granites; VAG—volcanic-arc granites; ORG—ocean-ridge granites; WPG—within-plate granites. (B) Zr versus Ga/Al discrimination diagram for granites (Whalen et al., 1987). (C) V versus Ti diagram for mafic to intermediate rocks (Shervais, 1982). Baja California field is from Kimbrough et al. (2015); Guerrero terrane field from Freydier et al. (2000); back-arc field from Shervais (1982). Numbers at the end of diagonal lines indicate the Ti (ppm)/V (ppm) values. (D) (Tb × 3)–Th–(Ta × 2) diagram of Cabanis and Thieblemont (1988). IAT—island arc tholeiites; BON—boninite; ARC—arc; MORB—mid-ocean ridge basalt; BAB—back-arc basin basalts; OFB—ocean-floor basalts; N-MORB—normal mid-ocean ridge basalt; E-MORB—enriched mid-ocean ridge basalt.

Igneous Petrogenesis

Triassic and Jurassic intermediate to felsic rocks have high LILE and HFSE, high LREE and HREE, negative anomalies in Nb, Ta, P, and Ti, negative $\varepsilon Nd_{(i)}$, and relatively high $^{87}Sr/^{86}Sr_{(i)}$, which indicate derivation from evolved crustal sources in a continental arc setting (Fig. 4). High content of REEs and negative anomalies in Eu, P, and Ti reflect fractional crystallization of plagioclase + apatite + sphene. For the majority of the magmatic events, inherited zircon data (Fig. 7), as well as crosscutting relationships, indicate melting and/or assimilation of older rocks.

The Realito Gabbro textural characteristics suggest a cumulate process, which is supported by >20 wt% Al_2O_3, >50 ppm Sc, and >200 ppm Ni (Pearce, 1996) compositions, and by positive anomalies in Sr and Eu. In turn, the Realito and Topaco dikes with lower Mg# and higher REE content are interpreted as derived by fractional crystallization, which is also indicated by slight negative anomalies in Eu and P. Negative $\varepsilon Nd_{(i)}$ and radiogenic $^{87}Sr/^{86}Sr_{(i)}$ values in both the Realito and Topaco units suggest crustal contamination during magma ascent or emplacement.

Post–Late Jurassic pre-Cenomanian amphibolites emplaced as dikes in older rocks have REE patterns similar to those of MORB, suggesting a depleted mantle source (Fig. 3H). However, high LILEs and negative anomalies in Nb and Ta indicate a subduction influence in the source. These geochemical characteristics have been associated with back-arc basins (Pearce and Stern, 2006). This setting is also supported by the geological relationships and tectonic diagrams (Figs. 6C, 6D). High La/Nb (1.80–3.92) and Nb/Ta (24.8–76) values, compared with depleted mantle values of 1.1 and 15.19 respectively (Salter and Stracke, 2004), suggest assimilation of continental crust. The $\varepsilon Nd_{(i)}$ varying from positive to slightly negative values and the variable $^{87}Sr/^{86}Sr_{(i)}$ radiogenic values support crustal assimilation. Large variations in Ba (27–495 ppm) and Sr (18–671 ppm) indicate mobility of these elements, probably during metamorphism.

TiO_2 and MgO compositions in post-tectonic Cenomanian mafic rocks suggest that these rocks are not cogenetic with amphibolites. Textural characteristics, high content of Al_2O_3, Sc, Cr, and Ni, and high Mg# in Cenomanian gabbros point to crystal fractionation processes from a mantle-derived magma. This interpretation is also supported by positive $\varepsilon Nd_{(i)}$ values and low $^{87}Sr/^{86}Sr_{(i)}$ (Fig. 4). Cenomanian diorites have $\varepsilon Nd_{(i)}$ and $^{87}Sr/^{86}Sr_{(i)}$ similar to those of the host gabbro, indicating a common mantle source but greater differentiation. The Macochin Gabbro in the Sierra Sonobari, with negative $\varepsilon Nd_{(i)}$ and more radiogenic $^{87}Sr/^{86}Sr_{(i)}$, must have experienced greater contamination by continental crust. Variation in Mg# and REE contents, as well as negative anomalies in Eu, P, and Ti in that unit, support such a fractionation-assimilation process. The Cenomanian Capomos Granodiorite has very similar REE content as coeval diorite of the WSC, although less positive $\varepsilon Nd_{(i)}$ values and more radiogenic $^{87}Sr/^{86}Sr_{(i)}$ point to a larger evolved source.

In a Nb/Th versus Th/Yb diagram (Fig. 8A), mafic rocks of the ESC have chemical affinity with the lower continental crust (LCC), with a slight tendency to upper continental crustal (UCC). Amphibolites and Cenomanian gabbros display a trend from depleted mantle (DM) to LCC, although amphibolites have slightly larger influence of the UCC. In a Hf/Yb versus Lu/Hf diagram (Fig. 8B), the majority of the samples display variable degrees of lower crust assimilation. The contamination trend is differentiated in the Th/Yb versus Nb/Yb diagram (Fig. 8C), where amphibolites and mafic rocks of the ESC tend to the UCC composition, while Cenomanian gabbros have a larger influence of the LCC.

One of the more conspicuous characteristics of the WSC is the widespread occurrence of peraluminous leucocratic dikes emplaced during Campanian time. The variations in LILEs, REEs, and trace elements indicate a complex origin of markedly evolved magmas. Clear negative anomalies in P and Ti indicate fractionation of apatite and sphene. Negative values in $\varepsilon Nd_{(i)}$ and radiogenic $^{87}Sr/^{86}Sr_{(i)}$ indicate a crustal source. Coeval with these magmas, tholeiitic basaltic rocks of the Guamuchil Formation were emplaced in the ESC.

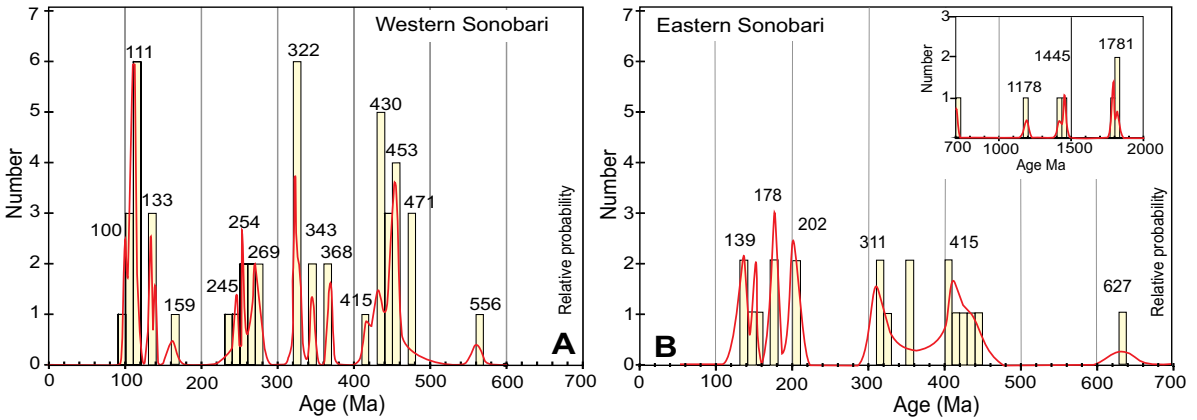

Figure 7. Histograms and relative probability plots of inherited zircons surrounded by magmatic zircon. Compiled from several rocks of the Western Sonobari Complex (rock ages varying from 241 Ma to 80 Ma) (A) and Eastern Sonobari Complex (rock ages varying from 161 Ma to 73 Ma) (B). Data are from Vega-Granillo et al. (2012) and Sarmiento-Villagrana et al. (2016).

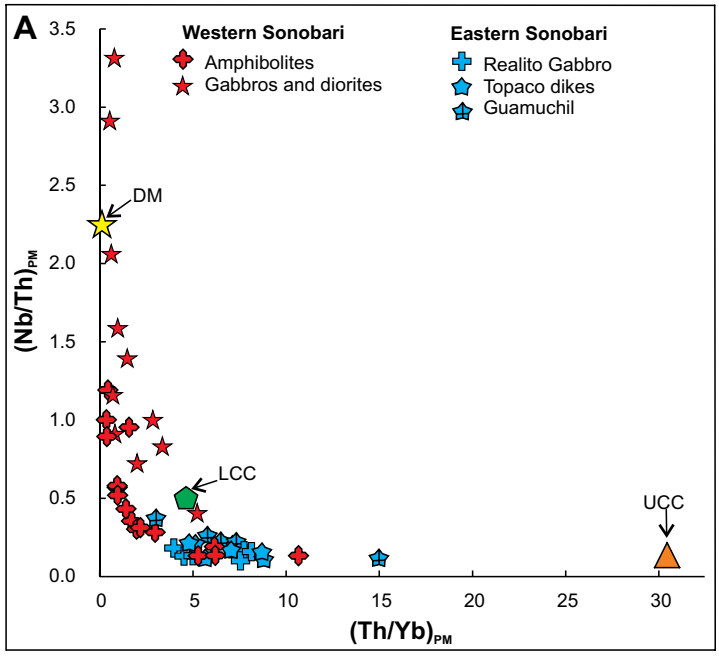

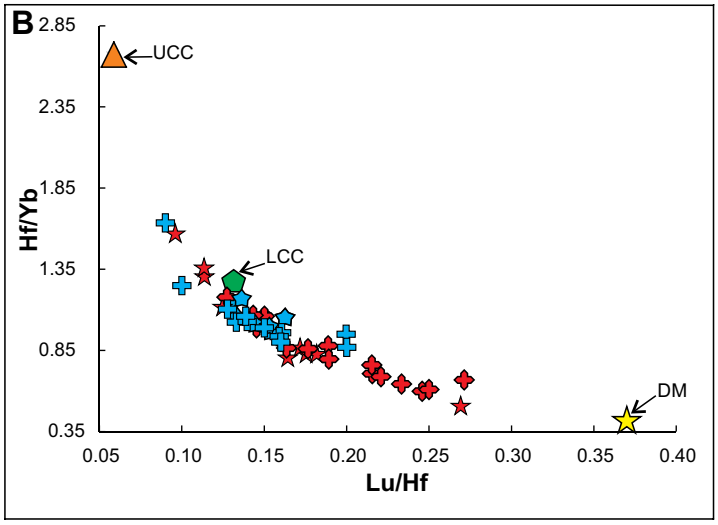

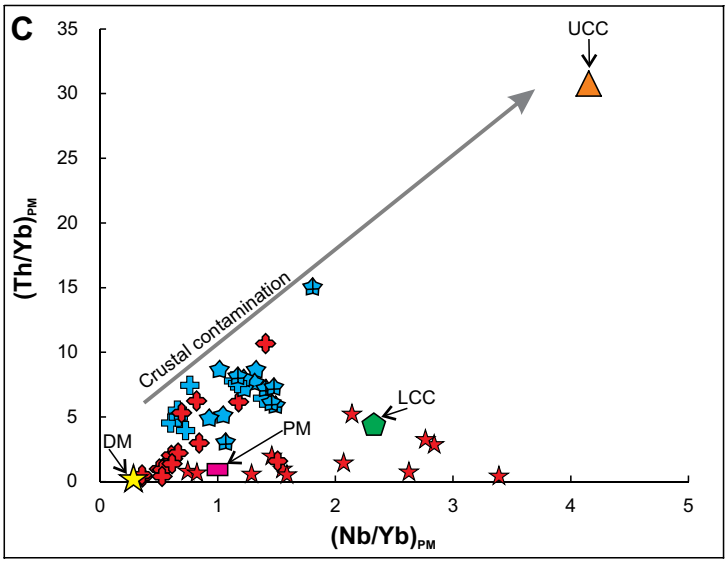

Figure 8. Diagrams to point out the source and crustal contamination of mafic rocks, Sonobari Complex. (A, B) $(Th/Yb)_{PM}$ versus $(Nb/Th)_{PM}$ (A) and Lu/Hf versus Hf/Yb (B) mixing diagrams show the geochemical relation of the rocks with mantle and crust (DM—depleted mantle; LCC—lower continental crust; UCC—upper continental crust). (C) The $(Nb/Yb)_{PM}$ versus $(Th/Yb)_{PM}$ diagram shows contamination tendencies of depleted mantle magmas. Data in panels A and C were normalized to primitive mantle (PM). Data for PM and DM are from Sun and McDonough (1989); data for LCC and UCC from Rudnick and Gao (2003).

The Mg# and REE content are interpreted as resulting from fractional crystallization, which is also supported by negative anomalies in Eu and P. Basalts have positive $\varepsilon Nd_{(i)}$ and $^{87}Sr/^{86}Sr_{(i)}$ similar to those of the mantle array, indicating their mantle derivation. Contamination by continental crust in these magmas is indicated by ages of inherited zircons and the mixing diagrams of Figure 8. The Paleocene Los Parajes Granodiorite displays moderate REE contents and $^{87}Sr/^{86}Sr_{(i)}$ of 0.706, indicative of a crustal influence. Negative anomalies in Nb and Ta reflect the influence of subduction-derived fluids in the origin of magmas.

Implication for Basement Configuration

In the study area, a geographic pattern in the variation of $\varepsilon Nd_{(i)}$ isotope ratios is not clear (Fig. 9); instead, $\varepsilon Nd_{(i)}$ is more radiogenic in mafic and Cenomanian rocks. Felsic rocks in the ESC have more radiogenic Sr and are richer in ^{207}Pb than felsic rocks of the WSC (Fig. 9). Variation in Pb isotopes seems to be controlled by the age and interaction with a heterogeneous basement, which may have been remnants of old blocks left behind after Pangea breakup. Rocks of the ESC have higher $^{207}Pb/^{204}Pb_{(i)}$ and more limited range in $^{206}Pb/^{204}Pb_{(i)}$ than rocks of the WSC (Fig. 5A), reinforcing the separation of these two zones previously proposed on geochronological grounds (Vega-Granillo et al., 2013). The Pb isotopic values of rocks in the ESC are very similar, suggesting a common homogeneous basement and/or assimilation of the Río Fuerte Formation, which is intruded by the Realito Gabbro, Topaco dikes, Cubampo Granite, and Capomos Granodiorite. In the $^{207}Pb/^{204}Pb$ versus $^{206}Pb/^{204}Pb$ diagram (Fig. 5A), ratios mostly coincide with those of the Grenville rocks of Mexico. Isotopic data in those rocks overlap with or are similar to data from the Colombian Santa Marta and Garzon Mesoproterozoic massifs (Lopez et al., 2001). Some Pb isotopic ratios in the Sonobari Complex fall in the range of the Arequipa-Antofalla craton, which is a Paleoproterozoic to Grenville basement terrane of eastern South America. However, our data clearly differ from those of the Grenville of Texas, USA. This suggests that the region may be underlain by a Grenvillian heterogeneous basement similar to the Oaxaquia microcontinent (Ortega-Gutierrez et al., 1995) of South American affinity (Fig. 10). However, the Cretaceous rocks have Pb isotopic signatures partially comparable to those of the Guerrero terrane and the Peninsular Ranges batholith (Figs. 5A, 10) (Potra et al., 2014; Shaw et al., 2003), suggesting that similar basements underlie these terranes, or at least did so in the time when the studied samples were formed. In the $^{208}Pb/^{204}Pb$ versus $^{206}Pb/^{204}Pb$ diagram (Fig. 5B), our values partially fit with data from the Grenville of Mexico represented by the Guchicovi Complex, and with those from the Colombian Garzon massif (Ruiz et al., 1999). Otherwise, our data differ from those obtained from the Laurentian Mojave and Mazatzal provinces (Fig. 5B) and from the basement of the Caborca area (Iriondo et al., 2004) but partially coincide with data of the Paleoproterozoic Yavapai province. Location of these provinces is displayed in Figure 10.

Neodymium and strontium isotopic values obtained in this work and previously published data were used to build a map encompassing different terranes of Mexico. The $\varepsilon Nd_{(i)}$ data (Fig. 10) show a clear isotopic variation from northern to southern Mexico, with more positive $\varepsilon Nd_{(i)}$ values in the south. That variation is supported by the Triassic rocks in the Sonobari Complex, which have less negative $\varepsilon Nd_{(i)}$ values than Triassic plutonic rocks in northern Sonora (Arvizu et al., 2009), indicating that the basement of the latter region is older than the basement in the Sonobari region. The $\varepsilon Nd_{(i)}$ values in the Sonobari Complex are similar to those of the Permo-Triassic granitoids of southern Mexico, which intrude the Oaxacan and Acatlan complexes (basements of the Oaxaca and Mixteco terranes, respectively; Fig. 10) (Torres et al., 1999), suggesting similar influences and probable relationships before the breakup of Pangea. Jurassic rocks in the Sonobari are isotopically similar to coeval rocks on Maria Madre Island (Fig. 10) (Pompa-Mera, 2014), whereas further south, the Jurassic Guerrero superterrane displays less radiogenic values. This suggests that the Sonobari Complex is located in the overlapping zone between older and younger basement terranes. The $^{87}Sr/^{86}Sr_{(i)}$ data show a clear isotopic variation from northern to southern Mexico (Fig. 10), with ratios being more radiogenic in north-central Sonora. In the study area, mixed values are found. The Triassic and Jurassic rocks tend to be more radiogenic than Cenomanian rocks, the latter having similar values to those in the Guerrero terrane, Maria Madre Island, Los Cabos block, and Alisitos–Santiago Peak terranes (Fig. 10), suggesting a common basement. Our initial Nd and Sr data are consistent with those of Valencia-Moreno et al. (2001), who ascribed the north-south variation to changes in the basements of the respective regions. Mahar et al. (2016) found that the Hf isotopes in the border between Chihuahua and Sinaloa, east of the study area, display analogous N-S variation. The $^{207}Pb/^{204}Pb_{(i)}$ values in the study area are similar to values reported in Chihuahua, and both are less radiogenic than those in northern Sonora (Housh and McDowell, 2005). The similarity of the Pb isotope ratios between the study area and Chihuahua suggest that the Mesoproterozoic basement of that region continues into southern Sonora and northern Sinaloa.

Tectonic Implications

In paleogeographic models and tectonic maps, the Sonobari Complex is located in the overlapping zone between Laurentia and Gondwana (Dickinson and Lawton, 2001; Poole et al., 2005; Vega-Granillo et al., 2008). Most authors have placed the northern limit of the composite Guerrero terrane to the north of this region (e.g., Campa and Coney, 1983; Centeno-García et al., 2008). However, surface boundaries between crustal blocks have been obliterated by superposed deformation, intrusion, and Cenozoic volcanic and sedimentary cover.

The earliest tectonic event in the area occurred in the ESC with amalgamation of the southern Laurentian passive margin with Gondwanan blocks approaching from the south (Poole et al., 2005; Vega-Granillo et al., 2008).

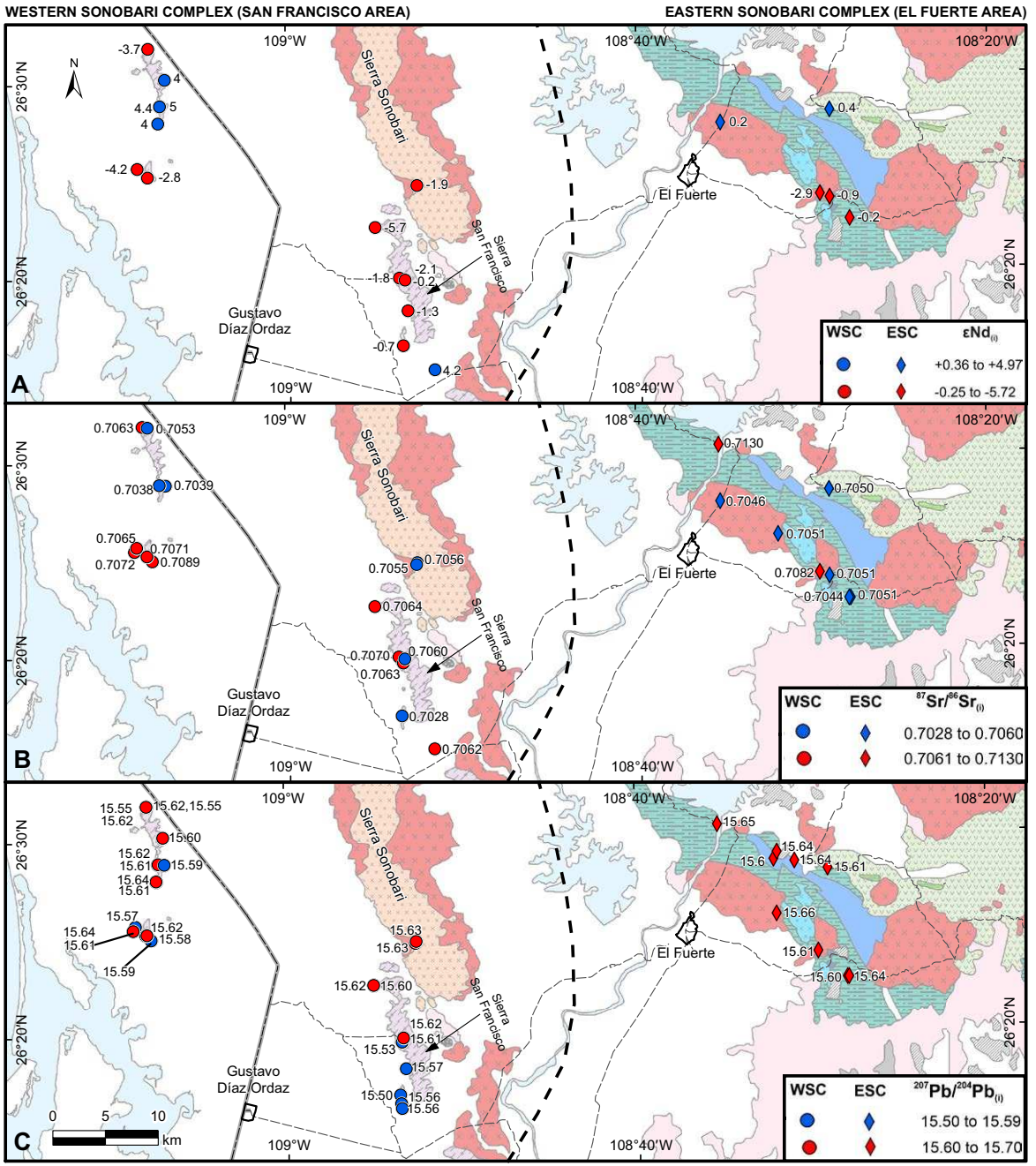

Figure 9. Regional maps showing distribution of initial εNd (A), initial Sr (B), and initial $^{207}Pb/^{204}Pb$ (C). Gray-shaded dashed line—highway; thin dashed line—roads; bold dashed line—proposed limit from the western and eastern Sonobari Complex (see Fig. 1 for geologic units, colors, and patterns). WSC—Western Sonobari Complex; ESC—Eastern Sonobari Complex.

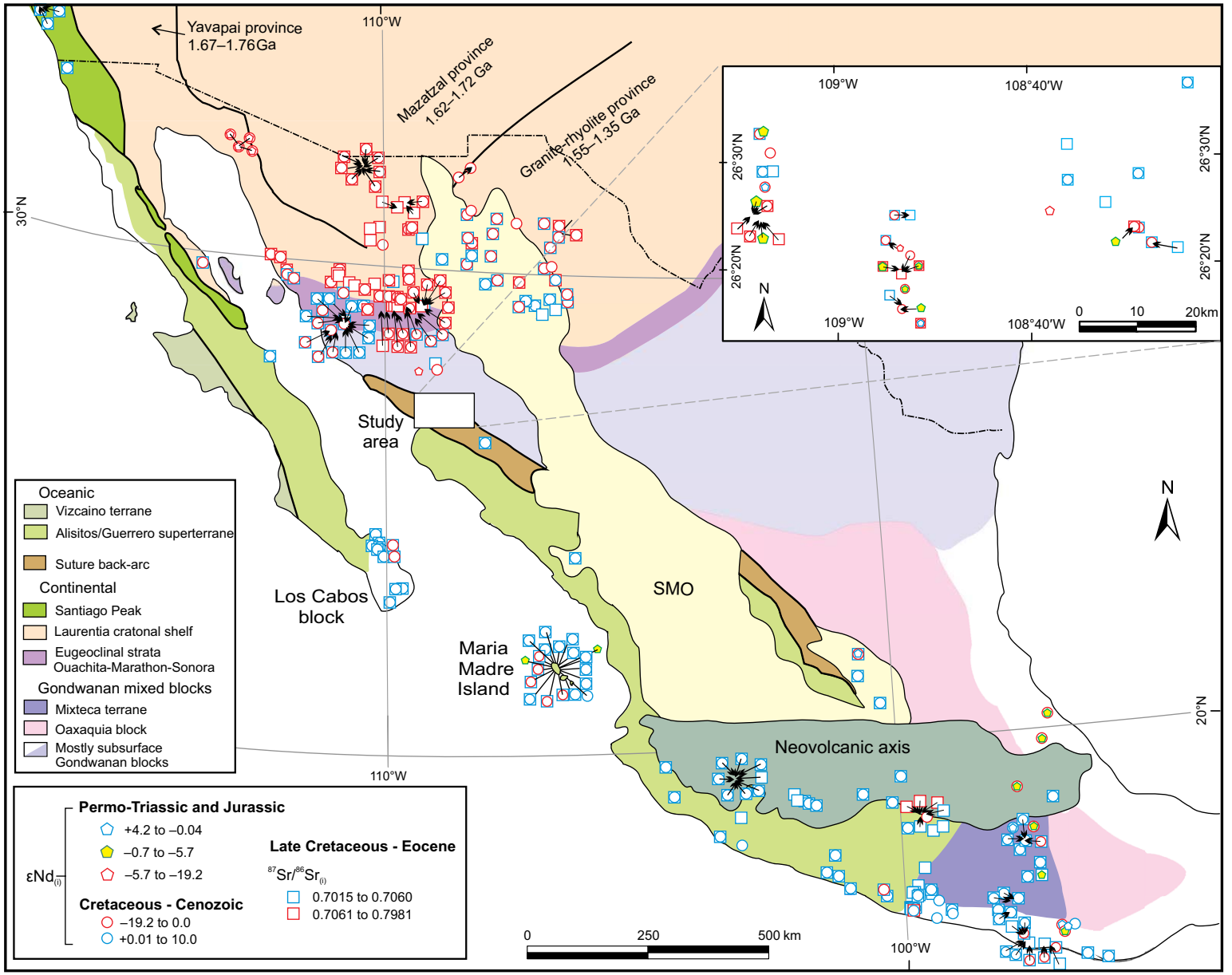

Figure 10. Map of initial Nd and Sr ratios of magmatic rocks in Mexico. Data from: this work; Freydier et al. (2000); Centeno-García et al. (1993); Villanueva -Lascurain et al. (2016); Pompa-Mera (2014); Herzig and Kimbrough (2014); Zurcher (2002); Schaaf et al. (2000); Arvizu et al. (2009); Torres et al. (1999); Valencia-Moreno et al. (2001); Roldán-Quintana et al. (2009); Pérez-Segura et al. (2013) and references therein; Morán-Zenteno et al. (2000) and references therein. SMO—Sierra Madre Occidental.

It is interpreted that this continental collision culminated during the late Permian with metamorphism of the Río Fuerte Formation in the study area (Vega-Granillo et al., 2008) and the thrusting of the Laurentian slope and basin assemblages over coeval platform sequences in central Sonora (Poole et al., 2005). From the Early Triassic to Late Jurassic (Oxfordian), the region was intruded by plutonic rocks derived from the subduction of oceanic lithosphere beneath the continental margin. These magmatic rocks evolved by differentiation of basic magmas and were contaminated by assimilation during their emplacement through previously amalgamated Paleozoic blocks. This scenario is consistent with tectonic models proposing the initiation of subduction along the western side of Pangea in Permo-Triassic times (Dickinson and Lawton, 2001; Dickinson, 2004; Arvizu et al., 2009). Therefore, Triassic rocks in the area are interpreted as the southward continuation of the Permo-Triassic magmatic belt occurring from southwestern USA (e.g., Barth et al., 1990, 1997; Barth and Wooden, 2006; Miller et al., 1995), eastern Peninsular Ranges batholith (Kimbrough et al., 2015; Schmidt et al., 2014), northern Sonora (Arvizu et al., 2009; Arvizu and Iriondo, 2015), eastern and southern Mexico (Torres et al., 1999; Weber et al., 2007; Ducea et al., 2004), and perhaps extending to South America (e.g., Cardona et al., 2010; Maksaev et al., 2014). Jurassic rocks also occur along a continental magmatic arc extending from southwestern USA through the Mojave and Sonora Deserts (Busby-Spera et al., 1990; Barth et al., 2017), northern Sonora (Anderson et al., 2005; Haxel et al., 2005), southern Sonora and northern Sinaloa (this work), central Sinaloa (Cuéllar-Cárdenas et al., 2012), and Maria Madre Island (Pompa-Mera et al., 2013). These rocks are also coeval with rocks in El Arco, Baja California, although the rocks from this region have a geochemical signature indicating an island arc setting (Weber and López-Martínez, 2006). The Late Jurassic magmatism in the eastern region seems to reflect initiation of an extensional phase with emplacement of bimodal plutons including the Realito-Topaco mafic rocks and the Cubampo Granite. However, felsic and mafic rocks display negative Nb and Ta anomalies typical of subduction-related magmatism, which are also found in basalts that underwent crustal contamination (Wilson, 2007) (Figs. 3 and 8). The Cubampo Granite may be related to the thermal input caused by intrusion of the Realito Gabbro into Paleozoic units (e.g., Huppert and Sparks, 1988; Meade et al., 2014). Emplacement of mafic dikes (amphibolites) in the WSC postdating the Kimmeridgian and predating the Cenomanian suggests a western migration of the extensional phase. Mixed MORB and subduction-related characteristics of these magmas have been associated with back-arc basins (e.g., Pearce and Stern, 2006), but an intra-arc setting cannot be precluded. This extensional back-arc or intra-arc setting is consistent with geologic relationships of mafic dikes intruding continental granitic rocks. An Early Cretaceous back-arc basin in northern Sonora–southern Arizona has been also proposed to form the depocenter of the Bisbee Group (Bilodeau, 1982; Dickinson and Lawton, 2001). The tectonic setting of the post–Late Jurassic pre-Cenomanian magmatism in the Sonobari is different from the oceanic arc setting of the partially coeval Alisitos arc of western Baja California (Busby et al., 2006).

Following emplacement of the mafic dikes, a collision event occurred, which caused deformation and orogenic metamorphism. Considering the age of the involved rocks, this event could be related to the collision of the Alisitos oceanic arc against the continental border (Sarmiento-Villagrana et al., 2016; Vega-Granillo et al., 2017). The final collisional event has been dated in Baja California at between 111 and 103 Ma (Johnson et al., 1999; Schmidt et al., 2014). This event closed the back-arc or intra-arc basin in the study area and caused amphibolite facies metamorphism and deformation in rocks older than ca. 100 Ma. Thermobarometry of the metamorphic rocks indicates that the region underwent burial to a depth of ~30 km (Vega-Granillo et al., 2017). During the latest stages of this event, the Río Fuerte Formation was thrust over the Topaco Formation causing heterogeneous mylonitic deformation and greenschist facies metamorphism in both units and in the Cubampo Granite (Vega-Granillo et al., 2011, 2017). In the WSC, thermal readjustment caused a temperature peak and migmatization at ca. 90 Ma (Sarmiento-Villagrana et al., 2016; Vega-Granillo et al., 2017), ca.10 Ma after cessation of the deformation event. That thermal peak was enhanced by Cenomanian post-tectonic gabbro plutons, and diorite, hornblendite, and pyroxenite dikes. Positive $\varepsilon Nd_{(i)}$ and low $^{87}Sr/^{86}Sr_{(i)}$ of these rocks suggest mantle sources, negative anomalies in Nb-Ta evidence continued influence of subduction-related fluids, while negative Th anomalies indicate little to no influence of the upper crust consistent with their emplacement deep within an overthickened crust. The MORB-BAB tectonic setting of these rocks (Fig. 6) and their isotopic signatures similar to that of oceanic-island basalt suggest that an extensional phase followed the main contractional event. Cenomanian magmatism occurred in a transitional period between the cessation of subduction underneath the Cordilleran margin, collision of the Alisitos arc, and inception of the Farallon plate subduction in the western side of Baja California. In the ESC, the Capomos Granodiorite originated at that time. Some Cenomanian rocks in the area have geochemical and isotopic compositions similar to those of post-tectonic mafic rocks in central Sinaloa (Henry et al., 2003), coeval gabbros in Baja California (Schmidt et al., 2014; Kimbrough et al., 2015), the Los Cabos block (Schaaf et al., 2000), and gabbros in the Guerrero terrane (Villanueva-Lascurain et al., 2016). Peraluminous magmatism similar to that of the 99–92 Ma La Posta suite reported in the Peninsular Ranges batholith has not been recognized in the study area.

Campanian (83–80 Ma) magmatism in the WSC represented by numerous post-tectonic leucocratic dikes is ascribed to partial melting of an overthickened crust during an active subduction process that generated the Laramide batholiths of Sonora and Sinaloa. Coeval magmatic rocks have been reported from coastal and central Sonora (e.g., McDowell et al., 2001; Ramos-Velázquez et al., 2008; Roldán-Quintana et al., 2009), Chihuahua-Sinaloa (Mahar et al., 2016), and Maria Madre Island (Pompa-Mera et al., 2013). In the ESC, the Guamuchil rocks have REE and trace element compositions very similar to those of the Topaco Formation. This suggests that the Guamuchil rocks originated from subduction-related magmatism in an extensional intra-arc environment. The Paleocene Los Parajes Granodiorite has a continental arc geochemical signature and is coeval with the extensively studied Laramide belt of Sonora and Sinaloa (e.g., Damon et al., 1983; Valencia-Moreno et al., 2001; Dickinson and Lawton, 2001; Henry et al., 2003).

CONCLUSIONS

The Sonobari Complex records an extended magmatic history starting in the Early Triassic and culminating in the Late Cretaceous (Campanian), which includes six main pulses related to or influenced by subduction processes. Intrusion of mafic rocks after the Late Jurassic and before the Campanian is interpreted as recording two extensional phases with an intervening compressional phase. The interpreted tectonic scenario of that period is complex, implying rifting behind a continental arc (i.e., back-arc or intra-arc), closing of a marginal sea by collision of the Alisitos arc against mainland Mexico, and rifting behind a continental arc when Farallon plate subduction initiated under western Baja California. Our geochemical and isotopic data indicate that the Sonobari Complex rocks were formed and evolved in a continental arc setting similar to that of the eastern Peninsular Ranges batholith and distinct from the oceanic arc setting of the Guerrero-Alisitos arc. Consequently, we suggest that the northern limit of the Guerrero terrane must be reappraised and may be located further south than the study area. Recent geophysical data suggest that the Alisitos arc runs parallel to continental rocks of the eastern Peninsular Ranges batholith (Langenheim et al., 2014) and does not continue into mainland Mexico as previous models proposed. The similarity of Pb isotopic compositions of the rocks in the study area and those of the Grenville rocks of Mexico, as well as the presence of inherited zircons in the magmatic rocks, indicate the existence of old basement blocks under the study area that have remained since Pangea breakup. These blocks are distinct from those in the Paleoproterozoic crust of northern Sonora.

ACKNOWLEDGMENTS

This work was supported by the Consejo Nacional de Ciencia y Tecnología (CONACYT), grant number 177668 to Ricardo Vega-Granillo. Special thanks to Mark Baker, laboratory manager in the Geosciences Department at the University of Arizona. Thanks to Frederick Arroyo and Analine Vázquez from the Universidad Autónoma de Guerrero for assistance with isotope chromatography. We appreciate the thorough and useful reviews by Andrew Barth, Peter Schaaf, and associate editor Nancy Riggs. The English version of the manuscript benefitted from the detailed review by Travis Ashworth, which is greatly appreciated.

REFERENCES CITED

Anderson, T.H., and Schmidt, V.A., 1983, The evolution of Middle America and the Gulf of Mexico–Caribbean Sea region during Mesozoic time: Geological Society of America Bulletin, v. 94, p. 941–966, https://doi.org/10.1130/0016-7606(1983)94<941:TEOMAA>2.0.CO;2.

Anderson, T.H., Rodríguez-Castañeda, J.L., and Silver, L.T., 2005, Jurassic rocks in Sonora, Mexico: Relations to the Mojave-Sonora megashear and its inferred northwestward extension, *in* Anderson, T.H., Nourse, J.A., McKee, J.W., and Steiner, M.B., eds., The Mojave-Sonora Megashear Hypothesis: Development, Assessment, and Alternatives: Geological Society of America Special Paper 393, p. 51–95, https://doi.org/10.1130/0-8137-2393-0.51.

Arvizu, H.E., and Iriondo, A., 2015, Control temporal y geología del magmatismo Permo-Triásico en Sierra Los Tanques, NW Sonora, México: Evidencia del inicio del arco magmático cordillerano en el SW de Laurencia: Boletín de la Sociedad Geológica Mexicana, v. 67, p. 545–586.

Arvizu, H.E., Iriondo, A., Izaguirre, A., Chávez-Cabello, G., Kamenov, G.D., Solís-Pichardo, G., and Cruz, L.S., 2009, Rocas graníticas pérmicas en la Sierra Pinta, NW de Sonora, México: Magmatismo de subducción asociado al inicio del margen continental activo del SW de Norteamérica: Revista Mexicana de Ciencias Geológicas, v. 26, p. 709–728.

Barth, A.P., and Wooden, J.L., 2006, Timing of magmatism following initial convergence at a passive margin, southwestern U.S. Cordillera, and ages of lower crustal magma sources: The Journal of Geology, v. 114, p. 231–245, https://doi.org/10.1086/499573.

Barth, A.P., Tosdal, R.M., and Wooden, J.L., 1990, A petrologic comparison of Triassic plutonism in the San Gabriel and Mule Mountains, southern California: Journal of Geophysical Research, v. 95, p. 20,075–20,096, https://doi.org/10.1029/JB095iB12p20075.

Barth, A.P., Tosdal, R.M., Wooden, J.L., and Howard, K.A., 1997, Triassic plutonism in southern California: Southward younging of arc initiation along a truncated continental margin: Tectonics, v. 16, p. 290–304, https://doi.org/10.1029/96TC03596.

Barth, A.P., Wooden, J.L., Miller, D.M., Howard, K.A., Fox, L.K., Schermer, E.R., and Jacobson, C.E., 2017, Regional and temporal variability of melts during a Cordilleran magma pulse: Age and chemical evolution of the Jurassic arc, eastern Mojave Desert, California: Geological Society of America Bulletin, v. 129, p. 429–448, https://doi.org/10.1130/B31550.1.

Bilodeau, W. L., 1982, Tectonic models for Early Cretaceous rifting in southeastern Arizona: Geology, v. 10, p. 466–470, doi:10.1130/0091-7613(1982)10<466:TMFECR>2.0.CO;2.

Busby, C., Adams, B.F., Mattinson, J., and Deoreo, S., 2006, View of an intact oceanic arc, from surficial to mesozonal levels: Cretaceous Alisitos arc, Baja California: Journal of Volcanology and Geothermal Research, v. 149, p. 1–46, https://doi.org/10.1016/j.jvolgeores.2005.06.009.

Busby-Spera, C.J., Martinson, J.M., Riggs, N.R., and Schermer, E.R., 1990, The Triassic-Jurassic magmatic arc in the Mojave-Sonoran Deserts and the Sierran-Klamath region: Similarities and differences in paleogeographic evolution, *in* Harwood, D.S., and Miller, M.M., eds., Paleozoic and Early Mesozoic Paleogeographic Relations: Sierra Nevada, Klamath Mountains, and Related Terranes: Geological Society of America Special Paper 255, p. 325–338, https://doi.org/10.1130/SPE255-p325.

Cabanis, B., and Thieblemont, D., 1988, La discrimination des tholeiites continentales et des basaltes arriere-arc: Proposition d'un nouveau diagramme, le triangle Th–3 × Tb–2 × Ta: Bulletin de la Société Géologique de France, v. 4, p. 927–935, https://doi.org/10.2113/gssgfbull.IV.6.927.

Cameron, K.L., and Ward, R.L., 1998, Xenoliths of Grenvillian granulite basement constrain models for the origin of voluminous Tertiary rhyolites, Davis Mountains, west Texas: Geology, v. 26, p. 1087–1090, https://doi.org/10.1130/0091-7613(1998)026<1087:XOGGBC>2.3.CO;2.

Campa, M.F., and Coney, P.J., 1983, Tectono-stratigraphic terranes and mineral resource distributions in Mexico: Canadian Journal of Earth Sciences, v. 20, p. 1040–1051, https://doi.org/10.1139/e83-094.

Cardona, A., Valencia, V., Garzón, A., Montes, C., Ojeda, G., Ruiz, J., and Weber, M., 2010, Permian to Triassic I to S-type magmatic switch in the northeast Sierra Nevada de Santa Marta and adjacent regions, Colombian Caribbean: Tectonic setting and implications within Pangea paleogeography: Journal of South American Earth Sciences, v. 29, p. 772–783, https://doi.org/10.1016/j.jsames.2009.12.005.

Centeno-García, E., Ruíz, J., Coney, P.J., Patchett, P.J., and Ortega-Gutiérrez, F., 1993, Guerrero terrane of Mexico: Its role in the Southern Cordillera from new geochemical data: Geology, v. 21, p. 419–422, https://doi.org/10.1130/0091-7613(1993)021<0419:GTOMIR>2.3.CO;2.

Centeno-García, E., Guerrero-Suástegui, M., and Talavera-Mendoza, O., 2008, The Guerrero composite terrane of western Mexico: Collision and subsequent rifting in a supra-subduction zone, *in* Draut, A.E., Clift, P.D., and Scholl, D.W., eds., Formation and Applications of the Sedimentary Record in Arc Collision Zones: Geological Society of America Special Paper 436, p. 279–308, https://doi.org/10.1130/2008.2436(13).

Cuéllar-Cárdenas, M.A., Nieto-Samaniego, Á.F., Levresse, G., Alaniz-Álvarez, S.A., Solari, L., Ortega-Obregón, C., and López-Martínez, M., 2012, Límites temporales de la deformación por acortamiento Laramide en el centro de México: Revista Mexicana de Ciencias Geológicas, v. 29, p. 179–203.

Damon, P.E., Shafiqullah, M., Roldán-Quintana, J., and Cochemé, J.J., 1983, El batolito Laramide (90–40 Ma) de Sonora, *in* Memorias Técnicas, XV Convención Nacional de la Asociación de Ingenieros de Minas, Metalurgistas y Geólogos de México, Guadalajara, Jalisco, 16–20 October, p. 63–95.

de Cserna, Z., Schmitter, E., Damon, P.E., Livingston, D.E., and Kulp, J.L., 1962, Edades isotópicas de rocas metamórficas del centro y sur de Guerrero y de una monzonita cuarcífera del norte de Sinaloa: Bulletin Instituto de Geologia, Universidad Nacional Autónoma de México, v. 64, p. 71–84.

DePaolo, D.J., and Wasserburg, G.J., 1979, Petrogenetic mixing models and Nd-Sr isotopic patterns: Geochimica et Cosmochimica Acta, v. 43, no. 4, p. 615–627, https://doi.org/10.1016/0016-7037(79)90169-8.

Dickinson, W.R., 2004, Evolution of the North American Cordillera: Annual Reviews of Earth and Planetary Sciences, v. 32, p. 13–45, https://doi.org/10.1146/annurev.earth.32.101802.120257.

Dickinson, W.R., and Lawton, T.F., 2001, Tectonic setting and sandstone petrofacies of the Bisbee basin (USA–Mexico): Journal of South American Earth Sciences, v. 14, p. 475–504, https://doi.org/10.1016/S0895-9811(01)00046-3.

Doe B.R., and Zartman R.E., 1979, Plumbotectonics, *in* Barnes, H.L. ed., Geochemistry of Hydrothermal Ore Deposits (third edition): New York, Wiley, p. 22–70.

Ducea, M., Sen, G., Eiler, J., and Fimbres, J., 2002, Melt depletion and subsequent metasomatism in the shallow mantle beneath Koolau volcano, Oahu (Hawaii): Geochemistry Geophysics Geosystems, v. 3, no. 2, https://doi.org/10.1029/2001GC000184.

Ducea, M.N., Gehrels, G.E., Shoemaker, S., Ruiz, J., and Valencia, V.A., 2004, Geologic evolution of the Xolapa Complex, southern Mexico: Evidence from U-Pb zircon geochronology: Geological Society of America Bulletin, v. 116, p. 1016–1025, https://doi.org/10.1130/B25467.1.

Escamilla-Torres, T., Saldaña-Saucedo, G., Polanco-Salas, A., Quevedo-León, A., and Moreno-López, M.H., 2000, Carta geológico-minera, Huatabampo G12-6: Sonora, Sinoloa y Chihuahua: Servicio Geológico Mexicano, scale 1:250,000, 1 sheet.

Evensen, N.M., Hamilton, P.J., and Onions, R.K., 1978, Rare-earth abundances in chondritic meteorites: Geochimica et Cosmochimica Acta, v. 42, p. 1199–1212, https://doi.org/10.1016/0016-7037(78)90114-X.

Faure, G., and Mensing, T.M., 2005, Isotopes: Principles and Applications: Hoboken, New Jersey, John Wiley & Sons Inc., 875 p.

Freydier, C., Lapierre, H., Ruiz, J., Tardy, M., Martinez-R, J., and Coulon, C., 2000, The Early Cretaceous Arperos basin: An oceanic domain dividing the Guerrero arc from nuclear Mexico evidenced by the geochemistry of the lavas and sediments: Journal of South American Earth Sciences, v. 13, p. 325–336, https://doi.org/10.1016/S0895-9811(00)00027-4.

Gale, A., Dalton, C.A., Langmuir, C.H., Su, Y., and Schilling, J.G., 2013, The mean composition of ocean ridge basalts: Geochemistry Geophysics Geosystems, v. 14, p. 489–518, https://doi.org/10.1029/2012GC004334.

Galer, S.J.G., and Abouchami, W., 1998, Practical application of lead triple spiking for correction of instrumental mass discrimination: Mineralogical Magazine, v. 62A, p. 491–492, https://doi.org/10.1180/minmag.1998.62A.1.260.

Hart, S.R., 1984, A large-scale isotope anomaly in the Southern Hemisphere mantle: Nature, v. 309, p. 753–757, https://doi.org/10.1038/309753a0.

Haxel, G.B., Wright, J.E., Riggs, N.R., Tosdal, R.M., and May, D.J., 2005, Middle Jurassic Topawa Group, Baboquivari Mountains, south-central Arizona: Volcanic and sedimentary record of deep basins within the Jurassic magmatic arc, *in* Anderson, T.H., Nourse, J.A., McKee, J.W., and Steiner, M.B., eds., The Mojave-Sonora Megashear Hypothesis: Development, Assessment, and Alternatives: Geological Society of America Special Paper 393, p. 329–357, https://doi.org/10.1130/0-8137-2393-0.329.

Henry, C.D., McDowell, F.W., and Silver, L.T., 2003, Geology and geochronology of the granitic batholithic complex, Sinaloa, México: Implications for Cordilleran magmatism and tectonics, *in* Johnson, S.E., Paterson, S.R., Fletcher, J.M., Girty, G.H., Kimbrough, D.L., and Martín-Barajas, A., eds., Tectonic Evolution of Northwestern Mexico and the Southwestern USA: Geological Society of America Special Paper 374, p. 237–273, https://doi.org/10.1130/0-8137-2374-4.237.

Herzig, C.T., and Kimbrough, D.L., 2014, Santiago Peak volcanics: Early Cretaceous arc volcanism of the western Peninsular Ranges batholith, southern California, *in* Morton, D.M., and Miller, F.K., eds., Peninsular Ranges Batholith, Baja California and Southern California: Geological Society of America Memoir 211, p. 345–363, https://doi.org/10.1130/2014.1211(09).

Housh, T.B., and McDowell, F.W., 2005, Isotope provinces in Laramide and mid-Tertiary igneous rocks of northwestern Mexico (Chihuahua and Sonora) and their relation to basement configuration, *in* Anderson, T.H., Nourse, J.A., McKee, J.W., and Steiner, M.B., eds., The Mojave-Sonora Megashear Hypothesis: Development, Assessment, and Alternatives: Geological Society of America Special Paper 393, p. 671–692, https://doi.org/10.1130/0-8137-2393-0.671.

Huppert, H.E., and Sparks, R.S.J., 1988, The generation of granitic magmas by intrusion of basalt into continental crust: Journal of Petrology, v. 29, p. 599–624, https://doi.org/10.1093/petrology/29.3.599.

Iriondo, A., Premo, W.R., Martínez-Torres, L.M., Budahn, J.R., Atkinson, W.W., Siems, D.F., and Guarás-González, B., 2004, Isotopic, geochemical, and temporal characterization of Proterozoic basement rocks in the Quitovac region, northwestern Sonora, Mexico: Implications for the reconstruction of the southwestern margin of Laurentia: Geological Society of America Bulletin, v. 116, p. 154–170, https://doi.org/10.1130/B25138.1.

Irvine, T.N., and Baragar, W.R.A., 1971, A guide to the chemical classification of the common volcanic rocks: Canadian Journal of Earth Sciences, v. 8, p. 523–548, https://doi.org/10.1139/e71-055.

Johnson, S.E., Tate, M.C., and Fanning, C.M., 1999, New geologic mapping and SHRIMP U-Pb zircon data in the Peninsular Ranges batholith, Baja California, Mexico: Evidence for a suture?: Geology, v. 27, p. 743–746, https://doi.org/10.1130/0091-7613(1999)027<0743:NGMASU>2.3.CO;2.

Keppie, J.D., Dostal, J., Miller, B.V., Ortega-Rivera, A., Roldán-Quintana, J., and Lee, J.W.K., 2006, Geochronology and geochemistry of the Francisco Gneiss: Triassic continental rift tholeiites on the Mexican margin of Pangea metamorphosed and exhumed in a Tertiary core complex: International Geology Review, v. 48, p. 1–16, https://doi.org/10.2747/0020-6814.48.1.1.

Kimbrough, D.L., Grove, M., and Morton, D.M., 2015, Timing and significance of gabbro emplacement within two distinct plutonic domains of the Peninsular Ranges batholith, southern and Baja California: Geological Society of America Bulletin, v. 127, p. 19–37, https://doi.org/10.1130/B30914.1.

Kovalenko, V.I., Naumov, V.B., Girnis, A.V., Dorofeeva, V.A., and Yarmolyuk, V.V., 2010, Average composition of basic magmas and mantle sources of island arcs and active continental margins estimated from the data on melt inclusions and quenched glasses of rocks: Petrology, v. 18, p. 1–26, https://doi.org/10.1134/S0869591110010017.

Langenheim, V.E., Jachens, R.C., and Aiken, C., 2014, Geophysical framework of the Peninsular Ranges batholith—Implications for tectonic evolution and neotectonics, *in* Morton, D.M., and Miller, F.K., eds., Peninsular Ranges Batholith, Baja California and Southern California: Geological Society of America Memoir 211, p. 1–20, https://doi.org/10.1130/2014.1211(01).

Lopez, R., Cameron, K.L., and Jones, N.W., 2001, Evidence for Paleoproterozoic, Grenvillian, and Pan-African age Gondwanan crust beneath northeastern Mexico: Precambrian Research, v. 107, p. 195–214, https://doi.org/10.1016/S0301-9268(00)00140-6.

Mahar, M.A., Goodell, P.C., and Feinstein, M.N., 2016, Tectono-magmatic evolution of the Chihuahua-Sinaloa border region in northern Mexico: Insights from zircon-apatite U–Pb geochronology, zircon Hf isotope composition and geochemistry of granodiorite intrusions: Lithos, v. 264, p. 555–576, https://doi.org/10.1016/j.lithos.2016.09.019.

Maksaev, V., Munizaga, F., and Tassinari, C., 2014, Timing of the magmatism of the paleo-Pacific border of Gondwana: U-Pb geochronology of Late Paleozoic to Early Mesozoic igneous rocks of the north Chilean Andes between 20° and 31° S: Andean Geology, v. 41, p. 447–506, https://doi.org/10.5027/andgeoV41n3-a01.

Maniar, P.D., and Piccoli, P.M., 1989, Tectonic discrimination of granitoids: Geological Society of America Bulletin, v. 101, p. 635–643, https://doi.org/10.1130/0016-7606(1989)101<0635:TDOG>2.3.CO;2.

Martiny, B., Martínez-Serrano, R., Ayuso, R.A., Macías-Romo, C., Morán Zenteno, D.J., and Alba-Aldave, L., 1997, Pb isotope geochemistry of Tertiary igneous rocks and continental crustal complexes, southern Mexico: Eos (Transactions, American Geophysical Union), v. 78, p. 844.

McDowell, F.W., Roldán-Quintana, J., and Connelly, J.N., 2001, Duration of Late Cretaceous–early Tertiary magmatism in east-central Sonora, Mexico: Geological Society of America Bulletin, v. 113, p. 521–531, doi:10.1130/00167606(2001)113<0521:DOLCET>2.0.CO;2.

Meade, F.C., Troll, V.R., Ellam, R.M., Freda, C., Font, L., Donaldson, C.H., and Klonowska, I., 2014, Bimodal magmatism produced by progressively inhibited crustal assimilation: Nature Communications, v. 5, 4199, https://doi.org/10.1038/ncomms5199.

Mendoza, O.T., and Suastegui, M.G., 2000, Geochemistry and isotopic composition of the Guerrero Terrane (western Mexico): Implications for the tectono-magmatic evolution of southwestern North America during the Late Mesozoic: Journal of South American Earth Sciences, v. 13, p. 297–324, https://doi.org/10.1016/S0895-9811(00)00026-2.

Miller, J.S., Glazner, A.F., Walker, J.D., and Martin, M.W., 1995, Geochronologic and isotopic evidence for Triassic-Jurassic emplacement of the eugeoclinal allochthon in the Mojave Desert region, California: Geological Society of America Bulletin, v. 107, p. 1441–1457, https://doi.org/10.1130/0016-7606(1995)107<1441:GAIEFT>2.3.CO;2.

Morán-Zenteno, D., Martiny, B., Tolson, G., Solís-Pichardo, G., Alba-Aldave, L., del Sol Hernandez-Bernal, Ma., Macías-Romo, C., Martínez-Serrano, R.G., Schaaf, P., and Silva-Romo, G.,

2000, Geocronología y características geoquímicas de las rocas magmáticas terciarias de la Sierra Madre del Sur: Boletin de la Sociedad Geológica Mexicana, v. LIII, p. 27–58.
Mullan, H.S., 1978, Evolution of part of the Nevadan orogen in northwestern Mexico: Geological Society of America Bulletin, v. 89, p. 1175–1188, https://doi.org/10.1130/0016-7606(1978)89<1175:EOPOTN>2.0.CO;2.
Ortega-Gutierrez, F., Ruiz, J., and Centeno-Garcia, E., 1995, Oaxaquia, a Proterozoic microcontinent accreted to North America during the late Paleozoic: Geology, v. 23, p. 1127–1130, https://doi.org/10.1130/0091-7613(1995)023<1127:OAPMAT>2.3.CO;2.
Pearce, J.A., 1996, A user's guide to basalt discrimination diagrams, *in* Wyman, D.A., ed., Trace Element Geochemistry of Volcanic Rocks: Applications for Massive Sulphide Exploration: Geological Association of Canada Short Course Notes 12, p. 79–113.
Pearce, J.A., and Stern, R.J., 2006, Origin of back-arc basin magmas: Trace element and isotope perspectives, *in* Christie, D.M., Fisher, C. R., Lee, S.-M., and Givens, S., Back-Arc Spreading Systems: Geological, Biological, Chemical, and Physical Interactions: American Geophysical Union Geophysical Monograph 166, p. 63–86, https://doi.org/10.1029/166GM06.
Pearce, J.A., Harris, N.B., and Tindle, A.G., 1984, Trace element discrimination diagrams for the tectonic interpretation of granitic rocks: Journal of Petrology, v. 25, p. 956–983, https://doi.org/10.1093/petrology/25.4.956.
Pérez-Segura, E., González-Partida, E., and Roldán-Quintana, J., 2013, Genetic implications of new Sr and Nd isotopic data of the intrusive rocks from the Laramide Arc in Northern Sonora, Mexico: Journal of Iberian Geology, v. 39, p. 131–146, https://doi.org/10.5209/rev_JIGE.2013.v39.n1.41755.
Pompa-Mera, V., 2014, Estudio geológico, geoquímico y geocronológico de la Isla María Madre, Nayarit [Ph.D. thesis]: Mexico, D.F., Universidad Nacional Autónoma de México, 270 p.
Pompa-Mera, V., Schaaf, P., Hernández-Treviño, T., Weber, B., Solís-Pichardo, G., Villanueva-Lascurain, D., and Layer, P., 2013, Geology, geochronology, and geochemistry of Isla María Madre, Nayarit, Mexico: Revista Mexicana de Ciencias Geológicas, v. 30, p. 1–23.
Poole, F.G., Perry, W.J., Madrid, R.J., and Amaya-Martínez, R., 2005, Tectonic synthesis of the Ouachita-Marathon-Sonora orogenic margin of southern Laurentia: Stratigraphic and structural implications for timing of deformational events and plate-tectonic model, *in* Anderson, T.H., Nourse, J.A., McKee, J.W., and Steiner, M.B., eds., The Mojave-Sonora Megashear Hypothesis: Development, Assessment, and Alternatives: Geological Society of America Special Paper 393, p. 543–596, https://doi.org/10.1130/0-8137-2393-0.543.
Poole, F.G., Amaya-Martínez, R., Premo, W.R., Berry, W.B.N., Sandberg, C.A., Roldán-Quintana, J., and Herrera-Urbina, S., 2010, Age and depositional setting of deep-marine Ordovician Río Fuerte and San José de Gracia formations in northern Sinaloa, Mexico: Remnants of the early Paleozoic Iapetus ocean: Geological Society of America Abstracts with Programs, v. 42, no. 5, p. 268.
Potra, A., Hickey-Vargas, R., Macfarlane, A.W., and Salters, V.J., 2014, Pb, Sr, and Nd isotopic characteristics of a variety of lithologies from the Guerrero composite terrane, west-central Mexico: Constraints on their origin: Revista Mexicana de Ciencias Geológicas, v. 31, p. 203–220.
Ramos-Velázquez, E., Calmus, T., Valencia, V., Iriondo, A., Valencia-Moreno, M., and Bellon, H., 2008, U-Pb and $^{40}Ar/^{39}Ar$ geochronology of the coastal Sonora batholith: New insights on Laramide continental arc magmatism: Revista Mexicana de Ciencias Geológicas, v. 25, p. 314–333.
Roldán-Quintana, J., McDowell, F.W., Delgado-Granados, H., and Valencia-Moreno, M., 2009, East-west variations in age, chemical and isotopic composition of the Laramide batholith in southern Sonora, Mexico: Revista Mexicana de Ciencias Geológicas, v. 26, p. 543–563.
Rudnick, R.L., and Gao, S., 2003, Composition of the continental crust, *in* Rudnick, R.L., ed., Treatise on Geochemistry, Volume 3: The Crust: Oxford, UK, Elsevier, 659 p., https://doi.org/10.1016/B0-08-043751-6/03016-4.
Ruiz, J., Tosdal, R.M., Restrepo, P.A., and Murillo-Muñetón, G., 1999, Pb isotope evidence for Colombia–southern Mexico connections in the Proterozoic, *in* Ramos, V.A., and Keppie, J.D., eds., Laurentia-Gondwana Connections before Pangea: Geological Society of America Special Paper 336, p. 183–197, https://doi.org/10.1130/0-8137-2336-1.183.
Salter, V.J.M., and Stracke, A., 2004, Composition of the depleted mantle: Geochemistry, Geophysics Geosystems, v. 5, Q05B07, https://doi.org/10.1029/2003GC000597.
Sarmiento-Villagrana, A., Vega-Granillo, R., Talavera-Mendoza, O., and Vidal-Solano, J.R., 2016, New age constraints on magmatism and metamorphism of the Western Sonobari Complex and their implications for an earliest Late Cretaceous orogeny on northwestern Mexico: Revista Mexicana de Ciencias Geológicas, v. 33, p. 170–182.
Schaaf, P., Böhnel, H., and Pérez-Venzor, J.A., 2000, Pre-Miocene palaeogeography of the Los Cabos Block, Baja California Sur: Geochronological and palaeomagnetic constraints: Tectonophysics, v. 318, p. 53–69, https://doi.org/10.1016/S0040-1951(99)00306-6.
Schmidt, K.L., Wetmore, P.H., Alsleben, H., and Paterson, S.R., 2014, Mesozoic tectonic evolution of the southern Peninsular Ranges batholith, Baja California, Mexico: Long-lived history of a collisional segment in the Mesozoic Cordilleran arc, *in* Morton, D.M., and Miller, F.K., eds., Peninsular Ranges Batholith, Baja California and Southern California: Geological Society of America Memoir 211, p. 645–668, https://doi.org/10.1130/2014.1211(20).
Sedlock, R.L., Ortega-Gutiérrez, F., and Speed, R.C., 1993, Tectonostratigraphic Terranes and Tectonic Evolution of Mexico: Geological Society of America Special Paper 278, 153 p., https://doi.org/10.1130/SPE278.
Shaw, S.E., Todd, V.R., and Grove, M., 2003, Jurassic peraluminous gneissic granites in the axial zone of the Peninsular Ranges, southern California, *in* Johnson, S.E., Paterson, S.R., Fletcher, J.M., Girty, G.H., Kimbrough, D.L., and Martín-Barajas, A., eds., Tectonic Evolution of Northwestern México and the Southwestern USA: Geological Society of America Special Paper 374, p. 157–183, https://doi.org/10.1130/0-8137-2374-4.157.
Shervais, J.W., 1982, Ti-V plots and the petrogenesis of modern and ophiolitic lavas: Earth and Planetary Science Letters, v. 59, p. 101–118, https://doi.org/10.1016/0012-821X(82)90120-0.
Smith, D.R., Barnes, C., Shannon, W., Roback, R., and James, E., 1997, Petrogenesis of Mid-Proterozoic granitic magmas: Examples from central and west Texas: Precambrian Research, v. 85, p. 53–79, https://doi.org/10.1016/S0301-9268(97)00032-6.
Stacey, J.T., and Kramers, L., 1975, Approximation of terrestrial lead isotope evolution by a two-stage model: Earth and Planetary Science Letters, v. 26, p. 207–221, https://doi.org/10.1016/0012-821X(75)90088-6.
Sun, S.S., and McDonough, W.S., 1989, Chemical and isotopic systematics of oceanic basalts: Implications for mantle composition and processes, *in* Saunders, A.D., and Norry, M.J., eds., Magmatism in the Ocean Basins: Geological Society of London Special Publication 42, p. 313–345, https://doi.org/10.1144/GSL.SP.1989.042.01.19.
Tosdal, R.M., 1996, The Amazon-Laurentian connection as viewed from the Middle Proterozoic rocks in the central Andes, western Bolivia and northern Chile: Tectonics, v.15, p. 827–842, https://doi.org/10.1029/95TC03248.
Thibodeau, A.M., Habicht-Mauche, J.A., Huntley, D.L., Chesley, J.T., and Ruiz, J., 2013, High precision isotopic analyses of lead ores from New Mexico by MC-ICP-MS: Implications for tracing the production and exchange of Pueblo IV glaze-decorated pottery: Journal of Archaeological Science, v. 40, p. 3067–3075, https://doi.org/10.1016/j.jas.2013.02.034.
Thibodeau, A.M., Killick, D.J., Hedquist, S.L., Chesley, J.T., and Ruiz, J., 2015, Isotopic evidence for the provenance of turquoise in the southwestern United States: Geological Society of America Bulletin, v. 127, p. 1617–1631, https://doi.org/10.1130/B31135.1.
Torres, R., Ruiz, J., Patchett, P.J., and Grajales, J.M., 1999, A Permo-Triassic continental arc in eastern Mexico: Tectonic implications for reconstructions of southern North America, *in* Bartolini, C., Wilson, J. L., and Lawton, T. F., eds., Mesozoic Sedimentary and Tectonic History of North-Central Mexico: Geological Society of America Special Paper 340, p. 191–196. https://doi.org/10.1130/0-8137-2340-X.191.
Valencia-Moreno, M., Ruiz, J., Barton, M.D., Patchett, P.J., Zürcher, L., Hodkinson, D.G., and Roldán-Quintana, J., 2001, A chemical and isotopic study of the Laramide granitic belt of northwestern Mexico: Identification of the southern edge of the North American Precambrian basement: Geological Society of America Bulletin, v. 113, p. 1409–1422, https://doi.org/10.1130/0016-7606(2001)113<1409:ACAISO>2.0.CO;2.
Vega-Granillo, R., Salgado-Souto, S., Herrera-Urbina, S., Valencia, V., Ruiz, J., Meza-Figueroa, D., and Talavera-Mendoza, O., 2008, U–Pb detrital zircon data of the Río Fuerte Formation (NW Mexico): Its peri-Gondwanan provenance and exotic nature in relation to southwestern North America: Journal of South American Earth Sciences, v. 26, p. 343–354, https://doi.org/10.1016/j.jsames.2008.08.011.
Vega-Granillo, R., Salgado-Souto, S., Herrera-Urbina, S., Valencia, V., and Vidal-Solano, J.R., 2011, Metamorphism and deformation in the El Fuerte region: Their role in the tectonic evolution of NW Mexico: Revista Mexicana de Ciencias Geológicas, v. 28, p. 10–23.
Vega-Granillo, R., Vidal-Solano, J.R., and Herrera-Urbina, S., 2012, Island arc tholeiites of Early Silurian, Late Jurassic and Late Cretaceous ages in the El Fuerte region, northwestern Mexico: Revista Mexicana de Ciencias Geológicas, v. 29, p. 492–513.
Vega-Granillo, R., Vidal-Solano, J.R., Solari, L.A., López-Martínez, M., Gómez-Juárez, O.S., and

Herrera-Urbina, S., 2013, Geochemical and geochronological constraints on the geologic evolution of the western Sonobari Complex, northwestern Mexico: Geologica Acta, v. 11, p. 443–463, http://doi.org/10.1344/105.000002059.

Vega-Granillo, R., Sarmiento-Villagrana, A., Salgado-Souto, S., and Araux-Sánchez, E., 2017, P-T conditions of earliest Late Cretaceous metamorphism in the Western Sonobari Complex, northwestern Mexico: Tectonic implications: International Geology Review, v. 59, p. 812–828, https://doi.org/10.1080/00206814.2016.1227942.

Villanueva-Lascurain, D., Solís-Pichardo, G., Schaaf, P., Hernández-Treviño, T., Salazar-Juárez, J., and Corona-Chávez, P., 2016, Age and origin of the gabbros in the Jilotlán pluton, Jalisco: Primitive magmatic rocks in the southern part of the Guerrero terrane: Revista Mexicana de Ciencias Geológicas, v. 33, p. 136–156.

Weber, B., and López-Martínez, M., 2006, Pb, Sr, and Nd isotopic and chemical evidence for a primitive island arc emplacement of the El Arco porphyry copper deposit (Baja California, Mexico): Mineralium Deposita, v. 40, p. 707–725.

Weber, B., Iriondo, A., Premo, W.R., Hecht, L., and Schaaf, P., 2007, New insights into the history and origin of the southern Maya block, SE México: U–Pb–SHRIMP zircon geochronology from metamorphic rocks of the Chiapas massif: International Journal of Earth Sciences, v. 96, p. 253–269, https://doi.org/10.1007/s00531-006-0093-7.

Whalen, J.B., Currie, K.L., and Chappell, B.W., 1987, A-type granites: Geochemical characteristics, discrimination and petrogenesis: Contributions to Mineralogy and Petrology, v. 95, p. 407–419, https://doi.org/10.1007/BF00402202.

Wilson, B.M., 2007, Igneous Petrogenesis: A Global Tectonic Approach: Dordrecht, Netherlands, Springer Science and Business Media, 466 p.

Winchester, J.A., and Floyd, P.A., 1977, Geochemical discrimination of different magma series and their differentiation products using immobile elements: Chemical Geology, v. 20, p. 325–343, https://doi.org/10.1016/0009-2541(77)90057-2.

Zurcher, L., 2002, Regional setting and magmatic evolution of Laramide porphyry copper systems in western Mexico [PhD. thesis]: Tucson, University of Arizona, 427 p.

4

Condiciones P-T del metamorfismo del Cretácico Tardío más temprano en el Complejo Sonobari del Oeste, noroeste de México: implicaciones tectónicas

Artículo:

Vega-Granillo, R., Sarmiento-Villagrana, A., Salgado-Souto, S., and Araux-Sánchez, E., 2017, P-T conditions of earliest Late Cretaceous metamorphism in the Western Sonobari Complex, northwestern Mexico: tectonic implications: International Geology Review, v. 59, no. 7, p. 812-828, doi: 10.1080/00206814.2016.1227942.

Ricardo Vega Granillo. Coordinación y participación en campo. Obtención de datos en la microsonda electrónica. Obtención de datos U-Pb, elaboración de gráficas, mapas y modelo tectónico. Consecución del financiamiento. Concepción, planteamiento del trabajo y escritura del manuscrito.

Alicia Sarmiento Villagrana. Participación en campo y muestreo de las rocas para fechar y microsonda electrónica. Preparación de las muestras, análisis en la microsonda electrónica y procesamiento de los datos. Elaboración de las pseudosecciones en el programa PERPLEX y gráficas de la química mineral. Obtención de los fechamientos U-Pb. Elaboración de la petrografía y anexos de los datos geocronológicos. Participación en escritura y revisión del manuscrito.

Sergio Salgado Souto. Determinación de la cadoluminiscencia de los zircones en alta resolución y obtención de los fechamientos U-Pb.

Elizabeth Sánchez Araux. Participación en campo, revisiones y aporte a la versión final del manuscrito.

International Geology Review

ISSN: 0020-6814 (Print) 1938-2839 (Online) Journal homepage: http://www.tandfonline.com/loi/tigr20

P-T conditions of earliest Late Cretaceous metamorphism in the Western Sonobari Complex, northwestern Mexico: tectonic implications

Ricardo Vega-Granillo, Alicia Sarmiento-Villagrana, Sergio Salgado-Souto & Elizabeth Araux-Sánchez

To cite this article: Ricardo Vega-Granillo, Alicia Sarmiento-Villagrana, Sergio Salgado-Souto & Elizabeth Araux-Sánchez (2017) P-T conditions of earliest Late Cretaceous metamorphism in the Western Sonobari Complex, northwestern Mexico: tectonic implications, International Geology Review, 59:7, 812-828, DOI: 10.1080/00206814.2016.1227942

To link to this article: http://dx.doi.org/10.1080/00206814.2016.1227942

INTERNATIONAL GEOLOGY REVIEW, 2017
VOL. 59, NO. 7, 812–828
http://dx.doi.org/10.1080/00206814.2016.1227942

Taylor & Francis
Taylor & Francis Group

P-T conditions of earliest Late Cretaceous metamorphism in the Western Sonobari Complex, northwestern Mexico: tectonic implications

Ricardo Vega-Granillo [a], Alicia Sarmiento-Villagrana [b], Sergio Salgado-Souto [c] and Elizabeth Araux-Sánchez [d]

[a]Departamento de Geología, Universidad de Sonora, Hermosillo, Mexico; [b]Instituto de Geología, Universidad Nacional Autónoma de México, Hermosillo, Mexico; [c]Unidad Académica de Ciencias de la Tierra, Universidad Autónoma de Guerrero, Taxco, Mexico; [d]Departamento de Ingeniería Civil y Minas, Universidad de Sonora, Hermosillo, Mexico

ABSTRACT

The Western Sonobari Complex in northwestern Mexico consists of metamorphosed rocks mostly derived from Palaeozoic (?) sedimentary and Mesozoic igneous protoliths. Rocks of this complex display amphibolite facies orogenic metamorphism, pervasive foliation, migmatization, and four folding phases. These features are ascribed to a contractional tectonic event with NNW–SSE shortening direction, which caused thrusting, thickening of the crust, and sinking of the lithological units. U–Pb geochronology of migmatitic leucosome bands indicates that peak metamorphic conditions were reached between ~93 and 89 Ma. Post-tectonic Late Cretaceous peraluminous aplite-pegmatite dikes transect the metamorphic foliation. Traditional thermobarometry in the metamorphic rocks yields average pressures and temperatures of 9.0–7.1 kbar and 745–663°C, typical of intermediate P/T Barrovian metamorphism. On the basis of its age and contractional character, the thickening event originating the metamorphism may be related to collision of the Alisitos island arc against crustal blocks of Mexico. Thermobarometric data of post-tectonic intrusives including Late Cretaceous granodiorite and Eocene gabbro indicate emplacement within an overthickened crust, while P-T conditions of post-tectonic dikes point towards an almost isothermal decompression path along the amphibolite facies field. Rock units of similar age and metamorphic character are discontinuously exposed from the Islas Marias offshore the Nayarit coast to the Peninsular Ranges batholith of Baja California, and even extend north into the Sierra Nevada batholith and the Sevier hinterland. This extensive belt of Barrovian metamorphic rocks thus provides a record of middle Cretaceous shortening and crustal thickening related to arc-continent collision followed by subduction resuming.

ARTICLE HISTORY
Received 15 June 2016
Accepted 20 August 2016

KEYWORDS
Geochronology; thermobarometry; Barrovian metamorphism; Sonobari Complex; tectonics

Introduction

The Western Sonobari Complex (WSC), located on the border of Sonora and Sinaloa states, northwestern Mexico, is regarded as part of an orogenic belt discontinuously exposed along 1300 km from Baja California to the Islas Marías in western Mexico (Sarmiento-Villagrana *et al.* 2016). Recent U–Pb geochronology in the WSC indicates that the plutonic protoliths were emplaced during Early Triassic, Late Triassic, Late Jurassic and earliest Late Cretaceous pulses (Sarmiento-Villagrana *et al.* 2016). Coeval magmatic pulses have been described from southwestern USA to southern Mexico (e.g. Torres *et al.* 1999; Kimbrough *et al.* 2001; Anderson *et al.* 2005; Barth *et al.* 2011; Sarmiento-Villagrana *et al.* 2016 and references therein). Zircon recrystallized rims of metamorphic rocks yield ages ranging 93–90 Ma, which are interpreted as dating the peak metamorphic event (Sarmiento-Villagrana *et al.* 2016). Rocks of similar metamorphic age and grade crop out in the eastern Peninsular Ranges batholith and the Los Cabos Block of Baja California, Central Sinaloa, and in the Marias Islands offshore the Nayarit coast (Aranda-Gómez and Pérez-Venzor 1989; Henry *et al.* 2003; Cuéllar-Cárdenas *et al.* 2012; Pompa-Mera *et al.* 2013; Schmidt *et al.* 2014). The metamorphic ages are coeval to $^{40}Ar/^{39}Ar$ in hornblende ages (93–92 Ma) of the voluminous La Posta-type intrusions in the Baja California Peninsular Ranges batholith (Kimbrough *et al.* 2001). Other rocks that can be correlated by their age and/or type of metamorphism with the WSC have been described in the coastal region of Sonora (Ramos-Velázquez *et al.* 2008), the Sierra Nevada batholith (Sams and Saaleby 1988; Saleeby *et al.* 2008) and the Sevier

CONTACT Ricardo Vega-Granillo rvega@ciencias.uson.mx Departamento de Geología, Universidad de Sonora, Rosales y Encinas S/N, Hermosillo, Sonora, Mexico 83000

The supplemental data for this article can be accessed here.

hinterland (e.g. DeCelles 2004). In western Mexico, orogenic metamorphic rocks mostly display amphibolite facies paragenesis imposed on sedimentary and igneous protoliths (Mullan 1978; Aranda-Gómez and Pérez-Venzor 1989; Keppie *et al*. 2006; Vega-Granillo *et al*. 2013; Schmidt *et al*. 2014). In addition, tectonites are usually intruded by Late Cretaceous to Eocene post-orogenic composite plutons, and covered by Mesozoic to Cenozoic volcanic and sedimentary sequences (Henry *et al*. 2003; Pompa-Mera *et al*. 2013; Vega-Granillo *et al*. 2013; Schmidt *et al*. 2014; Sarmiento-Villagrana *et al*. 2016). Studies in the above-mentioned locations have been mainly focused in cartography, and K–Ar, Rb–Sr or U–Pb geochronology of protoliths. In Mexico, metamorphism is assigned to the amphibolite facies mainly based on petrologic and petrographic grounds, only in Baja California a thermobarometric and thermodynamic calculation had been performed in the host rocks of the Peninsular Ranges batholith yielding peak metamorphic temperatures of 475–720°C and pressures of 3–6 kbar (Rothstein and Manning 2003).

Orogenic mid-Cretaceous metamorphism in the southern Sierra Nevada has been attributed to low-angle subduction-driven contraction and thickening (e.g. Saleeby *et al*. 2008) as in central Andes during Cenozoic orogenesis (e.g. Vietor and Echtler 2006). In northwestern Mexico, although contractional deformation is apparent since ca. 132 Ma (Schmidt and Paterson 2002), peak metamorphic pressures were recorded at ca. 100 Ma (Schmidt *et al*. 2009). The main metamorphic event nearly followed the latest Early Cretaceous collision of the Alisitos island arc against mainland Mexico (Johnson *et al*. 1999; Alsleben *et al*. 2008; Schmidt *et al*. 2014), therefore the role of this event in the origin of the orogenic belt requires to be evaluated.

Several issues remain unresolved for the WSC, such as its regional extent, relationships with the surrounding rocks, particularly with the Eastern Sonobari Complex, the age of the anatexis, and the P-T conditions of metamorphism. These issues will be addressed in this work, considering that specifying the time and P-T conditions of metamorphism is required for developing models of crustal thickening, petrogenesis and tectonic evolution.

Geological setting

The Sonobari Complex originally included orogenic metamorphic rocks exposed in southern Sonora–northern Sinaloa States, northwestern Mexico (De Cserna and Kent 1961). Vega-Granillo *et al*. (2013) proposed dividing the Sonobari Complex into eastern and western zones based on differences in provenance, lithology, protolith ages and metamorphic grade (Figure 1). The Eastern Sonobari Complex (ESC) includes the Rio Fuerte, Cubampo and Topaco formations, whereas the Western Sonobari Complex includes the Francisco Gneiss (Mullan 1978) and numerous leucocratic aplite-pegmatite dikes. In both regions, non-foliated gabbroic to granodioritic plutons, and mafic to ultramafic dikes intrude the tectonites (Mullan 1978; Vega-Granillo *et al*. 2008, 2013; Sarmiento-Villagrana *et al*. 2016). The Rio Fuerte Formation is a siliciclastic succession with uncommon calcareous layers containing Middle–Late Ordovician conodonts (Poole *et al*. 2005, 2010). Detrital zircon plots in that unit indicate a Gondwanan provenance (Vega-Granillo *et al*. 2008). The Rio Fuerte Formation underwent low-pressure greenschist to low-amphibolite facies metamorphism preceding intrusion of the Late Jurassic Cubampo Granite (Vega-Granillo *et al*. 2008, 2011). The Rio Fuerte and Cubampo Granite units were exhumed, eroded and their clasts were included in the volcanoclastic Upper Jurassic Topaco Formation (Vega-Granillo *et al*. 2012). A second low-grade orogenic metamorphism overprinted the Rio Fuerte, Cubampo Granite and Topaco formations, after the Late Jurassic (Vega-Granillo *et al*. 2011).

The Francisco Gneiss is composed of orthogneisses, amphibolites and paragneisses, overprinted by amphibolite facies metamorphism, anatexis and migmatization (Mullan 1978; Keppie *et al*. 2006; Vega-Granillo *et al*. 2013). The protoliths of the orthogneisses were Early Triassic granodiorite and quartz monzodiorite (249–243 Ma), Late Triassic granodiorite (213.7–203.7 Ma), Late Jurassic tonalite and granodiorite (163–159 Ma), and earliest Late Cretaceous tonalite (99 Ma) (Sarmiento-Villagrana *et al*. 2016). Detrital zircon ages of the Francisco paragneisses suggest a Laurentian provenance (Vega-Granillo *et al*. 2013).

Southeast and outside of the study region, a thick fossiliferous Carboniferous–Lower Permian deep-marine succession known as the San Jose de Gracia Formation is exposed (Carrillo-Martínez 1971; Gastil *et al*. 1991). This formation is composed of unmetamorphosed thin-bedded sandstone, siltstone, chert and minor limestones. Although exposures of the San Jose de Gracia Formation are proposed extending to the Mazatlán region (Poole *et al*. 2005; Centeno-García *et al*. 2008), unequivocal evidence for this correlation is not available.

Western Sonobari Complex

The Western Sonobari Complex crops out along ~N–S oriented ranges separated by wide alluvial valleys. In the westernmost exposures (Figure 1(b)), small blocks of metasedimentary rocks are exposed as roof

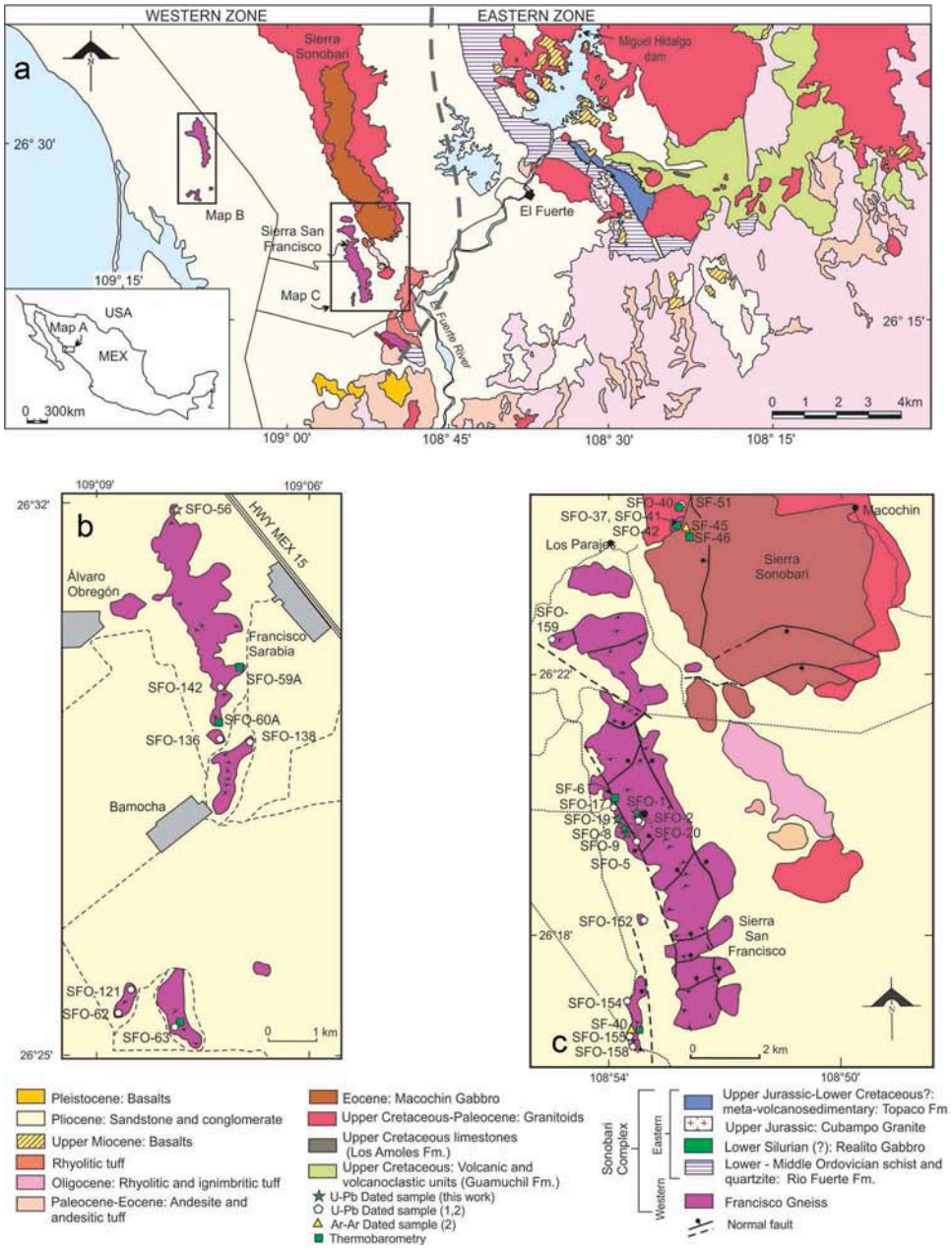

Figure 1. (a) Geological map of the Sonobari Complex (modified from Vega-Granillo *et al*. 2013); (b) and (c) Enlarged geological maps. (1) Sarmiento-Villagrana et al. (2016); (2) Vega-Granillo *et al*. (2013).

pendants in Late Jurassic granodiorite and tonalite (Sarmiento-Villagrana *et al*. 2016). Undated mafic dikes were intruded after the Late Jurassic and the earliest Late Cretaceous (Sarmiento-Villagrana *et al*. 2016). After that, amphibolite facies metamorphism and related pervasive foliation development transformed the metasediments, plutons and dikes into paragneiss-quartzite, orthogneiss and amphibolite, respectively. Anatexis is evidenced by stromatic migmatites defined by thin bands of leucosome parallel to the foliation (Figure 2(a–c)), leucosome patches with cores of amphibole, magnetite or garnet (Figure 2(d)) and by leucosome veins locally transecting the foliation (Figure 2(e)). These structures are typical of metatexite migmatites indicating low fraction of melt (Sawyer 2008). Non-foliated Late Cretaceous diorite (~100 Ma) and undated coarse-grained pyroxenite-hornblendite dikes intrude the stromatic migmatites. The youngest rocks are numerous post-orogenic leucocratic pegmatite-aplite dikes dated at 83.9 Ma (Sarmiento-Villagrana *et al*. 2016), which intrude older lithologies.

In Sierra San Francisco, the Francisco Gneiss consists of biotite-rich metasedimentary rocks, intruded by

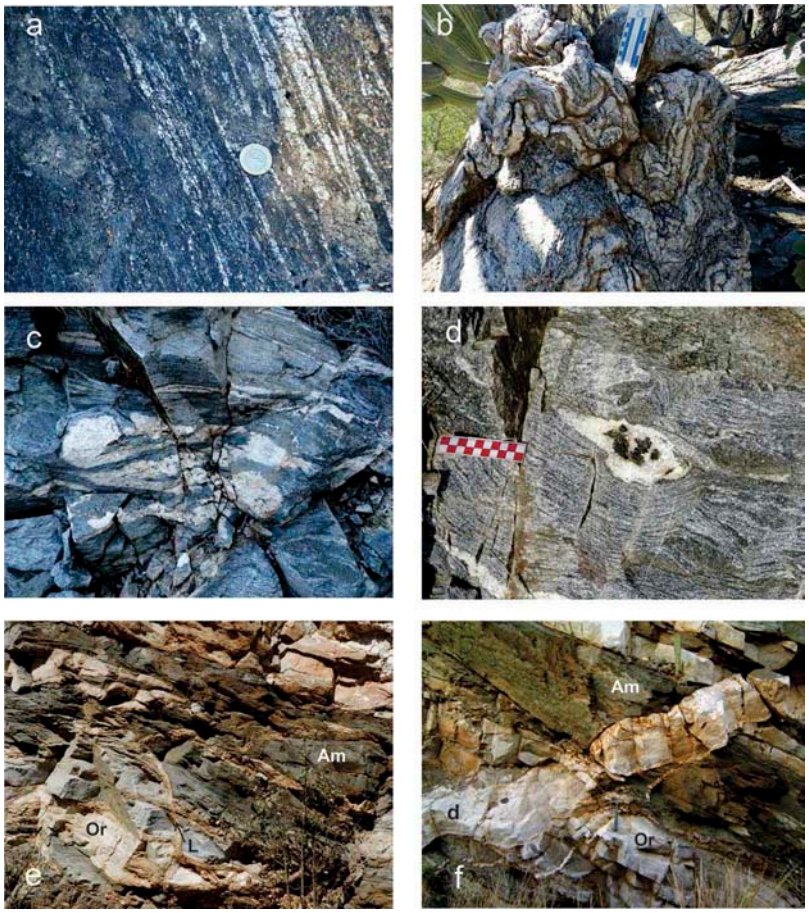

Figure 2. Exposure photographs of the main rocks in the Western Sonobari Complex. (a) Paragneiss with stromatic leucosomes, (b) Tightly folded stromatic leucosomes in paragneiss; (c) Strongly folded leucosome band in Upper Triassic orthogneiss; (d) Patch migmatite in Upper Jurassic orthogneiss; (e) Close-folded leucosome band (L) cross-cutting the foliation of amphibolite (Am) and Upper Triassic orthogneiss (Or). (f) Upper Cretaceous aplite dike (D) cross-cutting the foliation of amphibolite (Am) and the Upper Triassic orthogneiss (Or).

Early–Late Triassic, and Late Jurassic plutons (Sarmiento-Villagrana *et al*. 2016) and younger mafic dikes, all of them mapped as a single unit in Figure 1(c). Also, garnet-muscovite schists crop out in the southern Sierra Sonobari. The mafic dikes and their host rocks display amphibolite facies metamorphism, pervasive foliation, and metatexite migmatization (Figure 2(c)). As in the westernmost exposures, numerous post-tectonic garnet-two mica pegmatite and aplite dikes (Figure 2(f)) dated at 82.9 and 80.6 Ma, respectively (Sarmiento-Villagrana *et al*. 2016), transect the tectonites. In the southern Sierra Sonobari (Figure 1(c)), the Late Cretaceous Los Parajes Granodiorite (64 Ma; U–Pb zircon) and the Eocene Macochin Gabbro (54 Ma; ^{40}Ar–^{39}Ar hornblende; Vega-Granillo *et al*. 2013) intrude the tectonites.

Very poor exposures of the Francisco Gneiss extend to the south of the Sierra San Francisco where are intruded by granitic bodies and covered by Cenozoic volcanic rocks and surficial deposits. These rocks are juxtaposed along an undefined contact against andalusite-bearing metasedimentary rocks ascribed to the Middle–Late Ordovician Rio Fuerte Formation of the Eastern Sonobari Complex. A description of representative rocks mentioned in this chapter is included in the Supplementary Table 1.

Structural geology

The main structure of the WSC is a pervasive foliation developed in all metamorphic rocks. Original contacts between granite, sediments, and basic dikes, were tightly folded (F1) and transposed during the first deformational phase, becoming parallel to the main foliation. This foliation underwent at least three phases of folding, and interference patterns of type 3 superposed folds (Ramsay 1967) are common. The F2 phase is represented by isoclinal to subisoclinal folds that bend the main foliation and stromatic leucosome veins (Figure 2(c)). The F3 phase

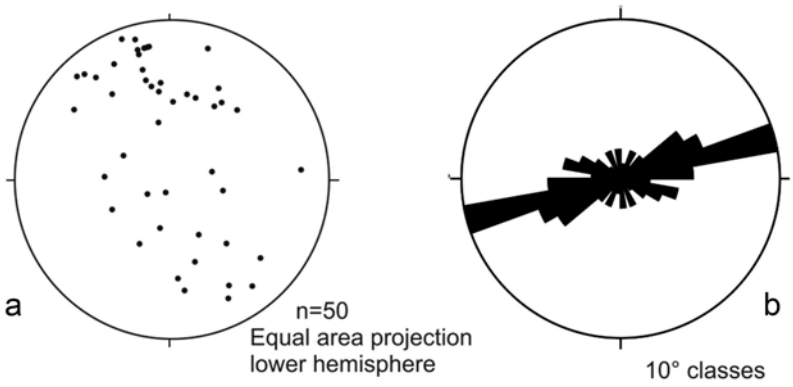

Figure 3. Foliation data in the Francisco Gneiss: (a) Poles to foliation; (b) Rose diagram for strikes of foliation.

produced NNW verging overturned tight folds (Figure 2(e)), while the F4 phase formed open folds with almost vertical axial surfaces. Foliation strikes mostly N70-80°E and dips to SE and NW (Figure 3) reflecting the folding phases.

Methods

U–Pb geochronology was applied to samples of leucosome veins in paragneisses and orthogneisses. Cathodoluminescence images were obtained in the Arizona LaserChron Center and the Laboratorio de Microscopía Electrónica de la Unidad Académica de Ciencias de la Tierra de la Universidad Autónoma de Guerrero. U–Pb geochronology of zircons was determined by laser ablation multicollector inductively coupled plasma mass spectrometry (LA-MC-ICPMS) at the Arizona LaserChron Center, University of Arizona, following procedures of Gehrels *et al*. (2009) and Johnston *et al*. (2009). Data were collected during several analytical sessions from 2013 and 2015, utilizing a Nu Plasma ICPMS connected to a Photon Machines Analyte G2 excimer laser. A complete data set of the U-Pb geochronology is included in the Supplementary Table 2. Ages of the zircon rims can be altered by mixing with xenocrysts or cores, or by loss of lead, mostly arising from the laser-spot size and the irregular morphology of the zircon rims. In these cases, the TuffZirc algorithm (Ludwig and Mundil 2002) was used. According to Ludwig (2008), this algorithm is largely insensitive to both Pb-loss and inheritance, and takes into consideration the information yielded by analytical errors.

Geochemistry of major elements was quantified by inductively coupled plasma atomic emission spectrometry (ICP-AES) at ALS Minerals commercial laboratory in Vancouver, Canada. The lower detection limit of this method is 0.01%. Mineral chemistry was performed using a CAMECA SX-50 or CAMECA SX-100 electron microprobe at the Department of Lunar and Planetary Sciences of the University of Arizona. Microprobe analytical error roughly varies between ±0.01 and 0.04 wt % (1σ).

Results

U–Pb geochronology

Two paths were followed in order to constrain the age of metamorphism: (a) dating of zircons and recrystallized zircon rims in leucosome veins either parallel to or transecting the main foliation (Figures 2(e) and 4); and (b) dating of recrystallized zircon rims in metamorphic rocks. Only a few large-enough zircon rims could be dated in each sample with the 35 µm standard laser spot; therefore, a 15 µm spot was used in some samples to obtain larger data set (Supplementary Table 2). Four samples of leucosome veins in the Sierra San Francisco were dated. Sample SFO-1 is a folded vein cross-cutting the main foliation of orthogneiss and amphibolite (Figure 2(e)). In this sample, 21 inherited zircon cores yield a Tuff–Zirc age of 208.09 ± 1.95 Ma (Figure 5(a)), while zircon rims yield a Tuff–Zirc age of 90.82 ± 3.65 Ma (Figure 5(b)). Sample SFO-8 is a concordant leucosome vein in a biotite orthogneiss, from which 15 inherited zircons yield a mean average age of 209.7 ± 2.3 Ma (Figure 5(c)), which matches the age of the host rock (Sarmiento-Villagrana *et al*. 2016). The zircon rims of this rock yield a TuffZirc age of 92.6 ± 3.3 Ma (Figure 5(d)). Sample SFO-9 is a leucosome vein transecting the foliation of the stromatic gneiss mentioned above. Inherited zircons in this rock provide a mean average age of 210.2 ± 2.7 Ma (Figure 5(e)). Analyses with 15 µm laser-spot in zircon rims yield a TuffZirc age of 88.95 ± 2.1 Ma (Figure 5(f)). Sample SFO-19 is a leucosome vein parallel to the foliation of paragneiss. In this sample, ages from 1652 to 335 Ma (Figure 5(g)) clearly derive from detrital zircons inherited

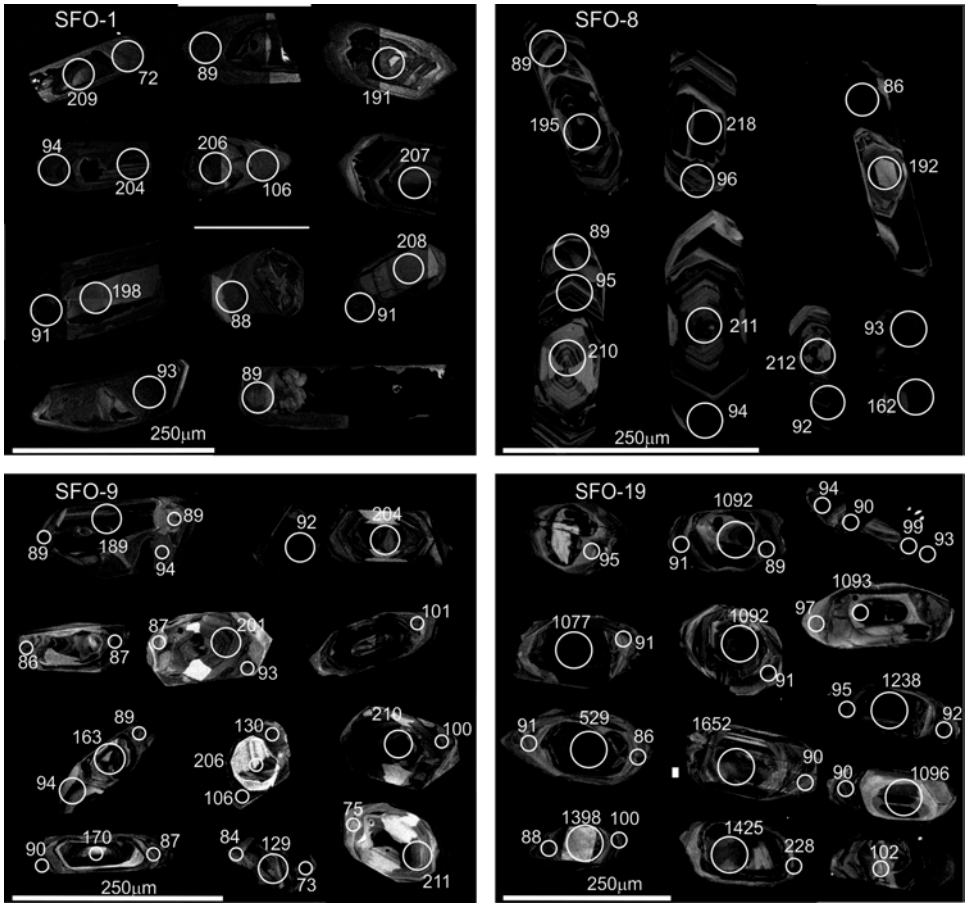

Figure 4. Cathodoluminescence images with selected laser spots of zircons derived from leucosomes of migmatitic rocks in the study area.

from its metasedimentary host (Vega-Granillo *et al*. 2013). The younger ages obtained from zircon rims dated with 15 μm laser-spot yield a TuffZirc age of 90.7 ± 1.45 Ma (Figure 5(h)). U–Pb dating of recrystallized zircon rims in metamorphic rocks was reported by Sarmiento-Villagrana *et al*. (2016). In that work, orthogneisses SFO-20 and SFO-152 yielded mean ages of 92.3 ± 4.1 Ma and 90.1 ± 1.3 Ma, which clearly coincide with the ages of leucosomes obtained in this work. A collection of previous (Sarmiento-Villagrana *et al*. 2016) and new data obtained from zircon rims of 10 samples yields a TuffZirc age of 91.3 ± 0.5 Ma derived from a coherent group of 54 analyses (Figure 5(i)). The U/Th ratios of the zircon rims in all samples are higher than 20 (Figure 5(j)). Large U/Th values have been regarded as indicative of metamorphic imprint (Rubatto 2002; Gehrels *et al*. 2009).

Thermobarometry

In order to define the P-T conditions of metamorphism of the WSC, point chemical analyses were performed near the boundary of selected minerals. Studied samples include amphibolite, orthogneiss, hornblendite, granodiorite, and gabbro (locations in Figure 1). Mineral assemblages are displayed in the Supplementary Table 1. Plagioclase is mostly andesine or oligoclase with only one sample (SFO-59A) containing albite (Figure 6(a)). Garnet is a solid solution mainly of almandine with decreasing amounts of grossularite, pyrope, and spessartite (Figure 6(b)). Amphibole of metamorphic rocks, the Los Parajes Granodiorite and the Macochin Gabbro is mostly tschermakite or Fe-tschermakite (Figure 6(c)). A hornblendite dike and one amphibolite mainly contain Mg-hornblende.

Classical thermobarometry was applied to metamorphic and igneous suites in the study area. Considering the mineral assemblages of the diverse lithologies, the garnet-plagioclase-amphibole-quartz (GPAQ) geothermobarometer (Kohn and Spear 1990), as well as the amphibole-plagioclase (Amp-Pl) geothermometer (Holland and Blundy 1994) with the Al^{IV} in Si geobarometer (Anderson and Smith 1995; Anderson 1996) were applied. The thermometer A of Holland and Blundy (1994) was used for assemblages with quartz, while the thermometer B was applied in

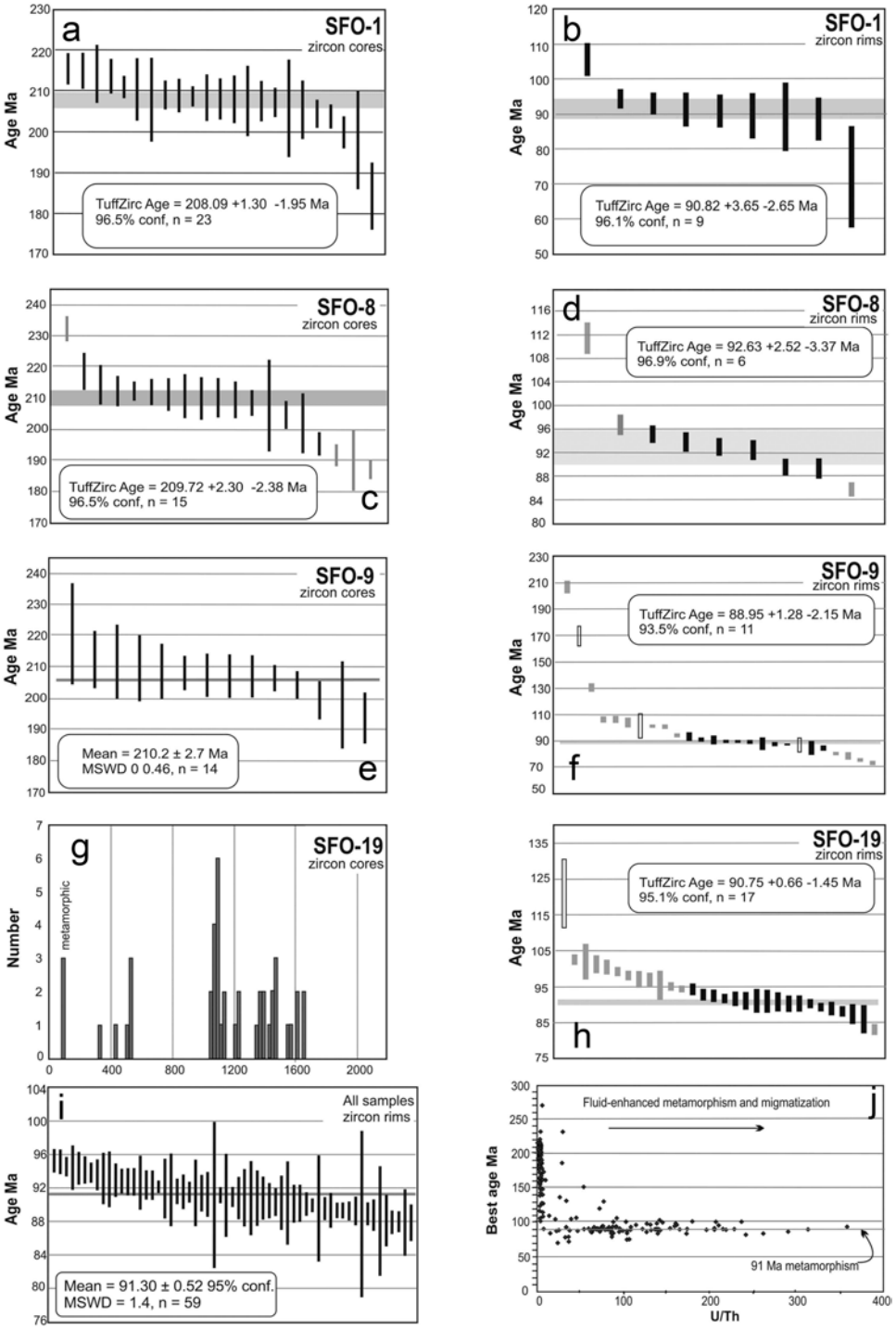

Figure 5. U–Pb geochronology results. In the Tuff–Zirc diagrams (a,b,c,d,f,h), black bars are data used for calculation of the mean age; grey and white bars are data discarded from the average age calculations. All bars are 1sigma. (e) and (i): mean ages. (g): Frequency histogram of inherited detrital zircon in paragneiss. (j): U/Th vs. age diagram for all dated zircon rims and cores. Data from the cores lay near the vertical axis.

quartz-lacking rocks. Analytical and temperature imprecisions for the GPAQ geothermobarometer yield a pressure uncertainty of about ±0.5 kbar (Kohn and Spear 1990). Typical temperature uncertainty for the Amp-Pl geothermometer is ±35–40°C (Holland and Blundy 1994), while the Al^{IV} in hornblende geobarometer can reach an uncertainty of ±1 kbar, considering the temperature and analytical errors (Anderson and Smith 1995).

In sierras San Francisco and southern Sonobari, GPAQ geothermobarometer in one amphibolite (SFO-41) and two orthogneisses (SF-6, SFO-42) yields average P-T

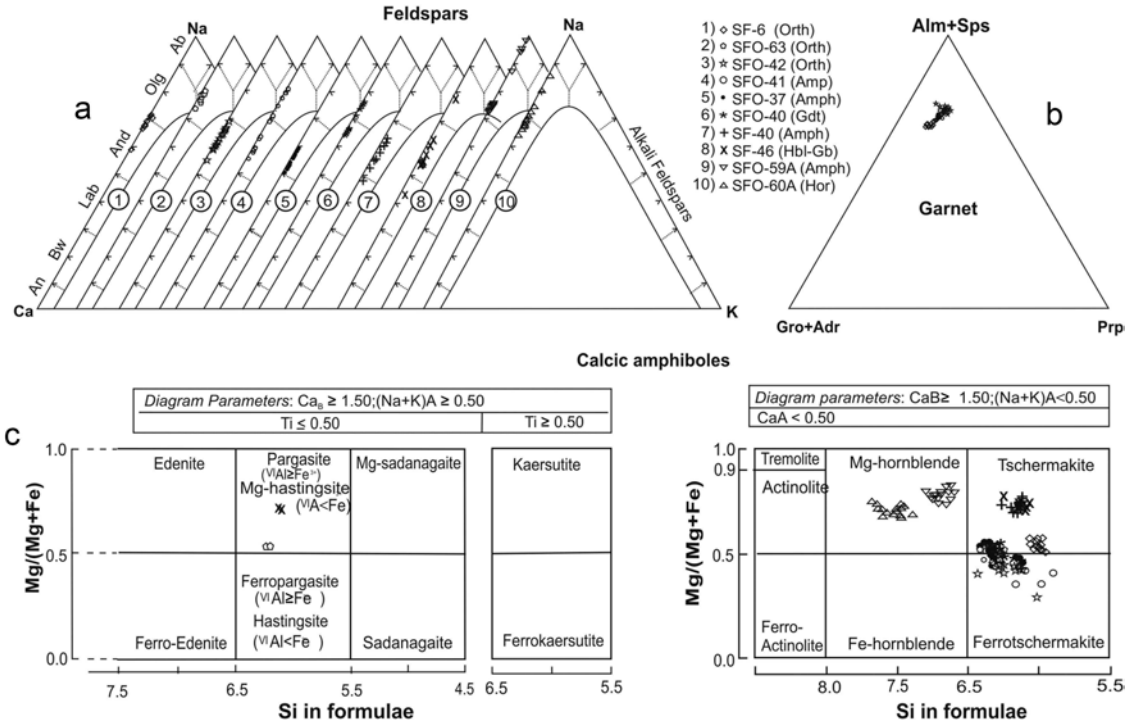

Figure 6. Classification diagrams for minerals used in thermobarometric studies: (a) Plagioclase; (b) Garnet; (c) Amphibole. Mineral abbreviations: An, Anorthite; Bw, Bitownite; Lab, Labradorite; And, Andesine; Olg, Oligoclase; *Ab*, Albite; Alm, Almandine; Sps, Spessartine; Gro, Grossularite; Adr, Andradite; Prp, Pyrope. Rock abbreviations: Orth, Orthogneiss; Amph, Amphibolite; Gdt, Granodiorite; Hbl-Gb, Hornblende gabbro; Hor, Hornblendite.

conditions of 7.1 kbar–663°C (standard deviation σ = 0.6 and 45), 7.2 kbar–697°C (σ = 0.8 and 35), and 9.0 kbar–678°C (σ = 0.9 and 62), respectively (Figure 7). In the same region, but using the Amp-Pl geothermometer and the Al^{IV} in hornblende geobarometer, two amphibolites (SF-40, SFO-37) yield average P-T conditions of 8.1 kbar–745°C (σ = 0.5 and 13) and 8.5 kbar–705°C (σ = 0.6 and 18), respectively (Figure 7(a)). A complete thermobarometry data set is included in the Supplementary Table 3. The Late Cretaceous Los Parajes Granodiorite (SFO-40) and the Eocene Macochin Gabbro (SF-46) yield average conditions of 8.9 kbar–685°C (σ = 1.0 and 14) and 8.1 kbar–739°C (σ = 0.6 and 23), respectively (Figure 7(b)). In the western exposures a Late Jurassic orthogneiss (SFO-63, Figure 1(b)) yields P-T conditions of 7.6 kbar–687°C (σ = 0.3 and 12; Figure 7(b)), an amphibolite (SFO-59A; Figure 7(b)) and a hornblendite dike (SFO-60A; Figure 7

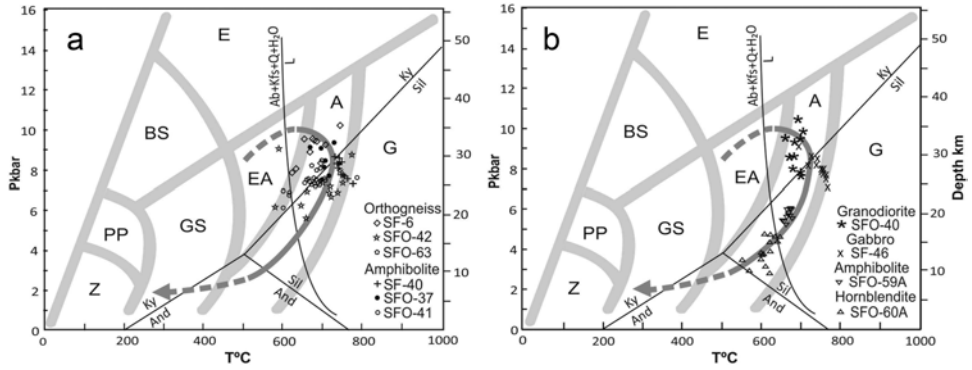

Figure 7. P-T diagrams with results of thermobarometric analyses of (a) metamorphic and (b) igneous rocks plot over metamorphic facies and some stability reactions according to Spear (1993). Middle grey line indicates the suggested P-T-t path. Facies: Z, Zeolite facies; PP, Prehnite-pumpellyte facies; BS, Blueschist facies; GS, Greenschist facies; E, Eclogite facies; EA, Epidote-amphibolite facies; A, Amphibolite facies; G, Granulite facies. Reactions: *Ab*, Albite; And, Andalusite; Kfs, Potassium feldspar; Ky, Kyanite; L, Liquidus; Q, Quartz; Sil, Sillimanite.

(b)) yield 5.7 kbar–665°C (σ = 0.7 and 25) and 3.9 kbar–614°C (σ = 0.2 and 25) conditions, respectively. The last two data are the lowest P-T conditions found in the study area.

The geothermobarometry results are synthetized in the P-T diagrams of Figure 7, which includes facies boundaries and some pertinent stability reactions according to Spear (1993). Metamorphism mostly occurred at average pressures between 9.0 and 7.1 kbar and temperatures between 745°C and 663°C, which are consistent with anatexis creating the metatexite migmatites. Several analyses fall in the kyanite stability field but some lie in the sillimanite field. Although relics of kyanite were not found, non-oriented muscovite aggregates are regarded as pseudomorphs after kyanite. Samples containing oligoclase and albite besides more calcic plagioclases are inferred that underwent retrograde metamorphism. In particular, P-T conditions of samples SFO-59A and SFO-60A may indicate exhumation along an almost isothermal decompression path in the amphibolite facies before the rocks underwent greenschist facies metamorphism (Figure 7(b)). The average pressure obtained from the igneous and metamorphic rocks, excepting the lowest P samples, is 8.0 kbar (σ = 0.9), whereas average T is 699°C (σ = 42). The average pressure corresponds to an estimated depth of ~30 km. The Late Cretaceous Los Parajes Granodiorite and the Eocene Macochin Gabbro yielding similar P/T conditions to the hosting metamorphic rocks are interpreted as emplaced deep in an overthickened crust. This interpretation is consistent with the geochemical character of the Macochin Gabbro, which indicates a larger assimilation of the lower continental crust than the amphibolite protoliths (Vega-Granillo *et al*. 2013).

Pseudo-section modelling

In order to evaluate the consistency of the thermobarometric data with the paragenesis of different lithologies in the study area, three P-T pseudo-sections were constructed. Pseudo-sections were calculated using PERPLEX_X 6.6.6 (http://www.perplex.ethz.ch/) following the approach of Connolly (1990, 2009) and Connolly and Petrini (2002), as well as the internally consistent thermodynamic dataset and equation of state for H_2O of Holland and Powell (1998). The following mineral solution models were used: biotite [Bio (HP)], clinopyroxene [Cpx(HP)], orthopyroxene [Opx (HP)], garnet [Gt(HP)], silicate melt [melt(HP)], staurolite [St(HP)], spinel [Sp(HP)], plagioclase [Pl(h)], K-feldspar (feldspar), cordierite (hCrd), mica (MaPa), Mica (CF), Ca-Amph (D).

P-T pseudo-sections display the fields of stability of different equilibrium mineral assemblages for a single bulk-rock composition. For amphibolites, the average composition of five samples was used. Besides, the paragneiss SFO-151 and the Late Triassic orthogneiss SFO-5 were selected. For the first two samples pseudo-sections were calculated in the NCKFMASHT system, while the orthogneiss pseudo-section was constructed in the NCKFMASH system. All pseudo-sections were calculated within the P-T range of 500–1000°C, 4.0–12.0 kbar (0.4–1.2 GPa).

For the pseudo-section A calculated from average amphibolite composition (Figure 8(a)), the characteristic assemblages are displayed in light colour and are composed of Pl+Gt+Amp+Bt+Q+Rt (abbreviations as Figure 8). Points indicate the P-T conditions obtained with thermobarometry of amphibolite samples. Zoisite and/or clinozoisite commonly occur in amphibolite perhaps as metastable phases formed under lower T/higher P conditions. Minor P or T changes can produce assemblages without rutile (light grey area) that also are found in some amphibolites. Melt was not considered for this pseudo-section because partial melting of mafic rocks occurs at higher temperatures and the melt produced is tonalitic (e.g. Sawyer *et al*. 2011). Uncommon granitic leucosome bands parallel to or transecting the amphibolite foliation derive from the orthogneiss intercalated with the amphibolite as indicated by zircon geochronology.

Pseudo-section B (Figure 8(b)) is calculated for the chemical composition of the paragneiss (sample SFO-151). Granitic leucosome layers forming ~10% rock volume (Figure 2(a,b)) are commonly intercalated with paragneisses. The mineral assemblage of this rock is Qtz +Bt+Pl+Ms+Grt+Rt. Significant melting of this rock may initiate at the invariant point where the melting curve intersects the muscovite dehydration reaction, which occurs at ~8.5 kbar, 670°C. Considering the mineral assemblage and the leucosome development, the stability fields for this rock in pseudo-section B are featured in light colour. Although this rock contains minor muscovite, slight changes in P or T can produce assemblages devoid of white mica with increasing leucosome volumes.

Pseudo-section C (Figure 8(c)) is calculated with the chemical composition of a Late Triassic orthogneiss (sample SFO-5). Leucosome bands following and/or transecting the gneiss foliation form less than 10% of the rock. Leucosome veins derive from the hosting orthogneiss as indicated by U-Pb geochronology. The mineral assemblage of the orthogneiss is Pl+Kfs+Qtz +Bt, which is displayed in light colour in Figure 8(c). In summary, mineral assemblages of amphibolite and

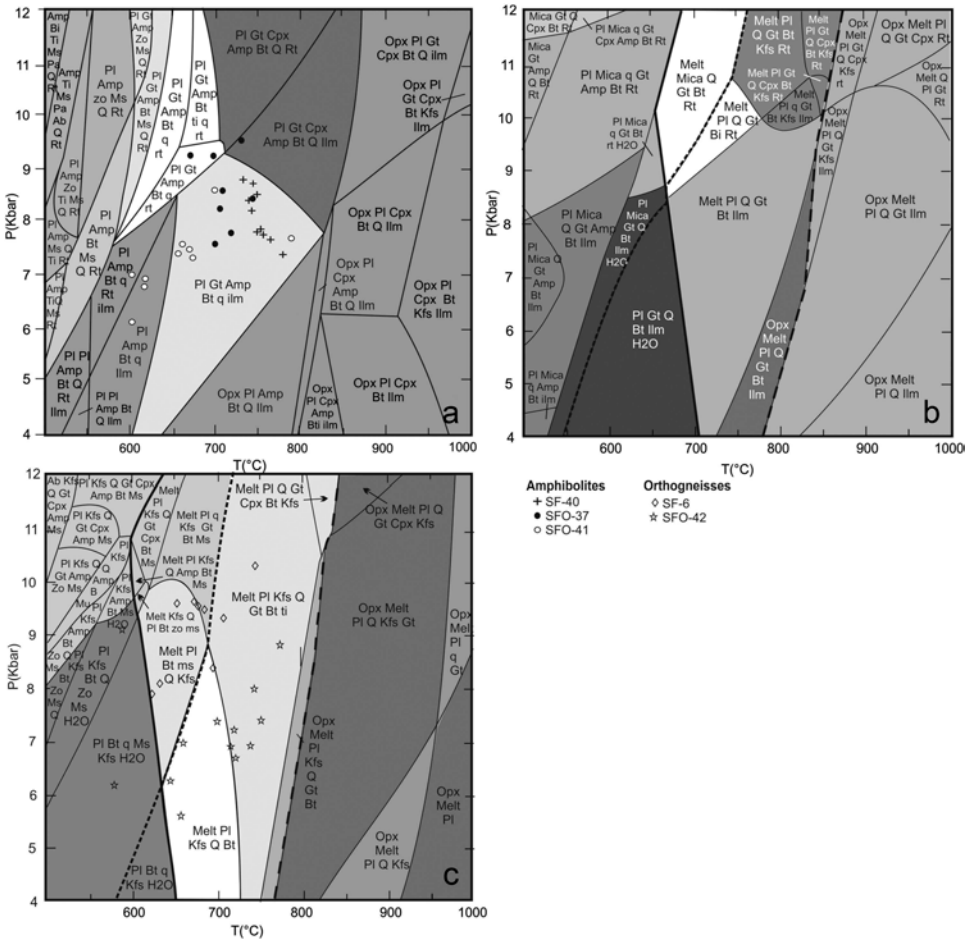

Figure 8. P-T pseudo-sections for the main lithologies of the Francisco Gneiss. The dehydration reactions of muscovite (Ms) and biotite (Bt) are highlighted by small dash and large dash lines respectively, the melting curve is indicated by a thick line. (a) P-T pseudo-section for average amphibolite composition. Composition used is: 48.64% SiO_2, 15.19% Al_2O_3, 13.18% FeO, 9.27% CaO, 5.90% MgO, 2.61%Na_2O, 1.66% TiO_2, and 0.84% K_2O, with H_2O in excess. (b) P-T pseudo-section for paragneiss (sample SFO-151). Composition used for calculation is: SiO_2 = 58.30%, Al_2O_3 = 17.25%, FeO = 8.44%, CaO = 3.90%, Na_2O = 2.93%, MgO = 2.88%, K_2O = 2.60%, HO_2 = 1.60, TiO_2 = 0.88%, with SiO_2 as saturated component. (c) P-T pseudo-section for orthogneiss (Sample SFO-05). Composition used for calculation is: 73.0% SiO_2, 13.95% Al_2O_3, 3.54 % CaO, 2.74% K_2O, Na_2O, 2.47%, 2.16% FeO, 0.70% MgO, and 0.55% H_2O, with SiO_2 as saturated component. *Ab*, Albite; Amp, Amphibole; Bt, Biotite; Chl, Chlorite; Ep, Epidote; Grt, Garnet; Ilm, Ilmenite; Kfs, Potassium feldspar; Ms, Muscovite; Pa, Paragonite; Pl, Plagioclase; Q, Quartz; Rt, Rutile; Ser, Sericite; Ti, Titanite; Zr, Zircon. Note: Minor transitional fields were excluded for clarity.

paragneiss and the widespread migmatization indicate pressures from ~7.5 to 10.5 kbar and temperatures between ~600°C and 750°C in the P-T pseudo-sections obtained from selected rock compositions.

Discussion

The oldest rocks of the WSC are metasediments whose protolith was interpreted as Cambrian (?) in age (Vega-Granillo *et al*. 2013) (Figure 9(a–b)). These rocks may underwent a first deformation and metamorphic phase during the late Palaeozoic amalgamation of Pangea (e.g. Poole *et al*. 2005; Vega-Granillo *et al*. 2008). The metasediments were intruded by Early Triassic, Late Triassic and Late Jurassic plutons with compositions ranging from granite to tonalite (Sarmiento-Villagrana *et al*. 2016) (Figure 9(c–d)). Coeval plutons are spread from the North America Cordillera to southern Mexico (e.g. Damon *et al*. 1983; Miller *et al*. 1995; Torres *et al*. 1999; Anderson *et al*. 2005; Barth *et al*. 2011; Riggs *et al*. 2012; Schmidt *et al*. 2014; Sarmiento-Villagrana *et al*. 2016; and references therein). After the Late Jurassic, mafic dikes transect previous plutons. Geochemistry of these dikes suggest a within-plate magmatism in a back-arc related setting (Keppie *et al*. 2006; Vega-Granillo *et al*. 2013) (Figure 9(e)). During the mid-Cretaceous time, a compressional event caused thrusting, thickening of the crust, and sinking of the lithological units to ~30 km depth (Figure 9(f)). This tectonic event caused orogenic metamorphism with related pervasive foliation,

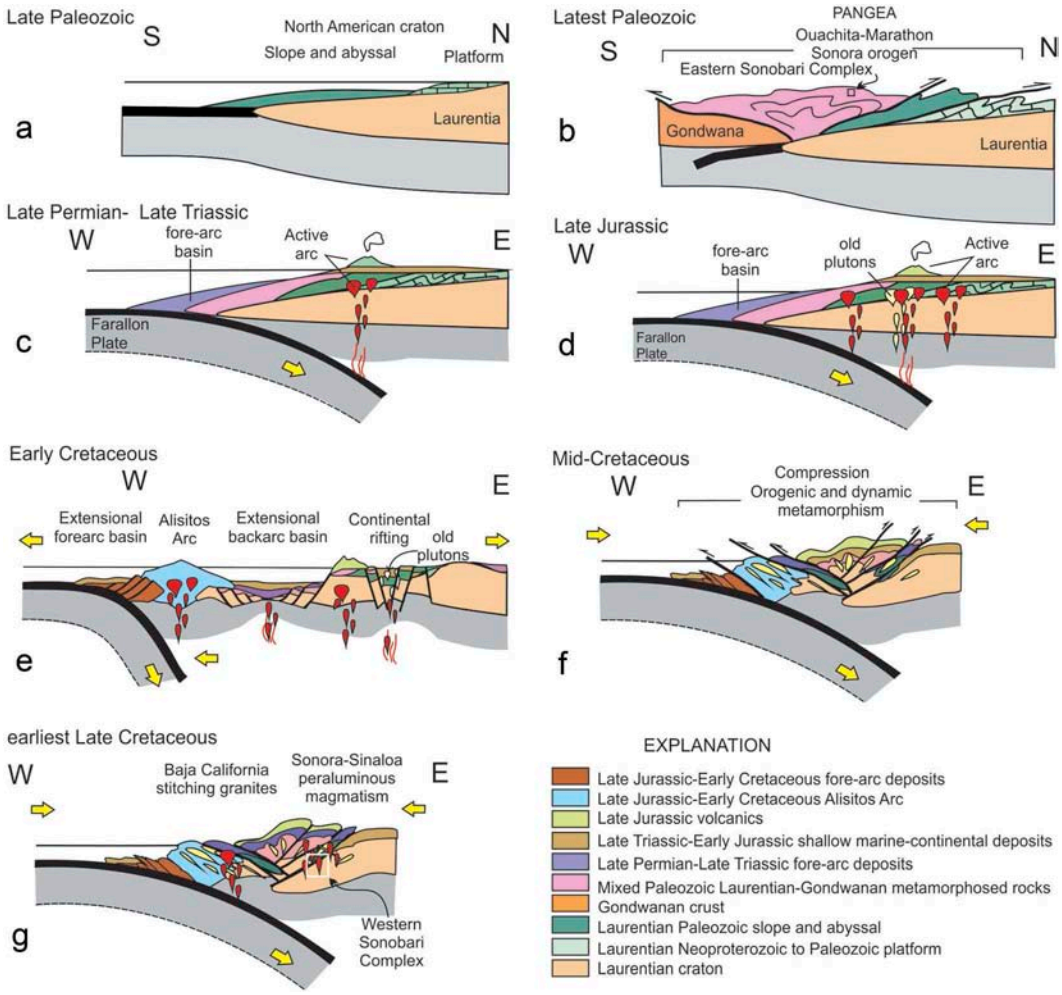

Figure 9. Hypothetical model for the tectonic evolution of the Western Sonobari Complex. Figures (a) and (b) oriented N–S are intended to resume the collision between Gondwanan and Laurentian blocks during the Pangea assemblage. (c to g) sections reflect the Cordilleran evolution related with collision of intraoceanic island arc and subduction of the Farallon plate under the North American plate.

anatexis, and several folding phases with NNW vergency. Average metamorphic conditions of 9.0–7.1 kbar and 745–663°C were obtained from the thermobarometric study. P-T pseudo-sections yield partially consistent data, indicating the region underwent an amphibolite facies intermediate P/T Barrovian metamorphism. However, thermobarometric data dispersion suggests a readjustment of the minerals during a clockwise exhumation path. P-T conditions obtained in this work are higher than P-T ranges of 6–3 kbar and 720–475°C obtained in metamorphic rocks of the Eastern Peninsular Ranges of Central Baja California (Rothstein and Manning 2003). Recrystallized zircon, both on metamorphic rocks and leucosome layers, indicate that peak metamorphic temperature was reached by the earliest Late Cretaceous (92–88 Ma) (Sarmiento-Villagrana *et al*. 2016; this work). We regard this metamorphic peak occurred after cessation of the main deformational event because leucosome veins follow and transect the main foliation (Figure 2(e)) and do not display crystalline deformation. The main deformation event must fading out about the earliest Late Cretaceous as indicated by intrusion of undeformed diorite and gabbro (Sarmiento-Villagrana *et al*. 2016). Tectonites were intruded by numerous peraluminous aplite-pegmatite dikes dated at 83–80 Ma (Sarmiento-Villagrana *et al*. 2016) (Figure 9(g)), whose post-tectonic character is evidenced by the unfoliated fabric and the cross-cutting relationships with respect to the orogenic foliation. The peraluminous magmatism indicates continuation of anatexis until the mid-Late Cretaceous but at deeper crustal level and with larger melt production than occurred during the orogenic metamorphism. The interval between the peak metamorphic event and the peraluminous magmatism is consistent with the ~10 Ma period between the end of a thickening event and

mobile granitoid magma generation predicted by Patiño-Douce *et al*. (1990).

The crustal thickening event to which the regional metamorphism and deformation of the WSC are related, may be ascribed to collision of the Late Jurassic–Early Cretaceous Alisitos island arc (e.g. Busby *et al*. 2006; Schmidt *et al*. 2014) against the North American craton and bordering sequences (Figure 9(e,f)). That collision occurred between ca. 111 and 103 Ma in central Baja California (Johnson *et al*. 1999; Alsleben *et al*. 2008; Schmidt *et al*. 2014) and was post-dated by La Posta-type peraluminous plutons with ages between 99 and 92 Ma (Kimbrough *et al*. 2001). In the southern Peninsular Ranges batholith, although contractional deformation is apparent since ca. 132 Ma (Schmidt and Paterson 2002), peak metamorphic pressures were recorded at ca. 100 Ma (Schmidt *et al*. 2009). It is important to point out that in most orogens metamorphism is not a transient phenomenon but a process generally lasting tenths of million years and that both metamorphism and deformation can be diachronic along an orogen (e.g. Berger *et al*. 2011; Fornelli *et al*. 2012). The time difference between the cessation of deformation in Baja California (111–103 Ma) and the reaching of the peak metamorphic temperatures in the Sonobari (92–88 Ma) can be ascribed to the time required for thermal readjustment of the crust after the main thickening event (e.g. England and Thompson 1984). Alternatively, the time discrepancy can be attributable to diachronism of deformation and metamorphism between the arc-continent collision at the west (Baja California) and the intraplate thrusting at the east (Sonobari) as displayed in Figure 9(f). In any case, the inception of the Farallon plate subduction under the North American margin, after collision of the Alisitos island arc, may play a role both in the thermal balance of the region and the post-tectonic magmatism indicated by La Posta-type intrusions in Baja California and pegmatite-aplite dikes in the WSC.

The main fabric formed during the collisional event is oriented ~NW-SE in Baja California (e.g. Alsleben *et al*. 2008) and ~WSW-ENE in the Sonobari. This change in the orogenic trend may be related either to North American pre-collision crustal geometry, which may have caused a bend in the Alisitos collisional boundary, or to reorientation originated by younger events. Rocks that may be correlated with the Alisitos arc are volcano-sedimentary exposures in the Sinaloa de Leyva–Porohui area (Ortega-Gutiérrez *et al*. 1978; Freydier *et al*. 1995; Gastil *et al*. 1999) ~90 km southeast of the study area (locations in Figure 10). The Porohui succession consists of basaltic pillow lavas intercalated with pelagic strata containing ammonites assigned to the Albian (Ortega-

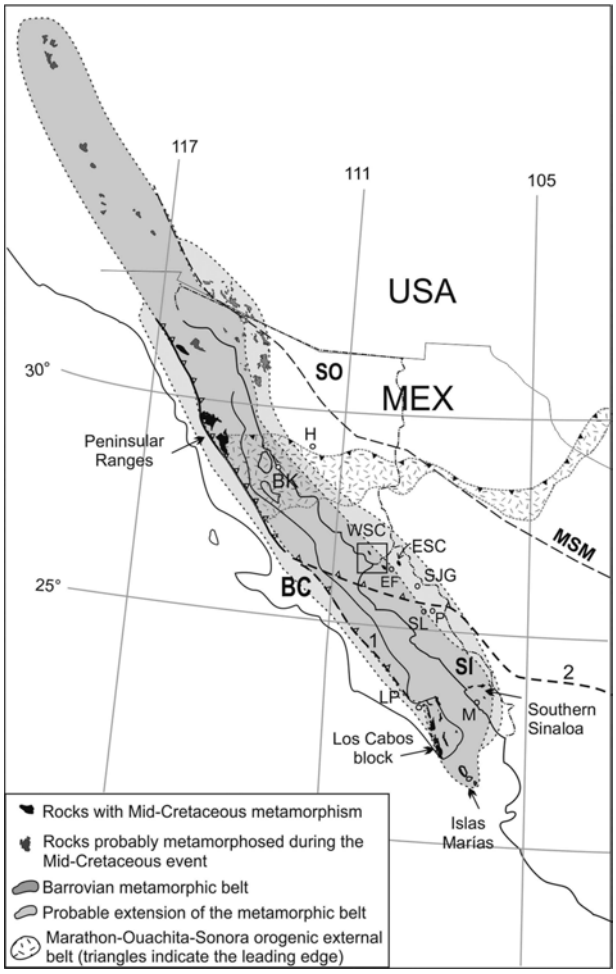

Figure 10. Proposed extension of the Mid-Cretaceous (~100–88 Ma) Barrovian metamorphic belt in Northwestern Mexico–Southwestern North America based in rocks with dated metamorphism (middle grey), and its probable extension based on rocks with undated metamorphism (light grey). Dashed lines indicate two probable boundaries between the Alisitos–Guerrero and mainland Mexico terranes, after 1: Geophysical evidence from Langenheim *et al*. (2014), and 2: Exposures interpretation (this work). MSM: Mojave–Sonora megashear; Countries: USA: United States of America, MEX: Mexico; States: BC: Baja California; SO: Sonora; SI: Sinaloa; Cities: BK: Bahía Kino; EF: El Fuerte; H: Hermosillo, LP: La Paz; M: Mazatlán; P: Porohui; SJG: San José de Gracia; SL: Sinaloa de Leyva. ESC: Eastern Sonobari Complex; WSC: Western Sonobari Complex. Extension of the Marathon–Ouachita–Sonora belt from Poole *et al*. (2005).

Gutiérrez *et al*. 1978); however, lava flows yield a Santonian (86 Ma) ^{40}Ar–^{39}Ar age (Gastil *et al*. 1999) contrasting with the palaeontological evidence. Towards the East of Sinaloa de Leyva we observe the upper Palaeozoic San José de Gracia Formation thrust to SSE over a volcano-sedimentary unit similar to the Porohui succession. This thrust may be the limit between volcano-sedimentary successions similar to those in the Alisitos-Guerrero composite terrane (e.g.

Mendoza and Suastegui 2000; Busby *et al*. 2006; Potra *et al*. 2014) and older supracrustal rocks of mainland Mexico. Impingement of the Alisitos Arc may have caused a NNW directed thrust of the San Jose de Gracia Formation over the Rio Fuerte Formation of the Eastern Sonobari Complex although that thrust cannot be seen in the field. In turn, the Río Fuerte Formation thrust over the WSC (Figure 1 and 9(f)). However, geophysical and palaeomagnetic studies seem preclude continuation of the Alisitos arc along the Mexican mainland (Kimbrough *et al*. 2014; Langenheim *et al*. 2014; Torres-Carrillo *et al*. 2015), contrasting with previous boundaries proposed for the Guerrero composite terrane (e.g. Campa and Coney 1983; Centeno-García *et al*. 2008).

Orogenic metamorphism coeval to that found in the WSC has been reported from the central North American Cordillera to central Mexico (Figure 10). The Sevier hinterland belt, extending several hundred kilometres from southern Idaho until northeastern California, contains high-grade (peak pressures of ~9 kbar and temperatures of ~800°C) Barrovian metamorphic rocks (DeCelles 2004) generally exposed in mid-Cenozoic metamorphic core complexes. Geochronology in that belt yields earliest Late Cretaceous ages (Camilleri and Chamberlain 1997; Mattinson *et al*. 2007) although Late Jurassic–Early Cretaceous ages have been also reported (e.g. Cruz-Uribe *et al*. 2008; Hoisch *et al*. 2014). In the southernmost Sierra Nevada, Early Cretaceous orthogneisses are intruded by earliest Late Cretaceous plutons (Sams and Saaleby 1988), and ductile deformation occurred about 90 Ma (Saleeby *et al*. 2008). In the southern Peninsular Ranges batholith of Baja California, south of the Agua Blanca fault according with Schmidt *et al*. (2014), upper-amphibolite facies metamorphism was achieved at ~100 Ma (Schmidt *et al*. 2014). In the Los Cabos Block of Baja California Sur, orogenic metamorphism and deformation allegedly occurred between 129 and 94 Ma (Pérez-Venzor 2013). Two mylonitic gneisses of the same region yield 91.5 and 97.1 Ma ages ($^{40}Ar/^{39}Ar$ on biotite and muscovite, respectively), which purportedly indicate the age of metamorphism (Cuéllar-Cárdenas *et al*. 2012). Deformed plutons yield K–Ar ages older than 98 Ma, whereas post-tectonic intrusives yield K–Ar ages between 98 and 65 Ma (Aranda-Gómez and Pérez-Venzor 1989). In central Sinaloa, syntectonic intrusions yield K–Ar hornblende ages ranging from 98 to 90 Ma; which are interpreted as cooling after regional metamorphism (Henry *et al*. 2003), whereas schist yielded a 94.47 Ma $^{40}Ar/^{39}Ar$ muscovite age (Cuéllar-Cárdenas *et al*. 2012). In the same area, tonalites regarded as syntectonic were dated at 97.1 and 98.0 Ma (U–Pb zircon, Cuéllar-Cárdenas *et al*. 2012), whereas post-tectonic intrusions were emplaced nearly continuously between 90 and 45 Ma (Henry *et al*. 2003). In the Islas Marías offshore of the Nayarit coast, two dated zircon rims from a latest Middle Jurassic orthogneiss yield 87 and 83 Ma ages that are regarded as indicating the metamorphic event (Pompa-Mera *et al*. 2013). In these islands, metamorphic rocks are intruded by 81–83 Ma (U–Pb, zircon) granites and overlain by Late Cretaceous volcanic rocks dated at 71–80 Ma (^{40}Ar–^{39}Ar, sanidine; Pompa-Mera *et al*. 2013). Other metamorphic rocks that might be coeval with those in the study area are exposed near Bahía Kino in coastal Sonora (Figure 10). In that region, metasedimentary units are intruded by syntectonic granodiorite dated at 90 Ma and post-tectonic intrusives dated from 84 to 69 Ma (Ramos-Velázquez *et al*. 2008).

Conclusions

Thermobarometry studies in metamorphic and igneous rocks of the Western Sonobari Complex yield an average temperature of 699°C (σ = 42) and pressure of 8.0 kbar (σ = 0.9), which corresponds to an estimated depth of ~30 km. Lower P-T data suggest a clockwise path along the amphibolite facies field. P-T pseudosections on amphibolite and paragneiss indicate pressures from ~7.5 to 10.5 kbar and temperatures between ~600°C and 750°C coincidental with thermobarometric data. U–Pb geochronology in zircon rims of leucosome veins indicates that peak metamorphic temperatures were reached between 92 and 88 Ma post-dating the main deformation fabric of the tectonites. However, metamorphism can be a protracted event as indicated by peak metamorphic pressures reached about 100 Ma in the Peninsular Ranges batholith host rocks (Schmidt *et al*. 2014). Peak temperatures in the Western Sonobari Complex can be produced by thermal readjustment occurring after crustal thickening derived from the latest Early Cretaceous (111–103 Ma; Johnson *et al*. 1999; Alsleben *et al*. 2008; Schmidt *et al*. 2014) collision of the Alisitos arc against mainland México. However, inception of the Farallon Plate subduction by the earliest Late Cretaceous, may play a role in the thermal budget of the region and the generation of the post-tectonic peraluminous magmatism.

Tectonites of the Western Sonobari Complex are part of a relatively narrow earliest Late Cretaceous Barrovian metamorphic belt extending from southern Idaho to the Nayarit coast of Western-Central Mexico. The belt is intruded by post-tectonic Late Cretaceous plutons of the Sinaloa–Sonora batholith and it is overlain by younger sedimentary and volcanic successions.

Thermobarometry of Late Cretaceous and Eocene plutons in the WSC suggests deep emplacement, indicating the permanence of the region in the lower crust at least until Palaeogene times. The variable metamorphic grade along the belt may be related to the level of exhumation in the respective areas. Rocks older than the mid-Cretaceous event but remaining in the upper crust level as the San Jose de Gracia Formation or the Barranca Group, may be unmetamorphosed.

Disclosure statement

No potential conflict of interest was reported by the authors.

Funding

This work was supported by the Consejo Nacional de Ciencia y Tecnología [grant number 177668].

ORCID

Ricardo Vega-Granillo http://orcid.org/0000-0001-6173-2510
Alicia Sarmiento-Villagrana http://orcid.org/0000-0002-6915-9226
Sergio Salgado-Souto http://orcid.org/0000-0002-9246-1650
Elizabeth Araux-Sánchez http://orcid.org/0000-0001-5165-2875

References

Alsleben, H., Wetmore, P.H., Schmidt, K.L., Paterson, S.R., and Melis, E.A., 2008, Complex deformation during arc–continent collision: Quantifying finite strain in the accreted Alisitos arc, Peninsular Ranges batholith, Baja California: Journal of Structural Geology, v. 30, no. 2, p. 220–236. doi:10.1016/j.jsg.2007.11.001

Anderson, J.L., 1996, Status of thermobarometry in granitic batholiths: Transactions of the Royal Society of Edinburgh, v. 87, p. 125–138. doi:10.1017/S0263593300006544

Anderson, J.L., and Smith, D.R., 1995, The effects of temperature and on the Al-in-hornblende barometer: American Mineralogist, v. 80, p. 549–559. doi:10.2138/am-1995-5-614

Anderson, T.H., Rodríguez-Castañeda, J.L., and Silver, L.T., 2005, Jurassic rocks in Sonora, Mexico: Relations to the Mojave-Sonora megashear and its inferred northwestward extension: Geological Society of America Special Papers, v. 393, p. 51–95.

Aranda-Gómez, J.J., and Pérez-Venzor, J.A., 1989, Estratigrafía del complejo cristalino de la región de Todos Santos, Estado de Baja California Sur: Universidad Nacional Autónoma de México, Revista, v. 8, p. 149–170.

Barth, A.P., Walker, J.D., Wooden, J.L., Riggs, N.R., and Schweickert, R.A., 2011, Birth of the Sierra Nevada magmatic arc: Early Mesozoic plutonism and volcanism in the east-central Sierra Nevada of California: Geosphere, v. 7, no. 4, p. 877–897. doi:10.1130/GES00737.1

Berger, A., Schmid, S.M., Engi, M., Bousquet, R., and Wiederkehr, M., 2011, Mechanisms of mass and heat transport during Barrovian metamorphism: A discussion based on field evidence from the Central Alps (Switzerland/northern Italy): Tectonics, v. 30, p. TC1007-1–TC1007-17. doi:10.1029/2009TC002622

Busby, C., Adams, B.F., Mattinson, J., and Deoreo, S., 2006, View of an intact oceanic arc, from surficial to mesozonal levels: Cretaceous Alisitos arc, Baja California: Journal of Volcanology and Geothermal Research, v. 149, p. 1–46. doi:10.1016/j.jvolgeores.2005.06.009

Camilleri, P.A., and Chamberlain, K.R., 1997, Mesozoic tectonics and metamorphism in the Pequop mountains and Wood Hills region, northeast Nevada: Implications for the architecture and evolution of the Sevier orogen: Geological Society of America Bulletin, v. 109, p. 74–94. doi:10.1130/0016-7606(1997)

Campa, U.M.F., and Coney, P., 1983, Tectono-stratigraphic terranes and mineral resource distributions in Mexico: Canadian Journal of Earth Sciences, v. 20, p. 1040–1051. doi:10.1139/e83-094

Carrillo-Martínez, M., 1971, Geología de la hoja San José de Gracia, Sinaloa [Bachelor thesis]: Mexico, D.F., Universidad Nacional Autónoma de México, Facultad de Ingeniería, 25 p.

Centeno-García, E., Guerrero-Suastegui, M., and Talavera-Mendoza, O., 2008, The Guerrero composite terrane of western Mexico: Collision and subsequent rifting in a supra-subduction zone, *in* Draut, A., Clift, P.D., and Scholl, D.W., eds., Formation and applications of the sedimentary record in arc collision zones: Geological Society of America Special Paper 436, p. 279–308. doi:10.1130/2008.2436(13)

Connolly, J.A.D., 1990, Multivariable phase diagrams: An algorithm based on generalized thermodynamics: American Journal of Science, v. 290, p. 666–718. doi:10.2475/ajs.290.6.666

Connolly, J.A.D., 2009, The geodynamic equation of state: What and how: Geochemistry Geophysics Geosystems, v. 10, p. 1–19. doi:10.1029/2009GC002540

Connolly, J.A.D., and Petrini, K., 2002, An automated strategy for calculation of phase diagram sections and retrieval of rock properties as a function of physical conditions: Journal of Metamorphic Geology, v. 20, p. 697–708. doi:10.1046/j.1525-1314.2002.00398.x

Cruz-Uribe, A.M., Hoisch, T.D., Wells, M.L., and Vervoort, J.D., 2008, Ages of Sevier thrusting from dating of metamorphic garnet using the Lu-Hf method: In AGU Fall Meeting Abstracts, v. 1, p. 2062.

Cuéllar-Cárdenas, M.A., Nieto-Samaniego, Á.F., Levresse, G., Alaniz-Álvarez, S.A., Solari, L., Ortega-Obregón, C., and López-Martínez, M., 2012, Límites temporales de la deformación por acortamiento Laramide en el centro de México: Revista Mexicana de Ciencias Geológicas, v. 29, no. 1, p. 179–203.

Damon, P.E., Shafiqullah, M., Roldán-Quintana, J., and Cochemé, J.J., 1983, El batolito Laramide (90-40 Ma) de Sonora: Guadalajara, Asociación de Ingenieros de Minas, Metalurgistas y Geólogos de Mexico (AIMMGM), Memoria técnica XV, p. 63–95.

De Cserna, Z., and Kent, B.H., 1961, Mapa geológico de reconocimiento y secciones estructurales de la región de San Blas y El Fuerte, Estado de Sinaloa: Cartas Geológicas y Mineras No. 4, escala 1:100,000: Instituto de Geología, Universidad Nacional Autónoma de México.

DeCelles, P.G., 2004, Late Jurassic to Eocene evolution of the Cordilleran thrust belt and foreland basin system, western USA: American Journal of Science, v. 304, no. 2, p. 105–168. doi:10.2475/ajs.304.2.105

England, P.C., and Thompson, A.B., 1984, Pressure-temperature-time paths of regional metamorphism I. Heat transfer during the evolution of regions of thickened continental crust: Journal of Petrology, v. 25, p. 894–928. doi:10.1093/petrology/25.4.894

Fornelli, A., Pascazio, A., and Piccarreta, G., 2012, Diachronic and different metamorphic evolution in the fossil Variscan lower crust of Calabria: International Journal of Earth Sciences, v. 101, no. 5, p. 1191–1207. doi:10.1007/s00531-011-0721-8

Freydier, C., Lapierre, H., Tardy, M., Coulon, C., Martinez-Reyes, J., and Orsini, J.B., 1995, Les formations magmatiques de Porohui (Sinaloa); temoins de l'evolution géodynamique mesozoique et tertiaire des Cordilleres mexicaines: Comptes Rendus de l'Académie des Sciences, Ser. 2: Sciences de la Terre et des Planètes, v. 321, p. 529–536.

Gastil, G., Miller, R., Anderson, P., Crocker, J., Campbell, M., Buch, P., Lothringer, C., Leier-Engelhardt, P., Delattre, M., Hoobs, J., and Roldán-Quintana, J., 1991, The relation between the Paleozoic strata on opposite sides of the Gulf of California, *in* Pérez-Segura, E., and Jacques-Ayala, C., eds., Studies of sonoran geology: Geological Society of America Special Paper 254, p. 7–17.

Gastil, G., Rector, R., Hazelton, G., Al-Riyami, R., Hanes, J., Farrar, E., Boehnel, H., Ortega-Rivera, A., and Guzman, J.G., 1999, Late Cretaceous pillow basalt, siliceous tuff and calc-turbidite near Porohui, northern Sinaloa, Mexico, *in* Bartolini, C., *et al*., eds., Mesozoic sedimentary and tectonic history of north-central Mexico: Geological Society of America Special Paper 340, p. 145–150. doi:10.1130/0-8137-2340-X.145

Gehrels, G., Rusmore, M., Woodsworth, G., Crawford, M., Andronicos, C., Hollister, L., Patchett, J., Ducea, M., Butler, R., Klepeis, K., Davidson, C., Friedman, R., Haggart, J., Mahoney, B., Crawford, W., Pearson, D., and Girard, J., 2009, U-Th-Pb geochronology of the Coast mountains batholith in north-coastal British Columbia: Constraints on age and tectonic evolution: Geological Society of America Bulletin, v. 121, no. 9–10, p. 1341–1361. doi:10.1130/B26404.1

Henry, C.D., McDowell, F.W., and Silver, L.T., 2003, Geology and geochronology of granitic batholitic complex, Sinaloa, México: Implications for Cordilleran magmatism and tectonics: Geological Society of America Special Paper 374, p. 237–273. doi:10.1130/0-8137-2374-4.237

Hoisch, T.D., Wells, M.L., Beyene, M.A., Styger, S., and Vervoort, J.D., 2014, Jurassic Barrovian metamorphism in a western US Cordilleran metamorphic core complex, Funeral mountains, California: Geology, v. 42, no. 5, p. 399–402. doi:10.1130/G35352.1

Holland, T.J.B., and Blundy, J., 1994, Non-ideal interactions in calcic amphiboles and their bearing on amphibole-plagioclase thermometry: Contributions to Mineralogy and Petrology, v. 116, p. 433–447. doi:10.1007/BF00310910

Holland, T.J.B., and Powell, R., 1998, An internally-consistent thermodynamic dataset for phases of petrological interest: Journal of Metamorphic Geology, v. 16, p. 309–344. doi:10.1111/j.1525-1314.1998.00140.x

Johnson, S.E., Tate, M.C., and Fanning, C.M., 1999, New geologic mapping and SHRIMP U-Pb zircon data in the Peninsular Ranges batholith, Baja California, Mexico: Evidence for a suture?: Geology, v. 27, no. 8, p. 743–746. doi:10.1130/0091-7613(1999)027<0743:NGMASU>2.3.CO;2

Johnston, S., Gehrels, G., Valencia, V., and Ruiz, J., 2009, Small-volume U–Pb zircon geochronology by laser ablation-multi-collector-ICP-MS: Chemical Geology, v. 259, p. 218–229. doi:10.1016/j.chemgeo.2008.11.004

Keppie, J.D., Dostal, J., Miller, B.V., Ortega-Rivera, A., Roldán-Quintana, J., and Lee, J.W.K., 2006, Geochronology and geochemistry of the Francisco Gneiss: Triassic continental rift tholeiites on the Mexican margin of Pangea metamorphosed and exhumed in a Tertiary core complex: International Geology Review, v. 48, no. 1, p. 1–16. doi:10.2747/0020-6814.48.1.1

Kimbrough, D.L., Grove, M., and Morton, D.M., 2014, Timing and significance of gabbro emplacement within two distinct plutonic domains of the Peninsular Ranges batholith, southern and Baja California: Geological Society of America Bulletin, v. 127, p. 19–37. doi:10.1130/B30914.1

Kimbrough, D.L., Smith, D.P., Mahoney, J.B., Moore, T.E., Grove, M., Gastil, R.G., and Ortega-Rivera, A., 2001, Forearc-basin sedimentary response to rapid Late Cretaceous batholith emplacement in the Peninsular Ranges of southern and Baja California: Geology, v. 29, no. 6, p. 491–494. doi:10.1130/0091-7613(2001)029<0491:FBSRTR>2.0.CO;2

Kohn, M.J., and Spear, F.S., 1990, Two new geobarometers for garnet amphibolites, with applications to southeastern Vermont: American Mineralogist, v. 75, p. 89–92.

Langenheim, V.E., Jachens, R.C., and Aiken, C., 2014, Geophysical framework of the Peninsular Ranges batholith – Implications for tectonic evolution and neotectonics, *in* Morton, D.M., and Miller, F.K., eds., Peninsular Ranges bathosdlith, Baja California and Southern California: Geological Society of America Memoir 211, p. 1–20. doi:10.1130/2014.1211(01)

Ludwig, K.L., 2008, Isoplot 3.70. A geochronological toolkit for Microsoft Excel. Berkeley Geochronology Center, 4 (Special Publication), p. 1–77.

Ludwig, K.L., and Mundil, R., 2002, Extracting reliable U-Pb ages and errors from complex populations of zircons from Phanerozoic tuffs: 12th Goldschmidt Conference, Davos, Switzerland, Journal of Conference Abstracts, A-463.

Mattinson, C.G., Colgan, J.P., Metcalf, J.R., Miller, E.L., and Joseph, L., 2007, Late Cretaceous to Paleocene metamorphism and magmatism in the Funeral Mountains metamorphic core complex, Death Valley, California: Geological Society of America Special Papers 419, p. 205–223. doi:10.1130/2006.2419(11)

Mendoza, O.T., and Suastegui, M.G., 2000, Geochemistry and isotopic composition of the Guerrero Terrane (western Mexico): Implications for the tectono-magmatic evolution of southwestern North America during the Late Mesozoic: Journal of South American Earth Sciences, v. 13, p. 297–324. doi:10.1016/S0895-9811(00)00026-2

Miller, J.S., Glazner, A.F., Walker, J.D., and Martin, M.W., 1995, Geochronologic and isotopic evidence for Triassic-Jurassic emplacement of the eugeoclinal allochthon in the Mojave Desert region, California: Geological Society of America Bulletin, v. 107, no. 12, p. 1441–1457. doi:10.1130/0016-7606(1995)107<1441:GAIEFT>2.3.CO;2

Mullan, H.S., 1978, Evolution of part of the Nevadan orogen in northwestern Mexico: Geological Society of America

Bulletin, v. 89, no. 8, p. 1175–1188. doi:10.1130/0016-7606(1978)89<1175:EOPOTN>2.0.CO;2

Ortega-Gutiérrez, F., Prieto-Vélez, R., Zúñiga, Y., and Flores, S., 1978, Una secuencia volcano-plutonica-sedimentaria cretácica en el norte de Sinaloa; complejo ofiolitico?: Universidad Nacional Autónoma de México, Inst. Geología, Revista, v. 3, no. 1, p. 1–8.

Patiño-Douce, A.E., Humphreys, E.D., and Johnston, A.D., 1990, Anatexis and metamorphism in tectonically thickened continental crust exemplified by the Sevier hinterland, western North America: Earth and Planetary Science Letters, v. 97, no. 3–4, p. 290–315. doi:10.1016/0012-821X(90)90048-3

Pérez-Venzor, J.A., 2013, Estudio geológico-geoquímico del borde oriental del Bloque de los Cabos, Baja California Sur, México [Ph.D. thesis]: México, D.F., Universidad Nacional Autónoma de México, 297 p.

Pompa-Mera, V., Schaaf, P., Hernández-Treviño, T., Weber, B., Solís-Pichardo, G., Villanueva-Lascurain, D., and Layer, P., 2013, Geology, geochronology, and geochemistry of Isla María Madre, Nayarit: Mexico: Revista Mexicana de Ciencias Geológicas, v. 30, no. 1, p. 1–23.

Poole, F.G., Amaya-Martínez, R., Premo, W.R., Berry, W.B.N., Sandberg, C.A., Roldán-Quintana, J., and Herrera-Urbina, S., 2010, Age and depositional setting of deep-marine Ordovician Río Fuerte and San José de Gracia formations in northern Sinaloa, Mexico: Remnants of the early Paleozoic Iapetus ocean: Geological Society of America Abstracts with Programs, v. 42, no. 5, p. 268.

Poole, F.G., Perry, W.J., Jr., Madrid, R.J., and Amaya-Martínez, R., 2005, Tectonic synthesis of the Ouachita–Marathon–Sonora orogenic margin of southern Laurentia: Stratigraphic and structural implications for timing of deformational events and plate-tectonic model: Geological Society of America Special Paper 393, p. 543–596, doi: 10.1130/0-8137-2393-0.543

Potra, A., Hickey-Vargas, R., MacFarlane, A.W., and Salters, V.J.M., 2014, Pb, Sr, and Nd isotopic characteristics of a variety of lithologies from the Guerrero composite terrane, west-central Mexico: Constraints on their origin: Revista Mexicana de Ciencias Geológicas, v. 31, no. 2, p. 203–220.

Ramos-Velázquez, E., Calmus, T., Valencia, V., Iriondo, A., Valencia-Moreno, M., and Bellon, H., 2008, U-Pb and $^{40}Ar/^{39}Ar$ geochronology of the coastal Sonora batholith: New insights on Laramide continental arc magmatism: Revista Mexicana de Ciencias Geológicas, v. 25, no. 2, p. 314–333.

Ramsay, J.G., 1967, Folding and fracturing of rocks: New York, McGraw-Hill. 568 p.

Riggs, N.R., Barth, A.P., González-León, C.M., Jacobson, C.E., Wooden, J.L., Howell, E.R., and Walker, J.D., 2012, Provenance of upper triassic strata in southwestern North America as suggested by isotopic analysis and chemistry of zircon crystals: Geological Society of America Special Paper 487, p. 13–36, doi: 10.1130/2012.2487(02)

Rothstein, D.A., and Manning, C.E., 2003, Geothermal gradients in continental magmatic arcs: Constraints from the eastern Peninsular Ranges batholith, Baja California, Mexico: Geological Society of America Special Paper 374, p. 337–354.

Rubatto, D., 2002, Zircon trace element geochemistry: Partitioning with garnet and the link between U–Pb ages and metamorphism: Chemical Geology, v. 184, no. 1, p. 123–138. doi:10.1016/S0009-2541(01)00355-2

Saleeby, J.B., Ducea, M.N., Busby, C.J., Nadin, E.S., and Wetmore, P.H., 2008, Chronology of pluton emplacement and regional deformation in the southern Sierra Nevada batholith, California, *in* Wright, J.E., and Shervais, J.W., eds., Ophiolites, arcs, and batholiths: A tribute to Cliff Hopson: Geological Society of America Special Paper 438, p. 397–427. doi:10.1130/2008.2438(14)

Sams, D.B., and Saaleby, J.B., 1988, Geology and petrotectonic significance of crystalline rocks of the southernmost Sierra Nevada, California, *in* Ernst, W.G., ed., Rubey volume VII, metamorphism and crustal evolution in the Western United States: Englewood Cliffs, NJ, Prentice-Hall, p. 866–893.

Sarmiento-Villagrana, A., Vega-Granillo, R., Talavera-Mendoza, O., and Vidal-Solano, J.R., 2016, New age constraints on magmatism and metamorphism of the Western Sonobari complex and its implications for an earliest Late Cretaceous orogeny on northwestern Mexico: Revista Mexicana de Ciencias Geológicas, v. 33, no. 2, p. 170–182.

Sawyer, E.W., 2008, Atlas of migmatites: The Canadian mineralogist: Ottawa, Special Publication 9, NRC Research Press. 371 p.

Sawyer, E.W., Cesare, B., and Brown, M., 2011, When the continental crust melts: Elements, v. 7, p. 229–234. doi:10.2113/gselements.7.4.229

Schmidt, K.L., and Paterson, S.R., 2002, A doubly vergent, fan structure in the Peninsular Ranges batholith: Transpression or complex flow along a crustal-scale discontinuity?: Tectonics, v. 21, no. 5, p. 14-1–14-19. doi:10.1029/2001TC001353

Schmidt, K.L., Paterson, S.R., Blythe, A.E., and Kopf, C., 2009, Mountain building across a lithospheric boundary during arc construction: The Cretaceous Peninsular Ranges batholith in the Sierra San Pedro Martir of Baja California, Mexico: Tectonophysics, v. 477, p. 292–310. doi:10.1016/j.tecto.2009.04.020

Schmidt, K.L., Wetmore, P.H., Alsleben, H., and Paterson, S.R., 2014, Mesozoic tectonic evolution of the southern Peninsular Ranges batholith, Baja California, Mexico: Long-lived history of a collisional segment in the Mesozoic Cordilleran arc: Geological Society of America Memoirs, v. 211, p. 645–668. doi:10.1130/2014.1211(20)

Spear, F.S., 1993, Metamorphic phase equilibria and pressure-temperature-time paths: Washington, DC, Mineralogical Society of America. 799 p.

Torres, R., Ruiz, J., Patchett, P.J., and Grajales, J.M., 1999, A permo-triassic continental arc in eastern Mexico: Tectonic implications for reconstructions of southern North America: Geological Society of America Special Paper 340, p. 191–196, doi: 10.1130/0-8137-2340-X.191

Torres-Carrillo, X.G., Delgado-Argote, L.A., Böhnel, H., Molina-Garza, R.S., and Weber, B., 2015, Palaeomagnetic assessment of plutons from the southern Peninsular Ranges batholith and the Jurassic Vizcaíno igneous suites, Baja California, México: International Geology Review, v. 58, no. 4, p. 489–509. doi:10.1080/00206814.2015.1089425

Vega-Granillo, R., Salgado-Souto, S., Herrera-Urbina, S., Valencia-Gómez, V., Ruiz, J., Meza-Figueroa, D., and Talavera-Mendoza, O., 2008, U-Pb detrital zircon data of

the Rio Fuerte formation (NW Mexico): Its peri-Gondwanan provenance and exotic nature in relation to southwestern North America: Journal of South American Earth Sciences, v. 26, p. 343–354. doi:10.1016/j.jsames.2008.08.011

Vega-Granillo, R., Salgado-Souto, S., Herrera-Urbina, S., Valencia-Gómez, V., and Vidal-Solano, J.R., 2011, Metamorphism and deformation in the El Fuerte region: Their role in the tectonic evolution of NW Mexico: Revista Mexicana de Ciencias Geológicas, v. 28, no. 1, p. 10–23.

Vega-Granillo, R., Vidal-Solano, J., Solari, L., López-Martínez, M., Gómez-Juárez, O.S., and Herrera-Urbina, S., 2013, Geochemical and geochronological constraints on the geologic evolution of the western Sonobari Complex, northwestern Mexico: Geologica Acta, v. 11, no. 4, p. 443–463. doi:10.1344/105.000002059

Vega-Granillo, R., Vidal-Solano, J.R., and Herrera-Urbina, S., 2012, Island arc tholeiites of Early Silurian, Late Jurassic and Late Cretaceous ages in the El Fuerte región, northwestern Mexico: Revista Mexicana de Ciencias Geológicas, v. 29, no. 2, p. 492–513.

Vietor, T., and Echtler, H., 2006, Episodic neogene southward growth of the andean subduction orogen between 30°S and 40°S – Plate motions, mantle flow, climate, and upper-plate structure, *in* Oncken, O., Chong, G., Franz, G., Giese, P., Götze, H.J., Ramos, V.A., Strecker, M.R., and Wigger, P., eds., The Andes, active subduction orogeny: Berlin, Springer, p. 375–400. doi:10.1007/978-3-540-48684-8_18

5

Discusión y conclusiones

Las unidades más antiguas encontradas en el Complejo Sonobari son rocas metasedimentarias paleozoicas polideformadas. Estudios U-Pb en zircones detríticos en los metasedimentos de la Formación Río Fuerte en la parte oriental del CS indican un origen gondwánico (Vega-Granillo et al., 2008), por lo que a esta secuencia se le atribuye un origen alóctono con respecto a Norteamérica. En el área Oeste, datos U-Pb en zircones detríticos del Gneis Francisco, indican una proveniencia Laurenciana (Vega-Granillo et al., 2013) sugiriendo un origen para-autóctono. La evolución tectónica temprana del Complejo Sonobari se considera que inició con la colisión entre Gondwana y Laurencia que amalgamó los bloques metasedimentarios que son el sustrato del CS y donde se emplazó un gran volumen de magma durante el mesozoico. Estudios de geocronología, geoquímicos, isotópicos y de geotermobarometría en rocas metamórficas de origen magmático, evidencian que la subducción en la parte oeste de Pangea se reanudó a finales del Pérmico e inicios del Triásico, inmediatamente después a la configuración de Pangea y continuó durante todo el Mesozoico. Tanto las rocas metasedimentarias como muchas de las rocas metamagmáticas preceden a un evento de metamorfismo orogénico.

Nuestros datos de fechamientos U-Pb indican que el magmatismo en el Complejo Sonobari fue amplio durante el Mesozoico y Cenozoico del que se identifican al menos seis pulsos, de los cuales, cinco fueron fechados en este trabajo. Cinco pulsos magmáticos,

incluyendo los diques máficos de anfibolita y plutones ultramáficos que no fueron fechados, preceden un evento de metamorfismo orogénico, por lo que las rocas son ortogneises, metagranitos y anfibolitas, mientras que el sexto pulso es post-orogénico. Al primer pulso pertenecen los ortogneises del Triásico Temprano (249-241 Ma), al segundo los ortogneises del Triásico Tardío (213-203 Ma), al tercero los ortogneises granodioríticos y tonalíticos del Jurásico Tardío (163-159 Ma), al cuarto pulso corresponde el emplazamiento de diques máficos, cuya edad se desconoce, pero que con base en relaciones de campo debieron intrusionarse entre el Jurásico Tardío (post-160 Ma) y el Cenomaniano (pre-99 Ma). El quinto pulso está constituido por ortogneises tonalíticos de 98.8 Ma y por una diorita no deformada de 99.9 Ma. La diorita no deformada corta a gabros sin deformación que se asocian con diques de hornblendita y piroxenita. El sexto pulso es post-orogénico y está representado por diques graníticos de 83.9-80.6 Ma. Con base en la similitud química y mineralógica así como por la edad similar se considera que los tres primeros pulsos magmáticos podrían estar relacionados a un cinturón magmático que cubre desde el Pérmico hasta el Jurásico y que se extiende desde el suroeste de la Cordillera en Estados Unidos (e.g. Miller, 1978; Miller et al., 1995; Barth and Wooden, 2006; Anderson et al., 2010; Barth, 2010; Ehret et al., 2010; Barth et al., 2011; Riggs et al., 2012; Riggs et al., 1993; Anderson et al., 2005; Haxel et al., 2005) con afloramientos de la misma edad en Baja California (Thompson and Girty, 1994; Schmidt and Paterson, 2002; Shaw et al., 2003; Valencia et al., 2006), que continua al norte del Estado de Sonora y hasta el centro y sur de México (Damon et al., 1981; Yáñez et al., 1991; Torres et al., 1999; Schaaf et al., 2002; Weber et al., 2005; Arvizu et al., 2009; Vega-Granillo et al., 2008; Cuéllar-Cárdenas et al., 2012; Pompa-Mera et al., 2013) y Sudamérica (Cochrane et al., 2013 y referencias incluidas en este trabajo). El pulso del Cretácico Tardío de este estudio se puede

correlacionar con el magmatismo de la misma edad en la Sierra Nevada (p. ej. Sams y Saleeby, 1988; Saleeby et al., 2008), el cinturón Batolito Peninsular (Schmidt y Paterson, 2002; Johnson et al., 2003; Wetmore et al., 2005; Peña-Alonso et al., 2012; Kimbrough et al., 2015) y centro de Sinaloa (Henry et al., 2003). El último pulso, está relacionado a la fusión parcial de la corteza continental por el alto gradiente termal al que se asocia el metamorfismo de alto grado, emplazado después del pico termal que ocurrió en ~93 y 89 Ma.

Los resultados geoquímicos e isotópicos de los distintos pulsos magmáticos en el Complejo Sonobari sugieren que el complejo estuvo sujeto a un emplazamiento continuo de magma desde el Triásico Temprano hasta el Paleoceno, terminando con granitoides de composición peraluminosa y metaluminosa y, en menor proporción, se emplazaron cuerpos máficos de afinidad toleítica. Las evidencias geoquímicas indican que el magmatismo del Triásico Temprano al Jurásico Tardío se emplazó en un régimen de subducción. Posterior al último periodo y antes del Cenomaniano, se emplazó magma máfico en forma de numerosos diques que cortan a las rocas graníticas y metasedimentarias. La geoquímica de estas rocas indica un carácter toleítico bajo un régimen de subducción. La geoquímica también sugiere que estos magmas se emplazaron en un contexto de cuenca tras-arco o intra-arco, asociado a procesos extensionales durante la subducción. Antes del Cenomaniano ocurrió un evento de compresión que causó la deformación y el inicio del metamorfismo de las rocas preexistentes, que se encuentran fuertemente foliadas y plegadas. Posteriormente a este evento compresional se produjo el emplazamiento de magmas máficos en forma de plutones relativamente pequeños y diques. La firma geoquímica también es toleítica pero con un empobrecimiento un poco mayor y con una anomalía negativa de torio característica, sugiriendo que la corteza superior no estuvo

involucrada en la generación de estos magmas. El contexto tectónico es de nuevo el de una cuenca tras-arco o intra-arco ya que la influencia de la subducción continúa siendo clara. Los isótopos de Nd y Sr indican que el magmatismo tiene dos fuentes: magmas derivados de fuentes continentales evolucionadas ($\varepsilon Nd_{(i)}$ = –5.7 a –0.5; $^{87}Sr/^{86}Sr_{(i)}$ = 0.70630 a 0.71302) y magmas derivados de fuentes mantélicas con asimilación cortical ($\varepsilon Nd_{(i)}$ = –1.9 a +5.0; $^{87}Sr/^{86}Sr_{(i)}$ = 0.70384 a 0.70626). A partir de nuestros datos isotópicos y los existentes en la literatura se interpreta que bajo el Complejo Sonobari pudiera existir un basamento que es distinto al basamento antiguo de Norteamérica (Iriondo et al., 2004, Arvizu et al., 2009), pero que son similares a los valores o relaciones isotópicas de rocas del grenvilliano Mexicano (López et al., 2001; Torres et al., 1999). Las firmas isotópicas, particularmente en las rocas del Cenomaniano son similares a los valores del terreno Guerrero, Isla María Madre, Bloque los Cabos y Alisitos-Santiago Peak, sugiriendo un basamento en común para todas estas regiones (Potra et al., 2014; Shaw et al., 2003). El contexto de arco continental del Complejo Sonobari difiere del contexto de arco oceánico del Alisitos-Terreno Guerrero indicando su falta de relación genética y descartando la extensión de dicho terreno en el área de estudio como había sido originalmente propuesto por Campa y Coney (1983), entre otros. Sin embargo, aunque en el área de estudio no se encontraron rocas correlacionables con el arco Alisitos, al sur del área estudiada en Sinaloa de Leyva y Porohui existen rocas vulcano-sedimentarias que han sido correlacionadas con este arco (Ortega-Gutiérrez at al., 1978; Freydier et al., 1995; Gastil et al., 1999). Hacia el este de Sinaloa de Leyva, nosotros observamos que la formación San José de Gracia del Paleozoico Superior cabalga a una sucesión vulcano-sedimentaria similar a la secuencia de Porohui, por lo que esta zona podría ser el limite.

Las rocas de la parte Oeste del Complejo Sonobari (Sierra San Francisco) son rocas metamórficas con foliación penetrativa, plegamiento y migmatización; que derivaron de protolitos sedimentarios e ígneos con edades que van del Paleozoico al Cretácico Temprano. Los datos petrográficos y geotermobarométricos indican que las rocas estuvieron sujetas a un metamorfismo en la facies de anfibolita de P/T intermedia con presiones entre 9.0 y 7.1 kbar y temperaturas entre 745 y 663°C. Los datos geotermobarométricos fueron confirmados mediante pseudo-secciones realizadas con el programa PERPLEX. Los datos geotermobarométricos en intrusivos ígneos post-tectónicos indican que éstos se emplazaron en una corteza sobre-engrosada, indicando la permanencia de esta región en la parte inferior de la corteza al menos hasta el Paleógeno. La geocronología U-Pb en sobrecrecimientos de zircones de las rocas metamórficas y en leucosomas indican que el pico metamórfico ocurrió entre 93 y 89 Ma. Por lo que se interpreta que cerca de la parte media del Cretácico ocurrió un evento compresional que causó cabalgamiento, engrosamiento de la corteza y el hundimiento de las unidades litológicas sedimentarias e ígneas a unos 30 km de profundidad. Este evento fue el causante del metamorfismo orogénico con foliación penetrativa, anatexis y varias fases de plegamiento con una vergencia NNW. El evento que causó el engrosamiento cortical, metamorfismo regional y deformación del Complejo Sonobari del Oeste, podría estar relacionado a la colisión del arco Alisitos contra el cratón de Norteamérica que ocurrió entre 111 y 103 Ma en San Pedro Mártir (Johnson et al., 1999; Alsleben et al., 2008; Schmidt et al., 2014) y en 97.3 en Compostela (Torres Carrillo et al., 2016). En la parte sur del Batolito Peninsular el pico metamórfico fue registrado cerca de 100 Ma (Schmidt et al., 2009). El metamorfismo en el Complejo Sonobari podría ser parte de un cinturón

metamórfico reportado en la parte central de la Cordillera de Norteamérica y que se extiende hasta la parte central de México.

Con base en los resultados reportados en los tres artículos que conforman el cuerpo de esta tesis doctoral se puede concluir lo siguiente:

El Complejo Sonobari está compuesto de rocas sedimentarias intrusionadas por plutones graníticos y diques que fueron sujetos a un metamorfismo orogénico. De acuerdo con nuestros datos de geocronología U-Pb y datos previos, el complejo registra una historia magmática extendida que inició en el Triásico Temprano y continuó hasta el Cretácico Tardío. La presencia de estas unidades plutónicas en el complejo, indican que los cinturones magmáticos del Permo-Triásico al Cretácico Superior de la Cordillera suroccidental se extiende a lo largo del Batolito Peninsular y hacia el noroeste de Sonora y hasta la región estudiada.

Los datos geoquímicos e isotópicos de los seis pulsos magmáticos indican que el magmatismo del Complejo Sonobari está relacionado o fue influenciado por procesos de subducción. Intrusivos máficos que se formaron después del Jurásico Tardío y antes del Campaniano se interpretan como el registro de dos fases extensionales con una fase compresional actuando. El escenario tectónico para este periodo es complejo, implicando rifting detrás de un arco continental o intra-arco y cierre de un mar marginal por colisión del arco Alisitos. Nuestros datos geoquímicos e isotópicos indican que las rocas del Complejo Sonobari se formaron y evolucionaron en un arco continental similar al Batolito Peninsular oriental y distinto del arco oceánico Guerrero-Alisitos. Por lo tanto, sugerimos que el límite norte del terreno Guerrero puede estar ubicado más al sur del área de estudio.

Los resultados de geotermobarometría de las rocas metamórficas e ígneas del Complejo Sonobari del Oeste, produjeron un promedio de temperatura de 699 Cº y una

presión de 8 kbar, el cual corresponde a una profundidad de mas o menos 30 km. La geocronología U-Pb en sobrecrecimientos de zircones de leucosomas, indican que las temperatura del pico térmico fueron alcanzadas entre 92 y 88 Ma.

6

Bibliografía

Alsleben, H., Wetmore, P.H., Schmidt, K.L., Paterson, S.R., and Melis, E.A., 2008, Complex deformation during arc–continent collision: Quantifying finite strain in the accreted Alisitos arc, Peninsular Ranges batholith, Baja California: Journal of Structural Geology, v. 30, no. 2, p. 220–236.

Anderson, J.L., Paterson, S., Memeti, V., Zhang, T., Economos, R., Barth, A.P., Pignotta, G., Mundil, R., Foley, B., Schmidt, K., 2010, Episodic downward crustal flow during Triassic to Cretaceous magma surges in the central Sierra arc: Geological Society of America Abstracts with Programs, v. 42, no. 4, p. 51.

Anderson, T. H., and Schmidt, V. A., 1983, The evolution of Middle America and the Gulf of Mexico–Caribbean Sea region during Mesozoic time: Geological Society of America Bulletin, v. 94, no. 8, p. 941-966.

Anderson, T.H., Rodríguez-Castañeda, J.L., Silver, L.T., 2005, Jurassic rocks in Sonora, Mexico: Relations to the Mojave-Sonora megashear and its inferred northwestward extension. Geological Society of America Special Papers v. 393, p. 51-95.

Arvizu, H.E., Iriondo, A., Izaguirre, A., Chávez-Cabello, G., Kamenov, G.D., Solís-Pichardo, G., Foster, D.A., Lozano-Santa Cruz, R., 2009, Rocas graníticas pérmicas en la Sierra Pinta, NW de Sonora, México: Magmatismo de subducción asociado al inicio del margen continental activo del SW de Norteamérica: Revista Mexicana de Ciencias Geológicas, v. 26, n. 3, p. 709-728.

Barth, A.P., 2010, Birth of the Sierra Nevada batholith: age and composition of the Scheelite Intrusive Suite and coeval volcanic rocks in the Saddlebag Lake Pendant, eastern California: Geological Society of America Abstracts with Programs, v. 42, no. 5, p. 102.

Barth, A.P., Wooden, J.L., 2006, Timing of magmatism following initial convergence at a passive margin, southwestern US Cordillera, and ages of lower crustal magma sources: Journal of Geology, v. 114, n. 2, p. 231-245.

Barth, A.P., Walker, J.D., Wooden, J.L., Riggs, N.R., Schweickert, R.A., 2011, Birth of the Sierra Nevada magmatic arc: Early Mesozoic plutonism and volcanism in the east-central Sierra Nevada of California: Geosphere, v. 7, no. 4, p. 877-897.

Campa, M. F., and Coney, P. J., 1983, Tectono-stratigraphic terranes and mineral resource distributions in Mexico: Canadian Journal of Earth Sciences, v. 20, no. 6, p. 1040-1051.

Centeno-García, E., Guerrero-Suástegui, M., and Talavera-Mendoza, O., 2008, The Guerrero composite terrane of western Mexico: Collision and subsequent rifting in a supra-subduction zone: Geological Society of America Special Paper, v. 436, p. 279-308.

Cochrane, R., Spikings,R., Gerdes, A., Ulianov, A., Mora, A., Villagómez, D., Putlitz, B., Chiaradia, M., 2013, Permo-Triassic anatexis, continental rifting and the disassembly of western Pangea: Lithos, v. 190-191, p. 383-402.

Cuéllar-Cárdenas, M.A., Nieto-Samaniego, Á.F., Levresse, G., Alaniz-Álvarez, S.A., Solari, L., Ortega-Obregón, C., López-Martínez, M., 2012, Límites temporales de la deformación por acortamiento Laramide en el centro de México: Revista Mexicana de Ciencias Geológicas, v. 29, no. 1, p. 179-203.

Damon, P.E., Shafiqullah, M., Clark, K.F., 1981, Evolución de los arcos magmáticos en México y su relación con la metalogénesis: Revista Mexicana de Ciencias Geológicas, v. 5, no. 2, p. 223-238.

Damon, P. E., Shafiqullah, M., Roldán-Quintana, J., and Cochemé, J. J., 1983, El batolito Laramide (90–40 Ma) de Sonora: XV Convención Nacional de la Asociación de Ingenieros de Minas, Metalurgistas y Geólogos de México, Guadalajara, Jalisco, Memorias Técnicas, p. 63-95.

De Cserna, Z., Kent, B.H., 1961. Mapa geológico de reconocimiento y secciones estructurales de la región de San Blas y El Fuerte, Estado de Sinaloa: Cartas Geológicas y Mineras Nº 4, escala 1:100,000, Instituto de Geología, Universidad Nacional Autónoma de México.

Ducea, M., Sen, G., Eiler, J., and Fimbres, J., 2002, Melt depletion and subsequent metasomatism in the shallow mantle beneath Koolau volcano, Oahu (Hawaii): Geochemistry, Geophysics, Geosystems, v. 3, no. 2.

Ehret, P., Culbert, K., Paterson, S., Cao, W., Memeti, V., Schmidt, K., 2010, Comparisons of detrital zircon ages and characteristics of metasedimentary packages in the Saddlebag Lake pendant, Sierra Nevada: implications for depositional environments and tectonic histories: Geological Society of America Abstracts with Programs, v. 42, no. 4, p. 65

Freydier, C., Lapierre, H., Tardy, M., Coulon, C., Martinez-Reyes, J., and Orsini, J.B., 1995, Les formations magmatiques de Porohui (Sinaloa); temoins de l'evolution géodynamique mesozoique et tertiaire des Cordilleres mexicaines: Comptes Rendus de l'Académie des Sciences, Ser.2: Sciences de la Terre et des Planètes,v.321,p.529–536.

Gastil, G., Rector, R., Hazelton, G., Al-Riyami, R., Hanes, J., Farrar, E., Boehnel, H., Ortega-Rivera, A., and Guzman, J.G., 1999, Late Cretaceous pillow basalt, siliceous tuff and calc-turbidite near Porohui, northern Sinaloa, Mexico, in Bartolini, C., et al., eds., Mesozoic sedimentary and tectonic history of north-central Mexico: Geological Society of America Special Paper 340,p.145–150.

Gehrels, G., Valencia, V., Pullen, A., 2006, Detrital Zircon Geochronology by Laser Ablation Multicollector ICPMS at the Arizona LaserChron Center, in Olszewski, T., ed., Geochronology: Emerging Opportunities: Paleontology Society Papers, v. 12, p. 67-76.

Gehrels, G.E., Valencia, V., Ruiz, J., 2008, Enhanced precision, accuracy, efficiency, and spatial resolution of U-Pb ages by laser ablation-multicollector-inductively coupled plasma-mass spectrometry: Geochemistry, Geophysics, Geosystems, v. 9, no. 3

Gehrels, G., Rusmore, M., Woodsworth, G., Crawford, M., Andronicos, C., Hollister, L., Patchett, J., Ducea, M., Butler, R. Klepeis, K. Davidson, C., Mahoney, B., Friedman, R., Haggart, J., Crawford, W., Pearson, D., Girardi, J., 2009, U-Th-Pb geochronology of the Coast Mountains Batholith in north-coastal British Columbia: constraints on age, petrogenesis, and tectonic evolution: GSA Bulletin, v. 121, no. 9/10, p. 1341-1361.

Haxel, G.B., Wright, J.E., Riggs, N.R., Tosdal, R.M., May, D.J., 2005, Middle Jurassic Topawa Group, Baboquivari Mountains, south-central Arizona: Volcanic and sedimentary record of deep basins within the Jurassic magmatic arc: Geological Society of America Special Paper, v. 393, p. 329-357.

Henry, C.D., McDowell, F.W., Silver, L.T., 2003, Geology and geochronology of granitic batholitic complex, Sinaloa, México: implications for Cordilleran magmatism and tectonics: Geological Society of America Special Paper, v. 374, p. 237-273.

Iriondo, A., Premo, W.R., Martínez-Torres, L.M., Budahn, J.R., Atkinson, W.W., Siems, D.F., and Guarás-González, B., 2004, Isotopic, geochemical, and temporal characterization of Proterozoic basement rocks in the Quitovac region, northwestern Sonora, Mexico: Implications for the reconstruction of the southwestern margin of Laurentia: Geological Society of America Bulletin, v. 116, p. 154-170.

Johnson, S.E., Fletcher, J.M., Fanning, C.M., Paterson, S.R., Vernon, R.H., Tate, M.C., 2003, Structure and emplacement of the San Jose tonalite pluton, Peninsular Ranges batholith, Baja California, Mexico: Journal of Structural Geology, v. 25, no. 11, p. 1933–1957.

Johnson, S.E., Tate, M.C., and Fanning, C.M., 1999, New geologic mapping and SHRIMP U-Pb zircon data in the Peninsular Ranges batholith, Baja California, Mexico: Evidence for a suture?: Geology, v. 27, no. 8, p. 743-746.

Ortega-Gutiérrez, F., Prieto-Vélez,R.,Zúñiga,Y., and Flores, S., 1978, Una secuencia volcano-plutonica-sedimentaria cretácica en el norte de Sinaloa; complejo ofiolitico?: Universidad Nacional Autónoma de México, Inst. Geología, Revista, v.3,no.1,p.1–8.

Keppie, J. D., Dostal, J., Miller, B. V., Ortega-Rivera, A., Roldán-Quintana, J., and Lee, J. W. K., 2006, Geochronology and geochemistry of the Francisco Gneiss: Triassic continental rift tholeiites on the Mexican margin of Pangea metamorphosed and exhumed in a Tertiary core complex: International Geology Review, v. 48, no. 1, p. 1-16.

Kimbrough, D.L., Grove, M., Morton, D.M., 2015, Timing and significance of gabbro emplacement within two distinct plutonic domains of the Peninsular Ranges batholith, southern and Baja California: Geological Society of America Bulletin, v. 127, no. 1-2, p.19-37.

Lopez, R., Cameron, K.L., and Jones, N.W., 2001, Evidence for Paleoproterozoic, Grenvillian, and Pan-African age Gondwanan crust beneath northeastern Mexico: Precambrian Research, v. 107, p. 195–214.

Ludwig, K., 2003, Isoplot 3.00. Special Publication 4, 70 pp., Berkeley Geochronology Center, Berkeley, Calif.

Miller, C.F., 1978, Monzonitic plutons, California, and a model for generation of alkali-rich, near silica-saturated magmas: Contributions to Mineralogy and Petrology, v. 67, no. 4, p. 349-355.

Miller, J.S., Glazner, A.F., Walker, J.D., Martin, M.W., 1995, Geochronologic and isotopic evidence for Triassic-Jurassic emplacement of the eugeoclinal allochthon in the Mojave Desert region, California: Geological Society of America Bulletin, v. 107, no. 12, p. 1441-1457.

Mullan, H.S., 1978, Evolution of part of the Nevadan orogen in northwestern Mexico: Geological Society of America Bulletin, v. 89, no. 8, p. 1175-1188.

Peiffer-Rangin, F., 1979. Les zones isopiques du Paléozoique inférieur du NW Mexicain. Temoins du relais

entre les Appalaches et la cordillère ouestaméricaine. Comptes Rendus Academie Sciences Paris t 288, série D, pp. 1517–1519.

Peña-Alonso, T.A., Delgado-Argote, L.A., Weber, B., Velasco-Tapia, F., Valencia, V., 2012, Geology and emplacement history of the Nuevo Rosarito plutonic suite in the southern Peninsular Ranges batholith, Baja California, México, Revista Mexicana de Ciencias Geológicas, v. 29, no. 1, p. 1-23.

Pompa-Mera, V., Schaaf, P., Hernández-Treviño, T., Weber, B., Solís-Pichardo, G., Villanueva-Lascurain, D., Layer, P., 2013, Geology, geochronology, and geochemistry of Isla María Madre, Nayarit, Mexico: Revista Mexicana de Ciencias Geológicas, v.30, no. 1, p.1-23.

Poole, F. G., Perry, W. J., Madrid, R. J., and Amaya-Martínez, R., 2005, Tectonic synthesis of the Ouachita-Marathon-Sonora orogenic margin of southern Laurentia: Stratigraphic and structural implications for timing of deformational events and plate-tectonic model: Geological Society of America Special Paper, v. 393, p. 543-596.

Poole, F.G., Amaya-Martínez, R., Premo, W.R., Berry, W.B.N., Sandberg, C.A., Roldán-Quintana, J., Herrera-Urbina, S., 2010, Age and depositional setting of deep-marine Ordovician Río Fuerte and San José de Gracia formations in northern Sinaloa, Mexico: remnants of the early Paleozoic Iapetus ocean, Geological Society of America Abstracts with Programs, v.42, no.5, p.268.

Potra, A., Hickey-Vargas, R., Macfarlane, A.W., and Salters, V.J., 2014, Pb, Sr, and Nd isotopic characteristics of a variety of lithologies from the Guerrero composite terrane, west-central Mexico: Constraints on their origin: Revista Mexicana de Ciencias Geológicas, v. 31, p. 203–220.

Riggs, N.R., Mattinson, J.M., Busby, C.J., 1993, Correlation of Jurassic eolian strata between the magmatic arc and the Colorado Plateau: New U-Pb geochronologic data from southern Arizona: Geological Society of America Bulletin, v.105, no. 9, p. 1231-1246.

Riggs, N.R., Barth, A.P., González-León, C.M., Jacobson, C.E., Wooden, J.L., Howell, E.R., Walker, J.D., 2012, Provenance of Upper Triassic strata in southwestern North America as suggested by isotopic analysis and chemistry of zircon crystals: Geological Society of America Special Paper, v. 487, p. 13-36.

Saleeby, J.B., Ducea, M.N., Busby, C.J., Nadin, E.S., Wetmore, P.H., 2008, Chronology of pluton emplacement and regional deformation in the southern Sierra Nevada batholith, California, in Wright, J.E., and Shervais, J.W., eds., Ophiolites, Arcs, and Batholiths: A Tribute to Cliff Hopson: Geological Society of America Special Paper, v. 438, p. 397-427.

Sams, D.B., Saaleby, J.B., 1988, Geology and petrotectonic significance of crystalline rocks of the southernmost Sierra Nevada, California, in Ernst, W.G. (ed.), Rubey Volume VII, Metamorphism and Crustal Evolution in the Western United States: Englewood Cliffs, New Jersey, Prentice-Hall, 866-893.

Sarmiento-Villagrana, A., Vega-Granillo, R., Talavera-Mendoza, O., Salgado-Souto, S. A., and Gómez-Landa, J. R., 2017, Geochemical and isotopic study of Mesozoic magmatism in the Sonobari Complex, western Mexico: Implications for the tectonic evolution of southwestern North America: Geosphere, v. 14, no. 1, p. 305-324.

Sarmiento-Villagrana, A., Vega-Granillo, R., Talavera-Mendoza, O., and Vidal-Solano, J. R., 2016, New age constraints on magmatism and metamorphism of the Western Sonobari Complex and their implications for an earliest Late Cretaceous orogeny on northwestern Mexico: Revista Mexicana de Ciencias Geológicas, v. 33, no. 2, p. 170-182.

Schaaf, P., Weber, B., Weis, P., Gross, A., Ortega-Gutiérrez, F., Kohler, H., 2002, The Chiapas Massif (Mexico) revised: New geologic and isotopic data and basement characteristics: Neues Jahrbuch fur Geologie und Palaontologie- Abhandlungen, v. 225, no.1, p. 1-23.

Schmidt, K.L., Paterson, S.R., 2002, A doubly vergent fan structure in the Peninsular Ranges batholith: Transpression or local complex flow around a continental margin buttress?: Tectonics, v. 21, no. 5, p. 14-1.

Schmidt, K.L., Paterson, S.R., Blythe, A.E., and Kopf, C., 2009, Mountain building across a lithospheric boundary duringarc construction: The Cretaceous Peninsular Ranges batholithin the Sierra San Pedro Martir of Baja California, Mexico: Tectonophysics, v. 477, p. 292–310.

Sedlock, R. L., Ortega-Gutiérrez, F., and Speed, R. C., 1993, Tectonostratigraphic terranes and tectonic evolution of Mexico: Geological Society of America Special Paper, v. 278, p. 1-153.

Shaw, S.E., Todd, V.R., Grove, M., 2003, Jurassic peraluminous gneissic granites in the axial zone of the Peninsular Ranges, southern California: Geological Society of America Special Paper, v. 374, p.157-183.

Torres, R., Ruiz, J., Patchett, P.J., Grajales, J.M., 1999, A Permo-Triassic continental arc in eastern Mexico: Tectonic implications for reconstructions of southern North America: Geological Society of America Special Paper, v. 340, p. 191-196.

Thibodeau, A. M., Habicht-Mauche, J. A., Huntley, D. L., Chesley, J. T., and Ruiz, J., 2013, High precision isotopic analyses of lead ores from New Mexico by MC-ICP-MS: Implications for tracing the production and

exchange of Pueblo IV glaze-decorated pottery: Journal of Archaeological Science, v. 40, no. 7, p. 3067-3075.

Thibodeau, A. M., Killick, D. J., Hedquist, S. L., Chesley, J. T., and Ruiz, J., 2015, Isotopic evidence for the provenance of turquoise in the southwestern United States: Geological Society of America Bulletin, v. 127, no. 11-12, p. 1617-1631.

Thompson, C.N., Girty, G. H., 1994, Early Cretaceous intra-arc ductile strain in Triassic-Jurassic and Cretaceous continental margin arc rocks, Peninsular Ranges, California: Tectonics, v. 13, no. 5, p. 1108-1119.

Valencia-Moreno, M., Ruiz, J., Barton, M. D., Patchett, P. J., Zürcher, L., Hodkinson, D. G., and Roldán-Quintana, J., 2001, A chemical and isotopic study of the Laramide granitic belt of northwestern Mexico: Identification of the southern edge of the North American Precambrian basement: Geological Society of America Bulletin, v. 113, no. 11, p.1409-1422.

Valencia, V.A., Barra, F., Weber, B., Ruiz, J., Gehrels, G., Chesley, J., Lopez-Martinez, M., 2006, Re–Os and U–Pb geochronology of the El Arco porphyry copper deposit, Baja California Mexico: implications for the Jurassic tectonic setting: Journal of South American Earth Sciences, v. 22, no. 1, p. 39-51.

Vega-Granillo, R., Salgado-Souto, S., Herrera-Urbina, S., Valencia, V., Ruiz, J., Meza-Figueroa, D., and Talavera-Mendoza, O., 2008, U–Pb detrital zircon data of the Rio Fuerte Formation (NW Mexico): Its peri-Gondwanan provenance and exotic nature in relation to southwestern North America: Journal of South American Earth Sciences, v. 26, no. 4, p. 343-354.

Vega-Granillo, R., Salgado-Souto, S., Herrera-Urbina, S., Valencia, V., and Vidal-Solano, J. R., 2011, Metamorphism and deformation in the El Fuerte region: their role in the tectonic evolution of NW Mexico: Revista Mexicana de Ciencias Geológicas, v. 28, no. 1, p. 10-23.

Vega-Granillo, R., Vidal-Solano, J. R., and Herrera-Urbina, S., 2012, Island arc tholeiites of Early Silurian, Late Jurassic and Late Cretaceous ages in the El Fuerte region, northwestern Mexico: Revista Mexicana de Ciencias Geológicas, v. 29, no. 2, p. 492-513.

Vega-Granillo, R., Vidal-Solano, J. R., Solari, L. A., Martínez, M. L., Juárez, O. G., and Urbina, S. H., 2013, Geochemical and geochronological constraints on the geologic evolution of the western Sonobari Complex, northwestern Mexico: Geologica Acta, v. 11, no. 4, p. 443-463.

Vega-Granillo, R., Sarmiento-Villagrana, A., Salgado-Souto, S., and Araux-Sánchez, E., 2017, P-T conditions of earliest Late Cretaceous metamorphism in the Western Sonobari Complex, northwestern Mexico: tectonic implications: International Geology Review, v. 59, no. 7, p. 812-828.

Weber, B., Cameron, K.L., Osorio, M., Schaaf, P., 2005, A Late Permian tectonothermal event in Grenville crust of the southern Maya terrane: U-Pb zircon ages from the Chiapas Massif, southeastern Mexico: International Geology Review, v. 47, no. 5, p. 509-529.

Wetmore, P.H., Alsleben, H., Paterson, S.R., Ducea, M.N., Gehrels, G.E., Valencia, V.A., 2005, Field trip to the northern Alisitos arc segment: Ancestral Agua Blanca fault region: Field Trip Guide for the VII International Meeting of the Peninsular Geological Society, 40 pp.

Yáñez, P., Ruiz, J., Patchett, P.J., Ortega-Gutierrez, F., Gehrels, G.E., 1991, Isotopic studies of the Acatlan complex, southern Mexico: Implications for Paleozoic North American tectonics: Geological Society of America Bulletin, v.103, no. 6, p.817-828.

ANEXOS 7

Anexo 1

Material suplementario publicado en línea del artículo:

Sarmiento-Villagrana, A., Vega-Granillo, R., Talavera-Mendoza, O., and Vidal-Solano, J. R., 2016, New age constraints on magmatism and metamorphism of the Western Sonobari Complex and their implications for an earliest Late Cretaceous orogeny on northwestern Mexico: Revista Mexicana de Ciencias Geológicas, v. 33, no. 2, p. 170-182.

Material:

S1. Muestreo y métodos analíticos.

S2. Datos analíticos de edades U-Pb.

SUPPLEMENTARY FILE 1

to the paper

New age constraints on magmatism and metamorphism of the Western Sonobari Complex and their implications for an earliest Late Cretaceous orogeny on northwestern Mexico

by

Alicia Sarmiento-Villagrana, Ricardo Vega-Granillo, Oscar Talavera-Mendoza, and Jesús Roberto Vidal-Solano

published in

Revista Mexicana de Ciencias Geológicas, 2016, 33(2), p. 170-182.

S1. METHODS

Sampling and analytical methods

Sixteen of the most representative samples of orthogneisses and plutonic rocks of the Western Sonobari Complex were collected for U-Pb geochronology. The samples were collected during several field sessions between 2012 and 2014.

Zircon separation

For zircon separation about five and six kilograms of fresh rock shards of each sample were collected. Some samples were prepared at the University of Arizona and several in the Universidad Autónoma de Guerrero laboratories. The procedures for zircon separation are described in Gehrels et al. (2006, 2008, 2009); they consisted of the following steps: First, the sample was reduced down to gravel size with a jaw crusher. Subsequently, the samples were reduced down to sand size (~0.063 – 2 mm) with a roller mill machine. Then, the heaviest minerals were separated from the lighter ones in a Wilfley table. The magnetic minerals were separated using a Frantz LB1 magnetic separator. The non-magnetic fraction was processed through Heavy Liquid Separation (using Methylene Iodide technique) in order to obtain just the zircons. The zircons were mounted in a 1-inch-diameter epoxy plug together with Sri Lanka, and R33 standard zircon and the surface was polished to expose the interior portions of most grains. Low resolution CL (cathodoluminescence) images were acquired from all dated samples in a Hitachi 3400N SEM. The CL images were used to characterize chemical zoning and identify core-rim relationship and inherited zircons. Forty to eighty zircons from each sample were analyzed.

Data adquisition and reduction

The U-Pb analyses were performed at the Arizona LaserChron Center of the University of Arizona. The analyses involved ablation of zircons with a Photon Machines Analyte G2 excimer laser using a spot diameter of 30 microns. In sample SFO-20 a spot diameter of 15 microns was used for the analisys of recrystallized zircon rims. The ablated material was carried with helium gas into the plasma source of a Nu HR MC-ICPMS, which is equipped with a flight tube of sufficient width that U, Th, and Pb isotopes are measured simultaneously. All measurements were made in static mode, using a Faraday detectors.

Data reduction took place off-line using a raw count data imported into an Excel spreadsheet. Data were corrected for downhole laser fractionation, elemental fractionation, and common Pb correction (see Thompson et al., 2012 for more detailed explanation). Fractionation of U, Th and Pb was corrected by comparing the standards (SL and R33) that were analyzed between every five unknown zircons. The uncertainty of the weighted mean was approximately 1% (2-sigma). Final data reduction and calculation of weighted mean ages, concordia ages and tuff-zirc ages, was done using Isoplot (Ludwig, 2003).

REFERENCES

Gehrels, G., Valencia, V., Pullen, A., 2006, Detrital Zircon Geochronology by Laser Ablation Multicollector ICPMS at the Arizona LaserChron Center, in Olszewski, T., ed., Geochronology: Emerging Opportunities: Paleontology Society Papers, Volume 12, p. 67-76)

Gehrels, G.E., Valencia, V., Ruiz, J., 2008, Enhanced precision, accuracy, efficiency, and spatial resolution of U-Pb ages by laser ablation-multicollector-inductively coupled plasma-mass spectrometry: Geochemistry, Geophysics, Geosystems, v. 9, Q03017, doi:10.1029/2007GC001805.

Gehrels, G., Rusmore, M., Woodsworth, G., Crawford, M., Andronicos, C., Hollister, L., Patchett, J., Ducea, M., Butler, R. Klepeis, K. Davidson, C., Mahoney, B., Friedman, R., Haggart, J., Crawford, W., Pearson, D., Girardi, J., 2009, U-Th-Pb geochronology of the Coast Mountains Batholith in north-coastal British Columbia: constraints on age, petrogenesis, and tectonic evolution: GSA Bulletin, v. 121, no. 9/10, p. 1341-1361.

Ludwig, K., 2003, Isoplot 3.00. Special Publication 4, 70 pp., Berkeley Geochronology Center, Berkeley, Calif.

Thompson, S.N., Gehrels, G.E., Ruiz, J., Buchwaldt, R., 2012, Routine low-damage apatite U-pb dating using laser ablation-multicollector-ICPMS: Geochemistry, Geophysics, Geosystems, 13(2), doi 10.1029/2011GC003928.

Supplementary File 2

S2. U-Pb geochronological data

to the paper: New age constraints on magmatism and metamorphism of the Western Sonobari Complex and their implications for an earliest Late Cretaceous orogeny on northwestern Mexico

by: Alicia Sarmiento-Villagrana, Ricardo Vega-Granillo, Oscar Talavera-Mendoza, and Jesús Roberto Vidal-Solano

Publisehd in: Revista Mexicana de Ciencias Geológicas, 2016, v. 33, núm. 2, p. 170-182.

				Isotope ratios							Apparent ages (Ma)								
Sample SFO-2	U (ppm)	206Pb 204Pb	U/Th	206Pb* 207Pb*	± (%)	207Pb* 235U*	± (%)	206Pb* 238U	± (%)	error corr.	206Pb* 238U*	± (Ma)	207Pb* 235U	± (Ma)	206Pb* 207Pb*	± (Ma)	Best age (Ma)	± (Ma)	Conc (%)
SFO-2-1	321	38773	3.0	19.6625	3.3	0.3185	7.2	0.0454	6.3	0.88	286.4	17.7	280.8	17.6	234.4	77.3	286.4	17.7	NA
SFO-2-2	509	12204	62.2	19.2000	12.6	0.0871	13.1	0.0121	3.5	0.26	77.7	2.7	84.8	10.6	289.1	288.7	77.7	2.7	NA
SFO-2-3	308	8908	4.5	17.4273	8.7	0.1069	9.8	0.0135	4.4	0.45	86.6	3.8	103.2	9.6	506.2	192.1	86.6	3.8	NA
SFO-2-5	59	3454	1.5	21.4762	39.3	0.1664	39.9	0.0259	7.1	0.18	164.9	11.5	156.3	57.9	26.9	976.5	164.9	11.5	NA
SFO-2-8	141	16010	1.3	22.7557	20.5	0.1997	20.9	0.0330	4.0	0.19	209.0	8.3	184.9	35.3	-113.7	509.6	209.0	8.3	NA
SFO-2-13	5847	27156	42.4	20.7081	0.6	0.1168	9.7	0.0175	9.7	1.00	112.1	10.8	112.2	10.3	113.5	13.2	112.1	10.8	NA
SFO-2-16	120	3643	1.8	39.4084	68.6	0.0425	69.0	0.0122	7.9	0.11	77.9	6.1	42.3	28.6	NA	NA	77.9	6.1	NA
SFO-2-18	2899	54215	80.1	21.1816	3.4	0.0789	7.0	0.0121	6.1	0.87	77.7	4.7	77.1	5.2	59.9	81.8	77.7	4.7	NA
SFO-2-20	3957	24943	90.2	20.4072	1.8	0.0870	5.6	0.0129	5.3	0.95	82.5	4.4	84.7	4.6	147.9	41.1	82.5	4.4	NA
SFO-2-23	4316	64596	90.0	20.5184	1.3	0.0853	3.7	0.0127	3.5	0.94	81.3	2.8	83.1	3.0	135.2	30.1	81.3	2.8	NA

				Isotope ratios							Apparent ages (Ma)								
Sample SFO-5	U (ppm)	206Pb 204Pb	U/Th	206Pb* 207Pb*	± (%)	207Pb* 235U*	± (%)	206Pb* 238U	± (%)	error corr.	206Pb* 238U*	± (Ma)	207Pb* 235U	± (Ma)	206Pb* 207Pb*	± (Ma)	Best age (Ma)	± (Ma)	Conc (%)
SFO-5-1	285	29841	1.3	19.8789	5.7	0.2092	6.2	0.0302	2.6	0.41	191.6	4.9	192.9	10.9	209.1	131.4	191.6	4.9	NA
SFO-5-2	188	6677	139.7	18.1487	18.2	0.1085	18.7	0.0143	4.4	0.23	91.4	4.0	104.6	18.6	416.3	409.3	91.4	4.0	NA
SFO-5-3	208	50100	1.8	19.4055	4.1	0.2293	4.7	0.0323	2.2	0.48	204.8	4.5	209.7	8.8	264.7	94.0	204.8	4.5	NA
SFO-5-4	298	32884	1.1	20.0645	3.4	0.2318	5.3	0.0337	4.1	0.77	213.9	8.5	211.7	10.1	187.5	79.1	213.9	8.5	NA
SFO-5-5	97	15926	2.0	19.3497	16.6	0.2324	17.6	0.0326	5.9	0.33	206.9	12.0	212.2	33.7	271.3	382.8	206.9	12.0	NA
SFO-5-6	292	59252	1.1	19.8275	5.8	0.2318	6.6	0.0333	3.2	0.48	211.4	6.6	211.7	12.5	215.1	133.3	211.4	6.6	NA
SFO-5-7	224	53288	1.6	20.2880	4.0	0.2155	4.7	0.0317	2.4	0.51	201.2	4.7	198.2	8.4	161.6	94.5	201.2	4.7	NA
SFO-5-8	365	15794	0.9	20.3193	2.9	0.2279	4.3	0.0336	3.2	0.74	213.0	6.7	208.5	8.1	158.0	68.0	213.0	6.7	NA
SFO-5-9	146	4616	88.5	26.2914	42.9	0.0792	43.1	0.0151	4.3	0.10	96.6	4.1	77.4	32.2	-482.7	1185.4	96.6	4.1	NA
SFO-5-10	530	44304	1.1	19.6064	2.8	0.2264	3.4	0.0322	2.0	0.58	204.3	4.0	207.2	6.5	241.0	64.8	204.3	4.0	NA
SFO-5-11	347	108899	1.3	19.7138	4.2	0.2306	4.5	0.0330	1.6	0.36	209.1	3.3	210.7	8.6	228.4	97.0	209.1	3.3	NA
SFO-5-12	109	11632	2.1	18.1799	13.5	0.2390	15.9	0.0315	8.3	0.52	200.0	16.4	217.6	31.1	412.4	303.6	200.0	16.4	NA
SFO-5-13	180	18624	1.6	20.5406	10.8	0.2214	11.0	0.0330	2.4	0.22	209.1	5.0	203.0	20.3	132.6	253.7	209.1	5.0	NA

SFO-5-14	4886	30265	0.5	20.2780	0.7	0.1147	17.4	0.0169	17.4	1.00	107.9	18.6	110.3	18.2	162.8	16.4	107.9	18.6	NA
SFO-5-15	397	23803	0.9	20.5637	3.7	0.2228	5.1	0.0332	3.5	0.68	210.8	7.2	204.3	9.4	130.0	87.1	210.8	7.2	NA
SFO-5-16	101	7893	0.7	22.6065	24.5	0.2071	25.5	0.0340	7.1	0.28	215.3	15.0	191.1	44.5	-97.6	610.6	215.3	15.0	NA
SFO-5-17	1259	38054	1.1	20.0686	2.7	0.1122	15.0	0.0163	14.8	0.98	104.4	15.3	108.0	15.4	187.0	64.0	104.4	15.3	NA
SFO-5-18	241	16873	1.4	21.2167	6.1	0.2119	6.2	0.0326	1.3	0.21	206.9	2.7	195.2	11.0	55.9	145.2	206.9	2.7	NA
SFO-5-20	295	27609	1.2	20.0823	5.9	0.2319	6.6	0.0338	3.0	0.46	214.1	6.4	211.8	12.7	185.4	137.1	214.1	6.4	NA
SFO-5-21	4827	455763	0.5	20.4585	0.6	0.1331	9.0	0.0197	9.0	1.00	126.0	11.2	126.9	10.7	142.1	15.2	126.0	11.2	NA
SFO-5-22	302	32731	1.3	19.6956	3.5	0.2300	4.2	0.0329	2.3	0.56	208.4	4.8	210.2	7.9	230.5	79.9	208.4	4.8	NA
SFO-5-23	1123	46747	4.0	20.1414	1.6	0.1616	8.8	0.0236	8.6	0.98	150.4	12.8	152.1	12.4	178.6	37.8	150.4	12.8	NA
SFO-5-24	485	35920	1.1	20.4576	3.0	0.2239	4.3	0.0332	3.1	0.72	210.7	6.5	205.2	8.0	142.1	69.8	210.7	6.5	NA
SFO-5-25	583	57050	0.9	19.8393	4.1	0.2301	4.5	0.0331	1.9	0.43	210.0	4.0	210.3	8.5	213.7	94.0	210.0	4.0	NA
SFO-5-26	355	18479	1.1	18.8074	4.2	0.2241	4.5	0.0306	1.5	0.34	194.1	2.9	205.4	8.4	336.1	96.1	194.1	2.9	NA
SFO-5-27	451	28750	0.8	20.5342	4.1	0.2157	5.1	0.0321	3.0	0.58	203.8	5.9	198.3	9.2	133.4	97.5	203.8	5.9	NA

				Isotope ratios							Apparent ages (Ma)								
Sample SFO-17	U (ppm)	206Pb 204Pb	U/Th	206Pb* 207Pb*	± (%)	207Pb* 235U*	± (%)	206Pb* 238U	± (%)	error corr.	206Pb* 238U*	± (Ma)	207Pb* 235U	± (Ma)	206Pb* 207Pb*	± (Ma)	Best age (Ma)	± (Ma)	Conc (%)
SFO-17-1	5826	212556	35.2	20.6148	0.7	0.1090	3.5	0.0163	3.4	0.98	104.2	3.5	105.1	3.5	124.1	15.9	104.2	3.5	NA
SFO-17-2	4946	7552	43.8	20.2933	2.3	0.0885	2.4	0.0130	0.7	0.28	83.4	0.5	86.1	2.0	161.1	53.5	83.4	0.5	NA
SFO-17-3	4852	8623	49.6	20.4187	1.2	0.0893	5.1	0.0132	5.0	0.97	84.7	4.2	86.8	4.3	146.6	28.2	84.7	4.2	NA
SFO-17-4	3588	130195	16.7	20.6022	1.9	0.0868	3.4	0.0130	2.8	0.83	83.1	2.3	84.6	2.8	125.6	44.2	83.1	2.3	NA
SFO-17-5	1798	108121	66.9	20.5110	3.3	0.0866	3.6	0.0129	1.4	0.39	82.6	1.1	84.4	2.9	136.1	77.4	82.6	1.1	NA
SFO-17-6	3320	72845	36.6	20.7537	1.4	0.0892	3.8	0.0134	3.6	0.93	86.0	3.1	86.8	3.2	108.3	33.7	86.0	3.1	NA
SFO-17-7	3865	118153	41.2	20.3963	1.6	0.0884	3.0	0.0131	2.5	0.85	83.8	2.1	86.1	2.5	149.2	37.7	83.8	2.1	NA
SFO-17-10	3217	287394	65.0	20.7233	1.0	0.0862	1.8	0.0130	1.6	0.86	83.0	1.3	83.9	1.5	111.8	22.4	83.0	1.3	NA
SFO-17-11	2049	38590	66.6	20.8345	1.6	0.0904	2.2	0.0137	1.6	0.70	87.4	1.4	87.9	1.9	99.1	37.2	87.4	1.4	NA
SFO-17-12	2952	41787	33.7	20.2692	1.8	0.0781	11.1	0.0115	10.9	0.99	73.6	8.0	76.4	8.1	163.8	41.3	73.6	8.0	NA
SFO-17-13	5819	255223	40.8	20.6482	0.8	0.0985	4.3	0.0147	4.2	0.98	94.4	3.9	95.4	3.9	120.4	17.8	94.4	3.9	NA
SFO-17-15	3227	23078	46.7	19.5173	8.2	0.0926	8.4	0.0131	1.8	0.21	83.9	1.5	89.9	7.2	251.5	188.9	83.9	1.5	NA
SFO-17-16	5354	96824	40.4	20.8375	0.8	0.0879	2.3	0.0133	2.2	0.95	85.1	1.9	85.6	1.9	98.8	17.9	85.1	1.9	NA
SFO-17-19	3977	26383	20.5	20.5185	1.5	0.0845	1.8	0.0126	1.1	0.58	80.6	0.8	82.4	1.4	135.2	34.8	80.6	0.8	NA
SFO-17-20	4819	11443	47.2	19.7437	5.0	0.0908	6.1	0.0130	3.4	0.57	83.3	2.8	88.2	5.1	224.9	115.3	83.3	2.8	NA
SFO-17-21	3836	80483	38.3	20.7419	2.0	0.0838	7.4	0.0126	7.2	0.96	80.8	5.7	81.7	5.8	109.7	46.3	80.8	5.7	NA
SFO-17-23	4572	35292	29.1	20.5966	1.3	0.0774	11.6	0.0116	11.5	0.99	74.1	8.5	75.7	8.4	126.3	29.6	74.1	8.5	NA

Isotope ratios Apparent ages (Ma)

Sample SFO-20	U (ppm)	206Pb 204Pb	U/Th	206Pb* 207Pb*	± (%)	207Pb* 235U*	± (%)	206Pb* 238U	± (%)	error corr.	206Pb* 238U*	± (Ma)	207Pb* 235U	± (Ma)	206Pb* 207Pb*	± (Ma)	Best age (Ma)	± (Ma)	Conc (%)
SFO-20-1	638	70683	0.7	19.6996	2.0	0.2257	2.2	0.0323	1.0	0.44	204.6	1.9	206.7	4.1	230.0	45.1	204.6	1.9	NA
SFO-20-2	104	3394	42.9	20.1135	25.0	0.1161	25.9	0.0169	6.8	0.26	108.3	7.4	111.5	27.4	181.8	589.7	108.3	7.4	NA
SFO-20-3	389	23895	1.2	19.8041	3.4	0.2326	3.9	0.0334	1.9	0.49	211.9	4.0	212.4	7.6	217.8	79.9	211.9	4.0	NA
SFO-20-4	233	10107	193.9	18.7277	9.6	0.1037	11.1	0.0141	5.6	0.50	90.2	5.0	100.2	10.6	345.7	217.7	90.2	5.0	NA
SFO-20-5	253	19458	1.2	20.7754	5.3	0.2173	5.8	0.0327	2.4	0.41	207.7	4.9	199.7	10.5	105.8	124.1	207.7	4.9	NA
SFO-20-6	218	135524	1.5	20.2234	10.0	0.2285	10.7	0.0335	3.9	0.36	212.5	8.2	209.0	20.3	169.1	234.2	212.5	8.2	NA
SFO-20-7	421	31295	0.9	19.5901	4.3	0.2350	7.5	0.0334	6.2	0.82	211.7	12.9	214.3	14.6	242.9	99.2	211.7	12.9	NA
SFO-20-8	240	13970	1.3	20.1100	6.7	0.2225	7.1	0.0325	2.2	0.31	205.9	4.5	204.0	13.1	182.2	156.6	205.9	4.5	NA
SFO-20-9	152	12892	0.9	20.8744	11.1	0.2110	11.2	0.0320	1.4	0.13	202.8	2.8	194.4	19.9	94.6	264.5	202.8	2.8	NA
SFO-20-10	230	19136	1.4	20.4337	9.3	0.2200	9.8	0.0326	3.0	0.30	206.9	6.1	201.9	17.9	144.9	218.9	206.9	6.1	NA
SFO-20-11	116	13887	1.0	18.7245	10.3	0.2513	11.6	0.0341	5.4	0.46	216.3	11.4	227.6	23.7	346.1	233.6	216.3	11.4	NA
SFO-20-12	372	20388	0.9	20.7134	7.9	0.2158	8.1	0.0324	1.6	0.20	205.7	3.2	198.4	14.6	112.9	187.3	205.7	3.2	NA
SFO-20-13	300	27691	1.1	20.0047	8.0	0.2163	8.3	0.0314	2.4	0.29	199.2	4.7	198.8	15.0	194.5	185.3	199.2	4.7	NA
SFO-20-14	407	35333	1.0	20.3533	2.5	0.2269	4.1	0.0335	3.3	0.80	212.4	6.9	207.7	7.7	154.1	57.4	212.4	6.9	NA
SFO-20-15	205	35658	1.2	19.3996	9.0	0.2328	9.6	0.0327	3.3	0.34	207.7	6.7	212.5	18.4	265.4	207.1	207.7	6.7	NA
SFO-20-16	59	3810	1.4	21.8237	21.3	0.2209	22.0	0.0350	5.8	0.26	221.5	12.7	202.7	40.5	-11.7	518.8	221.5	12.7	NA
SFO-20-17	381	38544	1.0	19.9183	4.8	0.2192	5.5	0.0317	2.6	0.48	200.9	5.2	201.2	10.0	204.5	112.0	200.9	5.2	NA
SFO-20-18	358	31897	1.2	20.2419	8.0	0.2198	8.5	0.0323	2.9	0.34	204.8	5.8	201.8	15.6	166.9	187.7	204.8	5.8	NA
SFO-20-18	612	37188	0.8	19.3909	2.2	0.2333	2.8	0.0328	1.7	0.63	208.2	3.5	213.0	5.3	266.4	49.6	208.2	3.5	NA
SFO-20-19	355	34835	0.8	19.9591	5.0	0.2265	9.2	0.0328	7.7	0.84	207.9	15.8	207.3	17.2	199.8	115.1	~~207.9~~	~~15.8~~	NA
SFO-20-20	398	40041	0.9	20.4054	4.4	0.2186	4.6	0.0324	1.4	0.30	205.3	2.8	200.8	8.3	148.1	102.2	205.3	2.8	NA
SFO-20-21	963	77706	1.1	20.2358	3.2	0.1713	3.5	0.0251	1.4	0.40	160.1	2.2	160.5	5.2	167.7	75.4	160.1	2.2	NA
SFO-20-22	315	28605	0.6	19.5470	3.4	0.2380	3.6	0.0337	1.3	0.37	213.9	2.8	216.8	7.1	248.0	77.4	213.9	2.8	NA
SFO-20-23	314	23816	1.1	19.7442	7.1	0.2406	8.1	0.0345	4.0	0.49	218.4	8.6	218.9	16.0	224.8	163.8	218.4	8.6	NA
SFO-20-24	347	36381	1.3	19.6649	4.1	0.2311	4.7	0.0330	2.4	0.52	209.1	5.0	211.1	9.1	234.2	93.9	209.1	5.0	NA
SFO-20-25	355	43533	1.1	19.2851	2.9	0.2345	3.4	0.0328	1.8	0.53	208.0	3.7	213.9	6.6	279.0	66.0	208.0	3.7	NA
SFO-20-26	183	9289	1.3	20.8377	8.7	0.2300	9.2	0.0348	3.2	0.34	220.3	6.8	210.2	17.5	98.8	205.4	220.3	6.8	NA
SFO-20-27	346	54363	0.9	19.8073	3.8	0.2378	4.5	0.0342	2.3	0.52	216.5	4.9	216.6	8.7	217.5	88.3	216.5	4.9	NA

				Isotope ratios							Apparent ages (Ma)								
Sample SFO-20 15 microns	U (ppm)	206Pb 204Pb	U/Th	206Pb* 207Pb*	± (%)	207Pb* 235U*	± (%)	206Pb* 238U	± (%)	error corr.	206Pb* 238U*	± (Ma)	207Pb* 235U	± (Ma)	206Pb* 207Pb*	± (Ma)	Best age (Ma)	± (Ma)	Conc (%)

spot diameter																		
SFO-20-IC-(	33	1563	47.5	19.0099	7.2	0.0911	10.1	0.0126	7.2	0.71	80.5	5.7	88.6	8.6	311.8	163.3	80.5	5.7	NA
SFO-20-IC-(	71	2777	117.4	20.0058	12.9	0.0949	13.3	0.0138	3.5	0.27	88.2	3.1	92.1	11.7	194.3	300.0	88.2	3.1	NA
SFO-20-IC-(	49	3360	-698.2	20.6979	5.9	0.0992	6.1	0.0149	1.4	0.24	95.3	1.4	96.1	5.6	114.6	139.0	95.3	1.4	NA
SFO-20-IC-(	80	3331	153.1	20.4935	5.1	0.0920	5.9	0.0137	3.1	0.51	87.6	2.7	89.4	5.1	138.0	119.8	87.6	2.7	NA
SFO-20-IC-(	200	31817	242.6	20.8521	1.8	0.0962	4.0	0.0145	3.6	0.90	93.1	3.3	93.2	3.6	97.1	41.5	93.1	3.3	NA
SFO-20-IC-(	64	2854	593.9	22.5038	5.6	0.0957	14.8	0.0156	13.7	0.93	99.9	13.6	92.8	13.2	-86.4	137.1	99.9	13.6	NA
SFO-20-IC-(	27	875	153.3	22.2143	6.0	0.0988	6.8	0.0159	3.2	0.47	101.8	3.2	95.6	6.2	-54.8	145.5	101.8	3.2	NA
SFO-20-IC-(	61	1089	226.3	24.6289	4.8	0.0855	5.4	0.0153	2.4	0.46	97.7	2.4	83.3	4.3	-312.5	122.3	97.7	2.4	NA
SFO-20-IC-(	47	1446	-241.7	23.7166	3.4	0.0921	3.6	0.0158	1.1	0.30	101.3	1.1	89.5	3.1	-216.7	86.7	101.3	1.1	NA
SFO-20-IC-	180	4949	230.5	20.5109	2.4	0.0958	2.7	0.0142	1.1	0.41	91.2	1.0	92.9	2.4	136.1	57.1	91.2	1.0	NA
SFO-20-IC-	53	4081	2188.8	21.9020	4.1	0.0970	4.9	0.0154	2.6	0.54	98.6	2.6	94.0	4.4	-20.4	98.9	98.6	2.6	NA
SFO-20-IC-	56	1778	74.7	20.8467	8.2	0.0880	10.0	0.0133	5.7	0.57	85.2	4.8	85.6	8.2	97.8	195.2	85.2	4.8	NA
SFO-20-IC-	39	4728	83.1	20.9933	12.1	0.0981	13.1	0.0149	5.1	0.39	95.6	4.8	95.0	11.9	81.1	287.2	95.6	4.8	NA
SFO-20-IC-	50	980	86.5	22.8848	5.3	0.0903	6.3	0.0150	3.5	0.55	95.9	3.3	87.8	5.3	-127.7	130.6	95.9	3.3	NA
SFO-20-IC-	219	11298	1.9	19.7835	1.8	0.2014	2.3	0.0289	1.4	0.59	183.7	2.5	186.3	3.9	220.2	42.6	183.7	2.5	NA
SFO-20-IC-	74	2286	34.8	20.2189	11.8	0.0972	15.3	0.0142	9.7	0.64	91.2	8.8	94.2	13.8	169.6	277.4	91.2	8.8	NA
SFO-20-IC-	130	5569	36.2	19.9577	3.6	0.0969	13.9	0.0140	13.4	0.97	89.8	12.0	93.9	12.5	199.9	84.3	89.8	12.0	NA
SFO-20-IC-	521	74225	40.4	19.6672	1.4	0.2085	1.8	0.0297	1.1	0.61	188.9	2.1	192.3	3.2	233.9	33.2	188.9	2.1	NA
SFO-20-IC-2	41	2179	220.7	21.5804	9.7	0.0914	10.0	0.0143	2.3	0.23	91.6	2.1	88.8	8.5	15.3	234.5	91.6	2.1	NA
SFO-20-IC-2	206	26440	1.5	19.9340	1.4	0.2373	1.8	0.0343	1.2	0.67	217.4	2.6	216.2	3.5	202.7	31.4	217.4	2.6	NA
SFO-20-IC-2	267	94236	1.8	19.5342	1.9	0.2169	6.2	0.0307	5.9	0.95	195.1	11.4	199.3	11.3	249.5	44.1	195.1	11.4	NA
SFO-20-IC-2	327	21801	1.3	19.8517	1.7	0.2311	1.8	0.0333	0.7	0.38	211.0	1.4	211.1	3.4	212.2	38.4	211.0	1.4	NA
SFO-20-IC-2	149	4722	186.7	21.0504	1.7	0.0889	2.3	0.0136	1.5	0.66	86.9	1.3	86.5	1.9	74.7	40.6	86.9	1.3	NA
SFO-20-IC-2	163	10757	5.8	19.5723	4.1	0.1976	6.5	0.0281	5.1	0.78	178.4	9.0	183.1	11.0	245.0	94.0	178.4	9.0	NA
SFO-20-IC-2	64	7729	2.4	19.8744	6.6	0.2262	7.3	0.0326	3.1	0.42	206.8	6.3	207.0	13.7	209.6	153.4	206.8	6.3	NA

				Isotope ratios							Apparent ages (Ma)								
Sample SFO-56	U (ppm)	206Pb 204Pb	U/Th	206Pb* 207Pb*	± (%)	207Pb* 235U*	± (%)	206Pb* 238U	± (%)	error corr.	206Pb* 238U*	± (Ma)	207Pb* 235U	± (Ma)	206Pb* 207Pb*	± (Ma)	Best age (Ma)	± (Ma)	Conc (%)
SFO-56-1	97	7323	1.0	20.5805	22.8	0.2671	22.9	0.0399	2.4	0.11	252.0	6.0	240.3	49.1	128.1	542.2	252.0	6.0	NA
SFO-56-2	102	9304	1.0	18.7175	19.8	0.2751	20.1	0.0373	3.9	0.19	236.4	9.0	246.8	44.1	346.9	450.6	236.4	9.0	NA
SFO-56-3	91	3776	0.9	21.3702	26.5	0.2468	27.1	0.0383	5.8	0.21	242.0	13.8	224.0	54.6	38.7	643.4	242.0	13.8	NA
SFO-56-5	126	8601	1.3	19.7476	12.3	0.2734	12.5	0.0392	2.1	0.17	247.6	5.2	245.4	27.2	224.4	285.6	247.6	5.2	NA
SFO-56-6	110	6855	1.0	18.4746	7.7	0.2907	8.2	0.0389	2.9	0.35	246.3	6.9	259.1	18.7	376.4	172.4	246.3	6.9	NA

SFO-56-7	57	2777	1.3	20.7295	19.6	0.2387	20.0	0.0359	3.7	0.18	227.3	8.3	217.4	39.1	111.0	467.5	227.3	8.3	NA
SFO-56-8	296	13326	2.7	19.9242	4.0	0.2524	4.5	0.0365	2.0	0.45	230.9	4.6	228.5	9.2	203.8	92.9	230.9	4.6	NA
SFO-56-9	78	7109	1.3	20.2569	25.0	0.2560	25.3	0.0376	3.7	0.15	238.0	8.7	231.5	52.4	165.2	592.9	238.0	8.7	NA
SFO-56-10	61	9581	1.4	22.8790	18.2	0.2222	18.8	0.0369	4.5	0.24	233.4	10.4	203.7	34.7	-127.1	453.2	233.4	10.4	NA
SFO-56-11	82	5787	1.2	20.7426	17.3	0.2628	17.6	0.0395	3.2	0.18	250.0	7.9	237.0	37.2	109.6	411.5	250.0	7.9	NA
SFO-56-12	127	8751	1.4	20.2196	7.3	0.2711	7.7	0.0398	2.4	0.31	251.4	5.9	243.6	16.6	169.5	169.9	251.4	5.9	NA
SFO-56-13	134	20258	1.4	13.4922	5.1	0.7771	10.5	0.0760	9.2	0.88	472.5	41.9	583.8	46.6	1044.6	102.1	472.5	41.9	45.2
SFO-56-14	52	4191	1.2	24.8176	39.7	0.2159	40.5	0.0389	8.1	0.20	245.8	19.5	198.5	73.1	-332.1	1055.6	245.8	19.5	NA
SFO-56-15	296	21363	3.6	19.9066	5.4	0.2730	5.8	0.0394	1.9	0.33	249.2	4.7	245.1	12.6	205.9	126.3	249.2	4.7	NA
SFO-56-16	135	10679	1.3	18.3506	10.1	0.2936	10.6	0.0391	3.3	0.32	247.1	8.1	261.4	24.5	391.5	226.4	247.1	8.1	NA
SFO-56-17	78	4731	1.1	23.9217	25.4	0.1961	25.9	0.0340	4.9	0.19	215.7	10.5	181.8	43.1	-238.4	650.0	215.7	10.5	NA
SFO-56-18	75	3042	1.0	23.9614	22.9	0.2085	23.2	0.0362	3.9	0.17	229.4	8.8	192.3	40.6	-242.6	583.7	229.4	8.8	NA
SFO-56-19	126	10617	1.3	20.3229	10.0	0.2634	10.4	0.0388	2.7	0.26	245.6	6.5	237.4	22.0	157.6	235.3	245.6	6.5	NA
SFO-56-20	85	5263	1.4	21.8579	19.6	0.2382	20.0	0.0378	3.9	0.20	238.9	9.2	216.9	39.0	-15.5	477.0	238.9	9.2	NA
SFO-56-21	107	12036	1.3	19.2776	15.0	0.2752	15.3	0.0385	2.9	0.19	243.3	7.0	246.8	33.4	279.9	344.4	243.3	7.0	NA
SFO-56-22	104	8069	1.4	18.0606	13.3	0.2661	13.5	0.0349	2.3	0.17	220.9	5.0	239.6	28.9	427.1	298.7	220.9	5.0	NA
SFO-56-23	303	108232	2.1	17.1397	1.2	0.5367	2.2	0.0667	1.8	0.84	416.4	7.4	436.3	7.8	542.7	26.3	416.4	7.4	76.7
SFO-56-24	69	2866	1.2	20.0294	23.6	0.2638	23.9	0.0383	3.6	0.15	242.5	8.6	237.8	50.7	191.6	556.6	242.5	8.6	NA
SFO-56-25	101	11165	1.0	21.3129	26.8	0.2473	27.2	0.0382	5.0	0.18	241.8	11.8	224.3	54.8	45.1	649.5	241.8	11.8	NA
SFO-56-26	72	5059	1.1	17.1057	16.8	0.2763	18.4	0.0343	7.4	0.40	217.3	15.8	247.7	40.4	547.0	369.5	217.3	15.8	NA
SFO-56-27	84	5302	1.8	17.7274	12.5	0.2841	12.8	0.0365	2.8	0.22	231.3	6.4	253.9	28.8	468.5	278.0	231.3	6.4	NA
SFO-56-28	85	5294	1.5	20.6115	23.4	0.2455	23.9	0.0367	4.8	0.20	232.3	10.9	222.9	47.8	124.5	557.7	232.3	10.9	NA
SFO-56-29	85	9138	0.9	20.8656	34.2	0.2420	34.6	0.0366	5.1	0.15	231.9	11.5	220.1	68.5	95.6	831.3	231.9	11.5	NA
SFO-56-30	74	4559	1.4	19.9303	14.9	0.2721	15.1	0.0393	2.3	0.15	248.7	5.6	244.3	32.7	203.1	347.1	248.7	5.6	NA
SFO-56-31	120	6857	1.3	20.3957	8.3	0.2626	8.6	0.0389	2.3	0.27	245.7	5.6	236.8	18.1	149.3	193.7	245.7	5.6	NA

				Isotope ratios							Apparent ages (Ma)								
Sample	U	206Pb	U/Th	206Pb*	±	207Pb*	±	206Pb*	±	error	206Pb*	±	207Pb*	±	206Pb*	±	Best age	±	Conc
SFO-62	(ppm)	204Pb		207Pb*	(%)	235U*	(%)	238U	(%)	corr.	238U*	(Ma)	235U	(Ma)	207Pb*	(Ma)	(Ma)	(Ma)	(%)
SFO-62-1	164	6967	1.4	19.8195	11.8	0.1729	12.9	0.0249	5.2	0.40	158.3	8.1	161.9	19.3	216.0	274.3	158.3	8.1	NA
SFO-62-2	325	12070	0.7	19.9212	8.3	0.1857	11.8	0.0268	8.4	0.71	170.7	14.2	173.0	18.8	204.1	191.9	170.7	14.2	NA
SFO-62-3	243	35726	1.3	19.8946	3.5	0.2615	7.9	0.0377	7.1	0.90	238.8	16.6	235.9	16.6	207.2	81.3	238.8	16.6	NA
SFO-62-4	233	13085	1.0	19.2433	7.5	0.1831	7.8	0.0256	2.4	0.30	162.7	3.8	170.7	12.3	283.9	171.2	162.7	3.8	NA
SFO-62-5	297	12176	4.9	23.5945	17.7	0.0967	18.3	0.0165	4.9	0.26	105.8	5.1	93.7	16.4	-203.7	446.1	105.8	5.1	NA
SFO-62-6	209	15088	1.1	20.5129	9.4	0.1823	10.1	0.0271	3.7	0.36	172.5	6.2	170.1	15.8	135.8	221.7	172.5	6.2	NA
SFO-62-7	556	31712	1.3	20.0171	5.3	0.1746	6.2	0.0253	3.2	0.52	161.4	5.2	163.4	9.4	193.0	123.5	161.4	5.2	NA

SFO-62-8	265	4074	1.5	16.7540	20.3	0.2005	21.9	0.0244	8.3	0.38	155.2	12.7	185.6	37.2	592.3	443.7	155.2	12.7	NA
SFO-62-9	215	9490	1.0	16.7708	5.3	0.5691	5.7	0.0692	1.9	0.33	431.4	7.9	457.4	20.8	590.1	115.6	431.4	7.9	73.1
SFO-62-10	92	19045	1.5	21.3649	41.1	0.1781	41.4	0.0276	5.6	0.13	175.5	9.7	166.4	63.7	39.3	1020.7	175.5	9.7	NA
SFO-62-11	214	12740	1.3	21.9005	14.9	0.1643	15.3	0.0261	3.5	0.23	166.1	5.7	154.4	21.9	-20.2	362.2	166.1	5.7	NA
SFO-62-12	608	21807	0.9	20.2661	3.3	0.1754	3.6	0.0258	1.5	0.42	164.1	2.5	164.1	5.5	164.2	76.7	164.1	2.5	NA
SFO-62-13	146	8507	1.1	22.2715	8.7	0.1550	9.5	0.0250	3.9	0.41	159.4	6.1	146.3	13.0	-61.0	211.8	159.4	6.1	NA
SFO-62-14	377	76907	1.4	17.6385	1.3	0.5643	4.9	0.0722	4.7	0.97	449.3	20.6	454.3	18.0	479.6	28.2	449.3	20.6	93.7
SFO-62-15	333	33548	1.7	19.6016	4.8	0.1762	5.3	0.0250	2.3	0.43	159.5	3.6	164.8	8.1	241.6	110.5	159.5	3.6	NA
SFO-62-16	241	37349	3.5	19.3138	3.5	0.2914	5.9	0.0408	4.7	0.80	257.9	12.0	259.7	13.6	275.5	81.0	257.9	12.0	NA
SFO-62-17	236	12560	2.7	20.9442	9.3	0.1526	10.2	0.0232	4.1	0.41	147.7	6.0	144.2	13.7	86.7	221.0	147.7	6.0	NA
SFO-62-18	669	62917	1.1	20.2776	2.9	0.1765	3.9	0.0260	2.7	0.69	165.2	4.4	165.0	6.0	162.8	66.8	165.2	4.4	NA
SFO-62-19	140	10022	1.6	21.9740	14.5	0.1668	14.7	0.0266	2.6	0.18	169.1	4.4	156.6	21.4	-28.3	353.1	169.1	4.4	NA
SFO-62-20	323	71850	1.2	20.3345	6.4	0.1748	7.4	0.0258	3.7	0.50	164.1	5.9	163.6	11.1	156.3	149.9	164.1	5.9	NA
SFO-62-21	281	20197	1.6	20.4453	9.8	0.1758	10.0	0.0261	2.1	0.21	165.9	3.5	164.4	15.2	143.6	230.1	165.9	3.5	NA
SFO-62-22	347	26002	1.2	19.9675	5.1	0.1758	6.0	0.0255	3.1	0.52	162.0	5.0	164.4	9.1	198.8	118.1	162.0	5.0	NA
SFO-62-23	279	22151	1.1	19.3726	9.5	0.1794	10.2	0.0252	3.6	0.35	160.4	5.7	167.5	15.7	268.6	218.5	160.4	5.7	NA
SFO-62-24	606	40447	2.0	20.6686	5.9	0.1363	6.9	0.0204	3.6	0.52	130.4	4.6	129.7	8.4	118.0	138.0	130.4	4.6	NA
SFO-62-25	266	15511	1.5	21.5054	6.3	0.1628	6.6	0.0254	2.0	0.30	161.7	3.2	153.2	9.4	23.6	151.5	161.7	3.2	NA
SFO-62-26	368	23185	0.7	20.4609	4.8	0.1699	5.2	0.0252	2.0	0.39	160.5	3.2	159.3	7.7	141.8	112.4	160.5	3.2	NA
SFO-62-27	156	7832	1.3	20.0732	17.9	0.1744	18.3	0.0254	4.1	0.22	161.6	6.5	163.2	27.7	186.5	419.4	161.6	6.5	NA

				Isotope ratios							Apparent ages (Ma)								
Sample	U	206Pb	U/Th	206Pb*	±	207Pb*	±	206Pb*	±	error	206Pb*	±	207Pb*	±	206Pb*	±	Best age	±	Conc
SFO-63	(ppm)	204Pb		207Pb*	(%)	235U*	(%)	238U	(%)	corr.	238U*	(Ma)	235U	(Ma)	207Pb*	(Ma)	(Ma)	(Ma)	(%)
SFO-63-1	217	18067	1.2	20.8936	4.1	0.1657	4.7	0.0251	2.4	0.50	159.8	3.7	155.7	6.8	92.5	97.5	159.8	3.7	NA
SFO-63-2	525	81145	0.7	20.1914	2.7	0.1746	3.7	0.0256	2.5	0.67	162.8	4.0	163.4	5.6	172.8	64.0	162.8	4.0	NA
SFO-63-3	340	53465	1.0	20.3982	3.8	0.1728	4.1	0.0256	1.6	0.38	162.7	2.5	161.8	6.1	149.0	88.6	162.7	2.5	NA
SFO-63-4	382	23243	0.9	20.6073	4.7	0.1712	5.1	0.0256	2.0	0.38	162.9	3.2	160.5	7.6	125.0	111.0	162.9	3.2	NA
SFO-63-5	151	26735	1.6	20.5249	4.4	0.1679	5.0	0.0250	2.2	0.45	159.1	3.5	157.6	7.3	134.4	104.3	159.1	3.5	NA
SFO-63-6	734	63614	0.5	20.1813	1.5	0.1745	1.8	0.0255	1.0	0.56	162.5	1.6	163.3	2.8	174.0	35.5	162.5	1.6	NA
SFO-63-7	175	27159	1.3	19.6214	4.1	0.1749	4.4	0.0249	1.6	0.36	158.5	2.5	163.7	6.7	239.3	94.9	158.5	2.5	NA
SFO-63-8	402	48992	0.8	20.4317	2.2	0.1709	2.7	0.0253	1.4	0.54	161.2	2.3	160.2	3.9	145.1	52.6	161.2	2.3	NA
SFO-63-9	328	18007	1.1	19.7886	4.4	0.1774	4.7	0.0255	1.7	0.35	162.0	2.7	165.8	7.2	219.7	101.9	162.0	2.7	NA
SFO-63-10	625	14493	1.0	20.3480	2.5	0.1665	3.0	0.0246	1.6	0.55	156.5	2.5	156.4	4.4	154.8	58.9	156.5	2.5	NA
SFO-63-11	475	21124	0.7	20.9014	3.9	0.1667	4.2	0.0253	1.4	0.34	160.9	2.3	156.6	6.1	91.5	93.3	160.9	2.3	NA
SFO-63-12	328	41528	1.0	20.1865	4.0	0.1752	5.6	0.0257	3.9	0.69	163.3	6.3	164.0	8.5	173.4	94.4	163.3	6.3	NA

SFO-63-14	539	52285	0.7	20.3793	1.8	0.1727	2.7	0.0255	2.0	0.74	162.4	3.3	161.7	4.1	151.1	43.0	162.4	3.3	NA
SFO-63-15	772	94303	0.5	20.1988	1.8	0.1746	2.1	0.0256	1.1	0.54	162.8	1.8	163.4	3.2	171.9	41.7	162.8	1.8	NA
SFO-63-16	542	46707	0.7	20.1934	2.4	0.1725	2.8	0.0253	1.6	0.55	160.9	2.5	161.6	4.3	172.6	55.7	160.9	2.5	NA
SFO-63-17	351	20282	1.2	20.4674	6.6	0.1741	7.0	0.0258	2.3	0.33	164.5	3.7	163.0	10.5	141.1	154.5	164.5	3.7	NA
SFO-63-18	557	16401	0.7	19.6754	5.5	0.1749	6.5	0.0250	3.5	0.54	159.0	5.5	163.7	9.8	232.9	125.9	159.0	5.5	NA
SFO-63-19	474	6973	0.9	20.0650	6.6	0.1605	7.1	0.0234	2.7	0.38	148.8	4.0	151.1	10.0	187.4	153.4	148.8	4.0	NA
SFO-63-20	481	43964	0.5	20.0508	3.1	0.1721	4.4	0.0250	3.0	0.69	159.3	4.7	161.2	6.5	189.1	73.3	159.3	4.7	NA
SFO-63-22	516	53361	0.6	20.2530	1.2	0.1709	1.8	0.0251	1.3	0.74	159.9	2.1	160.2	2.6	165.7	27.7	159.9	2.1	NA
SFO-63-23	499	39225	1.1	19.8966	1.8	0.1795	6.4	0.0259	6.1	0.96	164.9	10.0	167.7	9.9	207.0	41.5	164.9	10.0	NA
SFO-63-25	834	52666	0.5	20.1649	1.1	0.1753	2.7	0.0256	2.5	0.92	163.2	4.1	164.0	4.1	175.9	25.1	163.2	4.1	NA
SFO-63-26	506	19606	0.5	20.4286	1.4	0.1707	2.1	0.0253	1.5	0.73	161.0	2.4	160.0	3.1	145.5	33.1	161.0	2.4	NA
SFO-63-27	564	17003	0.9	19.8329	5.2	0.1712	5.5	0.0246	1.8	0.32	156.9	2.7	160.5	8.1	214.5	120.2	156.9	2.7	NA
SFO-63-28	439	47384	0.8	20.0955	3.5	0.1740	4.1	0.0254	2.0	0.50	161.4	3.3	162.9	6.2	183.9	82.6	161.4	3.3	NA
SFO-63-29	353	34760	1.1	20.5167	3.8	0.1722	4.4	0.0256	2.1	0.47	163.1	3.3	161.3	6.5	135.4	90.5	163.1	3.3	NA
SFO-63-31	890	62503	0.5	20.4784	1.6	0.1703	1.9	0.0253	1.1	0.59	161.0	1.8	159.7	2.9	139.8	36.9	161.0	1.8	NA
SFO-63-32	254	30697	1.2	19.6508	4.2	0.1781	4.6	0.0254	1.8	0.39	161.5	2.9	166.4	7.1	235.8	97.7	161.5	2.9	NA
SFO-63-33	218	26708	1.3	20.4456	8.7	0.1691	8.9	0.0251	1.9	0.21	159.7	2.9	158.6	13.0	143.5	203.6	159.7	2.9	NA
SFO-63-34	251	27954	1.4	19.9678	5.5	0.1738	5.7	0.0252	1.7	0.30	160.2	2.7	162.7	8.6	198.7	126.7	160.2	2.7	NA
SFO-63-35	479	31748	0.8	20.4614	2.2	0.1692	2.6	0.0251	1.3	0.49	159.9	2.0	158.7	3.8	141.7	52.7	159.9	2.0	NA
SFO-63-36	246	25802	1.0	20.2097	5.4	0.1740	5.7	0.0255	1.9	0.33	162.4	3.0	162.9	8.6	170.7	126.4	162.4	3.0	NA
SFO-63-37	513	39474	0.8	19.8971	3.2	0.1741	3.4	0.0251	1.1	0.33	159.9	1.8	162.9	5.1	207.0	73.8	159.9	1.8	NA
SFO-63-38	297	38685	1.1	20.2146	4.2	0.1705	4.4	0.0250	1.1	0.26	159.2	1.8	159.9	6.4	170.1	98.2	159.2	1.8	NA
SFO-63-39	395	44545	0.9	20.2102	1.4	0.1748	2.8	0.0256	2.5	0.87	163.1	4.0	163.6	4.3	170.6	32.4	163.1	4.0	NA
SFO-63-40	306	19814	0.7	20.4141	3.3	0.1741	4.4	0.0258	2.9	0.67	164.1	4.7	163.0	6.6	147.2	76.6	164.1	4.7	NA
SFO-63-41	646	14252	1.5	19.7448	4.6	0.1802	5.5	0.0258	3.0	0.54	164.2	4.9	168.2	8.5	224.8	106.8	164.2	4.9	NA
SFO-63-42	253	15827	1.2	20.0655	3.9	0.1723	4.1	0.0251	1.4	0.35	159.6	2.3	161.4	6.2	187.4	90.3	159.6	2.3	NA
SFO-63-43	396	21041	1.4	20.9662	5.2	0.1474	5.5	0.0224	1.7	0.31	142.9	2.4	139.6	7.2	84.2	124.5	142.9	2.4	NA
SFO-63-44	345	31822	0.9	19.7819	2.2	0.1720	3.0	0.0247	2.0	0.67	157.2	3.1	161.2	4.5	220.4	51.4	157.2	3.1	NA
SFO-63-45	386	16049	0.6	20.3702	4.4	0.1573	7.4	0.0232	6.0	0.80	148.1	8.7	148.3	10.2	152.2	104.1	148.1	8.7	NA
SFO-63-46	509	37673	2.2	19.9173	2.5	0.1743	2.8	0.0252	1.2	0.42	160.3	1.9	163.2	4.2	204.6	58.2	160.3	1.9	NA
SFO-63-47	121	7063	1.2	19.9159	9.7	0.1794	10.0	0.0259	2.3	0.23	164.9	3.7	167.5	15.4	204.8	226.5	164.9	3.7	NA
SFO-63-48	286	16411	5.9	20.2390	3.2	0.1692	3.8	0.0248	2.1	0.54	158.1	3.2	158.7	5.6	167.3	75.0	158.1	3.2	NA
SFO-63-49	391	21752	0.8	19.9806	4.0	0.1712	4.8	0.0248	2.7	0.56	158.0	4.2	160.5	7.1	197.3	92.8	158.0	4.2	NA
SFO-63-50	128	16301	1.2	21.7447	8.9	0.1622	9.3	0.0256	2.5	0.27	162.8	4.0	152.6	13.1	-3.0	215.6	162.8	4.0	NA
SFO-63-51	465	22803	1.6	20.5981	3.5	0.1531	4.1	0.0229	2.1	0.52	145.8	3.1	144.7	5.5	126.1	82.3	145.8	3.1	NA
SFO-63-52	743	32252	1.4	20.3844	1.5	0.1333	3.0	0.0197	2.7	0.87	125.8	3.3	127.1	3.6	150.5	34.8	125.8	3.3	NA
SFO-63-53	290	15809	1.1	20.1413	5.1	0.1630	5.3	0.0238	1.5	0.28	151.7	2.3	153.3	7.6	178.6	118.7	151.7	2.3	NA

SFO-63-54	601	76089	0.7	20.2677	1.9	0.1758	2.0	0.0258	0.7	0.35	164.4	1.1	164.4	3.0	164.0	43.5	164.4	1.1	NA
SFO-63-55	305	36003	0.9	20.5724	4.4	0.1765	4.5	0.0263	0.8	0.19	167.5	1.4	165.0	6.9	129.0	104.3	167.5	1.4	NA
SFO-63-56	468	42200	0.8	20.1391	2.6	0.1740	2.8	0.0254	1.1	0.37	161.8	1.7	162.9	4.3	178.8	61.5	161.8	1.7	NA
SFO-63-57	447	20905	0.9	20.2621	2.7	0.1755	3.2	0.0258	1.7	0.53	164.2	2.7	164.2	4.8	164.6	62.7	164.2	2.7	NA
SFO-63-58	696	18830	2.1	20.6712	3.7	0.1279	4.5	0.0192	2.5	0.57	122.5	3.1	122.2	5.1	117.7	86.5	122.5	3.1	NA
SFO-63-59	335	19466	1.0	20.1640	3.7	0.1680	4.0	0.0246	1.4	0.36	156.5	2.2	157.7	5.8	176.0	86.1	156.5	2.2	NA
SFO-63-60	673	97047	0.8	20.2624	2.1	0.1649	2.7	0.0242	1.7	0.63	154.4	2.6	155.0	3.9	164.6	48.9	154.4	2.6	NA

				Isotope ratios							Apparent ages (Ma)								
Sample SFO-121	U (ppm)	206Pb 204Pb	U/Th	206Pb* 207Pb*	± (%)	207Pb* 235U*	± (%)	206Pb* 238U	± (%)	error corr.	206Pb* 238U*	± (Ma)	207Pb* 235U	± (Ma)	206Pb* 207Pb*	± (Ma)	Best age (Ma)	± (Ma)	Conc (%)
SFO-121-1	162	15189	1.4	19.2146	10.4	0.1778	10.8	0.0248	3.0	0.28	157.8	4.7	166.2	16.6	287.4	238.7	157.8	4.7	NA
SFO-121-2	500	239347	1.4	17.9120	0.8	0.5845	9.2	0.0759	9.1	1.00	471.8	41.6	467.4	34.4	445.5	17.3	471.8	41.6	105.9
SFO-121-3	443	166852	1.1	20.5310	3.6	0.1718	3.9	0.0256	1.5	0.38	162.8	2.4	161.0	5.8	133.7	85.2	162.8	2.4	NA
SFO-121-4	58	35920	3.3	17.9292	17.6	0.1802	17.9	0.0234	3.0	0.17	149.3	4.5	168.3	27.7	443.4	394.4	149.3	4.5	NA
SFO-121-5	897	202619	0.8	20.3996	2.0	0.1736	2.2	0.0257	0.9	0.41	163.5	1.5	162.5	3.4	148.8	48.0	163.5	1.5	NA
SFO-121-6	307	189624	2.3	17.7574	1.6	0.5682	2.1	0.0732	1.3	0.61	455.3	5.6	456.9	7.7	464.8	36.5	455.3	5.6	98.0
SFO-121-7	132	37956	1.9	19.8465	10.5	0.1703	10.7	0.0245	2.1	0.19	156.1	3.2	159.7	15.7	212.8	242.8	156.1	3.2	NA
SFO-121-8	944	186238	1.4	20.2956	2.1	0.1697	4.6	0.0250	4.0	0.88	159.0	6.3	159.1	6.7	160.8	50.1	159.0	6.3	NA
SFO-121-9	177	68962	1.3	19.2335	8.5	0.1828	8.8	0.0255	2.0	0.23	162.3	3.2	170.4	13.8	285.1	195.7	162.3	3.2	NA
SFO-121-10	394	241510	0.4	18.8478	1.9	0.3099	4.8	0.0424	4.4	0.92	267.4	11.6	274.1	11.6	331.2	43.6	267.4	11.6	NA
SFO-121-11	193	38001	1.3	22.1006	15.6	0.1550	16.3	0.0248	4.5	0.27	158.2	7.0	146.3	22.1	-42.3	381.7	158.2	7.0	NA
SFO-121-12	206	32677	1.1	20.6503	6.9	0.1676	6.9	0.0251	0.9	0.13	159.8	1.4	157.3	10.1	120.1	162.1	159.8	1.4	NA
SFO-121-13	177	72294	2.0	17.0787	5.2	0.5632	8.3	0.0698	6.5	0.78	434.7	27.2	453.6	30.2	550.5	112.6	434.7	27.2	79.0
SFO-121-14	212	95966	1.1	19.8978	11.4	0.1737	12.2	0.0251	4.5	0.37	159.6	7.1	162.6	18.4	206.9	264.1	159.6	7.1	NA
SFO-121-15	160	61047	1.2	19.1252	3.4	0.3695	3.6	0.0512	1.1	0.31	322.2	3.5	319.3	9.9	298.0	78.2	322.2	3.5	NA
SFO-121-16	179	224360	1.0	17.9766	2.9	0.4516	3.3	0.0589	1.6	0.47	368.8	5.6	378.4	10.4	437.5	64.6	368.8	5.6	NA
SFO-121-17	1885	246825	0.6	20.3287	0.9	0.1258	8.7	0.0185	8.6	0.99	118.5	10.1	120.3	9.8	156.9	22.1	118.5	10.1	NA
SFO-121-18	174	75746	1.8	20.5474	7.5	0.1746	7.7	0.0260	1.7	0.22	165.6	2.8	163.4	11.6	131.9	175.7	165.6	2.8	NA
SFO-121-19	142	75537	1.3	19.2113	11.5	0.1849	11.6	0.0258	1.6	0.13	164.0	2.5	172.3	18.4	287.7	263.6	164.0	2.5	NA
SFO-121-20	96	64075	2.1	17.5460	4.6	0.5732	5.0	0.0729	1.8	0.36	453.9	7.9	460.1	18.4	491.2	102.6	453.9	7.9	92.4
SFO-121-21	162	110950	1.3	20.0962	7.5	0.1754	7.8	0.0256	2.3	0.30	162.7	3.7	164.1	11.9	183.8	174.5	162.7	3.7	NA
SFO-121-22	274	86418	0.9	20.4182	3.4	0.1754	3.7	0.0260	1.4	0.38	165.3	2.3	164.1	5.6	146.7	79.9	165.3	2.3	NA
SFO-121-23	954	120337	1.1	20.0377	1.9	0.1662	3.2	0.0241	2.6	0.80	153.8	3.9	156.1	4.6	190.6	44.8	153.8	3.9	NA
SFO-121-24	122	86716	0.8	19.1038	6.3	0.3969	6.6	0.0550	2.0	0.30	345.1	6.6	339.4	19.1	300.6	144.3	345.1	6.6	NA

SFO-121-25	145	44070	0.9	19.2697	7.8	0.1867	11.7	0.0261	8.8	0.75	166.0	14.4	173.8	18.8	280.8	178.7	166.0	14.4	NA
SFO-121-26	226	94035	0.9	20.2465	2.7	0.1753	3.1	0.0257	1.5	0.47	163.8	2.4	164.0	4.7	166.4	63.4	163.8	2.4	NA
SFO-121-28	385	117987	1.5	20.2125	4.2	0.1554	4.6	0.0228	2.0	0.44	145.2	2.9	146.6	6.3	170.4	97.5	145.2	2.9	NA
SFO-121-29	407	159825	2.7	20.2871	2.1	0.1659	2.4	0.0244	1.1	0.46	155.5	1.7	155.9	3.5	161.8	49.6	155.5	1.7	NA
SFO-121-30	180	41484	1.6	19.7373	5.4	0.1703	5.7	0.0244	1.8	0.31	155.3	2.7	159.7	8.4	225.7	125.6	155.3	2.7	NA
SFO-121-31	125	30542	1.7	19.9747	9.3	0.1758	9.8	0.0255	3.0	0.31	162.1	4.9	164.5	14.8	197.9	216.0	162.1	4.9	NA
SFO-121-32	181	65560	1.2	20.6962	13.2	0.1522	13.7	0.0228	3.9	0.28	145.6	5.6	143.8	18.4	114.9	311.8	145.6	5.6	NA
SFO-121-33	405	98007	2.0	20.3197	5.7	0.1723	6.2	0.0254	2.4	0.39	161.7	3.9	161.4	9.3	158.0	133.9	161.7	3.9	NA
SFO-121-34	323	96366	1.0	20.5061	2.6	0.1708	2.8	0.0254	1.1	0.40	161.7	1.8	160.1	4.2	136.6	61.2	161.7	1.8	NA
SFO-121-35	132	18845	1.8	20.2462	10.0	0.1847	11.0	0.0271	4.5	0.41	172.5	7.6	172.1	17.4	166.5	235.0	172.5	7.6	NA
SFO-121-36	204	106018	2.1	19.1979	7.2	0.1929	8.0	0.0269	3.4	0.42	170.9	5.7	179.1	13.1	289.3	165.4	170.9	5.7	NA
SFO-121-37	495	421321	1.1	17.8266	1.1	0.5364	4.5	0.0694	4.4	0.97	432.3	18.5	436.1	16.1	456.2	23.8	432.3	18.5	94.8
SFO-121-38	192	32139	1.5	18.9767	5.6	0.1806	6.3	0.0249	3.0	0.47	158.3	4.6	168.6	9.8	315.7	126.4	158.3	4.6	NA
SFO-121-39	484	133056	1.4	20.3674	3.2	0.1671	3.6	0.0247	1.5	0.41	157.2	2.3	156.9	5.2	152.5	75.9	157.2	2.3	NA
SFO-121-40	181	41378	1.0	20.4171	8.4	0.1693	8.4	0.0251	1.0	0.12	159.6	1.6	158.8	12.4	146.8	196.5	159.6	1.6	NA
SFO-121-41	158	47870	1.3	19.4680	11.3	0.1692	11.6	0.0239	2.8	0.24	152.2	4.2	158.7	17.0	257.3	259.5	152.2	4.2	NA
SFO-121-42	302	102278	1.4	20.5556	3.3	0.1408	6.6	0.0210	5.7	0.86	133.9	7.5	133.8	8.2	130.9	78.5	133.9	7.5	NA
SFO-121-43	531	104233	1.0	19.2495	8.1	0.1748	8.2	0.0244	1.1	0.14	155.5	1.7	163.6	12.3	283.2	185.3	155.5	1.7	NA
SFO-121-44	862	455724	0.8	20.0382	3.4	0.1727	3.5	0.0251	0.6	0.18	159.8	1.0	161.8	5.2	190.6	79.6	159.8	1.0	NA
SFO-121-45	207	239704	1.3	20.0429	5.2	0.1823	5.3	0.0265	1.2	0.23	168.6	2.0	170.0	8.3	190.0	120.7	168.6	2.0	NA
SFO-121-47	159	73786	4.2	20.1062	13.0	0.1408	13.7	0.0205	4.4	0.32	131.0	5.7	133.8	17.2	182.7	303.9	131.0	5.7	NA
SFO-121-48	441	120800	0.8	19.8807	4.5	0.1781	4.8	0.0257	1.7	0.35	163.4	2.7	166.4	7.4	208.9	105.0	163.4	2.7	NA
SFO-121-50	589	212689	1.3	19.7599	2.4	0.1747	2.5	0.0250	0.5	0.22	159.5	0.8	163.5	3.8	223.0	56.1	159.5	0.8	NA
SFO-121-51	181	87431	7.0	19.0047	9.8	0.1307	10.5	0.0180	3.9	0.37	115.1	4.4	124.7	12.4	312.4	223.3	115.1	4.4	NA
SFO-121-52	253	201477	0.9	20.0649	2.4	0.1760	2.7	0.0256	1.3	0.47	163.0	2.1	164.6	4.2	187.4	56.2	163.0	2.1	NA
SFO-121-53	160	148960	1.2	18.6839	4.4	0.3853	4.8	0.0522	1.8	0.38	328.1	5.8	331.0	13.6	351.0	100.4	328.1	5.8	NA
SFO-121-54	101	131117	1.0	18.4743	5.5	0.3823	6.3	0.0512	3.1	0.49	322.1	9.8	328.7	17.8	376.4	124.1	322.1	9.8	NA
SFO-121-55	200	107756	0.9	20.1216	6.4	0.1823	7.0	0.0266	2.7	0.39	169.3	4.5	170.1	10.9	180.9	150.1	169.3	4.5	NA
SFO-121-57	230	79488	1.6	20.1056	4.1	0.1623	5.0	0.0237	2.9	0.57	150.8	4.3	152.7	7.1	182.7	95.2	150.8	4.3	NA
SFO-121-58	483	321701	1.0	17.9075	0.9	0.5554	1.8	0.0721	1.6	0.87	449.0	6.9	448.5	6.6	446.1	20.3	449.0	6.9	100.7

				Isotope ratios							Apparent ages (Ma)								
Sample SFO-136	U (ppm)	206Pb 204Pb	U/Th	206Pb* 207Pb*	± (%)	207Pb* 235U*	± (%)	206Pb* 238U	± (%)	error corr.	206Pb* 238U*	± (Ma)	207Pb* 235U	± (Ma)	206Pb* 207Pb*	± (Ma)	Best age (Ma)	± (Ma)	Conc (%)
SFO-136-1	70	2488	1.5	28.7360	34.6	0.0724	34.9	0.0151	4.8	0.14	96.5	4.6	71.0	23.9	-724.6	988.7	96.5	4.6	NA
SFO-136-2	71	2824	1.9	40.2044	62.7	0.0533	63.4	0.0155	9.4	0.15	99.4	9.3	52.7	32.6	NA	NA	99.4	9.3	NA

SFO-136-3	163	11617	0.9	20.2912	11.5	0.1076	11.6	0.0158	1.7	0.15	101.3	1.7	103.8	11.4	161.3	268.6	101.3	1.7	NA
SFO-136-4	121	7693	1.2	28.2550	28.0	0.0758	28.3	0.0155	4.3	0.15	99.4	4.2	74.2	20.3	-677.7	785.9	99.4	4.2	NA
SFO-136-5	50	2900	1.6	19.7039	41.3	0.1102	42.6	0.0157	10.6	0.25	100.7	10.6	106.1	43.0	229.5	992.1	100.7	10.6	NA
SFO-136-6	112	5563	1.4	20.7113	20.3	0.1049	20.6	0.0158	3.2	0.16	100.8	3.2	101.3	19.9	113.2	484.3	100.8	3.2	NA
SFO-136-7	61	2386	1.6	23.1838	42.1	0.0949	42.6	0.0160	6.3	0.15	102.0	6.4	92.0	37.5	-159.9	1090.3	102.0	6.4	NA
SFO-136-8	109	9413	1.1	24.3802	17.4	0.0902	17.8	0.0159	3.7	0.21	102.0	3.8	87.7	14.9	-286.5	445.1	102.0	3.8	NA
SFO-136-9	109	7319	1.1	19.6749	25.0	0.1083	25.3	0.0155	3.7	0.14	98.9	3.6	104.4	25.1	232.9	585.5	98.9	3.6	NA
SFO-136-10	169	2250	1.2	18.6435	15.3	0.1127	15.9	0.0152	4.2	0.26	97.5	4.1	108.4	16.3	355.9	347.8	97.5	4.1	NA
SFO-136-11	128	6759	1.0	21.7870	12.8	0.0985	13.2	0.0156	3.2	0.25	99.6	3.2	95.4	12.1	-7.7	310.8	99.6	3.2	NA
SFO-136-12	48	3262	1.2	11.5940	156.2	0.1812	156.4	0.0152	7.7	0.05	97.5	7.4	169.1	248.4	1343.8	409.0	97.5	7.4	NA
SFO-136-13	88	4892	1.0	24.3261	45.8	0.0861	46.0	0.0152	4.9	0.11	97.2	4.7	83.8	37.0	-280.9	1221.4	97.2	4.7	NA
SFO-136-14	90	2594	0.9	22.1923	31.3	0.0973	31.9	0.0157	5.9	0.19	100.2	5.9	94.3	28.7	-52.4	779.3	100.2	5.9	NA
SFO-136-15	244	24664	1.2	22.1904	12.7	0.0975	13.3	0.0157	3.9	0.29	100.4	3.9	94.5	12.0	-52.1	310.1	100.4	3.9	NA
SFO-136-16	72	5758	1.2	22.5009	35.5	0.0947	35.8	0.0155	5.1	0.14	98.9	5.0	91.9	31.5	-86.1	893.4	98.9	5.0	NA
SFO-136-17	73	6075	1.2	17.3662	18.3	0.1238	18.9	0.0156	4.6	0.24	99.8	4.5	118.5	21.1	513.9	405.5	99.8	4.5	NA
SFO-136-18	133	21365	1.4	20.5355	18.8	0.1031	19.0	0.0154	2.0	0.11	98.3	2.0	99.7	18.0	133.2	446.5	98.3	2.0	NA
SFO-136-19	112	3518	1.6	16.3302	24.5	0.1312	25.4	0.0155	6.8	0.27	99.4	6.7	125.2	30.0	647.6	533.8	99.4	6.7	NA
SFO-136-20	121	4669	1.0	22.4483	11.1	0.0963	11.9	0.0157	4.4	0.37	100.2	4.4	93.3	10.6	-80.4	272.2	100.2	4.4	NA
SFO-136-21	109	4142	1.2	29.0691	23.7	0.0734	23.8	0.0155	2.8	0.12	99.0	2.7	71.9	16.6	-756.9	673.3	99.0	2.7	NA
SFO-136-22	153	18912	1.4	20.8171	12.2	0.1029	12.8	0.0155	3.8	0.29	99.4	3.7	99.4	12.1	101.1	290.4	99.4	3.7	NA
SFO-136-23	158	5257	1.4	21.0777	13.5	0.1026	13.8	0.0157	2.7	0.20	100.3	2.7	99.2	13.0	71.6	322.1	100.3	2.7	NA
SFO-136-24	54	1604	1.3	23.9555	30.3	0.0889	31.0	0.0154	6.2	0.20	98.8	6.1	86.4	25.7	-241.9	781.3	98.8	6.1	NA
SFO-136-25	89	5119	0.9	18.7405	20.6	0.1129	21.1	0.0153	4.6	0.22	98.2	4.5	108.6	21.8	344.1	471.0	98.2	4.5	NA
SFO-136-26	74	4806	1.1	33.1073	43.0	0.0653	43.2	0.0157	4.2	0.10	100.2	4.1	64.2	26.9	NA	NA	100.2	4.1	NA
SFO-136-27	80	3311	1.2	41.9655	51.4	0.0515	51.7	0.0157	5.6	0.11	100.3	5.6	51.0	25.7	NA	NA	100.3	5.6	NA
SFO-136-28	151	8854	0.9	21.6178	11.3	0.0987	11.6	0.0155	2.2	0.19	99.0	2.2	95.6	10.5	11.1	273.6	99.0	2.2	NA
SFO-136-29	110	7064	1.3	20.5677	23.6	0.1066	23.8	0.0159	2.9	0.12	101.7	3.0	102.8	23.3	129.6	563.0	101.7	3.0	NA
SFO-136-30	98	6360	1.8	25.8117	26.5	0.0857	26.8	0.0161	3.7	0.14	102.6	3.8	83.5	21.5	-434.1	707.1	102.6	3.8	NA
SFO-136-31	65	3741	1.0	21.8034	30.6	0.0966	31.7	0.0153	8.2	0.26	97.7	8.0	93.6	28.3	-9.5	753.6	97.7	8.0	NA
SFO-136-32	77	3611	1.1	30.7066	56.7	0.0705	56.8	0.0157	3.9	0.07	100.5	3.8	69.2	38.0	-913.6	1772.8	100.5	3.8	NA
SFO-136-33	104	7905	1.2	20.9673	16.0	0.1036	16.2	0.0157	2.9	0.18	100.7	2.9	100.0	15.5	84.1	381.4	100.7	2.9	NA
SFO-136-34	155	7564	0.8	23.4204	23.6	0.0912	23.7	0.0155	2.1	0.09	99.1	2.1	88.6	20.1	-185.2	597.8	99.1	2.1	NA
SFO-136-35	42	4233	2.4	13.1892	112.9	0.1641	113.2	0.0157	8.4	0.07	100.4	8.3	154.3	163.5	1090.3	330.5	100.4	8.3	NA
SFO-136-36	71	6722	1.7	18.7947	25.4	0.1160	25.7	0.0158	3.8	0.15	101.2	3.8	111.5	27.1	337.6	584.2	101.2	3.8	NA
SFO-136-37	135	12394	0.9	22.7020	15.2	0.0936	16.2	0.0154	5.6	0.35	98.6	5.5	90.9	14.1	-107.9	375.8	98.6	5.5	NA
SFO-136-38	91	5064	1.4	23.5928	41.8	0.0924	41.9	0.0158	2.8	0.07	101.1	2.8	89.7	36.0	-203.5	1090.2	101.1	2.8	NA
SFO-136-39	65	1708	1.7	24.3420	37.5	0.0900	37.8	0.0159	4.9	0.13	101.6	5.0	87.5	31.7	-282.5	984.4	101.6	5.0	NA

SFO-136-40	101	17136	1.7	23.3727	23.3	0.0918	23.5	0.0156	2.9	0.12	99.6	2.9	89.2	20.0	-180.1	587.5	99.6	2.9	NA

				Isotope ratios							Apparent ages (Ma)								
Sample SFO-138	U (ppm)	206Pb 204Pb	U/Th	206Pb* 207Pb*	± (%)	207Pb* 235U*	± (%)	206Pb* 238U	± (%)	error corr.	206Pb* 238U*	± (Ma)	207Pb* 235U	± (Ma)	206Pb* 207Pb*	± (Ma)	Best age (Ma)	± (Ma)	Conc (%)
SFO-138-1	100	47193	1.0	20.8381	21.6	0.1024	21.7	0.0155	2.5	0.11	99.0	2.4	99.0	20.5	98.7	515.5	99.0	2.4	NA
SFO-138-2	197	18018	0.7	22.2341	6.7	0.0945	7.0	0.0152	2.1	0.30	97.5	2.0	91.7	6.1	-56.9	162.8	97.5	2.0	NA
SFO-138-3	132	31007	0.8	18.1304	22.9	0.1133	23.7	0.0149	6.1	0.26	95.3	5.8	109.0	24.5	418.5	518.2	95.3	5.8	NA
SFO-138-4	61	8924	1.1	19.7429	33.2	0.1056	34.0	0.0151	7.4	0.22	96.8	7.1	101.9	33.0	225.0	786.9	96.8	7.1	NA
SFO-138-5	75	6409	1.1	27.9193	77.4	0.0737	77.7	0.0149	6.8	0.09	95.5	6.5	72.2	54.2	-644.8	2515.4	95.5	6.5	NA
SFO-138-6	70	8633	1.5	21.0197	34.6	0.1025	35.2	0.0156	6.6	0.19	100.0	6.6	99.1	33.2	78.1	843.1	100.0	6.6	NA
SFO-138-7	74	19842	1.0	21.8117	44.7	0.0971	45.0	0.0154	5.1	0.11	98.3	5.0	94.1	40.5	-10.4	1131.3	98.3	5.0	NA
SFO-138-8	99	10959	0.8	19.5912	39.1	0.1073	39.5	0.0152	5.4	0.14	97.5	5.3	103.5	38.9	242.8	934.0	97.5	5.3	NA
SFO-138-9	91	22384	0.9	24.6250	44.2	0.0873	44.6	0.0156	5.9	0.13	99.7	5.9	84.9	36.3	-312.1	1182.3	99.7	5.9	NA
SFO-138-10	91	12117	2.6	21.6973	36.7	0.0806	37.2	0.0127	6.2	0.17	81.2	5.0	78.7	28.2	2.3	911.0	81.2	5.0	NA
SFO-138-11	90	18394	1.0	20.1382	25.2	0.1072	25.8	0.0157	5.3	0.21	100.1	5.3	103.4	25.3	178.9	596.2	100.1	5.3	NA
SFO-138-12	78	9574	1.0	19.8093	23.2	0.1105	23.8	0.0159	5.3	0.22	101.6	5.4	106.5	24.0	217.2	542.9	101.6	5.4	NA
SFO-138-13	87	12753	0.9	21.2157	18.8	0.1011	19.2	0.0156	3.5	0.18	99.5	3.4	97.8	17.9	56.1	452.9	99.5	3.4	NA
SFO-138-14	70	11139	1.5	20.0667	23.9	0.1078	25.3	0.0157	8.5	0.34	100.4	8.5	104.0	25.0	187.2	562.3	100.4	8.5	NA
SFO-138-15	95	13987	0.9	22.3485	25.2	0.0964	25.7	0.0156	5.0	0.19	99.9	4.9	93.4	23.0	-69.5	625.0	99.9	4.9	NA
SFO-138-16	90	15258	0.9	23.2202	22.0	0.0920	22.8	0.0155	6.0	0.27	99.1	5.9	89.4	19.5	-163.8	552.2	99.1	5.9	NA
SFO-138-17	120	15323	0.8	26.7032	36.8	0.0806	37.0	0.0156	3.7	0.10	99.8	3.7	78.7	28.0	-524.1	1013.6	99.8	3.7	NA
SFO-138-18	84	29652	1.1	24.5654	29.7	0.0892	30.6	0.0159	7.5	0.25	101.6	7.6	86.7	25.5	-305.9	774.0	101.6	7.6	NA
SFO-138-19	78	13818	0.9	17.7304	28.3	0.1198	28.5	0.0154	3.5	0.12	98.5	3.4	114.9	31.0	468.2	638.1	98.5	3.4	NA
SFO-138-20	84	10959	0.9	19.4385	24.2	0.1122	24.5	0.0158	3.9	0.16	101.2	3.9	108.0	25.1	260.8	562.9	101.2	3.9	NA
SFO-138-22	81	12164	0.9	23.5213	33.7	0.0892	34.0	0.0152	4.6	0.13	97.3	4.4	86.7	28.3	-195.9	863.9	97.3	4.4	NA
SFO-138-23	185	45804	0.7	20.2565	10.6	0.1046	10.7	0.0154	1.7	0.16	98.3	1.6	101.0	10.3	165.3	247.6	98.3	1.6	NA
SFO-138-24	48	4469	1.1	32.0853	68.2	0.0668	68.4	0.0155	5.3	0.08	99.4	5.2	65.6	43.5	-1043.2	2286.5	99.4	5.2	NA
SFO-138-25	56	15138	3.9	30.6196	50.8	0.0694	51.7	0.0154	9.4	0.18	98.7	9.2	68.2	34.1	-905.3	1559.7	98.7	9.2	NA
SFO-138-26	50	11104	1.3	19.0723	31.4	0.1150	32.3	0.0159	7.4	0.23	101.8	7.5	110.6	33.8	304.3	731.6	101.8	7.5	NA
SFO-138-27	65	18215	1.4	23.6358	26.4	0.0877	26.9	0.0150	5.0	0.18	96.2	4.7	85.4	22.0	-208.1	672.9	96.2	4.7	NA
SFO-138-28	101	32032	0.9	27.7597	19.9	0.0780	20.3	0.0157	4.0	0.20	100.4	4.0	76.2	14.9	-629.1	549.5	100.4	4.0	NA
SFO-138-29	184	37410	0.7	21.2830	8.0	0.1009	8.4	0.0156	2.5	0.30	99.6	2.4	97.6	7.8	48.5	190.9	99.6	2.4	NA
SFO-138-30	85	15035	1.5	24.3996	35.0	0.0883	36.4	0.0156	9.9	0.27	99.9	9.9	85.9	30.0	-288.6	915.7	99.9	9.9	NA
SFO-138-31	97	28791	1.0	25.0303	19.1	0.0844	19.5	0.0153	3.8	0.20	98.1	3.7	82.3	15.4	-354.1	497.5	98.1	3.7	NA
SFO-138-32	72	12133	1.4	15.3259	28.2	0.1402	29.0	0.0156	7.1	0.24	99.7	7.0	133.2	36.3	782.4	603.1	99.7	7.0	NA

SFO-138-33	53	7533	1.2	21.6509	30.9	0.0996	31.2	0.0156	4.5	0.15	100.0	4.5	96.4	28.7	7.4	758.5	100.0	4.5	NA
SFO-138-34	94	12587	0.9	19.0013	13.7	0.1116	14.2	0.0154	3.4	0.24	98.4	3.3	107.4	14.4	312.8	314.1	98.4	3.3	NA
SFO-138-35	99	29546	1.0	25.0186	57.0	0.0876	57.1	0.0159	3.7	0.06	101.6	3.7	85.2	46.7	-352.8	1590.9	101.6	3.7	NA
SFO-138-37	176	22871	0.8	19.2748	9.1	0.1113	9.4	0.0156	2.3	0.25	99.6	2.3	107.2	9.6	280.2	209.1	99.6	2.3	NA
SFO-138-38	47	14179	1.2	31.6673	75.9	0.0730	76.1	0.0168	5.8	0.08	107.3	6.2	71.6	52.6	NA	NA	107.3	6.2	NA
SFO-138-39	93	13011	1.0	18.4848	26.7	0.1163	27.0	0.0156	4.3	0.16	99.7	4.3	111.7	28.6	375.1	610.3	99.7	4.3	NA
SFO-138-40	125	25672	1.3	17.9355	12.8	0.1189	13.4	0.0155	3.9	0.29	98.9	3.9	114.1	14.4	442.6	284.9	98.9	3.9	NA

				Isotope ratios							Apparent ages (Ma)								
Sample SFO-142	U (ppm)	206Pb 204Pb	U/Th	206Pb* 207Pb*	± (%)	207Pb* 235U*	± (%)	206Pb* 238U	± (%)	error corr.	206Pb* 238U*	± (Ma)	207Pb* 235U	± (Ma)	206Pb* 207Pb*	± (Ma)	Best age (Ma)	± (Ma)	Conc (%)
SFO-142-1	2287	104625	18.2	20.9879	1.2	0.0882	1.5	0.0134	0.8	0.55	86.0	0.7	85.8	1.2	81.7	28.9	86.0	0.7	NA
SFO-142-2	995	61060	30.9	21.1799	3.0	0.0902	5.8	0.0139	5.0	0.85	88.7	4.4	87.7	4.9	60.1	72.6	88.7	4.4	NA
SFO-142-3	1100	45910	16.7	20.8604	2.5	0.0892	4.0	0.0135	3.2	0.79	86.4	2.7	86.7	3.4	96.2	58.7	86.4	2.7	NA
SFO-142-4	2816	80222	8.2	20.8576	0.4	0.1118	4.2	0.0169	4.2	0.99	108.2	4.5	107.7	4.3	96.5	10.4	108.2	4.5	NA
SFO-142-5	2218	47702	15.9	20.9152	1.0	0.0826	10.3	0.0125	10.2	1.00	80.3	8.2	80.6	8.0	90.0	23.8	80.3	8.2	NA
SFO-142-6	968	40883	19.4	21.0281	3.1	0.0967	8.5	0.0147	7.9	0.93	94.3	7.4	93.7	7.6	77.2	74.6	94.3	7.4	NA
SFO-142-7	2606	89716	14.4	20.7680	1.0	0.0820	6.8	0.0123	6.7	0.99	79.1	5.3	80.0	5.2	106.7	22.9	79.1	5.3	NA
SFO-142-8	1927	22757	17.6	20.8122	2.0	0.0882	2.2	0.0133	0.9	0.40	85.2	0.7	85.8	1.8	101.7	48.0	85.2	0.7	NA
SFO-142-9	1140	183326	38.6	20.4751	2.7	0.0883	2.7	0.0131	0.6	0.23	84.0	0.5	85.9	2.3	140.2	62.5	84.0	0.5	NA
SFO-142-10	1554	23726	20.0	20.7219	1.6	0.0884	2.0	0.0133	1.2	0.59	85.1	1.0	86.0	1.6	111.9	37.4	85.1	1.0	NA
SFO-142-12	2274	87105	13.4	20.7502	1.2	0.0659	1.5	0.0099	0.9	0.62	63.6	0.6	64.8	0.9	108.7	27.3	63.6	0.6	NA
SFO-142-13	1338	80244	27.9	20.7840	2.3	0.0868	2.4	0.0131	0.6	0.27	83.8	0.5	84.5	2.0	104.9	55.0	83.8	0.5	NA
SFO-142-14	1290	95922	31.0	20.6988	1.9	0.0854	2.2	0.0128	1.0	0.47	82.1	0.8	83.2	1.7	114.5	45.1	82.1	0.8	NA
SFO-142-15	2827	256514	7.2	20.8182	0.6	0.1152	2.3	0.0174	2.2	0.96	111.1	2.4	110.7	2.4	101.0	14.6	111.1	2.4	NA
SFO-142-16	2825	142229	5.2	20.8562	0.5	0.1383	2.1	0.0209	2.1	0.97	133.5	2.7	131.5	2.6	96.7	11.8	133.5	2.7	NA
SFO-142-17	2817	108548	8.9	20.8739	0.7	0.1152	3.6	0.0174	3.6	0.98	111.4	3.9	110.7	3.8	94.7	15.5	111.4	3.9	NA
SFO-142-18	1381	93378	17.1	20.9413	2.2	0.0856	4.1	0.0130	3.4	0.85	83.2	2.9	83.4	3.3	87.0	51.0	83.2	2.9	NA
SFO-142-19	2799	101327	22.0	20.8132	0.8	0.0915	1.9	0.0138	1.7	0.90	88.4	1.5	88.9	1.6	101.6	19.9	88.4	1.5	NA
SFO-142-20	1427	61247	32.8	20.9734	2.4	0.0886	4.7	0.0135	4.1	0.86	86.3	3.5	86.2	3.9	83.4	56.5	86.3	3.5	NA
SFO-142-21	2810	181661	26.4	20.9055	1.2	0.1038	3.1	0.0157	2.9	0.92	100.7	2.9	100.3	3.0	91.1	29.3	100.7	2.9	NA
SFO-142-22	621	37250	42.3	21.5105	4.2	0.0837	4.4	0.0131	1.2	0.28	83.7	1.0	81.7	3.4	23.0	100.6	83.7	1.0	NA
SFO-142-23	2804	311448	12.7	20.7905	0.8	0.0947	3.3	0.0143	3.3	0.97	91.4	3.0	91.9	2.9	104.1	18.0	91.4	3.0	NA
SFO-142-24	1760	64692	30.7	20.6379	1.5	0.0871	3.3	0.0130	3.0	0.89	83.5	2.5	84.8	2.7	121.5	35.7	83.5	2.5	NA
SFO-142-25	2812	40599	16.8	20.7501	2.5	0.1157	7.6	0.0174	7.2	0.94	111.3	7.9	111.2	8.0	108.7	58.9	111.3	7.9	NA
SFO-142-26	1571	75585	31.8	20.9152	2.2	0.0839	5.7	0.0127	5.3	0.92	81.6	4.3	81.8	4.5	90.0	52.3	81.6	4.3	NA

SFO-142-27	2228	200558	30.5	20.7646	1.3	0.0869	1.9	0.0131	1.4	0.73	83.8	1.1	84.6	1.5	107.1	30.1	83.8	1.1	NA
SFO-142-28	2824	129678	9.6	20.9213	0.5	0.1364	3.5	0.0207	3.5	0.99	132.1	4.6	129.8	4.3	89.3	10.9	132.1	4.6	NA
SFO-142-29	1030	25603	12.1	20.8401	3.0	0.0863	6.0	0.0130	5.1	0.86	83.5	4.3	84.0	4.8	98.5	71.8	83.5	4.3	NA
SFO-142-30	1847	77080	19.1	21.0882	1.5	0.0869	1.9	0.0133	1.1	0.60	85.1	1.0	84.6	1.5	70.4	36.4	85.1	1.0	NA
SFO-142-31	2818	169815	17.8	20.8141	1.0	0.1159	2.9	0.0175	2.7	0.94	111.8	3.0	111.3	3.1	101.4	24.2	111.8	3.0	NA
SFO-142-32	1314	27503	16.8	20.7798	1.8	0.0857	2.3	0.0129	1.4	0.61	82.7	1.2	83.5	1.8	105.3	43.1	82.7	1.2	NA
SFO-142-33	721	41709	26.3	20.6988	3.3	0.0881	3.6	0.0132	1.5	0.42	84.7	1.3	85.7	3.0	114.5	77.6	84.7	1.3	NA
SFO-142-34	2826	306275	14.1	20.8272	0.6	0.1443	2.3	0.0218	2.2	0.96	139.0	3.0	136.9	2.9	100.0	14.4	139.0	3.0	NA
SFO-142-35	2821	124910	12.8	20.8189	0.5	0.1206	3.9	0.0182	3.9	0.99	116.3	4.5	115.6	4.3	100.9	11.9	116.3	4.5	NA
SFO-142-36	1686	64409	45.0	20.8820	1.9	0.0851	3.3	0.0129	2.6	0.81	82.6	2.2	83.0	2.6	93.8	45.1	82.6	2.2	NA
SFO-142-37	1831	79317	27.6	20.8285	1.5	0.0879	2.0	0.0133	1.4	0.69	85.1	1.2	85.6	1.7	99.8	34.5	85.1	1.2	NA
SFO-142-38	2443	148217	17.9	20.8036	1.0	0.0868	1.8	0.0131	1.5	0.82	83.9	1.2	84.5	1.5	102.6	24.5	83.9	1.2	NA
SFO-142-39	864	102598	39.2	20.8219	2.3	0.0835	2.7	0.0126	1.5	0.54	80.7	1.2	81.4	2.1	100.6	54.6	80.7	1.2	NA
SFO-142-40	2828	201909	9.8	20.8490	0.6	0.1678	6.0	0.0254	6.0	0.99	161.5	9.5	157.5	8.7	97.5	14.5	161.5	9.5	NA
SFO-142-41	729	48060	21.1	20.9649	3.9	0.0683	4.6	0.0104	2.5	0.54	66.6	1.7	67.1	3.0	84.3	92.6	66.6	1.7	NA
SFO-142-42	1996	98812	22.1	20.7607	1.5	0.0862	1.8	0.0130	1.1	0.60	83.1	0.9	83.9	1.5	107.6	34.8	83.1	0.9	NA
SFO-142-43	2117	56434	58.3	20.9479	0.7	0.0845	1.1	0.0128	0.8	0.72	82.3	0.6	82.4	0.8	86.3	17.7	82.3	0.6	NA
SFO-142-44	2264	114842	49.8	20.6639	0.8	0.0843	2.3	0.0126	2.1	0.93	81.0	1.7	82.2	1.8	118.6	20.0	81.0	1.7	NA
SFO-142-45	2807	28999	14.5	20.8088	0.7	0.1022	3.5	0.0154	3.4	0.98	98.6	3.4	98.8	3.3	102.0	16.9	98.6	3.4	NA

				Isotope ratios							Apparent ages (Ma)								
Sample	U	206Pb	U/Th	206Pb*	±	207Pb*	±	206Pb*	±	error	206Pb*	±	207Pb*	±	206Pb*	±	Best age	±	Conc
SFO-152	(ppm)	204Pb		207Pb*	(%)	235U*	(%)	238U	(%)	corr.	238U*	(Ma)	235U	(Ma)	207Pb*	(Ma)	(Ma)	(Ma)	(%)
SFO-152-2	232	67692	1.7	19.4409	6.0	0.1789	6.2	0.0252	1.6	0.26	160.6	2.5	167.1	9.5	260.5	137.1	160.6	2.5	NA
SFO-152-3	295	30895	1.5	20.6096	4.9	0.1711	5.9	0.0256	3.4	0.56	162.8	5.4	160.4	8.8	124.7	115.7	162.8	5.4	NA
SFO-152-4	231	10403	1.7	20.5155	4.0	0.1688	5.4	0.0251	3.6	0.67	159.9	5.7	158.4	7.9	135.5	94.5	159.9	5.7	NA
SFO-152-5	263	22350	1.8	20.8734	5.4	0.1459	7.2	0.0221	4.7	0.66	140.8	6.6	138.3	9.3	94.7	128.9	140.8	6.6	NA
SFO-152-6	1563	53431	1.1	19.0842	1.7	0.2810	2.4	0.0389	1.7	0.69	246.0	4.0	251.4	5.3	302.9	39.5	246.0	4.0	NA
SFO-152-7	266	25657	1.7	19.9967	5.4	0.1760	6.1	0.0255	2.8	0.46	162.5	4.5	164.7	9.3	195.4	126.1	162.5	4.5	NA
SFO-152-8	695	56929	1.3	20.1907	1.6	0.1676	2.2	0.0245	1.4	0.66	156.3	2.2	157.3	3.2	172.9	38.4	156.3	2.2	NA
SFO-152-9	105	15030	3.3	20.4630	13.9	0.1798	16.0	0.0267	7.8	0.49	169.7	13.1	167.9	24.7	141.5	327.9	169.7	13.1	NA
SFO-152-10	251	28272	1.8	21.0595	7.1	0.1636	7.4	0.0250	2.1	0.28	159.1	3.3	153.9	10.6	73.7	169.9	159.1	3.3	NA
SFO-152-11	136	16525	2.4	20.5535	13.7	0.1664	13.8	0.0248	1.6	0.11	158.0	2.4	156.3	20.0	131.1	323.4	158.0	2.4	NA
SFO-152-12	273	37651	1.9	19.8559	4.3	0.1747	4.6	0.0252	1.6	0.34	160.2	2.5	163.5	6.9	211.8	100.3	160.2	2.5	NA
SFO-152-13	168	11109	2.2	20.5919	7.8	0.1713	7.9	0.0256	1.3	0.16	162.9	2.0	160.6	11.8	126.8	184.6	162.9	2.0	NA
SFO-152-14	159	19862	1.6	20.7047	8.0	0.1725	10.1	0.0259	6.3	0.62	164.9	10.2	161.6	15.2	113.9	188.7	164.9	10.2	NA

SFO-152-15	218	12478	1.3	20.7214	8.1	0.1695	8.3	0.0255	1.4	0.17	162.2	2.3	159.0	12.2	112.0	192.4	162.2	2.3	NA
SFO-152-16	191	13208	1.9	21.5522	7.0	0.1622	7.1	0.0254	1.5	0.21	161.4	2.4	152.6	10.1	18.4	167.4	161.4	2.4	NA
SFO-152-17	170	22457	2.4	20.0415	11.8	0.1770	12.1	0.0257	2.8	0.23	163.7	4.6	165.5	18.5	190.2	274.9	163.7	4.6	NA
SFO-152-18	302	21558	1.9	21.0602	4.0	0.1796	5.1	0.0274	3.2	0.63	174.4	5.5	167.7	8.0	73.6	95.3	174.4	5.5	NA
SFO-152-19	98	1494	1.4	14.4100	28.1	0.2420	28.6	0.0253	5.3	0.19	161.0	8.4	220.0	56.6	910.5	589.9	161.0	8.4	NA
SFO-152-20	210	3362	1.9	16.8941	20.7	0.2108	21.2	0.0258	4.3	0.20	164.4	7.0	194.2	37.4	574.2	455.2	164.4	7.0	NA
SFO-152-21	491	43704	0.9	20.7540	3.6	0.1724	4.7	0.0259	3.0	0.65	165.1	4.9	161.5	7.0	108.3	84.3	165.1	4.9	NA
SFO-152-22	301	27662	1.6	21.1412	4.1	0.1638	4.6	0.0251	2.1	0.45	159.9	3.2	154.0	6.6	64.4	98.1	159.9	3.2	NA
SFO-152-23	626	25090	4.5	20.8072	2.5	0.1479	2.7	0.0223	1.0	0.36	142.3	1.4	140.1	3.6	102.2	60.2	142.3	1.4	NA
SFO-152-24	105	11226	3.0	20.8367	7.6	0.1571	8.0	0.0237	2.4	0.31	151.3	3.6	148.2	11.0	98.9	179.4	151.3	3.6	NA
SFO-152-25	330	50663	1.5	20.3886	3.5	0.1665	3.7	0.0246	0.9	0.26	156.8	1.4	156.4	5.3	150.1	82.8	156.8	1.4	NA
SFO-152-26	161	12564	2.3	19.1326	10.8	0.1824	11.1	0.0253	2.7	0.24	161.1	4.3	170.1	17.5	297.1	247.4	161.1	4.3	NA
SFO-152-27	172	20465	2.4	20.6472	5.7	0.1698	6.0	0.0254	1.7	0.28	161.9	2.7	159.3	8.8	120.5	135.5	161.9	2.7	NA
SFO-152-28	449	30776	1.8	19.8109	4.8	0.1752	5.8	0.0252	3.3	0.57	160.3	5.3	164.0	8.8	217.0	110.1	160.3	5.3	NA
SFO-152-29	180	31097	2.0	21.5290	7.2	0.1626	7.6	0.0254	2.4	0.31	161.6	3.8	152.9	10.8	21.0	174.0	161.6	3.8	NA
SFO-152-30	410	28620	1.4	18.7696	12.0	0.1890	13.3	0.0257	5.6	0.42	163.7	9.1	175.7	21.4	340.7	273.2	163.7	9.1	NA
SFO-152-31	592	30969	1.8	20.8856	2.9	0.1227	3.8	0.0186	2.4	0.64	118.7	2.8	117.5	4.2	93.3	68.4	118.7	2.8	NA
SFO-152-32	847	47130	23.5	20.7197	1.9	0.0935	2.2	0.0140	1.0	0.46	89.9	0.9	90.7	1.9	112.2	45.9	89.9	0.9	NA
SFO-152-33	193	18030	2.2	19.8486	5.4	0.1653	5.8	0.0238	2.3	0.39	151.6	3.4	155.4	8.4	212.6	124.6	151.6	3.4	NA
SFO-152-34	349	25036	102.8	21.4477	3.9	0.0780	8.6	0.0121	7.7	0.90	77.7	6.0	76.3	6.4	30.0	92.3	77.7	6.0	NA
SFO-152-35	286	21567	1.4	20.2357	4.6	0.1689	4.7	0.0248	1.1	0.24	157.9	1.7	158.5	6.9	167.7	106.4	157.9	1.7	NA
SFO-152-36	224	127166	1.8	19.5929	5.0	0.1790	5.3	0.0254	1.8	0.34	162.0	2.9	167.2	8.2	242.6	115.2	162.0	2.9	NA
SFO-152-37	558	35106	36.3	20.9634	3.8	0.0929	4.5	0.0141	2.4	0.53	90.4	2.1	90.2	3.9	84.5	90.0	90.4	2.1	NA
SFO-152-38	307	18698	289.3	19.4945	8.3	0.0987	8.6	0.0140	2.4	0.27	89.3	2.1	95.6	7.9	254.2	190.9	89.3	2.1	NA
SFO-152-39	155	17561	2.4	20.6036	4.2	0.1713	4.6	0.0256	1.9	0.42	162.9	3.1	160.5	6.9	125.4	99.2	162.9	3.1	NA
SFO-152-40	220	27924	1.6	20.3289	5.3	0.1710	5.5	0.0252	1.3	0.25	160.5	2.1	160.3	8.1	156.9	123.9	160.5	2.1	NA
SFO-152-41	369	18734	312.8	21.4115	5.9	0.0922	6.2	0.0143	1.7	0.27	91.6	1.5	89.5	5.3	34.1	142.3	91.6	1.5	NA
SFO-152-42	615	42174	1.1	20.2498	2.0	0.1647	2.2	0.0242	0.8	0.39	154.1	1.3	154.8	3.1	166.0	46.4	154.1	1.3	NA
SFO-152-43	276	27440	1.5	20.7061	4.2	0.1646	4.4	0.0247	1.5	0.34	157.4	2.4	154.7	6.4	113.7	98.7	157.4	2.4	NA
SFO-152-44	219	24415	2.3	19.7253	3.9	0.1777	4.6	0.0254	2.4	0.52	161.8	3.9	166.1	7.1	227.0	90.6	161.8	3.9	NA
SFO-152-45	331	43992	1.9	19.5030	1.5	0.3027	2.2	0.0428	1.6	0.73	270.3	4.2	268.5	5.1	253.2	33.9	270.3	4.2	NA
SFO-152-46	243	21263	1.9	20.0348	5.3	0.1707	5.6	0.0248	1.8	0.31	158.0	2.7	160.1	8.3	191.0	124.5	158.0	2.7	NA
SFO-152-47	237	21052	1.8	20.4884	5.8	0.1697	6.0	0.0252	1.7	0.28	160.6	2.7	159.2	8.9	138.6	135.7	160.6	2.7	NA
SFO-152-48	276	49790	1.8	19.9129	4.3	0.1731	5.9	0.0250	4.0	0.68	159.2	6.3	162.1	8.8	205.1	99.3	159.2	6.3	NA
SFO-152-49	327	29790	1.4	21.1431	4.2	0.1642	4.8	0.0252	2.2	0.47	160.3	3.6	154.3	6.8	64.3	100.5	160.3	3.6	NA
SFO-152-50	195	25482	2.4	20.1561	8.2	0.1727	8.7	0.0253	2.7	0.31	160.8	4.3	161.8	13.0	176.9	192.5	160.8	4.3	NA
SFO-152-51	159	11419	2.4	19.7744	7.2	0.1807	7.4	0.0259	1.7	0.23	164.9	2.8	168.6	11.5	221.3	166.2	164.9	2.8	NA

SFO-152-52	170	19078	2.7	21.6527	5.7	0.1665	6.2	0.0262	2.2	0.36	166.4	3.6	156.4	8.9	7.2	138.4	166.4	3.6	NA
SFO-152-53	154	13530	2.6	20.8907	13.3	0.1715	13.5	0.0260	2.2	0.17	165.4	3.7	160.7	20.1	92.8	316.8	165.4	3.7	NA
SFO-152-54	203	19088	2.1	21.3357	10.4	0.1632	10.6	0.0252	1.9	0.18	160.7	3.0	153.5	15.1	42.6	249.5	160.7	3.0	NA
SFO-152-55	177	12894	2.0	21.1802	7.0	0.1637	7.3	0.0251	1.9	0.26	160.1	3.0	153.9	10.4	60.1	166.9	160.1	3.0	NA
SFO-152-56	185	19439	2.0	20.8522	7.4	0.1664	7.5	0.0252	1.0	0.14	160.2	1.6	156.3	10.8	97.1	175.2	160.2	1.6	NA
SFO-152-57	409	33284	1.3	20.6395	3.8	0.1690	3.9	0.0253	0.9	0.22	161.0	1.4	158.5	5.7	121.3	89.3	161.0	1.4	NA
SFO-152-58	227	18626	1.6	21.6504	4.5	0.1619	4.7	0.0254	1.5	0.31	161.8	2.3	152.3	6.7	7.5	108.4	161.8	2.3	NA
SFO-152-59	501	26474	5.4	21.0925	4.9	0.1131	5.7	0.0173	3.0	0.52	110.6	3.3	108.8	5.9	70.0	115.9	110.6	3.3	NA
SFO-152-60	281	7502	1.6	20.0873	3.9	0.1773	5.3	0.0258	3.6	0.68	164.4	5.8	165.7	8.1	184.8	90.4	164.4	5.8	NA
SFO-152-61	471	16305	1.3	19.9156	4.4	0.1699	5.2	0.0245	2.7	0.51	156.3	4.1	159.4	7.6	204.8	103.0	156.3	4.1	NA
SFO-152-62	191	14641	1.9	20.7274	7.9	0.1659	8.3	0.0249	2.5	0.30	158.8	4.0	155.8	12.0	111.3	187.6	158.8	4.0	NA
SFO-152-63	429	158137	1.5	19.2730	1.2	0.2878	1.4	0.0402	0.8	0.57	254.3	2.0	256.9	3.2	280.4	26.7	254.3	2.0	NA
SFO-152-64	172	10152	2.3	19.1705	12.6	0.1785	12.7	0.0248	1.6	0.12	158.0	2.5	166.8	19.5	292.6	288.8	158.0	2.5	NA
SFO-152-65	296	31884	1.6	20.5150	3.9	0.1676	4.1	0.0249	1.1	0.26	158.8	1.7	157.3	5.9	135.6	92.3	158.8	1.7	NA
SFO-152-66	335	37513	1.4	20.3142	2.8	0.1717	3.0	0.0253	0.9	0.30	161.1	1.4	160.9	4.4	158.6	66.4	161.1	1.4	NA
SFO-152-67	280	30281	1.4	20.3364	5.6	0.1709	5.7	0.0252	1.2	0.22	160.5	1.9	160.2	8.5	156.1	130.7	160.5	1.9	NA
SFO-152-68	265	24942	1.8	20.2885	3.6	0.1682	3.7	0.0247	0.8	0.21	157.6	1.2	157.8	5.3	161.6	83.7	157.6	1.2	NA
SFO-152-69	160	11156	2.3	20.0860	9.5	0.1784	9.7	0.0260	1.6	0.17	165.4	2.7	166.7	14.9	185.0	222.7	165.4	2.7	NA
SFO-152-70	223	15624	1.8	20.5991	4.9	0.1667	5.0	0.0249	1.2	0.24	158.6	1.9	156.5	7.3	125.9	115.4	158.6	1.9	NA
SFO-152-71	370	40346	1.4	20.1151	2.6	0.1732	3.4	0.0253	2.2	0.64	160.8	3.5	162.2	5.1	181.6	61.3	160.8	3.5	NA
SFO-152-72	167	17828	1.8	19.7752	8.5	0.1809	9.1	0.0259	3.0	0.33	165.1	4.9	168.8	14.1	221.2	198.0	165.1	4.9	NA
SFO-152-73	387	26936	2.2	20.5411	3.2	0.1125	4.1	0.0168	2.6	0.62	107.1	2.7	108.2	4.2	132.6	75.6	107.1	2.7	NA
SFO-152-74	259	33204	1.9	21.3036	5.7	0.1653	5.9	0.0255	1.3	0.22	162.6	2.1	155.3	8.5	46.2	137.4	162.6	2.1	NA
SFO-152-75	275	25794	1.6	20.6779	4.6	0.1726	4.8	0.0259	1.3	0.27	164.8	2.1	161.7	7.1	117.0	108.1	164.8	2.1	NA
SFO-152-76	314	13187	2.2	19.6905	13.3	0.1599	15.5	0.0228	8.0	0.52	145.5	11.5	150.6	21.7	231.1	308.2	145.5	11.5	NA
SFO-152-77	153	19349	2.7	20.3593	14.1	0.1718	14.1	0.0254	0.9	0.06	161.5	1.4	160.9	21.0	153.5	331.1	161.5	1.4	NA
SFO-152-78	397	50043	5.0	20.9585	3.7	0.1207	4.3	0.0183	2.1	0.50	117.2	2.5	115.7	4.7	85.1	88.0	117.2	2.5	NA
SFO-152-79	331	15889	5.9	20.7406	6.6	0.0954	8.2	0.0143	4.8	0.58	91.8	4.3	92.5	7.2	109.8	157.1	91.8	4.3	NA
SFO-152-80	240	11005	1.8	21.0001	7.4	0.1658	7.5	0.0253	1.4	0.18	160.8	2.2	155.8	10.9	80.4	175.9	160.8	2.2	NA
SFO-152-81	181	20029	2.1	19.3704	5.5	0.1816	5.8	0.0255	1.8	0.31	162.4	2.9	169.5	9.1	268.8	127.3	162.4	2.9	NA
SFO-152-82	209	21830	2.2	20.0041	7.4	0.1776	7.6	0.0258	2.1	0.27	164.0	3.3	166.0	11.7	194.5	171.4	164.0	3.3	NA
SFO-152-83	174	17416	2.2	22.0904	6.2	0.1580	6.6	0.0253	2.1	0.32	161.2	3.3	149.0	9.1	-41.2	151.3	161.2	3.3	NA
SFO-152-84	118	14616	2.4	21.3450	19.2	0.1670	20.2	0.0259	6.2	0.31	164.5	10.1	156.8	29.3	41.6	462.2	164.5	10.1	NA
SFO-152-85	184	12713	1.9	21.5523	7.2	0.1621	7.3	0.0253	1.2	0.17	161.3	1.9	152.5	10.3	18.4	172.2	161.3	1.9	NA
SFO-152-86	175	20233	1.8	20.5338	7.2	0.1733	7.5	0.0258	2.2	0.29	164.3	3.5	162.3	11.3	133.4	169.2	164.3	3.5	NA
SFO-152-87	130	11043	1.3	19.3474	9.0	0.1861	9.4	0.0261	2.7	0.28	166.2	4.4	173.3	14.9	271.5	206.0	166.2	4.4	NA
SFO-152-89	166	18709	1.8	19.3328	11.7	0.1858	12.2	0.0261	3.2	0.26	165.8	5.3	173.0	19.4	273.3	270.0	165.8	5.3	NA

SFO-152-91	244	15047	1.8	20.0403	5.2	0.1767	5.4	0.0257	1.4	0.27	163.5	2.3	165.2	8.2	190.3	120.8	163.5	2.3	NA
SFO-152-92	181	12873	1.9	21.2411	10.1	0.1649	10.3	0.0254	2.1	0.20	161.7	3.4	155.0	14.9	53.2	242.0	161.7	3.4	NA
SFO-152-93	192	6419	4.2	19.1846	11.8	0.1470	12.4	0.0204	3.8	0.30	130.5	4.8	139.2	16.1	290.9	270.5	130.5	4.8	NA
SFO-152-94	221	11717	2.1	21.2875	4.1	0.1641	4.5	0.0253	1.7	0.38	161.3	2.7	154.3	6.4	48.0	98.4	161.3	2.7	NA
SFO-152-95	273	19039	1.6	20.6454	4.8	0.1687	5.0	0.0253	1.1	0.22	160.8	1.7	158.3	7.3	120.7	114.1	160.8	1.7	NA
SFO-152-96	147	26554	3.2	18.6709	5.2	0.3247	6.2	0.0440	3.4	0.55	277.4	9.2	285.5	15.4	352.5	117.0	277.4	9.2	NA
SFO-152-97	290	54574	1.6	19.0675	6.4	0.1827	7.0	0.0253	2.8	0.40	160.8	4.5	170.4	11.0	304.9	146.4	160.8	4.5	NA
SFO-152-98	396	27591	1.5	19.7122	5.6	0.1736	6.0	0.0248	2.2	0.36	158.0	3.4	162.5	9.0	228.6	129.2	158.0	3.4	NA
SFO-152-99	156	18027	2.1	21.4880	11.1	0.1640	11.4	0.0256	2.4	0.21	162.7	3.8	154.2	16.3	25.6	267.2	162.7	3.8	NA
SFO-152-10	309	22233	1.9	20.3636	3.6	0.1740	4.0	0.0257	1.7	0.43	163.6	2.8	162.9	6.0	152.9	84.3	163.6	2.8	NA

				Isotope ratios							Apparent ages (Ma)								
Sample	U	206Pb	U/Th	206Pb*	±	207Pb*	±	206Pb*	±	error	206Pb*	±	207Pb*	±	206Pb*	±	Best age	±	Conc
SFO-154	(ppm)	204Pb		207Pb*	(%)	235U*	(%)	238U	(%)	corr.	238U*	(Ma)	235U	(Ma)	207Pb*	(Ma)	(Ma)	(Ma)	(%)
SFO-154-1	237	16332	1.4	19.8110	7.6	0.2087	7.8	0.0300	1.8	0.23	190.5	3.3	192.5	13.6	217.0	175.3	190.5	3.3	NA
SFO-154-2	227	26150	1.9	19.5996	6.5	0.2118	6.6	0.0301	1.3	0.19	191.2	2.4	195.0	11.8	241.8	150.4	191.2	2.4	NA
SFO-154-3	197	12871	2.0	20.0695	5.1	0.2138	5.4	0.0311	1.7	0.31	197.6	3.3	196.7	9.7	186.9	119.8	197.6	3.3	NA
SFO-154-4	189	28851	1.2	19.9580	3.8	0.2371	4.7	0.0343	2.7	0.57	217.5	5.7	216.0	9.1	199.9	88.8	217.5	5.7	NA
SFO-154-5	188	13839	1.2	20.8208	7.0	0.2155	7.1	0.0325	1.2	0.17	206.4	2.5	198.1	12.7	100.7	164.9	206.4	2.5	NA
SFO-154-6	200	14629	1.6	19.4742	3.5	0.2336	4.0	0.0330	1.9	0.47	209.2	3.9	213.1	7.6	256.6	80.4	209.2	3.9	NA
SFO-154-7	214	16780	1.4	19.8037	3.1	0.2451	3.8	0.0352	2.2	0.59	223.0	4.9	222.6	7.5	217.9	70.7	223.0	4.9	NA
SFO-154-8	252	16489	1.0	19.3415	1.9	0.2328	2.7	0.0327	1.9	0.71	207.2	3.9	212.5	5.1	272.2	43.1	207.2	3.9	NA
SFO-154-10	147	25194	1.6	17.8214	8.5	0.2688	11.8	0.0347	8.1	0.69	220.2	17.6	241.7	25.3	456.8	188.3	220.2	17.6	NA
SFO-154-11	242	25525	2.0	20.0281	5.2	0.2154	5.6	0.0313	2.0	0.35	198.6	3.9	198.1	10.1	191.7	121.7	198.6	3.9	NA
SFO-154-12	179	42763	1.3	19.7969	3.3	0.2263	4.3	0.0325	2.8	0.65	206.1	5.6	207.1	8.1	218.7	75.9	206.1	5.6	NA
SFO-154-13	191	27221	1.4	19.7730	4.2	0.2316	6.4	0.0332	4.8	0.75	210.6	9.9	211.5	12.2	221.4	97.6	210.6	9.9	NA
SFO-154-14	168	22133	1.2	20.0872	6.1	0.2103	6.5	0.0306	2.1	0.33	194.6	4.1	193.8	11.4	184.8	142.4	194.6	4.1	NA
SFO-154-15	309	29724	1.0	17.4901	22.5	0.2491	22.6	0.0316	1.9	0.08	200.5	3.7	225.8	45.7	498.3	501.0	200.5	3.7	NA
SFO-154-16	199	21678	1.5	20.0381	6.0	0.2324	7.4	0.0338	4.3	0.58	214.1	9.0	212.2	14.1	190.6	139.7	214.1	9.0	NA
SFO-154-18	197	30338	1.6	20.7537	6.4	0.2201	6.5	0.0331	1.1	0.18	210.1	2.4	202.0	11.9	108.3	151.3	210.1	2.4	NA
SFO-154-19	133	19087	1.9	20.6740	7.0	0.2212	7.9	0.0332	3.6	0.46	210.4	7.5	202.9	14.5	117.4	165.5	210.4	7.5	NA
SFO-154-20	189	15616	1.4	20.2580	8.0	0.2105	8.2	0.0309	1.5	0.18	196.4	2.8	194.0	14.4	165.1	188.3	196.4	2.8	NA
SFO-154-21	105	12895	1.7	21.8447	10.6	0.2099	10.9	0.0333	2.7	0.25	210.9	5.6	193.5	19.3	-14.1	256.7	210.9	5.6	NA
SFO-154-22	177	15528	1.9	20.9494	7.5	0.2110	7.8	0.0321	2.1	0.26	203.4	4.1	194.4	13.8	86.1	178.9	203.4	4.1	NA
SFO-154-23	374	61180	1.3	19.9928	2.3	0.2267	3.7	0.0329	2.9	0.78	208.5	5.8	207.5	6.9	195.9	53.5	208.5	5.8	NA
SFO-154-24	233	55424	1.5	19.3708	4.6	0.2295	4.8	0.0322	1.5	0.32	204.5	3.1	209.8	9.2	268.8	105.4	204.5	3.1	NA

SFO-154-25	175	18473	1.8	20.4345	4.2	0.2192	5.0	0.0325	2.7	0.53	206.1	5.4	201.2	9.2	144.8	99.6	206.1	5.4	NA
SFO-154-26	162	27125	1.6	20.1462	4.9	0.2241	5.1	0.0327	1.4	0.28	207.7	2.9	205.3	9.5	178.0	114.2	207.7	2.9	NA
SFO-154-27	316	21595	1.4	19.7679	3.0	0.2208	3.2	0.0317	1.0	0.33	200.9	2.0	202.6	5.8	222.1	69.1	200.9	2.0	NA
SFO-154-28	205	18839	1.6	20.7949	3.6	0.2159	4.1	0.0326	2.1	0.51	206.5	4.3	198.5	7.5	103.6	84.1	206.5	4.3	NA
SFO-154-29	312	32408	1.4	20.0441	3.7	0.2167	4.1	0.0315	1.7	0.41	200.0	3.3	199.2	7.4	189.8	86.4	200.0	3.3	NA
SFO-154-30	104	9476	2.0	21.9617	8.0	0.1982	9.0	0.0316	4.1	0.45	200.3	8.1	183.6	15.2	-27.0	195.3	200.3	8.1	NA
SFO-154-31	426	6095	1.6	18.1627	7.8	0.2558	12.4	0.0337	9.7	0.78	213.6	20.4	231.3	25.7	414.6	174.1	213.6	20.4	NA
SFO-154-32	206	20492	1.4	21.1373	7.7	0.2017	7.9	0.0309	2.1	0.26	196.3	4.1	186.6	13.5	64.9	182.8	196.3	4.1	NA
SFO-154-33	167	32006	2.0	19.4584	5.6	0.2335	6.0	0.0330	2.1	0.35	209.0	4.4	213.1	11.5	258.4	128.7	209.0	4.4	NA
SFO-154-34	182	12070	2.1	20.0628	4.7	0.2182	5.0	0.0317	1.7	0.33	201.5	3.3	200.4	9.2	187.7	110.6	201.5	3.3	NA
SFO-154-35	468	85787	1.3	19.8763	3.0	0.2220	4.8	0.0320	3.7	0.78	203.1	7.5	203.6	8.8	209.4	68.5	203.1	7.5	NA
SFO-154-36	674	80840	3.4	19.7377	1.0	0.2295	1.8	0.0329	1.6	0.85	208.4	3.2	209.8	3.5	225.6	22.3	208.4	3.2	NA
SFO-154-37	1422	38811	12.1	19.8056	1.2	0.1902	1.7	0.0273	1.3	0.74	173.8	2.2	176.8	2.8	217.6	27.0	173.8	2.2	NA
SFO-154-38	166	7735	1.8	19.7403	9.3	0.2252	9.5	0.0322	1.9	0.20	204.6	3.8	206.2	17.7	225.3	215.5	204.6	3.8	NA
SFO-154-39	563	104183	1.4	19.5547	2.8	0.2319	3.1	0.0329	1.4	0.46	208.6	3.0	211.7	6.0	247.1	64.0	208.6	3.0	NA
SFO-154-40	494	77880	1.2	19.7031	2.1	0.2273	2.6	0.0325	1.6	0.61	206.0	3.2	207.9	4.9	229.6	47.9	206.0	3.2	NA
SFO-154-41	245	38413	1.0	20.0065	4.3	0.2070	7.8	0.0300	6.5	0.84	190.8	12.2	191.0	13.5	194.3	99.0	190.8	12.2	NA
SFO-154-42	518	44484	1.4	19.5910	2.0	0.2235	4.0	0.0318	3.4	0.86	201.6	6.7	204.8	7.4	242.8	47.2	201.6	6.7	NA
SFO-154-43	2017	86566	2.4	19.8814	0.5	0.2212	1.7	0.0319	1.6	0.96	202.4	3.3	202.9	3.1	208.8	10.5	202.4	3.3	NA
SFO-154-44	801	77642	1.5	19.7833	1.3	0.2215	5.0	0.0318	4.8	0.96	201.7	9.5	203.1	9.1	220.3	30.3	201.7	9.5	NA
SFO-154-44	300	29329	1.9	20.0097	3.8	0.2232	4.4	0.0324	2.3	0.52	205.5	4.6	204.6	8.1	193.9	87.5	205.5	4.6	NA
SFO-154-45	135	26124	1.9	19.6367	9.1	0.1987	9.6	0.0283	2.8	0.29	179.9	5.0	184.0	16.1	237.5	211.3	179.9	5.0	NA
SFO-154-45	526	218693	4.1	16.9626	0.4	0.7381	2.1	0.0908	2.1	0.98	560.3	11.3	561.3	9.2	565.3	8.9	560.3	11.3	99.1
SFO-154-46	126	19648	1.5	19.9893	7.1	0.2083	7.8	0.0302	3.2	0.41	191.8	6.1	192.1	13.6	196.3	164.7	191.8	6.1	NA
SFO-154-47	124	20541	1.7	19.8849	7.8	0.2204	8.2	0.0318	2.4	0.29	201.7	4.7	202.2	15.0	208.4	182.2	201.7	4.7	NA
SFO-154-48	1684	22084	12.2	19.9934	0.9	0.1834	1.4	0.0266	1.1	0.80	169.2	1.9	170.9	2.3	195.8	20.0	169.2	1.9	NA
SFO-154-49	223	32450	1.8	20.3873	5.3	0.2063	6.7	0.0305	4.1	0.61	193.7	7.9	190.5	11.7	150.2	124.8	193.7	7.9	NA
SFO-154-50	1804	23847	2.8	19.7443	1.1	0.1892	1.6	0.0271	1.2	0.74	172.3	2.0	175.9	2.5	224.8	24.4	172.3	2.0	NA
SFO-154-51	190	22735	1.8	20.0401	4.5	0.1853	5.5	0.0269	3.2	0.58	171.3	5.4	172.6	8.7	190.4	104.7	171.3	5.4	NA
SFO-154-52	392	46619	1.1	19.8091	2.3	0.2229	2.7	0.0320	1.2	0.47	203.2	2.5	204.3	4.9	217.2	54.2	203.2	2.5	NA
SFO-154-53	289	61559	1.1	19.8517	3.0	0.2209	3.2	0.0318	0.8	0.26	201.9	1.6	202.7	5.8	212.2	70.6	201.9	1.6	NA
SFO-154-54	210	26173	2.2	19.5951	4.9	0.2119	5.3	0.0301	2.2	0.41	191.3	4.1	195.1	9.4	242.3	112.1	191.3	4.1	NA
SFO-154-55	274	52132	2.0	20.0210	3.5	0.2146	4.2	0.0312	2.2	0.54	197.8	4.4	197.4	7.5	192.6	81.8	197.8	4.4	NA

				Isotope ratios							Apparent ages (Ma)								
Sample	U	206Pb	U/Th	206Pb*	±	207Pb*	±	206Pb*	±	error	206Pb*	±	207Pb*	±	206Pb*	±	Best age	±	Conc
SFO-155	(ppm)	204Pb		207Pb*	(%)	235U*	(%)	238U	(%)	corr.	238U*	(Ma)	235U	(Ma)	207Pb*	(Ma)	(Ma)	(Ma)	(%)

SFO-155-1	222	44401	1.6	19.2647	5.4	0.2425	5.5	0.0339	1.3	0.24	214.8	2.8	220.5	11.0	281.4	123.2	214.8	2.8	NA
SFO-155-2	192	22974	2.3	19.6272	6.4	0.2378	7.2	0.0338	3.3	0.46	214.6	7.0	216.6	14.0	238.6	147.4	214.6	7.0	NA
SFO-155-3	210	26588	2.0	20.0211	6.8	0.2333	7.1	0.0339	1.9	0.27	214.8	4.0	212.9	13.6	192.6	158.5	214.8	4.0	NA
SFO-155-4	195	41601	1.7	21.2313	6.7	0.2233	7.5	0.0344	3.5	0.47	217.9	7.5	204.6	14.0	54.3	159.1	217.9	7.5	NA
SFO-155-5	193	26455	1.3	20.7236	9.2	0.2289	9.7	0.0344	3.1	0.31	218.0	6.6	209.3	18.4	111.7	218.6	218.0	6.6	NA
SFO-155-6	223	18650	1.9	20.7193	4.3	0.2255	4.5	0.0339	1.4	0.30	214.9	2.9	206.5	8.4	112.3	100.8	214.9	2.9	NA
SFO-155-7	381	41286	1.1	19.3182	3.0	0.2436	3.7	0.0341	2.3	0.60	216.4	4.8	221.4	7.4	275.0	68.5	216.4	4.8	NA
SFO-155-8	184	19568	1.8	21.5093	6.3	0.2145	6.5	0.0335	1.9	0.29	212.2	4.0	197.4	11.7	23.2	150.2	212.2	4.0	NA
SFO-155-9	163	15929	2.0	19.6205	4.3	0.2444	6.7	0.0348	5.2	0.78	220.4	11.3	222.0	13.4	239.4	98.1	220.4	11.3	NA
SFO-155-10	306	51548	1.1	20.1200	4.3	0.2266	4.4	0.0331	1.2	0.27	209.7	2.4	207.4	8.3	181.1	99.3	209.7	2.4	NA
SFO-155-11	283	29719	1.5	19.8246	2.6	0.2351	3.2	0.0338	1.9	0.59	214.3	4.0	214.4	6.1	215.4	59.2	214.3	4.0	NA
SFO-155-12	354	29091	1.6	19.9614	4.5	0.2276	4.7	0.0329	1.3	0.27	209.0	2.7	208.2	8.9	199.5	105.3	209.0	2.7	NA
SFO-155-13	208	57557	1.4	20.1694	4.3	0.2259	5.7	0.0331	3.7	0.65	209.6	7.7	206.8	10.7	175.3	101.4	209.6	7.7	NA
SFO-155-14	193	21321	2.2	19.9920	5.1	0.2368	5.2	0.0343	1.3	0.24	217.6	2.7	215.8	10.1	195.9	117.7	217.6	2.7	NA
SFO-155-15	300	27428	1.7	19.6076	4.0	0.2273	5.6	0.0323	4.0	0.71	205.0	8.0	207.9	10.5	240.9	91.4	205.0	8.0	NA
SFO-155-16	303	37544	1.5	19.9433	5.6	0.2334	5.9	0.0338	1.8	0.31	214.1	3.8	213.0	11.3	201.6	129.5	214.1	3.8	NA
SFO-155-17	214	46074	1.9	20.4522	8.4	0.2252	8.8	0.0334	2.7	0.30	211.8	5.6	206.2	16.4	142.8	196.6	211.8	5.6	NA
SFO-155-18	175	40835	1.9	19.6398	7.5	0.2380	7.6	0.0339	1.4	0.19	214.9	3.0	216.8	14.8	237.1	172.0	214.9	3.0	NA
SFO-155-19	265	129002	1.6	19.3834	4.5	0.2507	6.6	0.0352	4.9	0.73	223.2	10.7	227.1	13.5	267.3	103.1	223.2	10.7	NA
SFO-155-20	164	28460	1.9	20.6790	5.9	0.2375	8.5	0.0356	6.1	0.72	225.7	13.6	216.4	16.5	116.8	138.3	225.7	13.6	NA
SFO-155-21	193	23536	2.3	19.9221	8.1	0.2342	8.3	0.0338	1.8	0.22	214.6	3.9	213.7	16.1	204.0	188.9	214.6	3.9	NA
SFO-155-22	274	36045	1.8	19.7005	2.9	0.2355	3.4	0.0337	1.8	0.53	213.4	3.7	214.8	6.5	229.9	66.5	213.4	3.7	NA
SFO-155-23	155	17651	2.0	20.4868	8.3	0.2329	8.8	0.0346	3.1	0.35	219.3	6.7	212.6	17.0	138.8	194.8	219.3	6.7	NA
SFO-155-24	205	26495	1.6	20.3895	6.6	0.2343	7.5	0.0346	3.5	0.47	219.5	7.6	213.7	14.4	150.0	154.3	219.5	7.6	NA
SFO-155-25	135	22144	2.0	19.6545	8.9	0.2492	9.4	0.0355	3.1	0.32	225.0	6.8	225.9	19.1	235.4	205.9	225.0	6.8	NA
SFO-155-26	228	16302	1.7	20.3147	4.6	0.2172	5.3	0.0320	2.5	0.47	203.1	5.0	199.6	9.6	158.6	108.6	203.1	5.0	NA
SFO-155-28	139	14245	2.2	20.3956	7.8	0.2259	8.1	0.0334	2.5	0.30	211.9	5.1	206.8	15.2	149.3	181.9	211.9	5.1	NA
SFO-155-29	236	70506	1.7	19.3331	4.3	0.2415	4.6	0.0339	1.8	0.38	214.7	3.7	219.7	9.2	273.2	98.2	214.7	3.7	NA
SFO-155-30	180	28481	2.2	20.7621	5.7	0.2266	6.3	0.0341	2.6	0.41	216.3	5.5	207.4	11.8	107.4	135.7	216.3	5.5	NA

				Isotope ratios							Apparent ages (Ma)								
Sample	U	206Pb	U/Th	206Pb*	±	207Pb*	±	206Pb*	±	error	206Pb*	±	207Pb*	±	206Pb*	±	Best age	±	Conc
SFO-158	(ppm)	204Pb		207Pb*	(%)	235U*	(%)	238U	(%)	corr.	238U*	(Ma)	235U	(Ma)	207Pb*	(Ma)	(Ma)	(Ma)	(%)
SFO-158-1	220	11200	1.0	19.9680	6.0	0.2286	6.3	0.0331	2.2	0.34	210.0	4.5	209.1	12.0	198.7	138.5	210.0	4.5	NA
SFO-158-2	144	6078	1.3	20.7873	10.2	0.2069	10.6	0.0312	2.9	0.27	198.0	5.6	191.0	18.5	104.5	241.8	198.0	5.6	NA

SFO-158-3	536	47984	0.4	20.0038	2.9	0.2158	4.6	0.0313	3.6	0.78	198.8	7.1	198.4	8.4	194.6	67.9	198.8	7.1	NA
SFO-158-4	187	25214	0.8	20.1804	3.3	0.2218	3.5	0.0325	1.3	0.36	205.9	2.5	203.4	6.5	174.1	76.2	205.9	2.5	NA
SFO-158-5	206	19024	1.1	20.6652	3.6	0.2192	3.6	0.0329	0.7	0.20	208.4	1.5	201.2	6.6	118.4	84.1	208.4	1.5	NA
SFO-158-6	354	42782	1.3	19.8880	2.5	0.2327	3.8	0.0336	2.9	0.76	212.9	6.1	212.5	7.3	208.0	57.9	212.9	6.1	NA
SFO-158-7	137	16671	1.7	20.6693	7.3	0.2290	7.6	0.0343	2.1	0.27	217.6	4.4	209.4	14.3	117.9	172.1	217.6	4.4	NA
SFO-158-8	188	8476	1.3	20.3828	7.2	0.2226	8.0	0.0329	3.4	0.43	208.7	7.0	204.1	14.8	150.8	169.4	208.7	7.0	NA
SFO-158-9	278	38003	1.0	20.0911	4.3	0.2227	4.9	0.0325	2.4	0.49	205.9	4.8	204.2	9.1	184.4	99.7	205.9	4.8	NA
SFO-158-10	241	21298	1.0	19.5040	4.9	0.2234	5.4	0.0316	2.3	0.42	200.6	4.5	204.7	10.0	253.1	112.4	200.6	4.5	NA
SFO-158-11	140	22221	1.6	19.5331	4.7	0.2318	5.2	0.0328	2.2	0.43	208.3	4.6	211.7	10.0	249.6	109.0	208.3	4.6	NA
SFO-158-13	642	33086	2.3	20.0032	1.4	0.2077	5.0	0.0301	4.8	0.96	191.4	9.0	191.6	8.7	194.6	32.6	191.4	9.0	NA
SFO-158-14	152	1677	1.5	16.5994	21.2	0.2828	22.4	0.0340	7.1	0.32	215.8	15.1	252.9	50.1	612.3	463.4	215.8	15.1	NA
SFO-158-15	120	34615	1.9	18.5745	9.6	0.2422	10.0	0.0326	2.9	0.29	206.9	5.8	220.2	19.8	364.2	216.3	206.9	5.8	NA
SFO-158-16	131	26959	1.5	20.1633	10.6	0.2176	10.7	0.0318	1.5	0.14	201.9	3.0	199.9	19.4	176.0	246.9	201.9	3.0	NA
SFO-158-17	381	34733	1.2	19.8659	3.9	0.2022	6.6	0.0291	5.4	0.81	185.1	9.8	187.0	11.3	210.6	90.2	185.1	9.8	NA
SFO-158-18	124	19587	1.7	20.6818	7.2	0.2126	7.4	0.0319	1.9	0.25	202.4	3.7	195.7	13.2	116.5	168.9	202.4	3.7	NA
SFO-158-19	345	32164	1.4	19.8574	4.5	0.2284	5.1	0.0329	2.4	0.47	208.7	4.9	208.9	9.7	211.6	104.9	208.7	4.9	NA
SFO-158-20	265	21026	2.5	19.8800	2.7	0.2294	3.7	0.0331	2.5	0.68	209.8	5.2	209.7	7.0	208.9	63.3	209.8	5.2	NA
SFO-158-21	113	8689	1.7	20.4694	14.9	0.2159	15.2	0.0321	3.0	0.20	203.4	5.9	198.5	27.3	140.8	350.6	203.4	5.9	NA
SFO-158-22	144	7197	1.6	20.2430	10.7	0.2106	11.0	0.0309	2.5	0.22	196.3	4.8	194.1	19.4	166.8	251.1	196.3	4.8	NA
SFO-158-23	229	24741	1.1	19.5380	3.2	0.2394	4.2	0.0339	2.8	0.66	215.1	5.9	217.9	8.2	249.0	72.7	215.1	5.9	NA
SFO-158-24	83	5601	1.9	21.2185	13.1	0.2100	13.8	0.0323	4.4	0.31	205.1	8.8	193.6	24.4	55.8	314.4	205.1	8.8	NA
SFO-158-25	105	23614	1.5	20.1547	6.7	0.2200	7.3	0.0322	2.8	0.38	204.1	5.6	201.9	13.3	177.0	156.3	204.1	5.6	NA
SFO-158-26	127	34194	1.9	20.8011	4.4	0.2181	4.8	0.0329	2.1	0.44	208.7	4.4	200.3	8.8	102.9	102.9	208.7	4.4	NA
SFO-158-27	187	45638	1.6	19.8325	5.0	0.2216	5.3	0.0319	1.5	0.29	202.3	3.0	203.3	9.7	214.5	116.4	202.3	3.0	NA
SFO-158-28	312	43930	1.2	20.2754	2.7	0.2095	3.2	0.0308	1.7	0.53	195.6	3.2	193.1	5.5	163.1	62.5	195.6	3.2	NA
SFO-158-29	220	31143	1.8	18.9564	4.7	0.2404	6.0	0.0331	3.7	0.62	209.7	7.6	218.8	11.8	318.2	107.1	209.7	7.6	NA
SFO-158-30	198	34373	1.0	20.4395	3.5	0.2133	4.0	0.0316	1.8	0.45	200.7	3.5	196.3	7.1	144.2	82.7	200.7	3.5	NA

				Isotope ratios							Apparent ages (Ma)								
Sample	U	206Pb	U/Th	206Pb*	±	207Pb*	±	206Pb*	±	error	206Pb*	±	207Pb*	±	206Pb*	±	Best age	±	Conc
SFO-159	(ppm)	204Pb		207Pb*	(%)	235U*	(%)	238U	(%)	corr.	238U*	(Ma)	235U	(Ma)	207Pb*	(Ma)	(Ma)	(Ma)	(%)
SFO-159-1	165	7872	1.1	20.5103	5.1	0.2629	5.3	0.0391	1.1	0.22	247.3	2.8	237.0	11.1	136.1	120.5	247.3	2.8	NA
SFO-159-2	121	9905	1.5	20.2367	7.8	0.2704	8.0	0.0397	1.5	0.19	250.9	3.7	243.0	17.3	167.6	183.5	250.9	3.7	NA
SFO-159-3	130	11019	1.3	19.9350	6.6	0.2635	6.8	0.0381	1.6	0.24	241.0	3.9	237.5	14.5	202.6	154.3	241.0	3.9	NA
SFO-159-4	141	11560	1.3	19.6322	5.3	0.2763	5.6	0.0393	1.9	0.34	248.7	4.7	247.7	12.4	238.0	122.2	248.7	4.7	NA
SFO-159-5	148	21001	1.1	20.1495	5.6	0.2639	5.9	0.0386	2.0	0.34	244.0	4.8	237.8	12.6	177.6	130.0	244.0	4.8	NA

SFO-159-6	184	37099	1.4	19.1355	4.5	0.2848	4.6	0.0395	1.0	0.22	249.9	2.5	254.5	10.3	296.8	101.7	249.9	2.5	NA
SFO-159-7	222	50059	1.6	18.9627	4.1	0.2905	4.6	0.0399	2.2	0.48	252.5	5.4	258.9	10.5	317.4	92.1	252.5	5.4	NA
SFO-159-8	150	22174	1.4	19.2153	2.7	0.2713	3.2	0.0378	1.7	0.53	239.2	4.1	243.7	7.0	287.2	62.8	239.2	4.1	NA
SFO-159-9	117	23276	1.4	20.2209	7.4	0.2675	7.5	0.0392	1.5	0.20	248.1	3.7	240.7	16.2	169.4	172.5	248.1	3.7	NA
SFO-159-10	235	5325	3.8	19.1216	4.7	0.2480	5.0	0.0344	1.5	0.31	218.0	3.3	224.9	10.0	298.4	107.7	218.0	3.3	NA
SFO-159-10	187	7590	1.7	19.2839	3.8	0.2733	4.0	0.0382	1.4	0.34	241.9	3.2	245.4	8.8	279.1	87.2	241.9	3.2	NA
SFO-159-11	138	24936	1.2	20.1456	4.8	0.2607	5.0	0.0381	1.5	0.31	241.0	3.6	235.2	10.5	178.1	111.2	241.0	3.6	NA
SFO-159-12	155	20581	1.8	19.7178	4.3	0.2690	4.9	0.0385	2.4	0.48	243.4	5.6	241.9	10.5	227.9	99.2	243.4	5.6	NA
SFO-159-13	167	15224	1.5	20.4051	5.4	0.2663	5.5	0.0394	1.0	0.19	249.2	2.5	239.8	11.7	148.2	125.8	249.2	2.5	NA
SFO-159-14	112	13449	1.4	20.8910	6.4	0.2617	6.5	0.0397	1.4	0.22	250.7	3.5	236.1	13.8	92.7	151.4	250.7	3.5	NA
SFO-159-15	86	22787	1.4	19.1620	11.0	0.2912	11.5	0.0405	3.6	0.31	255.7	9.0	259.5	26.4	293.6	250.8	255.7	9.0	NA
SFO-159-16	117	22242	1.6	19.9645	8.6	0.2745	8.9	0.0397	2.2	0.25	251.3	5.5	246.3	19.4	199.1	199.2	251.3	5.5	NA
SFO-159-17	201	5173	1.0	19.3785	6.4	0.2814	6.7	0.0396	2.2	0.32	250.0	5.3	251.8	15.0	267.9	146.8	250.0	5.3	NA
SFO-159-18	185	22390	1.3	19.7072	4.1	0.2712	4.3	0.0388	1.6	0.36	245.1	3.8	243.6	9.4	229.1	93.6	245.1	3.8	NA
SFO-159-19	188	12240	1.2	19.8905	4.6	0.2705	4.8	0.0390	1.4	0.29	246.8	3.3	243.1	10.3	207.8	106.1	246.8	3.3	NA
SFO-159-20	160	27672	0.8	18.7075	5.3	0.2887	6.0	0.0392	2.7	0.45	247.7	6.5	257.6	13.6	348.1	120.8	247.7	6.5	NA
SFO-159-21	125	27596	1.3	19.5677	5.8	0.2864	6.3	0.0406	2.6	0.40	256.9	6.4	255.7	14.3	245.5	133.3	256.9	6.4	NA
SFO-159-22	154	13411	1.2	20.4547	6.1	0.2646	6.3	0.0393	1.8	0.28	248.2	4.4	238.4	13.5	142.5	142.7	248.2	4.4	NA
SFO-159-23	125	9914	1.5	20.5415	6.3	0.2418	6.7	0.0360	2.1	0.32	228.1	4.7	219.9	13.2	132.5	149.4	228.1	4.7	NA
SFO-159-24	126	17962	1.2	19.6882	5.8	0.2769	5.9	0.0395	1.1	0.18	250.0	2.6	248.2	12.9	231.4	133.3	250.0	2.6	NA
SFO-159-25	116	24618	1.7	19.2887	6.6	0.2792	7.0	0.0391	2.3	0.33	247.0	5.7	250.0	15.6	278.6	151.7	247.0	5.7	NA
SFO-159-26	119	18770	1.2	19.6166	6.7	0.2839	8.4	0.0404	5.1	0.60	255.3	12.7	253.8	18.9	239.8	154.3	255.3	12.7	NA
SFO-159-27	161	35286	1.3	19.6374	2.5	0.2790	2.8	0.0397	1.3	0.48	251.2	3.3	249.9	6.3	237.3	57.3	251.2	3.3	NA
SFO-159-28	138	18093	1.6	21.1006	5.6	0.2585	5.8	0.0396	1.3	0.22	250.1	3.2	233.5	12.1	69.0	134.1	250.1	3.2	NA
SFO-159-29	109	20946	1.4	20.0292	6.0	0.2691	6.3	0.0391	2.0	0.32	247.2	5.0	242.0	13.6	191.6	138.6	247.2	5.0	NA
SFO-159-30	190	44185	1.1	19.5436	2.7	0.2766	3.0	0.0392	1.3	0.44	247.9	3.3	247.9	6.7	248.4	62.9	247.9	3.3	NA
SFO-159-31	123	16808	1.1	19.4839	8.1	0.2818	8.2	0.0398	1.1	0.13	251.7	2.6	252.1	18.2	255.4	186.6	251.7	2.6	NA
SFO-159-32	155	23095	1.3	20.1359	7.2	0.2274	7.5	0.0332	2.0	0.27	210.6	4.1	208.1	14.0	179.2	167.6	210.6	4.1	NA
SFO-159-33	160	24101	1.2	19.8322	4.4	0.2759	5.2	0.0397	2.9	0.55	250.9	7.0	247.4	11.5	214.6	101.2	250.9	7.0	NA
SFO-159-34	101	10610	1.3	20.0674	12.2	0.2712	12.4	0.0395	2.2	0.18	249.6	5.4	243.7	26.9	187.1	284.8	249.6	5.4	NA
SFO-159-35	119	12479	1.0	18.8460	6.2	0.2850	6.5	0.0390	2.0	0.30	246.4	4.7	254.6	14.7	331.5	141.5	246.4	4.7	NA
SFO-159-36	250	43218	2.0	19.7585	1.6	0.2781	1.8	0.0399	0.8	0.45	251.9	2.0	249.2	4.0	223.2	37.0	251.9	2.0	NA
SFO-159-37	224	23530	1.7	19.4380	3.3	0.2810	3.6	0.0396	1.5	0.40	250.5	3.6	251.5	8.1	260.8	76.8	250.5	3.6	NA
SFO-159-38	189	34660	2.0	19.5124	2.7	0.2793	2.9	0.0395	1.2	0.41	249.9	2.9	250.1	6.5	252.1	61.4	249.9	2.9	NA
SFO-159-39	162	24065	2.1	19.8481	3.5	0.2789	3.6	0.0401	0.5	0.15	253.7	1.3	249.8	7.9	212.7	81.6	253.7	1.3	NA
SFO-159-40	110	37319	1.6	20.0334	10.5	0.2771	10.6	0.0403	1.3	0.13	254.4	3.3	248.3	23.3	191.1	244.8	254.4	3.3	NA

Anexo 2

Material suplementario publicado en línea del artículo:

Sarmiento-Villagrana, A., Vega-Granillo, R., Talavera-Mendoza, O., Salgado-Souto, S., Gomez-Landa, J.R., 2017, Geochemical and isotopic study of Mesozoic magmatism in the Sonobari Complex, western Mexico: Implications for the tectonic evolution of southwestern North America

Material:

S1. Datos analíticos de edades U-Pb.

S2. Localización y descripciones petrográficas.

S3 y S4. Concentración de elementos mayores y tierras raras.

S4. Datos isotópicos de Nd, Sr y Pb.

ELECTRONIC SUPPLEMENT
for the article

Geochemical and isotopic study of Mesozoic magmatism in the Sonobari Complex western Mexico: Implications for the tectonic evolution of southwestern North America

by

Alicia Sarmiento-Villagrana1*, Ricardo Vega-Granillo2, Oscar Talavera-Mendoza3, Sergio Adrián Salgado-Souto3, Juan René Gómez-Landa2

TABLE S1. U-Pb GEOCHRONOLOGIC ANALYSIS OF SAMPLE SFO-14 CAPOMOS GRANODIORITE

Analysis	U (ppm)	206Pb 204Pb	U/Th	Isotope ratios 206Pb* 207Pb*	± (%)	207Pb* 235U*	± (%)	206Pb* 238U	± (%)	error corr.	Apparent ages (Ma) 206Pb* 238U*	± (Ma)	207Pb* 235U	± (Ma)	206Pb* 207Pb*	± (Ma)	Best age (Ma)	± (Ma)	Conc (%)
SFO14-19	110	1754	1.2	17.7016	31.1	0.1085	32.4	0.0139	9.0	0.28	89.2	8.0	104.6	32.2	471.7	704.9	89.2	8.0	NA
SFO14-17	95	2661	2.3	21.7258	26.8	0.0930	28.1	0.0147	8.3	0.30	93.8	7.7	90.3	24.3	-0.9	656.4	93.8	7.7	NA
SFO14-10	152	2416	1.7	24.0979	29.2	0.0839	29.7	0.0147	5.5	0.18	93.9	5.1	81.8	23.4	-256.9	753.1	93.9	5.1	NA
SFO14-13	125	7116	2.3	27.1778	44.5	0.0756	45.6	0.0149	10.0	0.22	95.3	9.5	74.0	32.6	-571.5	1254.8	95.3	9.5	NA
SFO14-7	274	5805	1.7	22.5890	13.8	0.0918	14.1	0.0150	3.1	0.22	96.3	3.0	89.2	12.1	-95.7	339.9	96.3	3.0	NA
SFO14-4	123	2224	2.1	20.9173	24.0	0.0994	24.3	0.0151	3.7	0.15	96.5	3.5	96.2	22.3	89.8	575.3	96.5	3.5	NA
SFO14-2	211	4374	1.6	22.9720	17.3	0.0906	17.5	0.0151	2.5	0.14	96.5	2.4	88.0	14.7	-137.1	431.0	96.5	2.4	NA
SFO14-11	180	9372	1.4	18.6230	23.2	0.1123	24.1	0.0152	6.5	0.27	97.1	6.3	108.1	24.7	358.3	529.3	97.1	6.3	NA
SFO14-3	135	3573	2.0	25.0975	54.4	0.0841	54.5	0.0153	3.8	0.07	98.0	3.7	82.0	43.0	-361.0	1507.7	98.0	3.7	NA
SFO14-11	213	7473	1.6	24.6274	24.2	0.0859	24.8	0.0154	5.7	0.23	98.2	5.6	83.7	20.0	-312.3	627.0	98.2	5.6	NA
SFO14-15	197	5781	1.6	22.0533	22.1	0.0965	22.3	0.0154	3.1	0.14	98.8	3.0	93.6	20.0	-37.1	542.7	98.8	3.0	NA
SFO14-5	134	5595	1.8	23.3812	30.5	0.0911	32.0	0.0154	9.6	0.30	98.8	9.4	88.5	27.1	-181.0	776.5	98.8	9.4	NA
SFO14-1	146	5820	1.9	23.9060	20.1	0.0891	20.4	0.0154	3.9	0.19	98.8	3.8	86.7	17.0	-236.7	510.8	98.8	3.8	NA
SFO14-23	132	11257	1.7	20.8745	18.2	0.1027	20.0	0.0155	8.4	0.42	99.4	8.3	99.2	18.9	94.6	433.2	99.4	8.3	NA
SFO14-21	108	3012	2.5	28.7275	33.8	0.0747	34.2	0.0156	4.7	0.14	99.6	4.6	73.2	24.1	-723.8	967.1	99.6	4.6	NA
SFO14-14	164	13746	2.7	26.4393	32.3	0.0812	32.7	0.0156	5.4	0.17	99.6	5.3	79.3	25.0	-497.7	877.0	99.6	5.3	NA
SFO14-6	285	6242	1.6	21.6096	16.1	0.1021	16.5	0.0160	3.7	0.23	102.3	3.8	98.7	15.5	12.0	389.4	102.3	3.8	NA
SFO14-20	153	12199	1.9	26.7919	34.2	0.1088	34.4	0.0211	3.6	0.11	134.9	4.8	104.9	34.3	-533.0	940.3	134.9	4.8	NA
SFO14-16	783	6930	1.9	19.3187	3.9	0.1574	4.8	0.0221	2.6	0.56	140.6	3.7	148.4	6.6	275.0	90.5	140.6	3.7	NA
SFO14-8	467	16848	1.1	19.6803	7.4	0.1670	7.5	0.0238	1.5	0.20	151.9	2.3	156.8	11.0	232.3	170.5	151.9	2.3	NA
SFO14-18	704	19215	2.3	19.1151	3.1	0.2027	3.3	0.0281	1.1	0.35	178.6	2.0	187.4	5.6	299.2	70.1	178.6	2.0	NA
SFO14-9	203	11640	1.5	17.8454	6.1	0.4026	7.2	0.0521	3.8	0.53	327.4	12.2	343.5	21.1	453.8	136.2	327.4	12.2	NA

UTM locati 746017
Zone 12R 3E+06

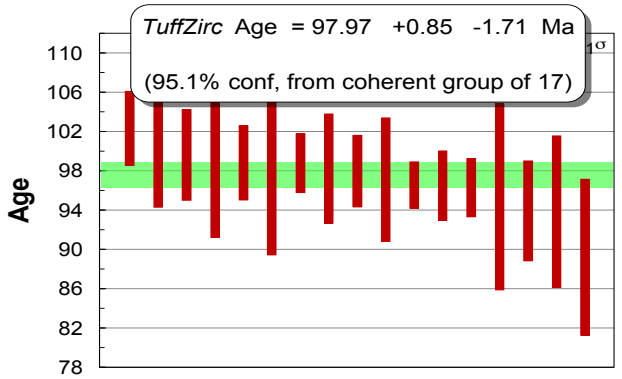

TABLE S2. LOCATION AND PETROGRAPHIC DESCRIPTION OF SAMPLES FROM SONOBARI COMPLEX, NORTHWESTERN MEXICO

Sample	UTM		Petrography	Mineral assemblage	Accessory and secondary minerals	Age(Ma)*
Western Sonobari Complex	**E**	**N**				
Early Triassic (orthogneisses)						
SFO-55	686235	2935748	Medium-grained mesocratic gneisses with isoclinal folding. These rocks are migmatized.	Pl + Bt + Amp + Qtz + Ep	Sph + Zr - Chl + Ms	
SFO-56	686235	2935748		Pl + Bt + Amp + Qtz + Ep	Sph + Zr - Chl + Ms	241.3 ± 1.2 U-Pb [1]
SFO-159	707809	2918858		Pl + Qtz + Bt + Amp + Ep	Sph + Zr + Ap	249.6 ± 2.1 U-Pb [1]
SFO-159A	707809	2918858		Pl + Qtz + Bt + Amp + Ep	Sph + Zr + Ap	
Late Triassic (orthogneisses)						
SFO-4	710652	2913886	Medium-grained leucocratic gneisses with typical banded structure. Locally, these rocks are overprinted by migmatization with selvedge structures and ptygmatic folding.	Pl + Qtz + Amp + Bt + Kfs	Sph + Zr + Ilm - Ep	
SFO-5	710515	2913490		Pl + Qtz + Bt + Ep	Zr - Chl	205.9 ± 2.9 U-Pb [1]
SFO-20	710652	2913886		Pl + Qtz + Bt + Kfs + Ep	Zr + Ap - Chl	207.4 ± 2.5 U-Pb [1]
SFO-154	710382	2908478		Pl + Bt + Qtz + Ep	Zr + Ilm - Chl	203.7 ± 2.4 U-Pb [1]
SFO-155	710474	2907659		Qtz + Pl + Bt + Ms	Zr + Ilm - Chl	213.7 ± 2.8 U-Pb [1]
SFO-158	710536	2907194		Pl + Qtz + Bt + Pl	Zr - Chl	205.5 ± 2.6 U-Pb [1]
Late Jurassic (orthogneisses)						
SFO-63	686202	2923555	Medium-grained leucocratic and mesocratic orthogneisses with well-developed foliation and crenulation. Locally, these rocks are migmatized with stromatic and patch structures.	Bt + Amp + Pl + Qtz + Ep	Zr - Ser + Chl	161.0 ± 0.3 U-Pb [1]
SFO-64	686706	2923093		Qtz + Pl + Bt + Ms	Zr + Ap	
SFO-112	685013	2923976		Qtz + Pl + Bt + Ms + Ep	Sph + Zr	
SFO-114	686202	2923555		Bt + Amp + Pl + Qtz + Ep	Zr - Ser + Chl	
SFO-121	685220	2924370		Pl + Qtz + Bt + Ep + Ms	Zr - Ser	159.1 ± 1.1 U-Pb [1]
SFO-152	710928	2910966		Qtz + Pl + Bt + Ep	Zr + Ilm - Chl	160.1 ± 0.6 U-Pb [1]
Post-Late Jurassic pre-Late Cretaceous (amphibolites)						
SFO-3	710652	2913886	Dark medium-grained amphibolites with well-developed continuous foliation defined by amphibole and biotite. Mylonitic deformation is overprinted in some rocks. Locally, these rocks show lenses with pegmatitic texture.	Pl + Amp + Bt + Qtz + Ep	Sph + Ilm - Chl	
SFO-18	709968	2913888		Pl + Amp + Bt + Qtz + Ep	Sph	
SFO-59	687809	2932819		Pl + Amp + Qtz + Ep	Sph + Ilm	
SFO-113	685011	2923967		Pl + Amp + Qtz + Bt + Ep	Sph	
SFO-118	687195	2928659		Pl + Amp + Bt + Ep	Sph + Ilm - Chl + Ms	
SFO-120	682004	2924010		Pl + Amp + Qtz + Ep	Sph - Chl	
SFO-126	686331	2923570		Pl + Amp + Qtz + Ilm	Sph	
Cenomanian (basic and ultrabasic rocks)						
SFO-39	711772	2922842	Dark coarse-grained undeformed gabbros, hornblendites and pyroxenites. Samples SFO-136 and SFO-138 are medium-grained leucocratic diorites. The first sample is undeformed rock. The second sample shows a penetrative foliation.	Amp + Pl + Ep	Rt + Sph + Ilm - Chl	
SFO-61	687050	2929825		Amp + Pl	Sph	
SFO-115	687190	2928680		Cpx	Talc + Tr + Ox - Chl	
SFO-116	687190	2928680		Amp + Pl + Cpx	Chl + Talc	
SFO-119	687190	2928680		Amp + Cpx + Pl	Ilm - Talc + Chl	

SFO-135	687358	2930299		Amp + Cpx + Pl	Sph + Rt + Ilm	
SFO-137	687311	2930288		Amp + Cpx + Pl	Sph	
SFO-136	687358	2930299		Pl + Amp + Qtz + Cpx	Sph + Zr + Rt + Ap	99.9 ± 1.6 U-Pb [1]
SFO-138	687942	2930260		Pl + Amp + Qtz + Kfs + Bt	Zr + Ilm - Ms + Chl	98.8 ± 1.6 U-Pb [1]
Campanian (leucocratic dikes)						
SFO-2	710652	2913886	Medium-grained leucocratic granites with magmatic foliation.	Qtz + Pl + Bt + Kfs + Grt	Ep + Zr + Ilm	80.6 ± 1.7 U-Pb [1]
SFO-58	686235	2935748		Qtz + Pl + Ms + Bt		
Paleocene (Los Parajes)						
SFO-40	711848	2923026	Medium-grained diorite with inequigranular-hypidiomorphic texture.	Pl + Qtz + Kfs + Bt + Amp	Ep + Zr - Chl	64 ± 10 U-Pb [2]
Eastern Sonobari Complex						
Late Jurassic (Realito = R; Topaco = T; Cubampo = C)						
SFO-12 (R)	752779	2919808	This pulse includes mafic and felsic rocks. Mafic rocks are undeformed coarse-grained gabbros and pyroxenites. Felsic rocks are medium to fine-grained with brittle deformation.	Cpx + Amp + Pl	Ilm - Chl + Ep	161U-Pb [3]
SFO-45 (R)	752907	2919831		Amp + Px	Ilm - Chl + Ep	
SFO-11 (T)	748361	2926033		Pl + Amp + Qtz	- Chl + Ep	
SFO-29 (T)	745720	2930931		Pl + Amp + Qtz	- Chl + Ep + Cc	
SFO-30 (T)	747695	2930763		Pl + Amp + Qtz	- Chl + Ep + Cc	
SFO-24 (C)	740353	2934245		Qtz + Pl + Bt + Ms	Zr - Ser	154.8 ± 4 U-Pb [4]
SFO-44 (C)	749993	2922211		Qtz + Pl + Ms + Bt + Kfs	Zr - Ser	150.8 ± 3 U-Pb [4]
HKM-02** (C)				Qtz + Pl + Bt	Zr - Ser	
Cenomanian (Capomos)						
SFO-14	746017	2925790	Medium-grained granodiorite with inequigranular-holocrystalline texture.	Pl + Qtz + Amp + Bt	Zr + Ap - Chl	97.9 U-Pb [3]
Campanian (Guamuchil)						
SFO-32	750860	2930110	Dark fine-grained mafic rocks with porphyritic texture.	Pl + Qtz + Amp	- Tr + Bt + Chl	73 ± 1.5 U-Pb [5]

*References: (1) Sarmiento et al., 2016; (2) Vega-Granillo et al., 2013; (3) this work; (4) Vega-Granillo et al., 2008; (5) Vega-Granillo et al., 2012.

Note: Qtz=Quartz, Pl=Plagioclase, Bt-=Biotite, Ms=Muscovite, Amp=Amphibole, Grt=Garnet, Ep=Epidote, Kfs=K-feldspar, Sph=Sphene, Zr=Zircon, Ap=Apatite, Ox=oxide, Tr=Tremolite, Ilm=Ilmenite, Cpx=Clinopyroxene, Chl=Chlorite, Rt=Rutile, Ser=Sericite, Cc=Calcite.

Note: UTM Zone 12R.

Table S3. Major and trace elment concentrations of samples from Western Sonobari Complex, northwestern Mexico.

Age	Early Triassic orthogneisses				Late Triassic orthogneisses						
Sample	SFO-55	SFO-56	SFO-159	SFO-159A	SFO-4	SFO-5	SFO-20	SFO-154	SFO-155	SFO-158	SFO-63
E	686,235	686,235	707,809	707,809	710,652	710,515	710,652	710,382	710,474	710,536	686,202
N	2,935,748	2,935,748	2,918,858	2,918,858	2,913,886	2,913,490	2,913,886	2,908,478	2,907,659	2,907,194	2,923,555
Ref**	1	1	1	1	1	1	1	1	1	1	1
SiO2 (wt %)	49.7	61.3	62.3	49.1	60.4	73	72.6	61.9	74.9	70	55.4
TiO2	1.04	0.58	0.54	1.65	0.52	0.22	0.19	0.55	0.16	0.37	0.6
Al2O3	19.6	17.25	17	15	14.85	13.95	14.6	14.1	13.5	15.85	17.05
FeO_T	9.02	6.07	5.96	13.1	5.86	2.16	1.68	8.76	1.53	2.96	8.43
MnO	0.15	0.09	0.1	0.21	0.08	0.03	0.02	0.19	0.03	0.04	0.1
MgO	5.24	2.79	2.78	6.51	4.43	0.7	0.62	3.86	0.67	1.09	5.44
CaO	9.29	6.39	5.73	10.7	7.77	2.47	3.22	2.08	1.14	2.92	5.77
Na2O	3.78	3.57	3.25	2.75	3.36	3.54	4.43	2.12	4.49	4.9	4.31
K2O	0.42	1.57	1.58	0.91	0.68	2.72	0.96	3.38	2.27	1.45	1.87
P2O5	0.26	0.21	0.16	0.22	0.13	0.07	0.05	0.13	0.04	0.1	0.09
LOI	1.4	1.37	0.72	0.55	0.83	0.55	0.46	2.02	0.41	0.48	1.13
Total	100.03	101.35	100.29	100.79	98.98	99.63	98.93	99.27	99.27	100.26	100.3
Cs (ppm)	0.33	1	1.27	0.19	0.22	0.55	0.34	1.49	0.35	0.67	0.75
Rb	8.3	50.8	52.2	9.5	12	56.6	25	106.5	49.2	50.7	47.3
Sr	644	607	608	229	259	241	341	118.5	136.5	239	303
Ba	396	806	853	235	209	1755	543	1340	948	630	535
V	223	139	142	345	154	32	29	126	16	55	158
Cr	30	10	10	180	140	10	10	20	<10	10	50
Ni	19	10	10	76	51	1	3	16	<1	1	31
Co	24	16	18	46	16	3	4	27	4	8	25
Zn	125	62	88	132	33	19	5	90	21	30	47
Sc	18	15	16	46	17	4	4	14	4	8	24
Cu	49	22	17	42	24	<1	27	5	2	1	<1
Li	10	10	20	10	<10	10	10	20	10	10	10
Th	<0.05	4.83	1.79	0.86	6.97	12.25	9.41	7.28	12.1	8.22	3.32
U	<0.05	2.46	0.65	0.26	1.46	2.98	2.19	3.6	1.6	1.78	0.76
Pb	<2	4	10	3	6	3	<2	2	2	2	<2
Y	15.6	15.1	11.4	29.6	18.9	13.4	11.1	18.2	15.7	17.8	17.4
Nb	3.1	7.4	6.6	2.5	3.1	6.2	6.4	4.9	8.4	5.8	3.7
Ga	21.1	18.3	19	20.5	16.5	13.8	13.6	20.8	13.7	15.2	16.1
Ta	0.1	0.6	0.4	0.2	0.3	0.3	0.5	0.4	0.6	0.6	0.3
Zr	66	105	140	103	120	140	103	144	149	152	82
Hf	1.8	2.7	3.6	2.7	3.2	3.9	3.1	3.9	4.4	4	2.2
La	6.4	15.7	8.5	7.2	24.5	25.6	20.6	19.9	26.9	25.3	9.7
Ce	17	32.3	18.7	18.8	45.2	42.9	36	39.8	52.3	48.3	21.7
Pr	2.7	4.23	2.31	2.74	5.07	4.54	3.82	4.52	5.45	5.21	3.03
Nd	13.8	18.1	10.7	14.8	18.7	15.1	13	18.5	19.3	19.6	13.1
Sm	3.68	3.82	2.47	4.28	3.83	2.78	2.37	3.88	3.83	3.66	2.92
Eu	1.08	0.94	0.76	1.36	1.05	0.68	0.49	1.08	0.48	0.91	0.81
Gd	3.33	3.09	2.28	5.16	3.75	2.16	2.06	3.52	3.08	3.12	2.89
Tb	0.5	0.47	0.37	0.85	0.52	0.36	0.29	0.56	0.47	0.49	0.47
Dy	3.07	2.65	2.06	5.19	3.19	2.17	1.87	3.3	2.78	3.09	2.93
Ho	0.57	0.56	0.39	1.16	0.66	0.44	0.38	0.68	0.57	0.65	0.65
Er	1.74	1.61	1.15	3.34	1.81	1.26	1.29	1.98	1.79	1.87	1.85
Tm	0.2	0.23	0.17	0.49	0.28	0.2	0.19	0.26	0.25	0.27	0.26
Yb	1.55	1.51	1.28	3.23	1.72	1.29	1.03	1.91	1.7	1.78	1.89
Lu	0.22	0.2	0.21	0.45	0.29	0.21	0.16	0.28	0.29	0.3	0.27
Mg#	31.81	33.20	36.75	31.49	43.05	24.48	26.96	30.59	30.45	26.91	39.22
$(Rb/Yb)_N$	31.66	2.28	4.16	26.12	5.42	34.06	18.84	43.29	22.47	22.11	19.43
$(La/Yb)_N$	4.48	1.50	2.79	7.02	9.61	13.39	13.50	7.03	10.68	9.59	3.46
Eu/Eu*	0.98	0.88	0.94	0.84	0.85	0.85	0.68	0.89	0.43	0.82	0.85

References**= 1 (This study).

N.D.-no data.

FeO_T=fierro total.

Note: UTM Zone 12R.

Table S3 (cont.). Major and trace elment concentrations of samples from Western Sonobari Complex, northwestern Mexico.

Age	Late Jurassic orthogneisses					Post-Late Jurassic pre-Cenomanian amphibolite dikes					
Sample	SFO-64	SFO-112	SFO-114	SFO-121	SFO-152	SFO-3	SFO-18	SFO-59	SFO-113	SFO-118	SFO-120
Location	686,706	685,013	686,202	685,220	710,928	710,652	709,968	687,809	685,011	687,195	682,004
N	2,923,093	2,923,976	2,923,555	2,924,370	2,910,966	2,913,886	2,913,888	2,932,819	2,923,967	2,928,659	2,924,010
Ref**	1	1	1	1	1	1	1	1	1	1	1
SiO2 (wt %	78.9	75.9	57.1	70.6	63.2	51.9	54.9	47.3	58.6	51.2	50.4
TiO2	0.28	0.28	0.58	0.42	0.67	0.89	1.45	2.93	1.29	0.97	1.63
Al2O3	12.35	14.1	17.1	14.6	14.95	16	14.8	12.9	17.3	17.8	16.15
FeO_T	2.02	1.28	8.66	3.65	7.96	9.77	13.2	16.9	4.97	8.62	9.52
MnO	0.05	0.02	0.1	0.03	0.11	0.15	0.24	0.19	0.05	0.14	0.11
MgO	0.61	0.61	5.29	1.16	4.5	5.39	4.71	5.91	3.27	4.76	7.16
CaO	0.39	2.66	5.55	2.66	2.01	9.31	8.07	6.1	8.66	8.4	11.55
Na2O	5.87	4.63	4.18	3.75	3.48	3.01	2.51	3.98	4.62	3.48	3.57
K2O	0.89	0.64	2.01	1.43	3.47	1.15	0.64	0.52	0.38	1.02	0.59
P2O5	0.03	0.05	0.08	0.12	0.16	0.15	0.3	0.58	0.32	0.31	0.29
LOI	0.44	0.85	1.18	0.8	0.7	1.07	0.85	1.1	0.57	1.38	0.9
Total	101.88	101.07	101.95	99.34	101.38	98.86	101.73	98.47	100.09	98.23	101.94
Cs (ppm)	0.1	0.7	0.83	0.66	3.28	0.39	0.12	0.5	0.04	0.21	0.08
Rb	20.2	27.7	53.8	54.5	110.5	22	11.3	15	3.9	14.8	5.5
Sr	47	269	290	266	139.5	259	241	171.5	440	671	291
Ba	339	193	551	733	1190	283	215	104	107	495	95.7
V	<5	28	160	63	121	263	395	339	252	202	355
Cr	<10	10	50	10	40	70	30	180	20	40	140
Ni	<1	4	28	6	14	30	38	113	23	21	63
Co	2	2	23	11	30	34	26	46	11	26	20
Zn	33	16	44	36	68	61	68	180	59	88	117
Sc	11	5	24	9	21	35	35	40	25	16	33
Cu	46	1	6	1	20	32	6	2	1	3	<1
Li	10	10	10	20	20	10	10	10	<10	10	<10
Th	7.68	13.5	2.93	16.65	5.92	1.82	3.56	0.86	6.24	0.35	1.81
U	1.83	2.64	0.64	3.46	2.08	0.92	1.12	0.33	2.82	0.13	2.7
Pb	3	3	2	3	<2	7	<2	8	<2	<2	<2
Y	31.5	24.4	17.5	21.7	20.8	20.4	29.6	52.2	30.8	13.9	32.6
Nb	8.2	11.2	3.4	5.9	6.1	2	5.7	4.1	6.9	2.8	4.3
Ga	12.7	13.7	17.3	14.9	18.1	16.9	19	20.8	16.8	21.7	20.6
Ta	0.4	1	0.2	0.3	0.4	0.1	0.3	0.3	0.5	0.2	0.3
Zr	232	201	78	196	120	75	124	218	150	35	109
Hf	6.2	5.6	1.9	5.2	3.1	2.1	3.3	5.4	4	1.1	2.8
La	39	25.8	7.9	40	21.5	7.6	16.3	15.4	12.4	10	9.5
Ce	69.2	49.6	18.9	77.8	41.4	18.3	34.2	38.8	30	21.4	29.4
Pr	8.58	5.51	2.5	8.43	4.74	2.72	4.65	6.09	4.09	2.96	4.43
Nd	35.3	20.4	11.6	32.5	19.9	12.4	20.6	29.7	20.6	14.9	21.8
Sm	7.81	4.01	2.87	5.99	4.38	3.64	4.61	8.19	5.45	3.39	5.65
Eu	1.39	0.53	0.78	1.02	1.14	1.22	1.62	2.72	1.15	1.28	1.38
Gd	6.36	3.77	3.28	5.49	4.33	3.98	5.56	9.05	5.87	3.42	6.43
Tb	0.92	0.6	0.49	0.79	0.61	0.59	0.91	1.51	0.9	0.49	1.03
Dy	5.48	3.98	2.98	4.32	3.84	3.67	5.31	9.3	5.54	2.83	6.26
Ho	1.09	0.83	0.67	0.87	0.84	0.74	1.13	1.97	1.2	0.52	1.31
Er	3.46	2.43	2.04	2.12	2.29	2.27	3.51	5.62	3.6	1.51	3.67
Tm	0.53	0.39	0.31	0.24	0.34	0.3	0.45	0.8	0.52	0.21	0.55
Yb	3.51	2.65	1.88	1.4	2.18	1.99	3.35	5.33	3.39	1.28	3.52
Lu	0.55	0.37	0.28	0.17	0.32	0.3	0.48	0.77	0.51	0.18	0.53
Mg#	23.19	32.28	37.92	24.12	36.12	35.55	26.30	25.91	39.68	35.58	42.93
$(Rb/Yb)_N$	4.47	8.12	22.22	30.22	39.35	8.583	2.619	2.185	0.893	8.977	1.213
$(La/Yb)_N$	7.50	6.57	2.84	19.29	6.66	2.578	3.284	1.950	2.469	5.273	1.822
Eu/Eu*	0.60	0.42	0.78	0.54	0.80	0.980	0.978	0.966	0.622	1.149	0.700

References**= 1 (This study); 2 (Keppie et al., 2006); 3 (Vega-Granillo et al., 2013).

N.D.-no data.

Note: UTM Zone 12R.

Table S3(cont.). Major and trace elment concentrations of samples from Western Sonobari Complex, northwestern Mexico

Age	Post-Late Jurassic pre-Cenomanian amphibolite dikes									
Sample	SF-9	SF-11	SF-13	SF-14	SF-42	FG-1	FG-4	FG-12	FG-21	FG-26
Location I	710,557	710,557	710,930	710,805	710,496	N.D.	N.D.	N.D.	N.D.	N.D.
N	2,914,014	2,914,014	2,913,793	2,913,946	2,907,574	N.D.	N.D.	N.D.	N.D.	N.D.
Ref**	3	3	3	3	3	2	2	2	2	2
SiO2 (wt %)	51.5	49.8	48.1	47.6	46.2	48.55	47.92	47.53	47.62	47.03
TiO2	1.47	1.81	1.53	1.57	1.91	1.63	1.52	1.75	1.78	2.08
Al2O3	14.15	15.5	16.25	15.3	14.75	16.11	16.17	14.75	14.64	14.42
FeO_T	15.8	12.1	11.7	12.2	14.1	12.22	11.93	13.02	12.92	13.87
MnO	0.22	0.19	0.23	0.22	0.28	0.28	0.22	0.22	0.18	0.27
MgO	4.56	5.78	5.74	6.26	7.15	6.58	5.81	6.55	6.18	6.62
CaO	7.16	8.86	10.2	10.1	10.05	8.95	10.54	10.62	10.41	10.58
Na2O	1.38	3.16	3.23	2.95	2.31	2.93	3.19	2.45	2.67	2.71
K2O	1.24	0.57	0.86	0.85	0.66	0.85	0.8	0.84	0.95	0.96
P2O5	0.3	0.24	0.21	0.18	0.21	0.22	0.2	0.22	0.23	0.23
LOI	1.5	1	0.98	1.17	1.28	1.03	0.79	0.84	1.11	0.6
Total	99.28	99.01	99.03	98.4	98.9	99.35	99.09	98.79	98.69	99.37
Cs (ppm)	N.D.	N.D.	N.D.	N.D.	N.D.	N.D.	N.D.	N.D.	N.D.	N.D.
Rb	33.4	9	10.4	14.2	13	16	8	13	17	14
Sr	124	247	303	256	232	213	299	196	210	242
Ba	258	208	258	98.4	205	76	27	N.D.	0	0
V	415	281	304	327	360	278	255	295	298	332
Cr	40	120	180	200	160	200	203	216	206	182
Ni	46	61	45	63	74	76	51	67	55	68
Co	29.2	30.2	30.1	37.3	46.4	52	46	51	51	56
Zn	79	55	105	92	129	131	106	64	66	94
Sc	N.D.	N.D.	N.D.	N.D.	N.D.	N.D.	N.D.	N.D.	N.D.	N.D.
Cu	8	155	76	15	123	N.D.	N.D.	N.D.	N.D.	N.D.
Li	N.D.	N.D.	N.D.	N.D.	N.D.	N.D.	N.D.	N.D.	N.D.	N.D.
Th	3.43	1.21	1.05	0.57	0.24	0.8	0.98	0.56	0.57	0.25
U	1.13	0.4	0.68	1.04	0.1	N.D.	N.D.	N.D.	N.D.	N.D.
Pb	4	4	4	4	4	N.D.	N.D.	N.D.	N.D.	N.D.
Y	28	29.8	28	29.2	32.6	30	30	33	34	38
Nb	3.8	3.1	2.7	2.5	1.8	2.9	2.9	2.7	2.7	2.1
Ga	N.D.	N.D.	N.D.	N.D.	N.D.	18	17	17	17	18
Ta	0.2	0.2	0.2	0.1	0.1	0.2	0.2	0.18	0.18	0
Zr	109	115	98	93	112	72	72	88	89	84
Hf	3.4	3.3	2.7	2.6	3	2.1	2	2.4	2.5	2.4
La	14.9	9.5	8.1	6.5	5.5	8.14	7.9	6.5	7.48	6.46
Ce	32.7	23.6	19	16.5	15.3	21.25	19.92	17.26	19.62	18.94
Pr	4.6	3.6	2.86	2.63	2.67	3.13	2.91	2.66	2.98	3.2
Nd	19.5	17	13.6	12.7	13.6	15.34	14.52	14.05	15.34	16.73
Sm	4.73	4.83	3.96	3.83	4.46	4.35	4.08	4.25	4.58	5.18
Eu	1.38	1.64	1.34	1.35	1.62	1.55	1.34	1.5	1.65	1.76
Gd	4.95	5.42	4.58	4.54	5.31	5.32	4.89	5.39	5.69	6.63
Tb	0.91	0.99	0.88	0.86	1	0.89	0.85	0.94	0.95	1.14
Dy	5.37	6.11	5.32	5.28	6.18	5.68	5.46	6.02	6.12	7.08
Ho	1.16	1.29	1.15	1.15	1.32	1.2	1.17	1.3	1.31	1.52
Er	3.32	3.64	3.33	3.42	3.76	3.51	3.52	3.8	3.77	4.41
Tm	0.54	0.58	0.53	0.54	0.59	0.5	0.5	0.54	0.55	0.62
Yb	3.2	3.23	3.08	3.41	3.49	3.27	3.29	3.49	3.53	3.99
Lu	0.51	0.5	0.51	0.56	0.53	0.49	0.5	0.53	0.54	0.59
Mg#	22.40	32.33	32.91	33.91	33.65	35.0	32.8	33.5	32.4	32.3
$(Rb/Yb)_N$	8.10	2.16	2.62	3.23	2.89	3.80	1.89	2.89	3.74	2.72
$(La/Yb)_N$	3.14	1.99	1.78	1.29	1.06	1.68	1.62	1.26	1.43	1.09
Eu/Eu*	0.87	0.98	0.96	0.99	1.02	0.99	0.92	0.96	0.99	0.92

References**= 1 (This study); 2 (Keppie et al., 2006); 3 (Vega-Granillo et al., 2013).

N.D.-no data.

Note: UTM Zone 12R.

Table S3(cont.). Major and trace elment concentrations of samples from Western Sonobari Complex, northwestern Mexico

Age	Cenomanian mafic and ultramafic rocks									
Sample	SF-45	SF-46	SF-49	SFO-39	SFO-61	SFO-115	SFO-116	SFO-119	SFO-135	SFO-137
Location E	711,721	711,749	711,779	711,772	687,050	687,190	687,190	687,190	687,358	687,311
N	2,922,837	2,922,841	2,922,843	2,922,842	2,929,825	2,928,680	2,928,680	2,928,680	2,930,299	2,930,288
Ref**	3	3	3	1	1	1	1	1	1	1
SiO2 (wt %)	47.3	44	45.5	45.7	46.2	40.4	47.4	44.4	46.4	48.1
TiO2	1.05	2.09	1.63	1.39	1.41	0.88	0.98	0.67	1.19	1.05
Al2O3	21.9	15	14.25	16.2	9.53	7.99	8.86	7.89	9.59	12.65
FeO_T	6.86	12.9	12.1	10.7	10.95	14.55	11.5	11.45	11.3	10.3
MnO	0.08	0.15	0.15	0.13	0.22	0.19	0.39	0.18	0.22	0.2
MgO	4.93	10.5	11.4	10.3	14.35	23	14.1	20.7	14.55	9.94
CaO	10.35	10.4	10.3	10.3	13.05	6.3	12.5	7.68	13.4	13.9
Na2O	3.34	2.24	1.88	2.55	1.22	0.82	1.29	0.64	1.32	1.98
K2O	0.8	0.51	0.86	0.39	0.67	0.18	0.5	0.13	0.55	0.56
P2O5	0.08	0.04	0.12	0.1	0.1	0.04	0.09	0.12	0.09	0.13
LOI	2.5	0.19	1.6	1.49	0.6	4.32	0.96	3.99	0.77	1.01
Total	99.19	98.02	99.79	99.35	98.44	99.01	98.65	98.1	99.54	99.91
Cs (ppm)	N.D.	N.D.	N.D.	0.31	0.02	0.13	0.11	0.1	0.09	0.05
Rb	12.2	5.5	14.9	5.2	3.8	1.5	4.6	1.5	3.7	3.9
Sr	689	262	234	380	88.1	99	115.5	31.1	96.2	293
Ba	521	185.5	420	226	134.5	198.5	88.8	42.1	92.1	136.5
V	253	529	507	468	276	205	317	181	325	295
Cr	10	150	180	120	710	2050	350	1740	910	230
Ni	22	71	104	99	165	465	175	485	145	82
Co	29.5	51.5	52.3	42	52	93	46	65	54	45
Zn	70	121	117	106	158	103	254	96	138	108
Sc	N.D.	N.D.	N.D.	50	65	19	58	29	75	77
Cu	79	78	85	53	11	54	18	42	36	105
Li	N.D.	N.D.	N.D.	10	10	<10	10	10	10	10
Th	0.46	0.26	0.3	0.3	0.23	0.09	0.18	0.63	0.24	0.41
U	0.2	0.12	0.11	0.09	0.39	0.08	2.09	0.28	0.45	0.24
Pb	7	4	4	<2	<2	<2	<2	<2	<2	3
Y	13.7	27.2	26.4	23.4	19.4	10.1	20.7	12.1	16.2	17.6
Nb	2.8	4.5	2.9	2.3	6.4	2.2	12.6	4.4	3.2	4.8
Ga	N.D.	N.D.	N.D.	19.5	14.8	10.8	22	10.3	15	18.2
Ta	0.2	0.2	0.1	0.1	0.3	0.2	0.6	0.3	0.2	0.3
Zr	28	52	57	44	59	22	32	50	43	78
Hf	1.1	2	2.1	1.7	2.2	0.8	1.3	1.5	1.6	2.5
La	5.1	6.3	6.2	5.9	8.8	1.8	2.9	6.1	5.5	9.7
Ce	13	19	18.4	15.5	24.2	6.4	9.1	14.9	15.2	25.1
Pr	2.05	3.25	3.19	2.61	3.79	1.23	1.67	2.09	2.39	3.51
Nd	10	16.8	16	14.3	18.8	7.4	9.3	10.2	13	17
Sm	2.71	5.18	4.93	4.07	4.45	2.35	3.15	2.54	3.56	4.18
Eu	0.93	1.45	1.43	1.31	1.33	0.75	1.11	0.67	1.08	1.25
Gd	2.82	5.4	5.5	4.59	4.46	2.44	3.53	2.66	3.7	4.33
Tb	0.5	0.88	0.93	0.68	0.68	0.37	0.57	0.39	0.58	0.63
Dy	2.83	5.55	5.23	4.62	3.85	2.05	3.71	2.41	3.15	3.64
Ho	0.57	1.09	1.07	0.9	0.73	0.38	0.74	0.48	0.63	0.66
Er	1.62	3.03	2.88	2.5	2.06	1.16	2.17	1.34	1.71	1.88
Tm	0.24	0.38	0.42	0.33	0.27	0.16	0.35	0.19	0.23	0.27
Yb	1.33	2.41	2.43	2.12	1.69	0.96	2.57	1.1	1.43	1.6
Lu	0.2	0.36	0.36	0.28	0.25	0.14	0.35	0.17	0.2	0.24
Mg#	41.82	44.87	48.51	49.05	56.72	61.25	55.08	64.39	56.29	49.11
Al/Na+K										
Al/Ca+Na+K										
$(Rb/Yb)_N$	7.12	1.77	4.76	1.90	1.75	1.21	1.39	1.06	2.01	1.89
$(La/Yb)_N$	2.59	1.76	1.72	1.88	3.51	1.27	0.76	3.74	2.60	4.09
Eu/Eu*	1.03	0.84	0.84	0.93	0.91	0.96	1.02	0.79	0.91	0.90

References**= 1 (This study); 3 (Vega-Granillo et al., 2013).

N.D.-no data.

Note: UTM Zone 12R.

Table S4. Major and trace elment concentrations of samples from Eastern Sonobari Complex, northwestern Mexico

Cenomanian diorites		Campanian aplites		Parajes	Age	Late Jurassic Realito Gabbro				
SFO-136	SFO-138	SFO-2	SFO-58	SFO-40	Sample	SFO-12	SFO-45	ELF-202	ELF-221	ELF-226A
687,358	687,942	710,652	686,235	711,848	Location E	752,779	752,907	752,782	753,262	751,704
2,930,299	2,930,260	2,913,886	2,935,748	2,923,026	N	2,919,808	2,919,831	2,919,810	2,920,168	2,920,600
1	1	1	1	1	Ref**	1	1	4	4	4
54.8	52	76.1	73.9	57.9	SiO2 (wt %)	46.1	44.8	44	44.5	44.7
0.43	1.06	0.05	0.02	0.72	TiO2	0.28	0.24	0.26	0.23	0.13
21.7	18.55	13.1	14.75	18.25	Al2O3	13.25	6.12	11.25	12.2	20.3
3.32	8.01	0.67	0.28	6.76	FeO_T	9.92	12.85	10.9	8.96	7.01
0.05	0.14	0.02	0.01	0.12	MnO	0.17	0.22	0.2	0.16	0.13
3.66	4.26	0.11	0.06	3.13	MgO	14.8	19.4	17.5	17.1	9.67
10.15	7.79	1.32	2.02	6.59	CaO	10.5	9.19	10.8	10.35	13.9
4.87	4.1	3.67	5.42	3.8	Na2O	0.7	0.22	0.42	0.36	0.71
0.4	1.04	3.65	1.14	1.16	K2O	0.86	0.07	0.21	0.31	0.14
0.3	0.35	0.02	0.01	0.22	P2O5	0.08	0.04	0.06	0.08	0.02
0.55	1.56	0.28	0.38	0.57	LOI	3.56	4.72	4.32	4.37	1.88
100.41	99.02	99.1	98.14	99.35	Total	100.43	98.1	99.92	98.62	98.59
0.34	0.32	0.55	0.13	0.76	Cs (ppm)	0.66	0.06	N.D.	N.D.	N.D.
5	17.6	68.2	18.1	29.6	Rb	24.1	0.9	4.8	7.6	4
1255	631	146.5	568	553	Sr	304	25.5	195.5	328	385
229	657	805	767	532	Ba	243	31.4	84.8	126	45.5
89	176	7	<5	156	V	145	192	139	97	116
50	70	<10	<10	10	Cr	980	1660	1350	1440	280
24	29	1	<1	3	Ni	316	428	353	420	68
16	26	<1	<1	14	Co	54	73	62.3	59.5	39.6
34	110	24	5	97	Zn	73	86	80	62	42
15	16	2	1	14	Sc	29	54	N.D.	N.D.	N.D.
11	8	7	2	7	Cu	35	22	14	10	5
<10	10	<10	<10	10	Li	10	<10	N.D.	N.D.	N.D.
0.73	0.9	1.27	2.6	0.58	Th	0.85	0.45	0.73	0.67	0.13
0.23	0.62	1.71	0.59	0.62	U	0.28	0.13	0.2	0.17	0.05
4	2	16	11	<2	Pb	2	<2	5	4	4
9.8	21.1	17.3	7.8	17.5	Y	6	5.3	5.2	4.5	1.8
2.5	7.5	4.7	0.8	4.8	Nb	0.8	0.5	0.6	0.8	0.2
21.2	23.5	18	14.4	21.6	Ga	11.9	7	N.D.	N.D.	N.D.
0.1	0.3	0.3	0.1	0.3	Ta	<0.1	<0.1	0.09	0.1	0.1
72	191	52	63	49	Zr	26	14	18	19	4
1.8	4.2	2.6	2.5	1.5	Hf	0.7	0.5	0.5	0.5	0.2
14.8	17.9	2.9	8.3	7.8	La	3.3	2	2.7	2.9	0.9
26.9	41.7	6.2	16.3	19.2	Ce	6.5	4.6	5.5	5.3	1.6
3.16	5.69	0.84	2.06	3.04	Pr	0.93	0.63	0.75	0.77	0.25
13.8	27.5	3.7	7.9	14.7	Nd	4	3	3.5	3.3	1.1
2.84	6.02	1.21	1.41	3.4	Sm	0.94	0.87	0.9	0.88	0.3
0.92	1.67	0.38	0.33	1.04	Eu	0.34	0.19	0.32	0.3	0.2
2.49	5.66	1.96	1.12	3.25	Gd	0.95	0.92	0.96	0.91	0.39
0.36	0.81	0.3	0.16	0.53	Tb	0.15	0.17	0.15	0.16	0.06
2	4.37	2.15	1.07	3.21	Dy	1.03	1.01	0.99	0.89	0.35
0.37	0.79	0.56	0.26	0.61	Ho	0.19	0.19	0.2	0.18	0.08
1.05	2.26	1.71	0.78	1.86	Er	0.63	0.55	0.63	0.51	0.22
0.12	0.28	0.23	0.14	0.29	Tm	0.09	0.08	0.09	0.1	0.06
0.81	1.83	1.59	1.07	1.7	Yb	0.56	0.52	0.56	0.49	0.19
0.12	0.24	0.24	0.16	0.27	Lu	0.07	0.08	0.08	0.07	0.03
52.44	34.72	14.10	17.65	31.65	Mg#	59.87	60.16	61.62	65.62	57.97
		1.31	1.45	2.43	$(Rb/Yb)_N$	33.41	1.34	6.65	12.04	16.34
		1.06	1.07	0.94	$(La/Yb)_N$	3.98	2.60	3.25	3.99	3.20
4.79	7.47	33.30	13.13	13.52	Eu/Eu*	1.10	0.65	1.05	1.02	1.79
12.33	6.60	1.23	5.24	3.10						
1.06	0.87	0.75	0.80	0.96						

Table S4. Major and trace elment concentrations of samples from Eastern Sonobari Complex, northwestern Mexico

Age			Late Jurassic Topaco dikes					
Sample	ELF-226B	ELF-226C	SFO-11	SFO-29	SFO-30	ELF-205	ELF-206	ELF-225
Location E	751,704	751,704	748,361	745,720	747,695	745,477	745,897	752,910
N	2,920,600	2,920,600	2,926,033	2,930,931	2,930,763	2,929,751	2,930,744	2,919,855
Ref**	4	4	1	1	1	4	4	4
SiO2 (wt %)	42.1	41.7	53	49.6	49.5	51.4	50.3	48.5
TiO2	0.14	0.14	0.7	0.69	0.6	0.72	0.61	0.64
Al2O3	18.4	18.45	14.85	15.1	14.65	16.55	14.8	15.6
FeO_T	9.55	10.15	9.22	10.45	7.64	9.68	8.4	10.35
MnO	0.16	0.17	0.23	0.18	0.13	0.18	0.15	0.33
MgO	10.1	10.6	9.76	8.97	6.82	5.76	7.84	7.38
CaO	13.9	13.1	8.43	8.75	7.73	10.2	7.84	10.7
Na2O	0.45	0.43	2.75	2.09	3	2.2	3.06	2.61
K2O	0.24	0.23	0.13	0.88	0.38	0.5	0.32	0.26
P2O5	0.02	0.02	0.07	0.1	0.09	0.2	0.11	0.21
LOI	3.85	4.06	1.54	2.69	7.43	2.3	6.61	1.9
Total	98.91	99.05	100.77	99.63	98.06	99.69	100.04	98.48
Cs (ppm)	N.D.	N.D.	0.57	2.39	0.46	N.D.	N.D.	N.D.
Rb	6	5.7	2.4	19.6	9.1	19.5	9.1	5.7
Sr	370	360	264	240	230	354	257	220
Ba	54.6	55.4	35.5	397	205	259	241	134
V	116	117	246	257	167	229	179	258
Cr	360	360	400	380	300	90	530	170
Ni	68	70	80	95	94	10	114	57
Co	44.9	48.4	37	41	31	29.6	37	24.4
Zn	47	52	85	92	101	101	98	144
Sc	N.D.	N.D.	28	35	19	N.D.	N.D.	N.D.
Cu	5	5	<1	100	2	14	4	5
Li	N.D.	N.D.	10	20	10	N.D.	N.D.	N.D.
Th	0.18	0.2	1.49	1.61	2.03	2.36	2.12	1.8
U	0.08	0.11	0.58	0.42	0.66	0.59	0.59	0.5
Pb	4	4	3	2	9	21	39	4
Y	2.1	2.1	18.1	17.7	15.5	16.1	15.1	11.1
Nb	0.2	0.2	2.4	2.8	2.8	3.5	3	2.3
Ga	N.D.	N.D.	16.9	15.3	13.7	N.D.	N.D.	N.D.
Ta	0.1	0.1	0.2	0.2	0.2	0.2	0.2	0.2
Zr	6	6	58	63	60	65	65	46
Hf	0.2	0.2	1.8	1.8	1.6	1.9	1.8	1.4
La	1.4	1.6	5.8	7	8.6	8.5	8.1	7.1
Ce	2.1	2.4	12.5	14.8	17.5	17.8	16.4	14.3
Pr	0.33	0.36	1.81	1.98	2.28	2.34	2.09	1.94
Nd	1.5	1.6	8.2	8.6	9.4	10.2	9.1	8.2
Sm	0.42	0.41	2.42	2.49	2.59	2.59	2.27	2.04
Eu	0.27	0.28	0.93	0.8	0.69	0.87	0.77	0.66
Gd	0.41	0.41	3.1	2.71	2.66	2.87	2.6	2.17
Tb	0.07	0.08	0.52	0.42	0.45	0.48	0.44	0.37
Dy	0.42	0.41	2.9	3.06	2.55	3.06	2.82	2.09
Ho	0.09	0.08	0.63	0.66	0.57	0.64	0.59	0.46
Er	0.25	0.25	1.9	1.96	1.87	1.89	1.76	1.34
Tm	0.06	0.06	0.28	0.3	0.27	0.26	0.26	0.21
Yb	0.23	0.21	1.77	1.82	1.53	1.83	1.7	1.2
Lu	0.04	0.04	0.27	0.27	0.26	0.27	0.24	0.19
Mg#	51.40	51.08	51.42	46.19	47.16	37.31	48.28	41.62
$(Rb/Yb)_N$	20.25	21.07	1.05	8.36	4.62	8.27	4.16	3.69
$(La/Yb)_N$	4.11	5.14	2.21	2.60	3.79	3.14	3.22	3.99
Eu/Eu*	1.99	2.09	1.04	0.94	0.80	0.98	0.97	0.96

References**= 1 (This study); 4 (Vega-Granillo et al., 2012).

N.D.-no data.

Note: UTM Zone 12R.

Age	sic Cubampo Granite					Capomos Granodiorite	an Guamuchil Formation			
Sample	SFO-24	SFO-44	ELF-200	ELF-201	ELF-204	SFO-14	SFO-32	ELF-207	ELF-208	ELF-209
Location E	740,353	749,993	750,053	750,083	747,307	746,017	750,860	750,851	751,247	752,069
N	2,934,245	2,922,211	2,922,074	2,922,086	2,928,560	2,925,790	2,930,110	2,930,090	2,929,960	2,929,907
Ref**	1	1	4	4	4	1	1	4	4	4
SiO2 (wt %)	80.5	75.6	74.50	65.70	77.60	69.2	54.1	49.4	52	52.3
TiO2	0.17	0.15	0.14	0.73	0.16	0.47	0.9	1.02	0.99	0.99
Al2O3	12.9	12.75	13.25	14.80	11.20	15.65	16.95	19.2	18.4	18.15
FeO_T	1.03	2.09	2.21	7.16	3.29	3.45	8.3	8.87	8.44	9.01
MnO	0.02	0.02	0.02	0.10	0.08	0.05	0.15	0.16	0.13	0.18
MgO	0.31	0.37	0.34	1.37	0.31	1.75	4.6	4.41	4.78	5.04
CaO	1.18	1.31	1.36	3.19	1.31	3.49	10.05	11.95	9.59	11.45
Na2O	2.54	3.76	3.77	3.65	4.16	4.26	2.95	2.75	2.96	1.85
K2O	1.99	2.2	2.55	1.87	1.01	2.27	1.2	1.07	1.25	0.33
P2O5	0.03	0.03	0.01	0.13	0.05	0.32	0.27	0.31	0.26	0.28
LOI	1.14	0.67	1.38	1.29	0.70	0.74	0.66	0.89	1	0.4
Total	101.93	99.1	99.53	99.99	99.87	101.85	100.24	100.03	99.8	99.98
Cs (ppm)	1.26	0.38	N.D.	N.D.	N.D.	1.85	0.3	N.D.	N.D.	N.D.
Rb	59.4	43.4	52.80	83.50	24.80	58.1	15.6	24.9	42.8	9.2
Sr	95.9	114	120.50	151.50	118.50	656	315	354	402	330
Ba	969	1280	1375	1445	843	1045	526	492	358	180
V	5	7	8	65	4	64	167	183	195	198
Cr	10	10	9	9	10	50	90	130	100	110
Ni	1	<1	4	4	4	13	47	48	29	33
Co	2	2	2	7	1.60	8	25	24.7	22.5	25.8
Zn	12	23	25	81	52	69	80	79	75	87
Sc	7	5	N.D.	N.D.	N.D.	5	19	N.D.	N.D.	N.D.
Cu	15	13	17	7	27	<1	1	16	24	55
Li	<10	<10	N.D.	N.D.	N.D.	20	<10	N.D.	N.D.	N.D.
Th	6.33	9.79	10.60	7.01	5.67	3.16	1.46	1.86	2.18	1.79
U	1.62	1.73	1.81	1.49	1.22	0.9	0.48	0.54	0.62	0.51
Pb	3	2	24.0	12	11.0	11	<2	30	24	13
Y	43.2	41.4	42.6	40.7	59.2	6.7	15.1	16.3	16.1	16
Nb	9.5	5.4	5.5	8.2	6.3	6.8	3.2	3.7	3.7	3.6
Ga	18.7	17.7	N.D.	N.D.	N.D.	21.5	15.2	N.D.	N.D.	N.D.
Ta	0.6	0.5	0.50	0.60	0.40	0.3	0.2	0.2	0.2	0.2
Zr	251	146	110	172	182	115	60	66	71	65
Hf	7.1	5	4	5.10	5.40	3.1	1.5	1.8	2	1.8
La	22.7	37.2	29.9	21.80	19.60	14.5	7.3	8.3	9.2	8.2
Ce	50.4	68.5	58.8	45.10	40.10	27.6	15.9	17.7	19.2	17.1
Pr	6.61	8.13	7.11	5.96	5.24	3.33	2.2	2.43	2.57	2.32
Nd	27.4	31.7	27.4	24.9	23.00	13.4	9.7	11.3	11.8	10.6
Sm	6.24	6.69	5.94	5.92	5.94	2.66	2.31	2.78	2.75	2.69
Eu	1.11	0.73	0.81	1.17	1.15	0.84	1	1.06	1.11	1.01
Gd	6.67	6.27	6.47	6.63	7.16	2.09	2.56	3.06	3.19	2.99
Tb	1.15	1.02	1.12	1.15	1.35	0.27	0.4	0.51	0.51	0.49
Dy	7.05	6.67	7.32	7.14	9.35	1.41	2.67	3.27	3.16	3.11
Ho	1.49	1.34	1.58	1.54	2.15	0.25	0.55	0.64	0.64	0.63
Er	5.07	4.38	4.95	4.66	6.78	0.6	1.71	1.88	1.86	1.87
Tm	0.81	0.7	0.72	0.71	1.05	0.09	0.22	0.27	0.28	0.27
Yb	4.99	4.11	4.79	4.73	7.03	0.63	1.46	1.78	1.74	1.71
Lu	0.77	0.65	0.74	0.69	1.12	0.08	0.2	0.26	0.26	0.25
Mg#	15.04	23.13	13.33	16.06	8.61	33.65	35.66	33.21	36.16	35.87
Al/Na+K	1.49	2.04	1.48	1.84	1.41	1.65				
Al/Ca+Na+K	1.16	1.52	1.16	1.07	1.09	0.99				
$(Rb/Yb)_N$	8.20	9.24	8.56	13.71	2.74	71.60	8.30	10.86	19.10	4.18
$(La/Yb)_N$	6.11	3.07	4.21	3.11	1.88	15.54	3.37	3.15	3.57	3.24
Eu/Eu*	0.34	0.53	0.40	0.57	0.54	1.09	1.26	1.11	1.15	1.09

References**= 1 (This study); 4 (Vega-Granillo et al., 2012).

N.D.-no data.

Note: UTM Zone 12R.

ELF-211	ELF-216	ELF-217	ELF-218	ELF-220
752,613	754,373	753,957	753,902	753,507
2,929,820	2,929,565	2,929,808	2,929,839	2,930,156
4	4	4	4	4
51.4	52.1	58.9	53	51.7
1.02	0.82	1.41	0.85	0.65
18.3	20.2	14.45	14.75	14.3
9.44	9.26	12.05	8.58	8.99
0.17	0.12	0.22	0.15	0.14
5.04	3.88	2.8	7.99	8.19
9.49	9.38	7.47	10.15	8.13
2.77	2.61	2.25	2.59	2.89
1	0.05	0.06	0.21	1.23
0.26	0.12	0.38	0.29	0.22
1.5	0.6	-0.1	0.79	1.59
100.39	99.14	99.89	99.35	98.03
N.D.	N.D.	N.D.	N.D.	N.D.
29.5	0.9	1.4	6.9	45
313	248	516	386	320
481	118	36.8	241	307
190	301	191	240	192
110	10	10	600	310
25	4	4	186	70
26.2	21.2	19.6	39.3	35
84	93	128	76	75
N.D.	N.D.	N.D.	N.D.	N.D.
39	23	24	90	4
N.D.	N.D.	N.D.	N.D.	N.D.
2.24	1	3.64	1.42	2.24
0.64	0.24	0.88	0.43	0.48
8	13	18	15	6
16.2	16.6	23.6	12.2	14.8
3.7	3.1	4.6	2.6	2.8
N.D.	N.D.	N.D.	N.D.	N.D.
0.2	0.2	0.3	0.1	0.2
71	67	82	41	59
2.1	1.9	2.6	1.2	1.8
9.4	7.3	12.3	6.4	8.2
19.9	15.7	26.1	13.4	16.5
2.59	2.07	3.38	1.82	2.18
11.8	9.5	15.1	8.3	9.6
2.88	2.28	3.79	2.12	2.44
1.12	0.87	1.3	0.81	0.8
3.23	2.79	4.32	2.3	2.76
0.53	0.48	0.71	0.37	0.44
3.25	3.04	4.57	2.37	2.84
0.67	0.66	0.97	0.48	0.57
1.94	2.03	2.87	1.42	1.73
0.27	0.28	0.41	0.19	0.23
1.82	1.91	2.71	1.29	1.63
0.27	0.29	0.4	0.19	0.23
34.81	29.53	18.86	48.22	47.67
12.58	0.37	0.40	4.15	21.43
3.49	2.58	3.06	3.35	3.40
1.12	1.05	0.98	1.12	0.94

TABLE S5. MEASURED AND AGE-CORRECTED ISOTOPIC RATIOS OF SAMPLES FROM SONOBARI COMPLEX, NORTHWEST

Sample	Age Ma	UTM		Sm (ppm)	Nd (ppm)	$^{147}Sm/^{144}Nd$	$(^{143}Nd/^{144}Nd_{(}$	% std err	$^{143}Nd/^{144}Nd_{(i}$	$\varepsilon nd_{(0)}$
Western Sonobari Comple		**E**	**N**							
Early Triassic (orthogneisses)										
SFO-55	241	686235	3E+06							
SFO-56	241	686235	3E+06	2.84	19.09	0.0901	0.512278	0.0008	0.512136	-7.03
SFO-159	249	707809	3E+06	1.87	7.40	0.1527	0.512273	0.0012	0.512024	-7.13
SFO-159A	249	707809	3E+06							
Late Triassic (orthogneisses)										
SFO-4	207	710652	3E+06							
SFO-5	205	710515	3E+06							
SFO-20	207	710652	3E+06	2.35	12.99	0.1096	0.512414	0.0007	0.512266	-4.37
SFO-154	203	710382	3E+06							
SFO-155	213	710474	3E+06	3.73	20.63	0.1094	0.512479	0.0012	0.512326	-3.10
SFO-158	205	710536	3E+06							
Mv-25a*	207			2.88	18.50	0.0942	0.512394		0.512256	
Late Jurassic (orhogneisses)										
SFO-63	161	686202	3E+06	3.20	14.16	0.1364	0.512430	0.0014	0.512286	-4.06
SFO-64	162	686706	3E+06							
SFO-112	162	685013	3E+06							
SFO-114	161	686202	3E+06							
SFO-121	159	685220	3E+06	3.99	19.95	0.1208	0.512342	0.0014	0.512216	-5.77
SFO-152	160	710928	3E+06	3.90	18.50	0.1275	0.512501	0.0010	0.512367	-2.68
Post-Late Jurassic pre-Late Cretaceous (amphibolites)										
SFO-3	9.99	710652	3E+06	3.11	11.57	0.1624	0.512603	0.0014	0.512497	-0.68
SFO-59	9.99	687809	3E+06	7.99	28.50	0.1694	0.512827	0.0012	0.512716	3.70
SFO-113	9.99	685011	3E+06							
SFO-118	9.99	687195	3E+06							
SFO-126	9.99	686331	3E+06							
Mv-25b*	9.99			3.87	12.99	0.1801	0.512829		0.512565	
Cenomanian (basic and ultrabasic rocks)										
SFO-39	9.99	711772	3E+06	3.97	13.87	0.1731	0.512526	0.0015	0.512413	-2.18
SFO-115	9.99	687190	3E+06	2.22	7.24	0.1852	0.512834	0.0018	0.512713	3.83
SFO-116	9.99	687190	3E+06							
SFO-119	9.99	687190	3E+06							
SFO-135	9.99	687358	3E+06	2.91	12.92	0.1361	0.512853	0.0009	0.512764	4.20
SFO-137	9.99	687311	3E+06							
SFO-136	9.99	687358	3E+06	2.62	13.69	0.1155	0.512808	0.0015	0.512732	3.31
SFO-138	9.99	687942	3E+06							
Campanian (leucocratic dikes)										
SFO-2	80.6	710652	3E+06							
SFO-58	80.6	686235	3E+06							
HKM-01**	80.6			2.88	18.50	0.0942	0.512394		0.512343	
Paleocene (Los Parajes)										
SFO-40	64	711848	3E+06							
Eastern Sonobari Complex										
Late Jurassic (Realito = R; Topaco = T; Cubampo = C)										
SFO-12 (R)	161	752779	3E+06	0.92	3.70	0.1498	0.512576	0.0017	0.512418	-1.22
SFO-45 (R)	161	752907	3E+06							
SFO-11 (T)	155	748361	3E+06							
SFO-29 (T)	155	745720	3E+06							
SFO-30 (T)	155	747695	3E+06							
SFO-24 (C)	154	740353	3E+06							
SFO-44 (C)	150	749993	3E+06	6.11	26.28	0.1405	0.512436	0.0007	0.512298	-3.93
HKM-02** (C)	150			5.79	26.61	0.1315	0.512451		0.512322	
SFO-167 (C)	159									
Cenomanian (Capomos)										
SFO-14	98	746017	3E+06							
MV-27*	98			2.70	14.17	0.1151	0.512618		0.512545	-1.93
MV-30*	98			2.21	10.77	0.1224	0.512566		0.512520	-0.93
Campanian (Guamuchil)										
SFO-32	73	750860	3E+06	2.27	9.15	0.1502	0.512634	0.0009	0.512562	-0.08

*Data recalculated from Valencia et al. (2001).
**Data recalculated from Zurcher (2002).

εNd calculated by using present-day CHUR (chondritic uniform reservoir values of $^{147}Nd/^{144}Nd$ = 0.1967 and $^{143}Nd/^{144}Nd$=0.512638. T
0.7102594 ± 0.0014 (n=5, 1σ). The estimated analytical ± 2σ uncertainties for samples in this study are $^{143}Nd/^{144}Nd$= 0.0007-0.0018%
0.052% at the ± 2σ.

(0) Measured ratios.
(i) Initial Ratios (age-corrected).

TERN MEXICO

#Ɛnd$_{(i)}$	Rb (ppm)	Sr (ppm)	$^{87}Rb/^{86}Sr$	$^{87}Sr/^{86}Sr$ (0)	% std err	$^{87}Sr/^{86}Sr$ (i)	Th (ppm)	U (ppm)	Pb (ppm)	$^{208}Pb/^{204}P$	% ± 2σ
							0.05	0.05	2	18.821	0.020
-3.74	50.8	607	0.242280	0.707142	0.0013	0.706308	4.83	2.46	4	20.597	0.026
-5.72	52.2	608	0.248548	0.707249	0.0013	0.706368	1.79	0.65	10	18.663	0.012
							0.86	0.26	3	18.887	0.020
							6.97	1.46	6	19.035	0.020
	56.6	241	0.679896	0.708286	0.0009	0.706304	12.25	2.98	3	19.482	0.011
-2.07							9.41	2.19	2	19.150	0.020
	106.5	118.5	2.601802	0.710392	0.0013	0.702881	7.28	3.60	2	19.786	0.027
-0.73							12.10	1.60	2	19.190	0.020
							8.22	1.78	2	19.362	0.024
-1.8	46	257	0.518165	).708679 ± 21		0.707154					
-2.82	47.3	303	0.451920	0.708161	0.0012	0.707127	3.32	0.76	2	18.738	0.012
	20.2	47	1.244218	0.711736	0.0009	0.708870	7.68	1.83	3	19.091	0.024
	27.7	269	0.298106	0.707865	0.0010	0.707183	13.50	2.64	3	19.848	0.011
							2.93	0.64	2	18.733	0.020
-4.24	54.5	266	0.593141	0.707865	0.0008	0.706524	16.65	3.46	3	19.612	0.024
-1.26							5.92	2.08	2	19.276	0.020
-0.25	22	259	0.245904	0.706394	0.0009	0.706045	1.82	0.92	7	18.931	0.011
4.04							0.86	0.33	8	18.457	0.020
							6.24	2.82	2	20.417	0.019
							0.35	0.13	2	18.736	0.020
							0.08	0.13	2	18.911	0.043
4.20	6	257	0.067587	).706353 ± 21		0.706257					
-1.88	5.2	380	0.039615	0.705568	0.0008	0.705512	0.3	0.09	2	18.852	0.011
3.97							0.09	0.08	2	18.782	0.043
							0.18	2.09	2	19.460	0.019
							0.63	0.28	2	19.169	0.042
4.97	3.7	96.2	0.111345	0.703998	0.0009	0.703840	0.24	0.45	2	18.939	0.028
							0.41	0.24	3	18.841	0.020
4.35							0.73	0.23	4	18.701	0.020
	17.6	631	0.080747	0.703966	0.0012	0.703852	0.9	0.62	2	18.763	0.025
							1.27	1.71	16	18.949	0.020
	18.1	568	0.092251	0.705453	0.0012	0.705344	2.6	0.59	11	18.747	0.012
-3.67	46.19	257.7	0.518891	0.709210		0.708598					
	29.6	553	0.154956	0.705734	0.0009	0.705593	0.58	0.62	2	18.895	0.024
-0.25	24.1	304	0.229502	0.704910	0.0011	0.704384	0.85	0.28	2	18.804	0.011
	0.9	25.5	0.102175	0.705362	0.0014	0.705128	0.45	0.13	2	19.012	0.024
							1.49	0.58	3	19.007	0.020
							1.61	0.42	2	18.722	0.020
							2.03	0.66	9	18.755	0.020
	59.4	95.9	1.793126	0.716964	0.0013	0.713018	6.33	1.62	3	19.357	0.027
-2.87	43.4	114	1.102117	0.710577	0.0010	0.708227	9.79	1.73	2	19.278	0.024
-2.40	37.8	116.8	0.936897	0.710007		0.708009					
							11.95	2.27	25	18.825	0.020
	58.1	656	0.256398	0.705420	0.0008	0.705064	3.16	0.9	11	18.899	0.024
0.62	48	178	0.780664	).705265 ± 41		0.704179					
-0.86	43	150	0.829889	).705782 ± 38		0.705110					
0.36	15.6	315	0.143370	0.705149	0.0010	0.705000	1.46	0.48	2	18.745	0.025

he Sr isotopic ratios were normalized to $^{86}Sr/^{88}Sr$ =0.1194, whereas Nd ratios normalized to $^{146}Nd/^{144}Nd$=0.7219. Average of La Jolla standa
% and $^{87}Sr/^{86}Sr$ = 0.0008-0.0014%. External errors for NBS-981standard $^{206}Pb/^{204}Pb$, $^{207}Pb/^{204}Pb$ and $^{208}Pb/^{204}Pb$ are between 0.0022% and (

$^{207}Pb/^{204}P$	% ± 2σ	$^{208}Pb/^{204}P$	% ± 2σ	$^{206}Pb/^{204}Pb$	$^{207}Pb/^{204}Pb$	$^{208}Pb/^{204}Pbi$
15.626	0.025	38.664	0.026	18.763	15.624	38.646
15.738	0.035	39.892	0.036	19.175	15.666	38.984
15.607	0.018	38.498	0.020	18.508	15.599	38.359
15.626	0.025	38.779	0.026	18.679	15.615	38.557
15.635	0.025	39.088	0.026	18.553	15.610	38.338
15.656	0.018	39.659	0.019	17.534	15.558	37.050
15.637	0.025	39.216	0.026	16.982	15.529	36.180
15.678	0.035	39.274	0.037	16.292	15.503	36.971
15.637	0.025	39.275	0.026	17.560	15.555	35.257
15.651	0.038	39.465	0.044	17.617	15.563	36.839
15.616	0.018	38.869	0.020	18.155	15.587	38.037
15.631	0.038	39.240	0.045	18.149	15.584	37.948
15.675	0.018	40.418	0.019	18.490	15.608	38.148
15.616	0.025	38.814	0.026	18.242	15.592	38.080
15.659	0.038	40.181	0.044	17.865	15.573	37.433
15.645	0.025	39.067	0.026	17.690	15.567	37.592
15.630	0.018	38.769	0.020	18.806	15.624	38.689
15.601	0.025	38.427	0.026	18.418	15.599	38.394
15.703	0.025	39.957	0.025	19.081	15.639	38.988
15.611	0.025	38.540	0.026	18.675	15.608	38.486
15.627	0.052	38.750	0.052	18.849	15.624	38.737
15.631	0.018	38.702	0.020	18.809	15.629	38.655
15.617	0.052	38.592	0.052	18.744	15.615	38.578
15.651	0.025	38.592	0.026	18.470	15.604	38.564
15.646	0.051	38.980	0.052	19.036	15.640	38.882
15.620	0.035	38.623	0.037	18.726	15.610	38.586
15.623	0.025	38.637	0.026	18.766	15.620	38.594
15.610	0.025	38.576	0.026	18.646	15.608	38.519
15.609	0.039	38.535	0.045	18.472	15.595	38.397
15.634	0.025	38.666	0.026	18.868	15.630	38.646
15.617	0.018	38.569	0.020	18.706	15.615	38.510
15.637	0.038	38.725	0.045	18.707	15.629	38.667
15.637	0.018	38.714	0.020	18.589	15.626	38.501
15.650	0.038	38.946	0.045	18.912	15.645	38.833
15.686	0.025	39.111	0.026	18.721	15.672	38.871
15.615	0.025	38.535	0.026	18.412	15.599	38.147
15.645	0.025	38.700	0.026	18.646	15.639	38.591
15.687	0.035	39.397	0.037	18.561	15.648	38.380
15.673	0.038	39.596	0.044	18.036	15.612	37.298
15.647	0.025	38.813	0.026	18.688	15.641	38.577
15.658	0.038	38.752	0.045	18.823	15.655	38.665
15.618	0.039	38.634	0.045	18.579	15.610	38.469

ard $^{143}Nd/^{144}Nd$ 0.511864 ± 2 (n=4). The NBS 987 standard $^{87}Sr/^{86}Sr$ =
0.020% at the ± 2σ. Relative error samples are between 0.011% and

Anexo 3

Material suplementario publicado en línea del artículo:

Vega-Granillo, R., Sarmiento-Villagrana, A., Salgado-Souto, S., and Araux-Sánchez, E., 2017, P-T conditions of earliest Late Cretaceous metamorphism in the Western Sonobari Complex, northwestern Mexico: tectonic implications: International Geology Review, v. 59, no. 7, p. 812-828, doi: 10.1080/00206814.2016.1227942.

Material:

Tabla 1. Petrografía.

Tabla 2. Datos analíticos de U-Pb.

Tabla 3. Datos de geotermobarometría.

Supplementary Table 1. Petrographic description of the studied samples

Sample	UTM (Zone 12R) Datum WGS84		Petrography	Mineral Assemblage	Secondary minerals	*Age (Ma)
Amphibolite						
SFO-37	711597	2922827	Dark medium-grained amphibolite with continuous foliation. Mylonitic deformation is evidenced by undulose extinction, deformation lamellae, and subgrains in quartz.	Pl + Amp + Qtz + Grt + Ti		
SF-40	710496	2907574	Lenses of pegmatitic amphibolite. This rocks is composed by amphibole crystals larger than 15 cm.	Amp + Pl + Bt + Rt + Ti + Ilm	Chl + Ep	67 ± 5 Ar-Ar **(1)**
SFO-41	711597	2922827	Dark medium-grained amphibolite with continuous foliation.	Pl + Amp + Qtz + Grt + Bt + Rt	Ep + Chl	
SFO-59A	687809	2932819	Dark medium-grained amphibolite with continuous foliation.	Pl + Amp + Qtz + Ti + Rt	Ep + Chl + Ser + Ab	
Orthogneiss						
SF-5	710515	2913490	Medium-grained leucocratic granodiorite orthogneiss with continuous foliation. This rock was affected by brittle deformation.	Pl + Qtz + Bt + Kfs		205.9 ± 2.9 U-Pb**(2)**
SF-6	709931	2914035	Medium-grained melanocratic orthogneiss with well-developed foliation. The rock contains leucocratic stromatic bands mainly made by quartz and feldspar, and minor garnet, whereas the melanocratic bands are formed by amphibole. Foliation is bend by isoclinal folding.	Pl + Amp + Qtz + Bt + Grt	Chl	
SFO-20	710652	2913886	Coarse-grained leucocratic orthogneiss of granodioritic composition with continuous foliation.	Pl + Kfs + Qtz + Bt + Ti		207.4 ± 2.5 U-Pb**(2)**
SFO-42	711597	2922827	Coarse-grained leucocratic orthogneiss with two deformation stages. The first stage is related to ductile deformation that yield penetrative foliation which is overprinted by mylonitic deformation.	Qtz + Pl + Amp + Grt + Ti	Ser + Ep + Chl	
SFO-63	686202	2923555	Medium-grained melanocratic rock of tonalitic composition. The rock display spaced schistosity defined by domains rich in Amp + Bt and domains rich in Pl + Qtz, commonly with stromatic leucosome bands.	Pl + Amp + Bt + Qtz + Kfs + Ti	Ser + Chl + Ep	161.0 ± 0.3 U-Pb **(2)**
SFO-152	710928	2910966	Medium-grained mesocratic rock of granodioritic composition. This rock display continuous schistosity defined by abundant biotite.	Pl + Qtz + Bt + Ep + Zr		160.1 ± 0.6 U-Pb (2)
Paragneiss						
SFO-151	709914	2914080	Medium-grained paragneiss with stromatic leucosome bands. The leucosome bans are of coarse-grained. This rock show dynamic recristalization.	Qtz + Pl + Bt + Ms ± Grt ± Rt		
Igneous rocks						
SFO-40	711848	2923026	This granodiorite display a coarse-grained (<4mm) hipidiomorphic-inequigranular texture. Ductile deformation is evidenced by undulose extinction, bands of deformation, subgrains, and deformation twinning in plagioclase and quartz.	Pl + Qtz + Kfs + Bt +Amp + Zr + Ms	Chl + Ep + Ser	64 ± 10 U-Pb **(1)**
SF-46	711779	2922843	This rock is a coarse-grained gabbro without deformation. It displays a hypidiomophic granular texture locally with plagioclase clusters.	Amp + Pl + Bt + Rt + Ti	Chl + Ep.	54 ± 10 Ar-Ar **(1)**
SFO-60A	687217	2930666	Coarse-grained undeformed hornblendite dike. It is composed of amphibole 88%, plagioclase 10%, and clinopyroxene 2%.	Amp + Pl + Cpx		
Leucosome						
SFO-1	710652	2913886	Folded vein crosscutting the main foliation of orthogneiss and amphibolite.	Qtz + Pl + Grt		92.5 ± 3.1 U-Pb **(3)**
SFO-8	710019	2914041	Concordant leucosome vein in biotite-rich orthogneiss	Qtz + Pl+ Kfs		92.6 ± 3 U-Pb **(3)**
SFO-9	710019	2914041	Leucosome vein transecting the foliation of previous stromatic gneiss	Qtz +Pl +Kfs		88.0 ± 1.7 U-Pb **(3)**
SFO-19	709908	2914122	Coarse-grained leucosome vein parallel to the main foliation of paragneiss.	Qtz +Pl +Kfs		90.3 ± 0.7 U-Pb **(3)**

*References: (1) Vega-Granillo et al., 2013; (2) Sarmiento et al., 2016; (3) This work

Note: Qtz=Quartz, Pl=Plagioclase, Bt-=Biotite, Ms=Muscovite, Amp=Amphibole, Grt=Garnet, Ep=Epidote, Kfs=K-feldspar, Ti=Titanite, Zr=Zircon, Chl=Chlorite, Rt=Rutile, Ilm=Ilmenite, Ser= Sericite, Ab=Albite, Kfs=Potassium feldspar

Supplemental file 2

Nu Plasma HR multicollector ICPMS data of magmatic and metamoprhic rims zircon from leucosome **(SFO-1)**, Western Sonobari Complex, Mexico.

Spot 35 micron				Isotope ratios							Apparent ages (Ma)								
Analysis	U (ppm)	206Pb 204Pb	U/Th	206Pb* 207Pb*	± (%)	207Pb* 235U*	± (%)	206Pb* 238U	± (%)	error corr.	206Pb* 238U*	± (Ma)	207Pb* 235U	± (Ma)	206Pb* 207Pb*	± (Ma)	Best age (Ma)	± (Ma)	Conc (%)
SFO-1-13	113	2578	22.3	25.1430	36.1	0.0616	41.5	0.0112	20.5	0.49	72.0	14.7	60.7	24.4	-365.7	960.1	72.0	14.7	NA
SFO-1-28	126	3106	70.1	22.5261	33.5	0.0843	34.3	0.0138	7.6	0.22	88.2	6.6	82.2	27.1	-88.8	840.5	88.2	6.6	NA
SFO-1-33	145	4253	101.8	18.1696	15.3	0.1055	19.0	0.0139	11.3	0.59	89.0	10.0	101.9	18.4	413.7	343.3	89.0	10.0	NA
SFO-1-31	122	3036	96.8	22.5311	48.6	0.0856	49.2	0.0140	7.2	0.15	89.5	6.4	83.4	39.4	-89.4	1259.7	89.5	6.4	NA
SFO-1-2	103	2217	62.3	18.4254	26.2	0.1062	26.7	0.0142	4.9	0.18	90.8	4.4	102.5	26.0	382.4	598.7	90.8	4.4	NA
SFO-1-4	143	1788	71.9	24.9993	31.5	0.0785	32.0	0.0142	5.6	0.17	91.1	5.0	76.7	23.6	-350.9	830.0	91.1	5.0	NA
SFO-1-11	198	5578	93.0	19.3948	17.2	0.1035	17.5	0.0146	3.3	0.19	93.2	3.0	100.0	16.6	266.0	396.3	93.2	3.0	NA
SFO-1-18	275	14197	31.5	22.6084	17.5	0.0900	17.7	0.0148	2.8	0.16	94.5	2.6	87.5	14.8	-97.8	431.6	94.5	2.6	NA
SFO-1-9	172	8274	19.3	19.5227	13.2	0.1172	14.1	0.0166	4.9	0.34	106.1	5.1	112.5	15.0	250.8	305.5	106.1	5.1	NA
SFO-1-23	554	28646	1.1	19.9124	3.4	0.2007	5.7	0.0290	4.5	0.80	184.2	8.2	185.7	9.7	205.2	79.8	184.2	8.2	NA
SFO-1-27	219	9280	1.8	16.0796	17.7	0.2591	19.2	0.0302	7.5	0.39	191.9	14.2	234.0	40.2	680.7	380.5	~~191.9~~	~~14.2~~	NA
SFO-1-1	101	3776	2.4	21.6660	23.3	0.1982	24.2	0.0312	6.4	0.26	197.7	12.5	183.6	40.6	5.7	568.1	197.7	12.5	NA
SFO-1-5	296	19355	1.9	19.8844	5.1	0.2183	5.4	0.0315	2.0	0.37	199.9	4.0	200.5	9.9	208.5	117.2	199.9	4.0	NA
SFO-1-24	263	30223	1.6	20.7045	8.4	0.2138	8.5	0.0321	1.5	0.17	203.7	2.9	196.7	15.2	113.9	198.3	203.7	2.9	NA
SFO-1-19	278	20482	1.6	20.0872	5.7	0.2210	5.9	0.0322	1.8	0.30	204.3	3.6	202.7	10.9	184.8	132.1	204.3	3.6	NA
SFO-1-22	218	7391	1.6	20.4868	9.4	0.2177	10.1	0.0323	3.7	0.36	205.2	7.5	200.0	18.4	138.8	221.9	205.2	7.5	NA
SFO-1-10	79	2401	3.3	23.0267	22.2	0.1946	23.0	0.0325	6.1	0.26	206.1	12.3	180.5	38.1	-143.0	556.4	206.1	12.3	NA
SFO-1-17	184	11646	1.5	21.1351	16.4	0.2129	16.5	0.0326	1.9	0.12	207.0	4.0	196.0	29.4	65.1	391.7	207.0	4.0	NA
SFO-1-15	621	43927	0.9	20.1420	4.3	0.2238	4.9	0.0327	2.4	0.50	207.4	5.0	205.0	9.1	178.5	99.1	207.4	5.0	NA
SFO-1-29	166	5302	1.7	23.1759	13.5	0.1947	14.1	0.0327	4.2	0.30	207.6	8.6	180.7	23.4	-159.0	336.9	207.6	8.6	NA
SFO-1-8	365	16812	1.3	19.7527	4.3	0.2288	5.1	0.0328	2.8	0.55	208.0	5.8	209.2	9.7	223.8	99.2	208.0	5.8	NA
SFO-1-3	226	12628	1.7	19.9225	9.3	0.2270	9.6	0.0328	2.4	0.25	208.1	5.0	207.8	18.0	204.0	215.2	208.1	5.0	NA
SFO-1-26	132	10491	1.9	19.8945	13.7	0.2275	14.0	0.0328	2.7	0.20	208.2	5.6	208.1	26.4	207.3	319.6	208.2	5.6	NA
SFO-1-12	262	12004	3.0	19.2828	6.1	0.2353	6.2	0.0329	1.2	0.20	208.7	2.5	214.6	12.0	279.3	139.0	208.7	2.5	NA
SFO-1-16	189	14066	2.8	20.7403	11.9	0.2188	12.1	0.0329	2.0	0.17	208.8	4.2	200.9	22.0	109.9	282.1	208.8	4.2	NA
SFO-1-25	244	31761	1.2	19.9273	5.7	0.2281	6.0	0.0330	1.8	0.30	209.1	3.7	208.6	11.2	203.4	131.9	209.1	3.7	NA
SFO-1-7	409	20748	1.1	19.4741	4.0	0.2337	7.1	0.0330	5.8	0.82	209.4	12.0	213.3	13.7	256.6	92.8	209.4	12.0	NA
SFO1-35	374	30397	1.1	19.7200	5.3	0.2314	6.4	0.0331	3.5	0.55	209.9	7.2	211.3	12.1	227.7	122.8	209.9	7.2	NA
SFO-1-6	236	9987	2.1	20.4592	4.0	0.2243	4.2	0.0333	1.2	0.29	211.0	2.6	205.4	7.9	142.0	95.1	211.0	2.6	NA
SFO-1-14	497	24237	1.4	20.0427	2.9	0.2313	3.4	0.0336	1.8	0.52	213.2	3.7	211.3	6.4	190.1	66.7	213.2	3.7	NA
SFO-1-34	301	14304	1.7	20.2457	3.8	0.2292	5.0	0.0337	3.2	0.65	213.4	6.8	209.6	9.4	166.5	87.8	213.4	6.8	NA
SFO-1-20	372	30637	1.4	20.1408	5.1	0.2313	5.5	0.0338	2.0	0.37	214.2	4.3	211.2	10.6	178.6	120.1	214.2	4.3	NA
SFO-1-36	389	24142	1.1	20.5408	3.7	0.2283	4.1	0.0340	1.8	0.44	215.6	3.9	208.8	7.8	132.6	87.5	215.6	3.9	NA

Nu Plasma HR multicollector ICPMS data of magmatic and metamoprhic rims zircon from leucosome **(SFO-8)**, Western Sonobari Complex, Mexico.

Spot 35 micron				Isotope ratios							Apparent ages (Ma)								
Analysis	U (ppm)	206Pb 204Pb	U/Th	206Pb* 207Pb*	± (%)	207Pb* 235U*	± (%)	206Pb* 238U	± (%)	error corr.	206Pb* 238U*	± (Ma)	207Pb* 235U	± (Ma)	206Pb* 207Pb*	± (Ma)	Best age (Ma)	± (Ma)	Conc (%)
SFO8-23	2208	72199	6.1	20.9429	1.7	0.0881	2.2	0.0134	1.3	0.62	85.7	1.1	85.8	1.8	86.9	40.6	85.7	1.1	NA
SFO8-5	784	24435	38.3	21.3030	5.6	0.0902	6.0	0.0139	1.9	0.32	89.3	1.7	87.7	5.0	46.2	135.0	89.3	1.7	NA
SFO8-32	784	34039	38.1	21.7040	4.7	0.0888	5.0	0.0140	1.7	0.33	89.5	1.5	86.4	4.1	1.5	113.5	89.5	1.5	NA
SFO8-29	996	33162	23.7	20.9884	4.7	0.0949	5.1	0.0144	1.9	0.37	92.4	1.7	92.0	4.5	81.7	112.0	92.4	1.7	NA
SFO8-19	965	59026	26.0	20.8609	3.4	0.0959	3.8	0.0145	1.6	0.42	92.9	1.5	93.0	3.3	96.2	80.8	92.9	1.5	NA
SFO8-2	1581	52480	29.9	20.8355	1.8	0.0968	2.6	0.0146	2.0	0.74	93.6	1.8	93.8	2.4	99.0	42.0	93.6	1.8	NA
SFO8-4	1086	26795	36.8	20.2314	3.7	0.1013	4.1	0.0149	1.6	0.38	95.2	1.5	98.0	3.8	168.2	87.4	95.2	1.5	NA
SFO8-13	651	14612	33.2	21.0372	5.6	0.0989	5.9	0.0151	1.8	0.30	96.5	1.7	95.8	5.4	76.2	134.1	96.5	1.7	NA
SFO8-11	339	11271	5.6	20.3009	8.0	0.1184	8.3	0.0174	2.1	0.26	111.4	2.4	113.6	8.9	160.2	187.2	111.4	2.4	NA
SFO8-35	585	55993	14.6	20.2884	4.9	0.1413	6.9	0.0208	4.8	0.70	132.6	6.3	134.2	8.6	161.6	115.1	132.6	6.3	NA
SFO8-17	589	30626	11.2	19.6512	5.1	0.1510	6.9	0.0215	4.6	0.67	137.2	6.2	142.8	9.1	235.8	117.9	137.2	6.2	NA
SFO8-9	1027	32752	23.7	20.5330	1.9	0.1611	2.4	0.0240	1.4	0.60	152.9	2.1	151.7	3.3	133.5	44.3	152.9	2.1	NA
SFO8-18	322	58168	3.7	20.4232	3.9	0.1717	7.5	0.0254	6.4	0.85	161.9	10.3	160.9	11.2	146.1	91.5	161.9	10.3	NA
SFO8-20	235	41343	2.9	21.2677	12.6	0.1778	12.9	0.0274	2.7	0.21	174.4	4.6	166.2	19.8	50.2	302.9	174.4	4.6	NA
SFO8-26	240	22765	1.9	19.2127	8.8	0.2109	9.0	0.0294	1.7	0.19	186.7	3.1	194.3	15.9	287.6	202.0	186.7	3.1	NA
SFO8-27	159	8933	1.7	19.4460	7.4	0.2102	9.5	0.0296	6.0	0.63	188.4	11.1	193.7	16.7	259.9	169.2	188.4	11.1	NA
SFO8-22	212	10861	1.8	20.8842	6.9	0.1991	7.1	0.0302	1.8	0.26	191.5	3.5	184.3	12.0	93.5	163.3	191.5	3.5	NA
SFO8-31	344	42675	1.2	19.7705	3.7	0.2141	4.1	0.0307	1.8	0.45	194.9	3.5	197.0	7.4	221.8	85.1	194.9	3.5	NA
SFO8-25	231	13747	1.1	19.9161	9.1	0.2200	10.3	0.0318	4.9	0.47	201.7	9.6	201.9	18.8	204.8	210.8	201.7	9.6	NA
SFO8-24	156	15086	1.1	21.2569	10.2	0.2090	10.4	0.0322	2.1	0.21	204.4	4.3	192.7	18.3	51.4	243.7	204.4	4.3	NA
SFO8-33	148	16061	1.5	19.3582	18.1	0.2328	19.5	0.0327	7.3	0.37	207.3	14.8	212.5	37.4	270.3	418.0	207.3	14.8	NA
SFO8-14	155	7482	1.1	19.8760	11.3	0.2277	11.5	0.0328	2.0	0.17	208.2	4.1	208.3	21.6	209.4	262.1	208.2	4.1	NA
SFO8-8	124	7194	1.6	20.8877	8.5	0.2178	9.0	0.0330	2.8	0.31	209.3	5.8	200.1	16.3	93.1	202.1	209.3	5.8	NA
SFO8-21	266	18181	1.3	19.2686	4.9	0.2366	5.7	0.0331	2.9	0.51	209.7	6.0	215.7	11.1	280.9	111.9	209.7	6.0	NA
SFO8-10	106	3764	1.2	23.3214	12.4	0.1955	12.8	0.0331	3.2	0.25	209.7	6.7	181.3	21.3	-174.6	310.9	209.7	6.7	NA
SFO8-3	139	18349	1.5	21.1741	9.5	0.2162	10.1	0.0332	3.3	0.33	210.5	6.9	198.7	18.2	60.7	226.5	210.5	6.9	NA
SFO8-15	215	26490	1.5	20.9866	9.6	0.2184	10.0	0.0332	2.5	0.25	210.8	5.2	200.5	18.1	81.9	229.2	210.8	5.2	NA
SFO8-1	122	6734	1.5	18.8946	8.5	0.2434	8.7	0.0334	2.0	0.23	211.5	4.2	221.2	17.3	325.6	192.5	211.5	4.2	NA
SFO8-30	289	42493	1.4	20.0605	5.4	0.2298	5.6	0.0334	1.4	0.26	212.0	3.0	210.0	10.6	187.9	125.1	212.0	3.0	NA
SFO8-28	174	20474	1.2	20.9068	9.7	0.2207	10.0	0.0335	2.3	0.23	212.2	4.7	202.5	18.4	90.9	231.2	212.2	4.7	NA
SFO8-34	95	7651	1.2	18.5802	14.9	0.2505	15.2	0.0338	3.0	0.20	214.1	6.3	227.0	31.0	363.5	338.4	214.1	6.3	NA
SFO8-12	368	34411	0.8	19.8238	4.1	0.2396	4.9	0.0345	2.7	0.55	218.3	5.9	218.1	9.7	215.5	95.4	218.3	5.9	NA
SFO8-16	775	84107	1.2	19.5803	1.2	0.2584	2.2	0.0367	1.8	0.83	232.3	4.1	233.4	4.5	244.0	27.5	232.3	4.1	NA

Nu Plasma HR multicollector ICPMS data of magmatic and metamoprhic rims zircon from leucosome **(SFO-9)**, Western Sonobari Complex, Mexico.

Spot 35 micron				Isotope ratios							Apparent ages (Ma)								
Analysis	U (ppm)	206Pb 204Pb	U/Th	206Pb* 207Pb*	± (%)	207Pb* 235U*	± (%)	206Pb* 238U	± (%)	error corr.	206Pb* 238U*	± (Ma)	207Pb* 235U	± (Ma)	206Pb* 207Pb*	± (Ma)	Best age (Ma)	± (Ma)	Conc (%)
SFO9-12	1898	69543	80.4	20.7134	2.0	0.0947	2.4	0.0142	1.4	0.56	91.0	1.2	91.8	2.1	112.9	47.7	91.0	1.2	NA
SFO9-10	505	11560	118.3	22.7295	9.7	0.0872	10.5	0.0144	3.9	0.37	92.0	3.5	84.9	8.5	-110.9	240.2	92.0	3.5	NA
SFO9-16	641	31462	62.5	20.0844	4.7	0.1013	5.1	0.0147	2.1	0.41	94.4	1.9	97.9	4.8	185.2	108.5	94.4	1.9	NA
SFO9-23	167	6434	4.5	20.3863	28.1	0.1363	28.3	0.0201	3.7	0.13	128.6	4.8	129.7	34.5	150.3	669.5	128.6	4.8	NA
SFO9-5	103	8943	3.3	20.2369	26.4	0.1736	27.1	0.0255	6.3	0.23	162.2	10.2	162.5	40.8	167.5	626.3	162.2	10.2	NA
SFO9-15	290	8297	4.2	21.2299	9.1	0.1665	10.6	0.0256	5.3	0.50	163.2	8.6	156.4	15.3	54.5	218.2	163.2	8.6	NA
SFO9-13	253	16794	3.3	20.5217	9.2	0.1888	10.0	0.0281	4.0	0.39	178.7	7.0	175.6	16.2	134.8	217.1	178.7	7.0	NA
SFO9-21	245	12963	1.8	19.0549	6.9	0.2071	7.7	0.0286	3.4	0.45	181.9	6.1	191.1	13.4	306.4	156.5	181.9	6.1	NA
SFO9-20	289	26606	1.6	21.3485	6.8	0.1918	7.2	0.0297	2.4	0.33	188.7	4.5	178.2	11.8	41.2	162.4	188.7	4.5	NA
SFO9-2	206	31897	1.4	20.3901	7.1	0.2143	7.7	0.0317	3.1	0.40	201.1	6.2	197.1	13.9	149.9	166.3	201.1	6.2	NA
SFO9-11	266	37967	1.6	19.5700	4.6	0.2268	7.0	0.0322	5.2	0.75	204.2	10.5	207.5	13.1	245.3	106.1	204.2	10.5	NA
SFO9-24	279	48554	1.3	19.5234	10.1	0.2286	10.3	0.0324	2.3	0.22	205.4	4.6	209.1	19.5	250.7	232.3	205.4	4.6	NA
SFO9-14	213	17104	1.0	20.0823	8.3	0.2264	8.4	0.0330	1.6	0.19	209.1	3.2	207.2	15.8	185.4	193.2	209.1	3.2	NA
SFO9-4	163	11244	1.6	21.4844	10.1	0.2134	10.2	0.0333	1.4	0.14	210.9	3.0	196.4	18.2	26.0	242.2	210.9	3.0	NA
SFO9-1	101	7802	1.6	21.3182	11.2	0.2152	11.4	0.0333	2.5	0.22	211.0	5.1	197.9	20.5	44.6	267.3	211.0	5.1	NA
SFO9-7	188	18986	1.1	18.9283	7.1	0.2425	7.5	0.0333	2.5	0.34	211.1	5.2	220.5	14.9	321.6	161.0	211.1	5.2	NA
SFO9-3	267	20167	1.3	20.0917	6.2	0.2289	6.6	0.0334	2.4	0.37	211.5	5.1	209.3	12.6	184.3	144.0	211.5	5.1	NA
SFO9-8	453	52857	1.0	19.5775	4.4	0.2357	4.8	0.0335	1.9	0.40	212.2	4.0	214.9	9.4	244.4	102.4	212.2	4.0	NA
SFO9-9	143	11898	2.1	18.7835	9.9	0.2458	10.4	0.0335	3.2	0.31	212.3	6.7	223.2	20.9	338.9	225.1	212.3	6.7	NA
SFO9-22	156	15450	1.3	17.9606	7.2	0.2580	8.2	0.0336	3.8	0.47	213.1	8.0	233.1	17.0	439.5	161.1	213.1	8.0	NA
SFO9-18	158	12113	1.1	18.9907	6.0	0.2460	7.4	0.0339	4.3	0.58	214.8	9.0	223.3	14.8	314.1	136.7	214.8	9.0	NA
SFO9-6	146	18231	1.8	20.3231	7.2	0.2302	7.9	0.0339	3.3	0.42	215.1	7.1	210.4	15.1	157.6	168.5	215.1	7.1	NA
SFO9-17	101	4425	1.0	17.5822	26.4	0.2739	27.0	0.0349	5.7	0.21	221.3	12.4	245.8	59.0	486.7	591.1	221.3	12.4	NA
SFO9-19	473	33887	3.2	19.4821	3.4	0.3027	5.2	0.0428	4.0	0.76	270.0	10.6	268.5	12.4	255.6	77.7	270.0	10.6	NA

Ion counters Nu Plasma HR multicollector ICPMS data of magmatic and metamoprhic rims zircon from leucosome **(SFO-9)**, Western Sonobari Complex, Mexico.

Ion counters 15 micron				Isotope ratios							Apparent ages (Ma)								
Analysis	U (ppm)	206Pb 204Pb	U/Th	206Pb* 207Pb*	± (%)	207Pb* 235U*	± (%)	206Pb* 238U	± (%)	error corr.	206Pb* 238U*	± (Ma)	207Pb* 235U	± (Ma)	206Pb* 207Pb*	± (Ma)	Best age (Ma)	± (Ma)	Conc (%)
SFO9-IC-25	5766	36665	34.3	20.6178	0.9	0.0758	2.3	0.0113	2.1	0.92	72.7	1.5	74.2	1.6	123.8	20.6	72.7	1.5	NA
SFO9-IC-30	536	3967	104.8	20.1515	6.4	0.0800	6.6	0.0117	1.6	0.24	74.9	1.2	78.1	5.0	177.4	149.6	74.9	1.2	NA
SFO9-IC-13	635	4889	30.8	18.8214	10.1	0.0891	10.7	0.0122	3.6	0.34	77.9	2.8	86.7	8.9	334.4	229.3	77.9	2.8	NA
SFO9-IC-26	1524	19036	84.8	20.5172	1.2	0.0837	2.0	0.0125	1.6	0.79	79.8	1.2	81.6	1.5	135.3	28.0	79.8	1.2	NA
SFO9-IC-2	115	2388	259.0	21.1494	2.8	0.0855	3.5	0.0131	2.2	0.63	84.0	1.9	83.3	2.8	63.5	65.8	84.0	1.9	NA
SFO9-IC-17	1231	25232	82.9	20.7852	1.1	0.0870	6.1	0.0131	6.0	0.98	84.0	5.0	84.7	4.9	104.7	25.4	84.0	5.0	NA
SFO9-IC-29	539	5705	44.6	20.0053	1.1	0.0928	6.5	0.0135	6.4	0.99	86.2	5.5	90.1	5.6	194.4	24.7	86.2	5.5	NA
SFO9-IC-14	201	2972	1172.7	21.5162	2.4	0.0869	2.5	0.0136	0.8	0.30	86.8	0.7	84.6	2.1	22.4	57.9	86.8	0.7	NA
SFO9-IC-20	818	12342	83.8	20.8775	1.0	0.0897	1.9	0.0136	1.6	0.86	87.0	1.4	87.3	1.6	94.3	23.3	87.0	1.4	NA
SFO9-IC-22	354	5030	47.5	20.4179	1.3	0.0922	5.2	0.0136	5.1	0.97	87.4	4.4	89.5	4.5	146.7	29.7	87.4	4.4	NA
SFO9-IC-7	1699	35101	78.8	20.8133	0.7	0.0920	1.8	0.0139	1.7	0.92	88.9	1.5	89.4	1.5	101.6	16.4	88.9	1.5	NA
SFO9-IC-9	284	3104	202.7	21.3207	1.2	0.0902	1.6	0.0140	1.1	0.67	89.3	0.9	87.7	1.3	44.3	28.2	89.3	0.9	NA
SFO9-IC-28	628	9773	105.7	20.6157	0.7	0.0933	1.3	0.0140	1.1	0.82	89.3	1.0	90.6	1.1	124.0	17.7	89.3	1.0	NA
SFO9-IC-23	208	4246	134.1	20.8154	0.9	0.0934	3.8	0.0141	3.6	0.97	90.2	3.3	90.6	3.3	101.3	21.7	90.2	3.3	NA
SFO9-IC-18	1012	13486	93.8	21.0727	1.0	0.0923	2.1	0.0141	1.9	0.88	90.3	1.7	89.6	1.8	72.2	23.7	90.3	1.7	NA
SFO9-IC-24	220	4869	355.3	21.4956	1.8	0.0929	3.9	0.0145	3.5	0.88	92.7	3.2	90.2	3.4	24.7	44.1	92.7	3.2	NA
SFO9-IC-27	498	7691	86.2	20.3040	1.5	0.0996	1.9	0.0147	1.3	0.66	93.9	1.2	96.4	1.8	159.8	34.2	93.9	1.2	NA
SFO9-IC-16	91	1622	234.5	21.8694	2.2	0.0990	2.7	0.0157	1.5	0.57	100.5	1.5	95.9	2.5	-16.8	53.8	100.5	1.5	NA
SFO9-IC-1	292	5206	100.0	20.2452	2.0	0.1072	2.2	0.0157	1.0	0.44	100.7	1.0	103.4	2.2	166.6	46.4	100.7	1.0	NA
SFO9-IC-10	207	6816	86.2	20.2700	1.1	0.1074	9.0	0.0158	8.9	0.99	101.0	8.9	103.6	8.9	163.7	26.4	101.0	8.9	NA
SFO9-IC-8	121	561	139.5	14.3069	9.6	0.1557	10.3	0.0162	3.6	0.35	103.3	3.7	146.9	14.0	925.3	197.7	103.3	3.7	NA
SFO9-IC-15	288	4236	43.6	21.7560	1.7	0.1050	3.0	0.0166	2.4	0.82	105.9	2.6	101.4	2.9	-4.2	41.0	105.9	2.6	NA
SFO9-IC-6	204	6211	90.2	20.1433	1.4	0.1136	2.4	0.0166	1.9	0.80	106.1	2.0	109.3	2.5	178.4	33.4	106.1	2.0	NA
SFO9-IC-4	246	5713	75.5	20.4822	1.1	0.1372	2.5	0.0204	2.2	0.90	130.1	2.9	130.6	3.0	139.4	25.0	130.1	2.9	NA
SFO9-IC-19	215	4979	3.0	20.0215	1.3	0.1837	4.6	0.0267	4.4	0.96	169.7	7.4	171.3	7.3	192.5	29.8	169.7	7.4	NA
SFO9-IC-5	83	4671	1.7	20.3311	0.9	0.2211	2.6	0.0326	2.4	0.93	206.8	4.9	202.8	4.7	156.7	21.4	206.8	4.9	NA

Nu Plasma HR multicollector ICPMS data of magmatic and metamoprhic rims zircon from leucosome **(SFO-19)**, Western Sonobari Complex, Mexico.

Spot 35 micron				Isotope ratios							Apparent ages (Ma)								
Analysis	U	206Pb	U/Th	206Pb*	±	207Pb*	±	206Pb*	±	error	206Pb*	±	207Pb*	±	206Pb*	±	Best age	±	Conc
	(ppm)	204Pb		207Pb*	(%)	235U*	(%)	238U	(%)	corr.	238U*	(Ma)	235U	(Ma)	207Pb*	(Ma)	(Ma)	(Ma)	(%)
SFO19-15	1449	59612	69.8	20.6992	2.5	0.0959	2.6	0.0144	0.8	0.30	92.2	0.7	93.0	2.3	114.5	58.6	92.2	0.7	NA
SFO19-14	1570	34244	65.2	20.4062	3.2	0.0979	3.6	0.0145	1.7	0.48	92.8	1.6	94.9	3.3	148.0	74.3	92.8	1.6	NA
SFO19-17	528	17307	78.1	20.2400	5.4	0.0989	5.8	0.0145	2.1	0.37	92.9	2.0	95.8	5.3	167.2	126.8	92.9	2.0	NA
SFO19-07	118	36182	2.1	18.0504	9.0	0.4085	10.0	0.0535	4.2	0.42	335.8	13.8	347.8	29.3	428.4	201.3	335.8	13.8	NA
SFO19-32	102	9294	1.4	17.3670	5.2	0.5600	5.7	0.0705	2.4	0.43	439.4	10.4	451.5	20.8	513.8	113.7	439.4	10.4	85.5
SFO19-45	121	26677	2.9	14.0384	4.2	0.8066	6.6	0.0821	5.1	0.77	508.8	24.8	600.5	29.9	964.1	86.4	508.8	24.8	52.8
SFO19-13	83	16789	1.5	18.3572	7.7	0.6423	7.9	0.0855	1.6	0.20	529.0	8.0	503.7	31.3	390.7	173.7	529.0	8.0	135.4
SFO19-38	118	11962	1.6	17.5465	6.3	0.6752	6.6	0.0859	1.8	0.28	531.4	9.3	523.9	26.8	491.2	139.0	531.4	9.3	108.2
SFO19-28	34	2737	1.5	21.5759	29.8	0.5521	30.2	0.0864	4.7	0.16	534.2	24.0	446.4	109.5	15.8	731.3	534.2	24.0	3389.7
SFO19-49	439	168292	3.3	13.4128	0.8	1.5512	1.9	0.1509	1.7	0.91	906.0	14.2	951.0	11.5	1056.6	15.8	1056.6	15.8	85.7
SFO19-06	168	61696	1.1	13.3907	1.0	1.4757	3.0	0.1433	2.8	0.94	863.4	22.9	920.5	18.2	1059.9	20.6	1059.9	20.6	81.5
SFO19-55	143	156330	1.9	13.3879	1.4	1.8859	1.9	0.1831	1.3	0.66	1084.0	12.5	1076.1	12.5	1060.3	28.5	1060.3	28.5	102.2
SFO19-11	150	21550	1.8	13.3448	2.0	1.8177	2.5	0.1759	1.6	0.62	1044.7	15.0	1051.9	16.5	1066.8	40.0	1066.8	40.0	97.9
SFO19-20	440	221566	2.6	13.2780	0.6	1.8209	0.9	0.1754	0.7	0.76	1041.6	6.6	1053.0	6.0	1076.9	12.0	1076.9	12.0	96.7
SFO19-16	195	50899	3.3	13.2780	1.8	1.5538	2.7	0.1496	2.0	0.75	898.9	17.2	952.0	16.9	1076.9	36.6	1076.9	36.6	83.5
SFO19-50	117	48265	1.9	13.2281	2.6	1.9172	6.9	0.1839	6.4	0.93	1088.4	64.1	1087.1	46.1	1084.4	52.0	1084.4	52.0	100.4
SFO19-25	151	43886	1.3	13.1782	2.0	1.8688	2.3	0.1786	1.1	0.50	1059.4	11.0	1070.1	15.0	1092.0	39.4	1092.0	39.4	97.0
SFO19-31	89	40025	1.4	13.1725	2.7	1.9460	3.2	0.1859	1.7	0.54	1099.2	17.6	1097.1	21.6	1092.8	54.1	1092.8	54.1	100.6
SFO19-40	102	58246	1.1	13.1487	1.4	1.9303	2.1	0.1841	1.6	0.76	1089.2	16.2	1091.6	14.3	1096.5	28.0	1096.5	28.0	99.3
SFO19-08	55	23823	1.1	13.1396	2.9	1.8849	4.3	0.1796	3.1	0.72	1064.9	30.2	1075.8	28.3	1097.8	59.0	1097.8	59.0	97.0
SFO19-10	91	27847	1.8	13.1377	1.9	1.9199	2.4	0.1829	1.5	0.61	1083.0	14.7	1088.0	16.3	1098.1	38.8	1098.1	38.8	98.6
SFO19-03	305	107716	1.4	13.0024	0.8	1.9319	2.5	0.1822	2.4	0.95	1078.9	23.8	1092.2	16.9	1118.8	15.9	1118.8	15.9	96.4
SFO19-18	134	60678	1.3	12.9931	1.1	1.9479	1.8	0.1836	1.5	0.80	1086.4	14.7	1097.7	12.4	1120.3	22.2	1120.3	22.2	97.0
SFO19-30	228	59154	1.7	12.9470	0.7	2.0584	1.7	0.1933	1.6	0.91	1139.2	16.6	1135.1	11.9	1127.3	14.5	1127.3	14.5	101.1
SFO19-41	59	16220	0.9	12.3742	2.8	2.3253	3.4	0.2087	1.8	0.54	1221.8	20.1	1220.0	23.8	1216.9	55.5	1216.9	55.5	100.4
SFO19-37	218	161539	21.9	12.2567	0.9	2.2448	2.2	0.1996	2.0	0.90	1172.9	21.3	1195.2	15.5	1235.7	18.5	1235.7	18.5	94.9
SFO19-39	131	74444	0.8	12.2382	1.8	2.3115	2.4	0.2052	1.6	0.66	1203.0	17.6	1215.8	17.1	1238.6	35.5	1238.6	35.5	97.1
SFO19-47	135	41502	2.5	11.5465	1.3	2.3766	1.7	0.1990	1.1	0.65	1170.1	11.7	1235.6	12.0	1351.7	24.5	1351.7	24.5	86.6
SFO19-04	141	45618	1.5	11.4547	0.9	2.2813	3.1	0.1895	2.9	0.95	1118.8	30.1	1206.5	21.7	1367.1	18.2	1367.1	18.2	81.8
SFO19-27	305	135969	2.3	11.3980	1.1	2.5197	2.6	0.2083	2.3	0.91	1219.7	26.1	1277.7	18.7	1376.7	20.4	1376.7	20.4	88.6
SFO19-44	61	23582	1.6	11.2697	2.8	2.4636	6.0	0.2014	5.3	0.88	1182.6	56.8	1261.4	43.1	1398.4	54.1	1398.4	54.1	84.6
SFO19-01	108	108594	2.3	11.2610	2.0	2.6690	7.9	0.2180	7.7	0.97	1271.2	88.8	1319.9	58.7	1399.9	37.8	1399.9	37.8	90.8
SFO19-42	123	57510	1.5	11.1115	1.5	3.1483	2.6	0.2537	2.1	0.82	1457.6	28.0	1444.6	20.2	1425.4	28.9	1425.4	28.9	102.3
SFO19-54	299	292614	2.1	11.0048	0.5	3.1658	1.8	0.2527	1.7	0.96	1452.3	22.6	1448.9	14.0	1443.8	9.3	1443.8	9.3	100.6
SFO19-21	103	65807	0.9	10.9454	1.0	3.1705	2.3	0.2517	2.0	0.89	1447.2	26.4	1450.0	17.6	1454.2	19.4	1454.2	19.4	99.5
SFO19-53	61	58574	1.1	10.9057	2.7	3.2099	3.7	0.2539	2.5	0.68	1458.5	32.8	1459.6	28.8	1461.1	52.1	1461.1	52.1	99.8
SFO19-29	170	63963	4.6	10.8858	0.9	3.1586	1.7	0.2494	1.4	0.84	1435.3	17.9	1447.1	12.8	1464.5	17.1	1464.5	17.1	98.0
SFO19-09	130	110252	2.9	10.8651	1.0	3.2534	2.4	0.2564	2.2	0.90	1471.3	28.8	1470.0	18.8	1468.1	19.9	1468.1	19.9	100.2
SFO19-46	73	68974	0.9	10.4421	2.1	3.1913	2.6	0.2417	1.6	0.61	1395.5	19.9	1455.1	20.2	1543.2	39.0	1543.2	39.0	90.4
SFO19-43	217	155991	0.9	10.2949	1.0	3.3495	1.5	0.2501	1.2	0.78	1438.9	15.5	1492.7	12.1	1569.8	18.2	1569.8	18.2	91.7
SFO19-52	88	36276	1.3	10.0687	1.0	3.9205	1.5	0.2863	1.0	0.71	1623.0	15.0	1617.9	11.9	1611.3	19.1	1611.3	19.1	100.7
SFO19-56	61	39456	1.6	10.0505	1.6	3.3616	5.5	0.2450	5.2	0.96	1412.8	66.3	1495.5	42.8	1614.7	30.1	1614.7	30.1	87.5

SFO19-34	174	106382	1.5	9.8722	0.6	3.9867	1.9	0.2854	1.8	0.95	1618.7	26.3	1631.5	15.7	1647.9	10.9	1647.9	10.9	98.2
SFO19-48	117	121385	1.5	9.8476	0.7	4.0430	1.6	0.2888	1.4	0.90	1635.3	20.4	1642.9	12.8	1652.6	12.7	1652.6	12.7	99.0

Ion counters Nu Plasma HR multicollector ICPMS data of magmatic and metamoprhic rims zircon from leucosome **(SFO-19)**, Western Sonobari Complex, Mexico.

counters 15 micron				Isotope ratios							Apparent ages (Ma)								
Analysis	U	206Pb	U/Th	206Pb*	±	207Pb*	±	206Pb*	±	error	206Pb*	±	207Pb*	±	206Pb*	±	Best age	±	Conc
	(ppm)	204Pb		207Pb*	(%)	235U*	(%)	238U	(%)	corr.	238U*	(Ma)	235U	(Ma)	207Pb*	(Ma)	(Ma)	(Ma)	(%)
SFO19-IC-18	538	66820	240.8	20.4242	0.8	0.0876	2.0	0.0130	1.8	0.91	83.1	1.5	85.3	1.6	146.0	19.8	83.1	1.5	NA
SFO19-IC-30	373	43170	87.4	20.1956	0.6	0.0915	4.7	0.0134	4.7	0.99	85.8	4.0	88.9	4.0	172.3	14.3	85.8	4.0	NA
SFO19-IC-31	539	43444	126.1	20.6267	0.9	0.0911	3.2	0.0136	3.1	0.96	87.2	2.7	88.5	2.7	122.8	20.4	87.2	2.7	NA
SFO19-IC-34	470	42072	94.1	20.6413	1.0	0.0918	1.9	0.0137	1.6	0.86	88.0	1.4	89.1	1.6	121.1	22.7	88.0	1.4	NA
SFO19-IC-2	770	85188	73.5	20.8613	0.9	0.0917	2.3	0.0139	2.1	0.92	88.8	1.9	89.1	2.0	96.1	21.1	88.8	1.9	NA
SFO19-IC-19	455	30068	84.8	20.8886	1.0	0.0921	1.6	0.0139	1.3	0.80	89.3	1.2	89.4	1.4	93.0	23.5	89.3	1.2	NA
SFO19-IC-27	211	15203	218.2	20.5516	1.4	0.0944	2.1	0.0141	1.6	0.73	90.1	1.4	91.6	1.9	131.4	34.0	90.1	1.4	NA
SFO19-IC-1	362	44571	63.4	20.3732	1.6	0.0953	2.9	0.0141	2.5	0.84	90.1	2.2	92.4	2.6	151.8	37.1	90.1	2.2	NA
SFO19-IC-15	503	47519	137.5	20.5112	2.0	0.0947	3.2	0.0141	2.5	0.78	90.2	2.2	91.9	2.8	136.0	47.1	90.2	2.2	NA
SFO19-IC-23	406	33355	139.0	21.2664	0.9	0.0919	3.0	0.0142	2.9	0.95	90.7	2.6	89.3	2.6	50.4	21.5	90.7	2.6	NA
SFO19-IC-9	450	22661	131.0	20.4955	3.0	0.0954	4.7	0.0142	3.6	0.77	90.8	3.3	92.5	4.2	137.8	70.8	90.8	3.3	NA
SFO19-IC-10	523	34437	164.0	20.3036	0.8	0.0964	3.8	0.0142	3.7	0.98	90.8	3.4	93.4	3.4	159.9	19.5	90.8	3.4	NA
SFO19-IC-20	684	51724	139.5	21.1541	0.8	0.0925	2.9	0.0142	2.8	0.96	90.9	2.5	89.9	2.5	63.0	18.3	90.9	2.5	NA
SFO19-IC-29	489	61509	79.8	20.9999	0.8	0.0938	2.5	0.0143	2.3	0.94	91.4	2.1	91.0	2.2	80.4	19.3	91.4	2.1	NA
SFO19-IC-26	695	53250	173.0	20.7485	0.6	0.0950	1.5	0.0143	1.4	0.93	91.5	1.3	92.1	1.3	108.9	13.0	91.5	1.3	NA
SFO19-IC-32	163	31876	153.3	20.9974	1.9	0.0948	2.7	0.0144	1.9	0.70	92.4	1.7	91.9	2.4	80.7	45.9	92.4	1.7	NA
SFO19-IC-17	765	38910	69.5	20.9999	1.0	0.0952	2.0	0.0145	1.8	0.88	92.8	1.7	92.3	1.8	80.4	23.1	92.8	1.7	NA
SFO19-IC-14	877	62045	74.3	21.4325	0.7	0.0947	1.9	0.0147	1.7	0.93	94.2	1.6	91.8	1.7	31.8	17.1	94.2	1.6	NA
SFO19-IC-21	280	20286	107.9	20.7337	1.4	0.0982	1.6	0.0148	0.8	0.48	94.5	0.7	95.1	1.5	110.6	33.6	94.5	0.7	NA
SFO19-IC-22	592	83652	75.2	20.8952	1.3	0.0979	1.8	0.0148	1.3	0.70	94.9	1.2	94.8	1.6	92.2	30.5	94.9	1.2	NA
SFO19-IC-28	140	33194	158.7	20.5118	1.5	0.1000	4.5	0.0149	4.3	0.94	95.2	4.1	96.8	4.2	136.0	35.2	95.2	4.1	NA
SFO19-IC-3	246	10266	113.8	21.7029	1.1	0.0960	2.4	0.0151	2.2	0.89	96.7	2.1	93.1	2.1	1.6	26.4	96.7	2.1	NA
SFO19-IC-24	209	11440	161.2	20.9678	1.4	0.0996	2.8	0.0152	2.4	0.86	96.9	2.3	96.4	2.5	84.0	32.8	96.9	2.3	NA
SFO19-IC-5	366	21985	130.2	21.3518	1.3	0.0988	1.9	0.0153	1.4	0.72	97.9	1.3	95.7	1.7	40.8	31.8	97.9	1.3	NA
SFO19-IC-16	262	31731	126.1	20.5376	1.7	0.1041	2.1	0.0155	1.3	0.63	99.2	1.3	100.5	2.0	133.0	39.0	99.2	1.3	NA
SFO19-IC-6	245	21590	160.0	21.5564	1.7	0.1003	2.7	0.0157	2.2	0.79	100.3	2.1	97.0	2.5	17.9	40.2	100.3	2.1	NA
SFO19-IC-13	155	7778	144.5	21.7239	1.4	0.1003	2.9	0.0158	2.5	0.88	101.1	2.5	97.1	2.7	-0.7	33.4	101.1	2.5	NA
SFO19-IC-36	199	11606	206.1	20.9660	1.7	0.1046	5.5	0.0159	5.2	0.95	101.7	5.3	101.0	5.3	84.2	40.2	101.7	5.3	NA
SFO19-IC-38	220	20356	179.1	21.7139	1.1	0.1016	1.9	0.0160	1.6	0.81	102.3	1.6	98.3	1.8	0.4	27.0	102.3	1.6	NA
SFO19-IC-7	262	24708	71.3	16.6761	10.6	0.1565	13.2	0.0189	7.8	0.59	120.8	9.4	147.6	18.1	602.3	230.6	120.8	9.4	NA
SFO19-IC-8	357	71464	29.0	14.5677	3.1	0.3422	3.4	0.0362	1.4	0.42	228.9	3.3	298.8	8.8	888.1	63.9	228.9	3.3	NA
SFO19-IC-25	84	128077	1.7	13.1708	0.6	1.9273	1.8	0.1841	1.7	0.94	1089.4	17.1	1090.6	12.2	1093.1	12.5	1093.1	12.5	99.7
SFO19-IC-33	259	268985	2.5	12.7911	0.6	2.0328	2.7	0.1886	2.6	0.98	1113.7	26.6	1126.6	18.1	1151.4	11.1	1151.4	11.1	96.7

				Isotope ratios							Apparent ages (Ma)								
Analysis	U (ppm)	206Pb 204Pb	U/Th	206Pb* 207Pb*	± (%)	207Pb* 235U*	± (%)	206Pb* 238U	± (%)	error corr.	206Pb* 238U*	± (Ma)	207Pb* 235U	± (Ma)	206Pb* 207Pb*	± (Ma)	Best age (Ma)	± (Ma)	Conc (%)
Sample SFO-1 with 35µc spot *(1)																			
SFO-1-13	113	2578	22.3	25.1430	36.1	0.0616	41.5	0.0112	20.5	0.49	72.0	14.7	60.7	24.4	-365.7	960.1	72.0	14.7	NA
SFO-1-28	126	3106	70.1	22.5261	33.5	0.0843	34.3	0.0138	7.6	0.22	88.2	6.6	82.2	27.1	-88.8	840.5	88.2	6.6	NA
SFO-1-33	145	4253	101.8	18.1696	15.3	0.1055	19.0	0.0139	11.3	0.59	89.0	10.0	101.9	18.4	413.7	343.3	89.0	10.0	NA
SFO-1-31	122	3036	96.8	22.5311	48.6	0.0856	49.2	0.0140	7.2	0.15	89.5	6.4	83.4	39.4	-89.4	1259.7	89.5	6.4	NA
SFO-1-2	103	2217	62.3	18.4254	26.2	0.1062	26.7	0.0142	4.9	0.18	90.8	4.4	102.5	26.0	382.4	598.7	90.8	4.4	NA
SFO-1-4	143	1788	71.9	24.9993	31.5	0.0785	32.0	0.0142	5.6	0.17	91.1	5.0	76.7	23.6	-350.9	830.0	91.1	5.0	NA
SFO-1-11	198	5578	93.0	19.3948	17.2	0.1035	17.5	0.0146	3.3	0.19	93.2	3.0	100.0	16.6	266.0	396.3	93.2	3.0	NA
SFO-1-18	275	14197	31.5	22.6084	17.5	0.0900	17.7	0.0148	2.8	0.16	94.5	2.6	87.5	14.8	-97.8	431.6	94.5	2.6	NA
SFO-1-9	172	8274	19.3	19.5227	13.2	0.1172	14.1	0.0166	4.9	0.34	106.1	5.1	112.5	15.0	250.8	305.5	106.1	5.1	NA
Sample SFO-5 with 35µc spot *(2)																			
SFO5-2	188	6677	139.7	18.1487	18.2	0.1085	18.7	0.0143	4.4	0.23	91.4	4.0	104.6	18.6	416.3	409.3	91.4	4.0	NA
SFO5-9	146	4616	88.5	26.2914	42.9	0.0792	43.1	0.0151	4.3	0.10	96.6	4.1	77.4	32.2	-482.7	1185.4	96.6	4.1	NA
Sample SFO-8 with 35µc spot *(1)																			
SFO8-23	2208	72199	6.1	20.9429	1.7	0.0881	2.2	0.0134	1.3	0.62	85.7	1.1	85.8	1.8	86.9	40.6	85.7	1.1	NA
SFO8-5	784	24435	38.3	21.3030	5.6	0.0902	6.0	0.0139	1.9	0.32	89.3	1.7	87.7	5.0	46.2	135.0	89.3	1.7	NA
SFO8-32	784	34039	38.1	21.7040	4.7	0.0888	5.0	0.0140	1.7	0.33	89.5	1.5	86.4	4.1	1.5	113.5	89.5	1.5	NA
SFO8-29	996	33162	23.7	20.9884	4.7	0.0949	5.1	0.0144	1.9	0.37	92.4	1.7	92.0	4.5	81.7	112.0	92.4	1.7	NA
SFO8-19	965	59026	26.0	20.8609	3.4	0.0959	3.8	0.0145	1.6	0.42	92.9	1.5	93.0	3.3	96.2	80.8	92.9	1.5	NA
SFO8-2	1581	52480	29.9	20.8355	1.8	0.0968	2.6	0.0146	2.0	0.74	93.6	1.8	93.8	2.4	99.0	42.0	93.6	1.8	NA
SFO8-4	1086	26795	36.8	20.2314	3.7	0.1013	4.1	0.0149	1.6	0.38	95.2	1.5	98.0	3.8	168.2	87.4	95.2	1.5	NA
SFO8-13	651	14612	33.2	21.0372	5.6	0.0989	5.9	0.0151	1.8	0.30	96.5	1.7	95.8	5.4	76.2	134.1	96.5	1.7	NA
Sample SFO-9 with 35µc spot *(1)																			
SFO9-12	1898	69543	80.4	20.7134	2.0	0.0947	2.4	0.0142	1.4	0.56	91.0	1.2	91.8	2.1	112.9	47.7	91.0	1.2	NA
SFO9-10	505	11560	118.3	22.7295	9.7	0.0872	10.5	0.0144	3.9	0.37	92.0	3.5	84.9	8.5	-110.9	240.2	92.0	3.5	NA
SFO9-16	641	31462	62.5	20.0844	4.7	0.1013	5.1	0.0147	2.1	0.41	94.4	1.9	97.9	4.8	185.2	108.5	94.4	1.9	NA
Sample SFO-9 with ion counter 15 µc spot *(1)																			
SFO9-IC-2	115	2388	259.0	21.1494	2.8	0.0855	3.5	0.0131	2.2	0.63	84.0	1.9	83.3	2.8	63.5	65.8	84.0	1.9	NA
SFO9-IC-17	1231	25232	82.9	20.7852	1.1	0.0870	6.1	0.0131	6.0	0.98	84.0	5.0	84.7	4.9	104.7	25.4	84.0	5.0	NA
SFO9-IC-29	539	5705	44.6	20.0053	1.1	0.0928	6.5	0.0135	6.4	0.99	86.2	5.5	90.1	5.6	194.4	24.7	86.2	5.5	NA
SFO9-IC-14	201	2972	1172.7	21.5162	2.4	0.0869	2.5	0.0136	0.8	0.30	86.8	0.7	84.6	2.1	22.4	57.9	86.8	0.7	NA
SFO9-IC-20	818	12342	83.8	20.8775	1.0	0.0897	1.9	0.0136	1.6	0.86	87.0	1.4	87.3	1.6	94.3	23.3	87.0	1.4	NA
SFO9-IC-22	354	5030	47.5	20.4179	1.3	0.0922	5.2	0.0136	5.1	0.97	87.4	4.4	89.5	4.5	146.7	29.7	87.4	4.4	NA
SFO9-IC-7	1699	35101	78.8	20.8133	0.7	0.0920	1.8	0.0139	1.7	0.92	88.9	1.5	89.4	1.5	101.6	16.4	88.9	1.5	NA
SFO9-IC-9	284	3104	202.7	21.3207	1.2	0.0902	1.6	0.0140	1.1	0.67	89.3	0.9	87.7	1.3	44.3	28.2	89.3	0.9	NA
SFO9-IC-28	628	9773	105.7	20.6157	0.7	0.0933	1.3	0.0140	1.1	0.82	89.3	1.0	90.6	1.1	124.0	17.7	89.3	1.0	NA
SFO9-IC-23	208	4246	134.1	20.8154	0.9	0.0934	3.8	0.0141	3.6	0.97	90.2	3.3	90.6	3.3	101.3	21.7	90.2	3.3	NA
SFO9-IC-18	1012	13486	93.8	21.0727	1.0	0.0923	2.1	0.0141	1.9	0.88	90.3	1.7	89.6	1.8	72.2	23.7	90.3	1.7	NA
SFO9-IC-24	220	4869	355.3	21.4956	1.8	0.0929	3.9	0.0145	3.5	0.88	92.7	3.2	90.2	3.4	24.7	44.1	92.7	3.2	NA
SFO9-IC-27	498	7691	86.2	20.3040	1.5	0.0996	1.9	0.0147	1.3	0.66	93.9	1.2	96.4	1.8	159.8	34.2	93.9	1.2	NA
Sample SFO-19 with 35µc spot *(1)																			
SFO19-15	1449	59612	69.8	20.6992	2.5	0.0959	2.6	0.0144	0.8	0.30	92.2	0.7	93.0	2.3	114.5	58.6	92.2	0.7	NA
SFO19-14	1570	34244	65.2	20.4062	3.2	0.0979	3.6	0.0145	1.7	0.48	92.8	1.6	94.9	3.3	148.0	74.3	92.8	1.6	NA

SFO19-17	528	17307	78.1	20.2400	5.4	0.0989	5.8	0.0145	2.1	0.37	92.9	2.0	95.8	5.3	167.2	126.8	92.9	2.0	NA
Sample SFO-19 with ion counter 15 µc spot *(1)																			
SFO19-30	373	43170	87.4	20.1956	0.6	0.0915	4.7	0.0134	4.7	0.99	85.8	4.0	88.9	4.0	172.3	14.3	85.8	4.0	NA
SFO19-31	539	43444	126.1	20.6267	0.9	0.0911	3.2	0.0136	3.1	0.96	87.2	2.7	88.5	2.7	122.8	20.4	87.2	2.7	NA
SFO19-34	470	42072	94.1	20.6413	1.0	0.0918	1.9	0.0137	1.6	0.86	88.0	1.4	89.1	1.6	121.1	22.7	88.0	1.4	NA
SFO19-2	770	85188	73.5	20.8613	0.9	0.0917	2.3	0.0139	2.1	0.92	88.8	1.9	89.1	2.0	96.1	21.1	88.8	1.9	NA
SFO19-19	455	30068	84.8	20.8886	1.0	0.0921	1.6	0.0139	1.3	0.80	89.3	1.2	89.4	1.4	93.0	23.5	89.3	1.2	NA
SFO19-27	211	15203	218.2	20.5516	1.4	0.0944	2.1	0.0141	1.6	0.73	90.1	1.4	91.6	1.9	131.4	34.0	90.1	1.4	NA
SFO19-1	362	44571	63.4	20.3732	1.6	0.0953	2.9	0.0141	2.5	0.84	90.1	2.2	92.4	2.6	151.8	37.1	90.1	2.2	NA
SFO19-15	503	47519	137.5	20.5112	2.0	0.0947	3.2	0.0141	2.5	0.78	90.2	2.2	91.9	2.8	136.0	47.1	90.2	2.2	NA
SFO19-23	406	33355	139.0	21.2664	0.9	0.0919	3.0	0.0142	2.9	0.95	90.7	2.6	89.3	2.6	50.4	21.5	90.7	2.6	NA
SFO19-9	450	22661	131.0	20.4955	3.0	0.0954	4.7	0.0142	3.6	0.77	90.8	3.3	92.5	4.2	137.8	70.8	90.8	3.3	NA
SFO19-10	523	34437	164.0	20.3036	0.8	0.0964	3.8	0.0142	3.7	0.98	90.8	3.4	93.4	3.4	159.9	19.5	90.8	3.4	NA
SFO19-20	684	51724	139.5	21.1541	0.8	0.0925	2.9	0.0142	2.8	0.96	90.9	2.5	89.9	2.5	63.0	18.3	90.9	2.5	NA
SFO19-29	489	61509	79.8	20.9999	0.8	0.0938	2.5	0.0143	2.3	0.94	91.4	2.1	91.0	2.2	80.4	19.3	91.4	2.1	NA
SFO19-26	695	53250	173.0	20.7485	0.6	0.0950	1.5	0.0143	1.4	0.93	91.5	1.3	92.1	1.3	108.9	13.0	91.5	1.3	NA
SFO19-32	163	31876	153.3	20.9974	1.9	0.0948	2.7	0.0144	1.9	0.70	92.4	1.7	91.9	2.4	80.7	45.9	92.4	1.7	NA
SFO19-17	765	38910	69.5	20.9999	1.0	0.0952	2.0	0.0145	1.8	0.88	92.8	1.7	92.3	1.8	80.4	23.1	92.8	1.7	NA
SFO19-14	877	62045	74.3	21.4325	0.7	0.0947	1.9	0.0147	1.7	0.93	94.2	1.6	91.8	1.7	31.8	17.1	94.2	1.6	NA
SFO19-21	280	20286	107.9	20.7337	1.4	0.0982	1.6	0.0148	0.8	0.48	94.5	0.7	95.1	1.5	110.6	33.6	94.5	0.7	NA
SFO19-22	592	83652	75.2	20.8952	1.3	0.0979	1.8	0.0148	1.3	0.70	94.9	1.2	94.8	1.6	92.2	30.5	94.9	1.2	NA
SFO19-28	140	33194	158.7	20.5118	1.5	0.1000	4.5	0.0149	4.3	0.94	95.2	4.1	96.8	4.2	136.0	35.2	95.2	4.1	NA
Sample SFO-4 with 35µc spot *(2)																			
SFO20-4	233	10107	193.9	18.7277	9.6	0.1037	11.1	0.0141	5.6	0.50	90.2	5.0	100.2	10.6	345.7	217.7	90.2	5.0	NA
Sample SFO-20 with ion counter 15 micron spot *(2)																			
SFO-20-IC-04	80	3331	153.1	20.4935	5.1	0.0920	5.9	0.0137	3.1	0.51	87.6	2.7	89.4	5.1	138.0	119.8	87.6	2.7	NA
SFO-20-IC-02	71	2777	117.4	20.0058	12.9	0.0949	13.3	0.0138	3.5	0.27	88.2	3.1	92.1	11.7	194.3	300.0	88.2	3.1	NA
SFO-20-IC-10	180	4949	230.5	20.5109	2.4	0.0958	2.7	0.0142	1.1	0.41	91.2	1.0	92.9	2.4	136.1	57.1	91.2	1.0	NA
SFO-20-IC-17	74	2286	34.8	20.2189	11.8	0.0972	15.3	0.0142	9.7	0.64	91.2	8.8	94.2	13.8	169.6	277.4	91.2	8.8	NA
SFO-20-IC-20	41	2179	220.7	21.5804	9.7	0.0914	10.0	0.0143	2.3	0.23	91.6	2.1	88.8	8.5	15.3	234.5	91.6	2.1	NA
SFO-20-IC-05	200	31817	242.6	20.8521	1.8	0.0962	4.0	0.0145	3.6	0.90	93.1	3.3	93.2	3.6	97.1	41.5	93.1	3.3	NA
SFO-20-IC-03	49	3360	-698.2	20.6979	5.9	0.0992	6.1	0.0149	1.4	0.24	95.3	1.4	96.1	5.6	114.6	139.0	95.3	1.4	NA
SFO-20-IC-14	39	4728	83.1	20.9933	12.1	0.0981	13.1	0.0149	5.1	0.39	95.6	4.8	95.0	11.9	81.1	287.2	95.6	4.8	NA
SFO-20-IC-15	50	980	86.5	22.8848	5.3	0.0903	6.3	0.0150	3.5	0.55	95.9	3.3	87.8	5.3	-127.7	130.6	95.9	3.3	NA
SFO-20-IC-08	61	1089	226.3	24.6289	4.8	0.0855	5.4	0.0153	2.4	0.46	97.7	2.4	83.3	4.3	-312.5	122.3	97.7	2.4	NA
Sample SFO-64 with 35µc spot *(1)																			
SFO-64-29	427	13425	8.0	20.4255	6.0	0.0998	6.1	0.0148	1.2	0.19	94.6	1.1	96.6	5.6	145.9	140.8	94.6	1.1	NA
Sample SFO-141 with spot 35µc *(1)																			
SFO-141-10	1675	36479	50067.7	19.8299	1.6	0.0927	1.9	0.0133	0.9	0.49	85.4	0.8	90.0	1.6	214.8	37.4	85.4	0.8	NA
Sample SFO-152 with 35µc spot *(2)																			
SFO-152-38	307	18698	289.3	19.4945	8.3	0.0987	8.6	0.0140	2.4	0.27	89.3	2.1	95.6	7.9	254.2	190.9	89.3	2.1	NA
SFO-152-32	847	47130	23.5	20.7197	1.9	0.0935	2.2	0.0140	1.0	0.46	89.9	0.9	90.7	1.9	112.2	45.9	89.9	0.9	NA
SFO-152-37	558	35106	36.3	20.9634	3.8	0.0929	4.5	0.0141	2.4	0.53	90.4	2.1	90.2	3.9	84.5	90.0	90.4	2.1	NA
SFO-152-41	369	18734	312.8	21.4115	5.9	0.0922	6.2	0.0143	1.7	0.27	91.6	1.5	89.5	5.3	34.1	142.3	91.6	1.5	NA
SFO-152-79	331	15889	5.9	20.7406	6.6	0.0954	8.2	0.0143	4.8	0.58	91.8	4.3	92.5	7.2	109.8	157.1	91.8	4.3	NA
Sample SFO-163 with 35µc spot *(1)																			

SFO-163-44	213	9514	12.8	17.6251	14.4	0.0961	17.3	0.0123	9.5	0.55	78.7	7.5	93.2	15.4	481.3	319.3	78.7	7.5	NA
SFO-163-47	240	11589	22.8	22.1225	9.8	0.0889	10.3	0.0143	2.9	0.29	91.3	2.7	86.4	8.5	-44.7	239.7	91.3	2.7	NA
SFO-163-94	135	13238	27.6	24.3348	43.1	0.0845	43.3	0.0149	3.1	0.07	95.5	2.9	82.4	34.2	-281.8	1145.0	95.5	2.9	NA

Supplementary file 3. Thermobarometric data

	Sample	Temperature °C	Pressure Kbar	Temp. Average	Temp. Std. Deviatic	Pressure ave.	Pressure Std. Dev.
Orthogneiss	**SFO-6**	708	9.2	**678**	**35**	**9.0**	**0.8**
		744	10.2				
		686	9.4				
		634	8.0				
		670	8.9				
		655	9.5				
		683	9.4				
		676	9.5				
		624	7.8				
		696	8.3				
Orthogneiss	**SFO-63**	696	7.5	**688**	**12**	**7.6**	**0.3**
		706	7.6				
		679	7.6				
		686	8.0				
		665	7.5				
		673	8.2				
		688	7.3				
		685	7.5				
		696	8.1				
		693	7.2				
		708	7.5				
		683	7.2				
		680	7.3				
Orthogneiss	**SFO-42**	718	6.8	**697**	**62**	**7.2**	**0.9**
		663	6.8				
		594	9.0				
		722	7.0				
		740	6.8				
		744	7.9				
		583	6.1				
		754	7.3				
		724	6.6				
		775	8.7				
		647	6.2				
		702	7.2				
Amphibolite	**SFO-41**	608	6.9	**663**	**56**	**7.1**	**0.6**
		665	7.4				
		661	7.3				
		672	7.3				
		680	7.2				
		607	6.0				

		701	8.4				
		623	6.7				
		791	7.5				
		622	6.7				
Amphibolite	**SFO-37**	698	8.4	**705**	**18**	**8.5**	**0.6**
		690	9.5				
		707	8.1				
		707	8.4				
		704	8.1				
		698	9.1				
		701	8.7				
		743	8.3				
		730	9.3				
		700	8.8				
		670	9.1				
		699	7.5				
		718	7.6				
Amphibolite	**SF-40**	745	8.3	**745**	**13**	**8.0**	**0.5**
		749	7.6				
		727	8.6				
		738	8.1				
		772	7.3				
		758	7.5				
		750	7.8				
		738	8.6				
		743	7.7				
		732	8.3				
Granodiorite	**SFO-40**	658	9.5	**685**	**14**	**8.9**	**1.0**
		681	9.2				
		669	8.5				
		697	7.8				
		698	7.5				
		690	10.4				
		696	9.4				
		704	9.8				
		680	8.5				
		678	8.0				
Gabbro	**SF-46**	694	9.0	**739**	**23**	**8.1**	**0.6**
		768	7.0				
		742	8.4				
		727	8.5				
		752	7.9				
		739	8.1				
		756	7.7				
		756	7.9				

	718	8.1				
General average	**699**	**8.0**				
Std. Deviation	**42**	**0.9**				
SFO-59A	675	6.0	**668**	**9**	**5.6**	**0.3**
	668	5.2				
	672	5.7				
	683	5.5				
	666	5.3				
	667	5.8				
	664	5.4				
	644	5.5				
	674	6.1				
	669	5.6				
	668	5.7				
	672	5.9				
	664	5.6				
SFO-60A	648	4.2	**633**	**24**	**3.8**	**0.6**
	645	3.8				
	612	3.0				
	646	2.7				
	571	3.7				
	637	3.1				
	652	3.6				
	634	4.7				
	628	3.5				
	611	3.6				
	660	4.6				
	639	3.7				
	649	4.6				